Axon diameter mapping using diffusion MRI

Lebina Shrestha Kakkar

A dissertation submitted in partial fulfillment

of the requirements for the degree of

Doctor of Philosophy

of

University College London.

Department of Medical Physics and Bioengineering

University College London

August 31, 2017

I, Lebina Shrestha Kakkar, confirm that the work presented in this thesis is my own. Where information has been derived from other sources, I confirm that this has been indicated in the work.

Abstract

Axon diameter plays a key role in the function and performance of nerve pathways of the central and peripheral nervous system. Therefore, there is a growing interest in imaging axon diameter non-invasively. One such technique is using diffusion MRI. The purpose of this thesis is to test the feasibility of axon diameter imaging using diffusion MRI. This thesis provides for the first time a thorough experimental framework for evaluation and comparison of diffusion MR sequences, specifically two promising sequences: SDE and OGSE.

The thesis involves designing a phantom to determine intrinsic sensitivity of the diffusion sequences to axon diameters. Additional experiments involving an *ex vivo* monkey brain and a viable rat sciatic nerve are carried out. The comparison of OGSE and SDE sequences across all different experiments demonstrate that OGSE is better than SDE. Diameter estimates of the optimal sequences are compared to the ground truth and the accuracy are found to depend on the gradient strength and SNR. For clinical scanners (G=62 mT/m and SNR$>$20), diameters of 5 μm are below the resolution limit. At G=300 mT/m and SNR=20, the resolution limit is 2.5 μm within an *ex vivo* monkey brain, causing overestimated diameters; however, an excellent prediction of the low-high-low diameter trend across the corpus callosum is observed. For G=800 mT/m and SNR=10, the resolution limit is at 2.5-3 μm for a viable rat sciatic nerve and excellent histology match is obtained.

This thesis demonstrates that axon diameter imaging using diffusion MRI is possible in the nervous system. The small axons of the central nervous system require strong gradients, which are increasingly becoming more available, and peripheral nervous system have axons that are large enough to be imaged at clinical

gradient strengths. This, therefore, opens up possibilities of using axon diameters as biomarkers for neurodegenerative diseases and peripheral nerve regeneration studies.

Acknowledgements

I am most thankful to my supervisor Dr. Ivana Drobnjak for her guidance and support throughout the last four years. You have been a great friend and a great supervisor from whom I have learned a lot about life lessons and diffusion! Thank you for not giving up on me.

I am also thankful to my second supervisor, Dr. David Atkinson, and fellow colleagues Dr. Rachel Chan and Dr. Bernard Siow for their time, patience and generosity, especially whilst doing all the late night and early morning MR scanning sessions.

I would like to thank the microstructure imaging group (MIG) for making the last four years very enjoyable and enriching my knowledge on diffusion MRI. More importantly, I would like to say a huge thanks to the MIG foodies group (Jiaying Zhang, Maira Tariq, Dr. Andrada Ianus and Dr. Elisenda Bonet-Carne), who have supported me through countless discussions on my work and kept me sane through coffee and lunch breaks, and also proof-read parts of my thesis.

Finally, I would like to thank both of my families without whom I would not be here. Aja and Aji, thank you for taking care of me and bringing me up. Mummy and daddy, thank you for the sacrifices you have made in life to get me to where I am. Ma and dad, without your understanding I would not have been able to go through the last four years as smoothly as it has done. Especially, Ma, thank you for taking care of me. I am lucky to have a mother as kind-hearted as you. Last but not the least, I would like to say my special thanks to my husband and my best friend, Sachin Kakkar. I would not be on this doctoral journey without your love and encouragement.

Publications

Journal publications and book chapters

L S Kakkar, O F Bennett*, B Siow, S Richardson, T Quick, D Atkinson, J B Phillips and I Drobnjak. Comparison of OGSE and SDE ActiveAx for axon diameter mapping: An experimental study in viable nerve tissue. (In Press, Accepted to NeuroImage)

*shared first author

L S Kakkar, I Drobnjak, A Ianus and T Dyrby. Axon diameter imaging in a monkey corpus callosum: OGSE outperforms PGSE. (In Preparation)

L S Kakkar, D Atkinson, R W Chan, B Siow, A Ianus and I Drobnjak. Pore diameter mapping on a clinical scanner using orientationally-invariant OGSE ActiveAx, Computational Diffusion MRI, MICCAI Workshop 2016.

Conference Publications

L S Kakkar, O F Bennett, B Siow, S Richardson, T Quick, D Atkinson, J B Phillips and I Drobnjak. Low frequency oscillating gradient spin-echo sequences improves sensitivity to axon diameter an experimental validation study in live nerve tissue. In Proceedings of the International Society for Magnetic Resonance in Medicine 24th Scientific Meeting, Singapore city, Singapore, 2016. - oral presentation

L S Kakkar, D Atkinson, R W Chan, B Siow, A Ianus and I Drobnjak. Imaging microstructure: Application of oscillating gradient diffusion sequences on a 3T clinical MRI scanner. In Proceedings of the Joint International Society for Magnetic Resonance in Medicine and European Society for Magnetic Resonance in Medicine and Biology Scientific Meeting, Milan, Italy, 2014 - poster presentation

L S Kakkar, D Atkinson, R W Chan and I Drobnjak. Imaging microstructure: Application of oscillating gradient diffusion sequences on a 3T clinical MRI scan-

ner. In Proceedings of the 23rd British Chapter International Society for Magnetic Resonance in Medicine and European Society for Magnetic Resonance in Medicine Postgraduate Symposium Scientific Meeting, Cardiff, U.K., 2014 - poster presentation

Academic awards

- Awarded the *summa cum laude* honor for the conference abstract on 'Low frequency oscillating gradient spin-echo sequences improves sensitivity to axon diameter an experimental validation study in live nerve tissue' at the International Society for Magnetic Resonance in Medicine 24th Scientific Meeting, Singapore, 2016.

Contents

List of Figures

List of Tables

Chapter 1

Introduction

Axon diameter is an important factor in the conduction velocity of signal transmission throughout the neural pathways in the central nervous system (CNS) and peripheral nervous system (PNS) [1, 2].

In CNS, bundles of axons form white matter tracts, which connect different regions of the brain and spinal cord. Estimates of axon diameter can provide essential information on the performance and function of white matter pathways [3–6], which can be used in studies of ageing [7] or CNS diseases, such as amyotrophic lateral sclerosis [8, 9] and schizophrenia [10, 11], as well as pscyhiartic conditions such as autism [12, 13], where axonal degeneration can lead to abnormal axon diameters.

In PNS, bundles of axons form peripheral nerves, which connect CNS to other parts of the body and unlike CNS axons, PNS axons can regenerate. In damaged nerves, axon diameter estimates can be used to accurately monitor and quantify the extent of axon regeneration [14, 15].

Developing a realistic technique to measure axon diameter is thus of great interest. Traditionally this has only been possible through biopsy and histology, which provide the gold standard. However traditional methods are invasive. Diffusion magnetic resonance imaging (MRI) is a non-invasive technique that has been developed over the last 20 years for investigating and understanding the microstructure of biological tissues. The diffusion signal is dependent on the displacement of water molecules and hence structural information can be inferred at the microscopic level *in vivo*.

A number of methods that use diffusion MRI for estimating axon diameter have been proposed, such as q-space imaging (QSI) [16], double diffusion encoding (DDE) sequences [17, 18], AxCaliber [19] and ActiveAx [20]. The techniques use either single diffusion encoding (SDE) sequences or DDE sequences, which have similar sensitivity to diameters as SDE sequences [21, 22]. These techniques are not reliable yet and are still under development as they usually require advanced MR hardware and long scan times. In all cases, the diameter estimates are larger than those from histology suggesting that the techniques are not sensitive to changes in axon diameters. However, various authors suggest that oscillating gradient spin-echo (OGSE) offers benefits over the standard SDE sequences for imaging diameters [23–25].

OGSE sequences have a lot of potential to provide detailed maps of microstructure. As the name suggests, OGSE sequences have oscillating gradient waveforms that replace the typical single pulsed field gradient waveforms in SDE sequences. The oscillations allow for shorter effective diffusion times and hence can probe shorter distances. Theoretically [24, 25], it has been shown that low frequency OGSE sequences show additional sensitivity to axon diameters in realistic cases of unknown orientation and fibre dispersion compared to SDE sequences [24] and this sensitivity increases further with larger gradient strengths. However, this has not been studied in practice.

Here we experimentally investigate the feasibility of imaging axon diameters using diffusion MRI, more specifically OGSE and SDE sequences. We explore the potential of the sequences for axon diameter imaging, both in clinical and preclinical settings, using non-biological and biological substrates.

1.1 Scope and objectives

The aim of this thesis is to test the feasibility of axon diameter imaging using diffusion MRI in practice. Here we especially focus on the potential of OGSE sequences in imaging axon diameters of biological tissues and compare their performance to the standard SDE technique. The scope of this investigation covers clinical and pre-

clinical settings and substrates including glass micro-capillaries, *ex vivo* monkey brain and viable rat sciatic nerve tissue.

Our specific objectives are to:

1. Implement and validate OGSE sequences on a clinical scanner.
2. Design a physical phantom that represent the cylindrical geometry of axons in nerve tissue.
3. Investigate the feasibility of using diffusion MRI for measuring diameters on a clinical scanner using the physical phantom designed in 2.
4. Apply and compare OGSE and SDE protocols on an *ex vivo* monkey brain together with simulation studies on a preclinical scanner.
5. Assess the performance of OGSE and SDE using diffusion MRI for measuring diameters on a preclinical scanner using the physical phantom designed in 2.
6. Assess the performance of OGSE and SDE beyond the standard tissue model using simulations on a preclinical scanner.
7. Apply and compare OGSE and SDE protocols on a viable rat sciatic nerve tissue on a preclinical scanner.

1.2 The outline of the thesis and contributions made

This thesis is structured as follows, with contributions made appearing in *italic*:

- In **Chapter 2**, we give an overview of the importance of axons in the central and peripheral nervous system, which is followed by the background theory on MRI, diffusion MRI and axon diameter mapping techniques using diffusion MRI.
- In **Chapter 3**, *we implement and validate OGSE sequences on a Philips 3T clinical scanner.* With issues surrounding patient safety, which has to comply

with safety standards set by International Electrotechnical commission (IEC), and hardware safety, implementing oscillating gradients onto a clinical MRI system faces many considerations. We show that implemented OGSE sequences pass through the safety checks of the Philips MRI scanner simulator and also stay within the manufacturer set limits for both patient safety (peripheral nervous stimulation (PNS)) and hardware safety (gradient coil and amplifier heating). We also validate the implementation of OGSE sequences on the MR scanner using gelatine phantoms to ensure images are artefact free. *We conclude the chapter with successful implementation and validation of OGSE sequences on the clinical scanner.*

- In **Chapter 4**, *we test the feasibility of using OGSE sequences on a clinical scanner to estimate axon diameters.* The translation of axon diameter imaging techniques to clinical MR scanners is a big challenge due to the limited gradient strengths $\leq$ 60mT/m. Here we use a phantom with varying microcapillaries diameters (5, 10 and 20 μm), which we specifically developed to represent the geometry of nerve tissue, and image this phantom with a range of OGSE sequences. We assess the feasibility of using OGSE sequences by reporting the accuracy and precision of the estimated pore diameters of the phantom. *We conclude the chapter stating that axon diameter mapping of the human brain is not currently possible at G = 60 mT/m because at this gradient strength diameters below 5 μm cannot be distinguished even in the simplest of phantoms.*

- In **Chapter 5**, *we evaluate the performance of optimised OGSE sequences over optimised SDE sequences in an ex vivo monkey brain on a preclinical 4.7 T MR scanner at a gradient strength of 300 mT/m.* We also confirm the findings from *ex vivo* white matter tissue *in silico* using multi-diameter substrates. *We show for the first time in experiments that OGSE sequences are more sensitive than SDE sequences to smaller axon diameters at G = 300 mT/m.*

- From Chapter 6 onwards, we investigate the performance of OGSE and SDE sequences optimised for a viable rat sciatic nerve on a preclinical 9.4 T MR scanner at a gradient strength of 800 mT/m. In **Chapter 6**, *we design a new phantom containing a range of microcapillaries and use the phantom to test the innate sensitivity of the optimised OGSE and SDE protocols to the diameters of the microcapillaries. We conclude the chapter by demonstrating OGSE gives slightly more accurate estimates of the smallest diameter (2μm) than SDE sequences, especially when the number of measurements are reduced.* In addition to this, we also determine the range of diameters in the new phantom that are accurately estimated by the optimised sequences, which can serve as a guideline for the range of diameters that can detected under the best circumstances in tissue when using the same sequences.

- In **Chapter 7**, *we investigate the performance of OGSE and SDE sequences in synthetic substrates that mimic the axon distribution of a rat sciatic nerve and further determine whether the standard tissue model is the best tissue model to represent the rat sciatic nerve*. We use synthetic substrates with a range of intra-axonal volume fractions and cylinders that range from single diameters to multi-diameters. *We find that the standard tissue model requires a simple modification to give accurate diameter estimates and improves the agreement of the measured signal with the analytical signal model. Regardless of the model used, we also find the OGSE gives higher accuracy than SDE.*

- In **Chapter 8**, *we perform axon diameter mapping for the first time on a viable rat sciatic nerve tissue using the optimised OGSE and compare its performance to the optimised SDE protocols.* We assess the ability of the two sequences to give accurate tissue model parameter estimates that are robust when the number of measurements are reduced by comparing the results with histology. *We conclude by demonstrating accurate axon diameter mapping in the viable rat sciatic nerve tissue, with OGSE giving more accurate axon diameter estimates than SDE.*

- In **Chapter 9**, we discuss the findings and conclusions of the previous chapters and suggest some potential future applications of OGSE sequences in clinical and pre-clinical environments.

Chapter 2

Background

This chapter provides the background knowledge for axon diameter imaging using diffusion MRI. The first section describes our main tissue of interest, the axons. The second section presents the basic principles of MRI, including the nuclear magnetic resonance phenomenon, signal excitation and imaging. The third section describes the theory of diffusion weighted MRI, especially analytical expressions for modelling free and restricted diffusion. The fourth section introduces different methods of axon diameter imaging which includes some model-based and some model-free methods. The fifth section explains the clinical MRI hardware constraints that are relevant to diffusion MRI.

2.1 Axons

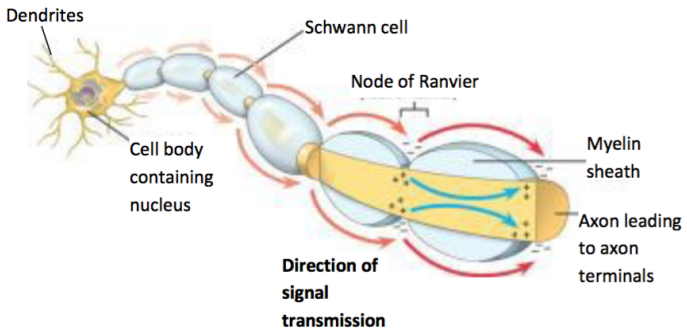

Figure 2.1: The components of a typical nerve cell and the pathway of the electrical signal. Diagram adapted from [26].

An axon is the long wire-like portion of a nerve cell which conducts signal

towards other nerve cells. Figure 2.1 illustrates the structure of a typical axon. Billions and billions of nerve cells (also known as neurons) participate in cell-to-cell communication, like electrical wires, to build a communication network, which make up a large part of the nervous system. The nervous system (as shown in Figure 2.2), which comprises of the central nervous system (CNS) and peripheral nervous system (PNS), uses this communication network to coordinate and control the functions of the body [27].

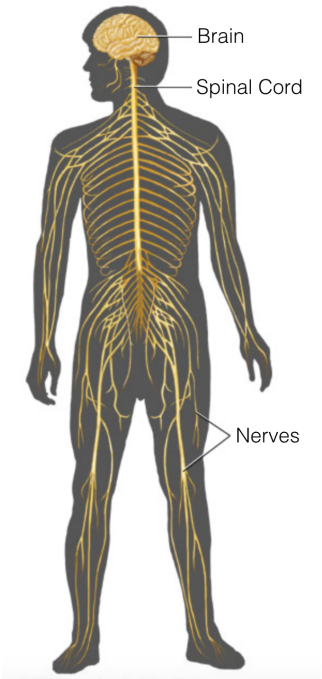

Figure 2.2: The nervous system is divided into the central nervous system (CNS) and the peripheral nervous system (PNS). The brain and spinal cord make up the CNS, and the peripheral nerves that reach all others parts of the body make up the PNS. Image as featured in [28].

In general, communication between nerve cells begins from the arrival of an electrical signal from a neighbouring nerve cell. The signal is received by the dendrites of the nerve cell and is passed along to its cell body. Here the signal is processed and passed towards the axon. At the axon, the signal is conducted along the length of the axon and is transmitted across a gap (synapse) to the dendrites of the adjacent nerve cells. Figure 2.1 describes this process pictorially and a more rigorous description is provided in Section 2.3.4.1.

The speed of signal transfer along the axons are determined by two primary

factors: insulation of the axon and diameter of the axon. Axons of most nerve cells are surrounded by an electrically insulating tissue known as the myelin sheath. The myelin sheath insulates the signal, whilst nodes that separate the myelin sheaths (known as nodes of Ranveir) allow the signal to 'jump' to the next node of Ranveir, speeding up the signal transmission [27].

The diameter of the axon is the main focus of this thesis. Axon diameter is directly proportional to the conduction velocity of myelinated axons [1, 2]. As a result, imaging axon diameter is very important because it can provide information on the role and performance of neural pathways of the nervous system.

2.1.1 The central nervous system (CNS)

The central nervous system (CNS) is made up of the brain and spinal cord. They are responsible for processing sensory information and coordinating the associated body function, both voluntarily or involuntarily. The brain alone is also responsible for complex functions such as emotions, memory and speech [27].

Axons of the central nervous system are mostly present in the white matter of the brain and spinal cord. Their diameters usually range from 0 to 3 μm in a human brain [29–31] and 1 to 10 μm in the human spinal cord [32, 33]. The axons are surrounded by myelin sheath, produced by glial cells that are specific to the CNS (oligodendrocytes), which increases the speed of signal transfer. The myelinated axons are usually tightly packed into large bundles, known as tracts. These tracts connect different functional regions of the brain and enable communication.

White matter is only one of the three main components of CNS. The other two components are grey matter and the cerebrospinal fluid (CSF). Grey matter comprises mostly of nerve cell bodies, which are the information processing centres of the brain. Cell bodies with similar functions and structures are grouped together to form larger functional areas called nuclei. These nuclei then work together to perform simple to complex tasks using the white matter tracts as the means for communication between the nuclei. Unlike the grey matter and white matter, both of which are involved in information processing, CSF mainly exists in the CNS to provide a mechanical and immunological protection to the brain.

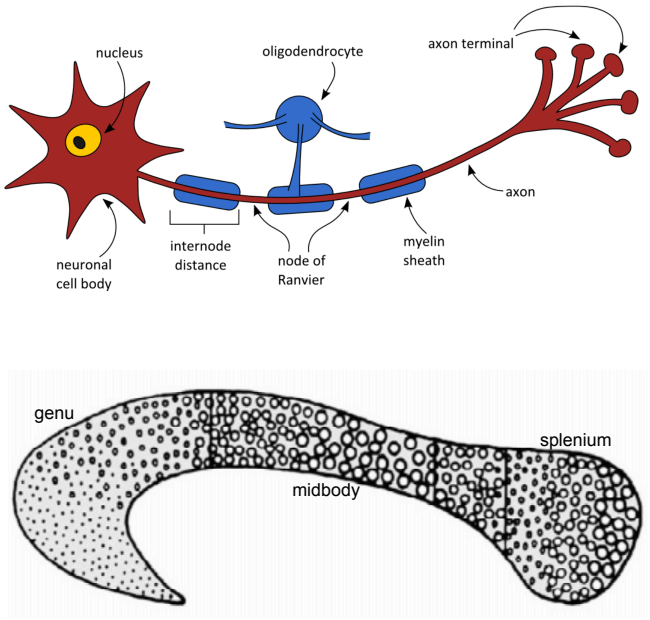

Figure 2.3: (a) An example of a typical CNS axon (as featured in [34]) (top). (b) An example of axons within a white matter region, known as the corpus callosum (as featured in [3]) (bottom).

.

2.1.2 The peripheral nervous system (PNS)

The peripheral nervous system (PNS) consists of spinal and cranial nerves (known as peripheral nerves) which connect the CNS to the entire body and carry information between them. PNS is further subdivided into the somatic and autonomic nervous system. The former is involved in the voluntary control of body movements and the latter regulates automated body functions such as heart rate and blood pressure.

Axons of the peripheral nervous system are housed deep within a peripheral nerve, as shown in Figure 2.4. Their diameters usually range from 1 to 14 μm in humans [36, 37]. These axons are surrounded by myelin sheath, produced by glial cells that are specific to the PNS (Schwann cells), which increases the speed of signal transfer. The myelinated axons are surrounded by a connective tissue known as the endoneurium. The ensemble is bound by the perineurium into a structure called fascicle. Multiple fascicles, along with some blood vessels, are then bound by the epineurium to form a peripheral nerve [28]. As an example, Figure 2.4 shows the largest single peripheral nerve in the body called the sciatic nerve, which originates

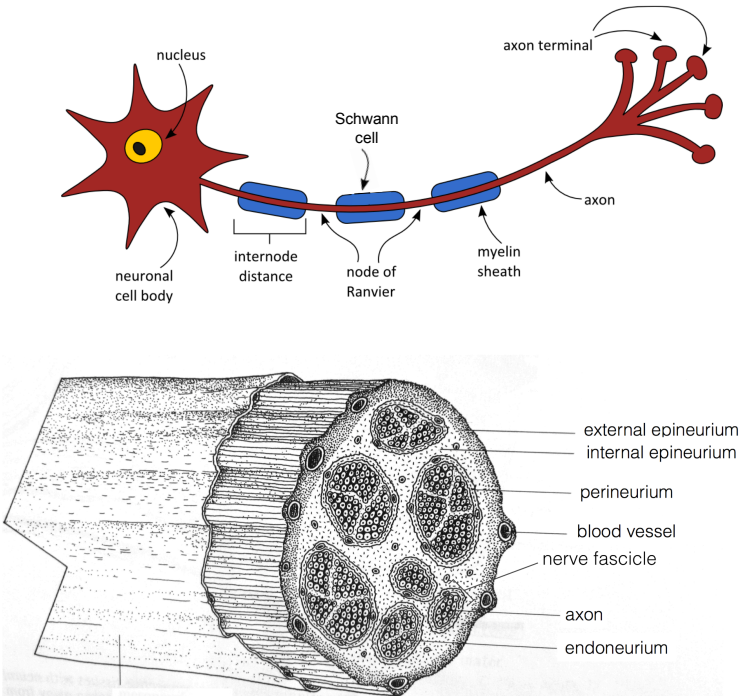

Figure 2.4: (a) An example of a typical PNS axon (adapted from [34]) (top). (b) An example of a peripheral nerve (as featured in [35]) (bottom).

from the lower portion of the spinal cord and is responsible for the nervous system of the whole leg.

2.1.3 Importance of axon diameter imaging

Axon diameter is important in both CNS and PNS. As mentioned before, diameters of myelinated axons are directly correlated with the conduction velocity of signal transfer along the axon [1, 2]. The location and diameter of axons, therefore, are a good indicator of the roles and functions of the areas that receive/send the information [30].

A key white matter region is the corpus callosum (CC) which is shown in Figure 2.3. It is a collection of tracts, known as the commissural fibres that connect many different functional areas between the left and right hemispheres of the brain. The CC is divided into three smaller regions: genu (located at the front of the CC), midbody (located at the middle of the CC) and splenium (located at the back of the CC) [38]. Densely packed small-diameter axons at the genu connect the left and right prefrontal cortices to provide a diverse amount of information that is required

by the cortices to make complex decisions. Large-diameter axons in the midbody connect the left and right motor cortices to provide fast signal processing which are required for the coordination of voluntary movement. Similar to the genu, at the splenium, densely packed small diameter axons connect the left and right temporoparietal visual areas [29, 38, 39]. This distinct low-high-low axon diameter trend, along with the high-low-high axon density, has been repeatedly observed in humans [29] and in monkeys [39].

In the PNS, axons with large diameters are present in motor pathways where rapid signalling is required. Small-diameter axons, on the other hand, are found in pathways that require slower neuronal communication such as those responsible for temperature and nociceptive sensations [40]. In general, axon diameters can help us understand and determine the roles of the functional areas in the CNS and PNS.

Understanding and detecting neurological diseases related to the CNS or PNS is one of the main factors for axon diameter imaging. Abnormal axon diameters in patients, in comparison to controls, can indicate the presence of certain neurological diseases. For instance, swollen axons appear in amyotrophic lateral sclerosis (ALS) [8, 9] and schizophrenia [10, 11], both of which arise from a process called demyelination. The demyelination in ALS occurs from damage to healthy myelin sheath, which progressively leads to loss of all voluntary movement. On the other hand, the demyelination in schizophrenia occurs from disruption to the function of the glial cells supporting the axons. Psychiatric conditions like autism have also shown a higher density of unusually small axons in the anterior cingulate and orbitofrontal cortices, which is associated with the mechanism responsible for the abnormalities in emotion and attention seen in the disorder [12, 13].

Another key reason for axon diameter imaging is to monitor regeneration rate of peripheral nerves. Physical injuries, such as road traffic accidents, can damage axons or the nerves that house the axons, causing either a physical division of the nerve (very severe) or crushing of the nerve (less severe). The injuries therefore lead to either delayed or completely halted signal transfer. Damaged nerves further undergo a process known as Wallerian degeneration over a period of several days,

which involves the decay of the distal portion of the axon (the part that is disconnected from the associated cell body of the nerve cell [41]). Following this, the PNS axons are able to regenerate to restore the function of the affected nerve, provided the injury site has been cleared by macrophages [42]. Unfortunately, axon recovery is inhibited in CNS [43] and therefore CNS injuries permanently impact the quality of life of the affected person. In PNS, the nerve regeneration process involves the release of chemicals by the distal targets of the affected peripheral nerve to guide and enhance the growth of proximal axons towards the distal targets. When severed nerves occur, surgical intervention is required to bridge the gap between the transected peripheral nerves to allow axonal regrowth. As such, the non-invasive monitoring of nerve regeneration rate is essential [44] for ensuring that the nerves re-grow correctly. A good indicator of nerve regeneration rate has been shown to be the axon length and axon diameter [14, 15]. Hence imaging axon diameters can also assist in non-invasive monitoring of nerve regeneration rate.

2.1.4 Traditional approach for axon diameter imaging

The traditional approach of imaging axon diameters is using histology. The tissue of interest (white matter or peripheral nerve) has to be carefully dissected, fixed and then stained to ensure visibility of the myelinated axons. The tissue samples are then viewed under a light microscope, which provides an imaging resolution in the order of micrometres [29, 45]. The use of electron microscopy (see Figure 2.5) is more common nowadays with resolution at the nanoscale that allows detailed imaging and quantification of axon structure, their diameter, distribution of axon size and density [29, 39]. Currently, histology is perceived as the gold standard for axon diameter imaging. However, the method also poses a few disadvantages. First, sample preparation, involving tissue fixation and staining needs to be carried out carefully but quickly to prevent tissue sample deterioration. Second, the fixation process used to preserve the tissue tends to cause shrinkages of up to a factor of 30% [31]. The final and main disadvantage of using histology for clinical use is that painful invasive biopsies are required to obtain tissue samples, and additionally in the brain biopsies are possible but are extremely invasive.

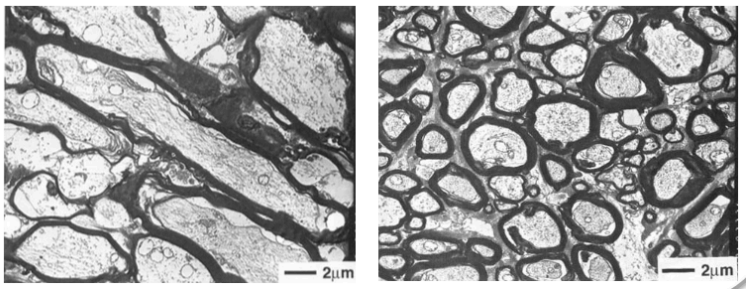

Figure 2.5: An electron-micrograph of bovine optic nerve in the parallel (left) and perpendicular (right) to the axis of the main fibre orientation. The Figure is as featured in [46].

.

As a result, there have been a lot of research into developing methods for non-invasively imaging axon diameters. Most of these methods involve the use of MRI. We describe these methods in Section 2.3 and Section 2.4 but first in the next section, we will describe the foundations of MRI.

2.2 Magnetic Resonance Imaging (MRI)

Throughout the past few decades, MRI has become a powerful imaging modality, especially for imaging soft tissues in the human body. The popularity of MRI stems from using non-ionising radiation (unlike X-rays and γ-rays) to generate high resolution images that allow non-invasive probing of the internal structures and functions of biological tissues. MRI also provides variety of contrast mechanisms (such as T1-weighted, T2-weighted and diffusion-weighted imaging) depending on the application. Such advantages make MRI a safe, reliable and a universal imaging tool for people of all ages, as well as animals.

2.2.1 Spins, magnetic moments and bulk magnetization

MRI is an application of a physical phenomenon known as nuclear magnetic resonance (NMR). NMR was first observed in the late 1945 by Purcell and Bloch. The phenomenon relies on the interaction between atomic nuclei with a non-zero spin and a magnetic field. In most MRI applications, the nucleus of interest is hydrogen because of the abundant hydrogen atoms found in biological tissues.

The nucleus of hydrogen consists of one proton and therefore has a charge,

mass and a quantum mechanic property called 'spin', $\mathbf{I} = \frac{1}{2}$. The mass and spin give rise to the quantum angular momentum of the proton, $\mathbf{J}$. In addition, the combination of angular momentum and charge of the proton induces a magnetic field, known as the nuclear magnetic moment, μ.

$$\mu = \gamma \mathbf{J} \tag{2.1}$$

where $\gamma = 2.68 \times 10^8$ $s^{-1}T^{-1}$, the gyromagnetic ratio for ^1H.

When no external magnetic field is present, the direction of μ is random due to the thermal movements of hydrogen atoms. Therefore, the magnetic moments cancel each other out resulting in a zero net magnetization. This is illustrated in Figure 2.6.

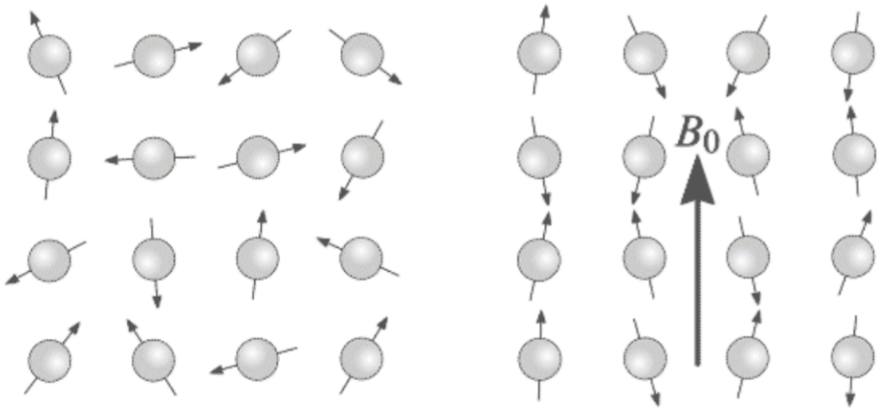

Figure 2.6: Hydrogen atoms and the directions of their magnetic moments in absence of a static external magnetic field (left) and presence of the static external magnetic field (right). Note the parallel and and anti-parallel alignment to the B_0 field. Figure extracted from [47].

However, when an external static magnetic field, B_0, is applied, the magnetic moment interacts with the external magnetic field producing a torque that causes the protons to precess about the main axis of B_0, at an angular frequency known as the Larmor frequency:

$$\omega_0 = \gamma B_0 \tag{2.2}$$

In the presence of the external magnetic field, quantum mechanics states that hydrogen has two discrete energy levels: 'spin up'/parallel to B_0 and 'spin

down'/anti-parallel to B_0, as illustrated in Figure 2.6. The ratio of the number of atoms in the spin-up state ($N_{\uparrow\uparrow}$) to the spin-down state ($N_{\downarrow\downarrow}$) is defined by the Boltzmann distribution (Equation 2.3). This ratio is dependent on the strength of B_0 and depends inversely on temperature (T) of the sample.

$$\frac{N_{\uparrow\uparrow}}{N_{\downarrow\downarrow}} = e^{\frac{\Delta E}{kT}} = e^{\frac{\gamma\hbar B_0}{kT}} \tag{2.3}$$

where k = 1.38 $\times$ 10^{-23} J/K, the Boltzmann constant and $\hbar$ = 1.05 $\times$ 10^{-34} Js, the reduced Planck constant.

For example, at typical body temperature (37^oC) and for a standard MRI system (B_0 = 3 T), for every 100,000 spin-down nuclei, there are an extra 2 spin-up nuclei and for an animal MR system (B_0 = 9.4 T), there are an extra 6 spin-up nuclei. The net sum of the magnetic moments, due to these extra magnetic moments, creates an equilibrium magnetization, M_0, parallel to the direction of the main magnetic field B_0:

$$M_0 = \frac{N\gamma^2\hbar^2 B_0}{4kT} \tag{2.4}$$

where N is the number of protons per unit volume.

As the net magnetization is measured from a volume, and not from individual nuclei, in an MRI experiment, their average behaviour can be described using classical mechanics, instead of quantum mechanics [48].

2.2.2 Excitation and detection of MR signal

The net magnetization per unit volume gives rise to the macroscopic magnetization, **M**. In order to be able to measure **M**(t), it has to be perturbed from the thermal equilibrium position (away from the main magnetic field B_0). This is done by applying a RF (radiofrequency) pulse, perpendicular to the B_0, for a specific duration and is commonly referred to as the B_1 field. The B_1 field rotates at the same frequency as the precession frequency of the macroscopic magnetization, and allows **M** to be tipped away from the main field. This is called the 'resonance effect'.

The evolution of **M** with time t, in the presence of a magnetic field, **B**(t) is

describe by Equation 2.5 from which information on the sample of interest can be characterized.

$$\frac{d\mathbf{M}(t)}{dt} = \gamma.\ \mathbf{M}(t) \times \mathbf{B}(t) \tag{2.5}$$

which can be expanded to:

$$\frac{dM_x(t)}{dt} = \gamma(M_y(t)B_z(t) - M_z(t)B_y(t)) \tag{2.6}$$
$$\frac{dM_y(t)}{dt} = \gamma(M_z(t)B_x(t) - M_x(t)B_z(t)) \tag{2.7}$$
$$\frac{dM_z(t)}{dt} = \gamma(M_x(t)B_y(t) - M_y(t)B_x(t)) \tag{2.8}$$

When the B_0 field is parallel to the z-axis, $B_z(t) = B_0$, a constant, whereas $B_x(t) = B_y(t) = 0$. Hence, the evolution of **M**(t) from Equation 2.5 becomes:

$$\frac{dM_x(t)}{dt} = \gamma M_y(t)B_z(t) \tag{2.9}$$
$$\frac{dM_y(t)}{dt} = -\gamma M_x(t)B_z(t) \tag{2.10}$$
$$\frac{dM_z(t)}{dt} = 0 \tag{2.11}$$

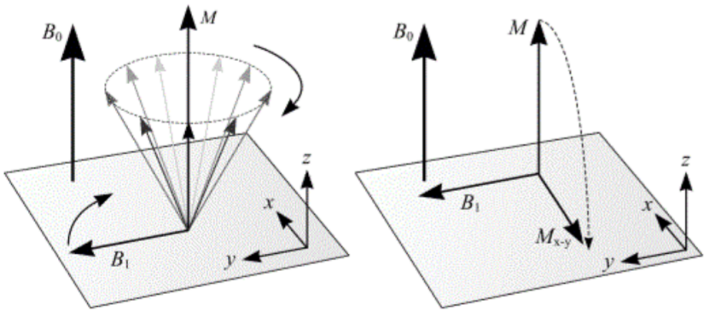

Figure 2.7: Tipping of M due to application of B_1 shown in (a) the stationary frame and (b) the rotating frame of the B_1 field . These figures are featured in [47].

In the presence of the B_1 field, $B_x(t) = B_1\cos(\omega t)$, $B_y(t) = B_1\sin(\omega t)$ and $B_z(t)=B_0$. Here, **M** will be tipped away from the z-axis provided that the $\omega=\omega_0$. Typically in most MRI applications, a 90^o RF pulse is applied to allow **M** to reach

the xy plane. Figure 2.7 illustrates the tipping in the stationary frame of reference (left) and rotating frame of reference (right).

The macroscopic magnetization has a tendency to realign with the main B_0 field. Hence, when the RF pulse is switched off, the z-component of **M**, M_z, will increase in magnitude via a process known as longitudinal relaxation (or T1 relaxation) and M_{xy} will decrease in magnitude in the xy plane by another independent mechanism called transverse relaxation (or T2 relaxation). This is described by the Bloch equations below:

$$\frac{dM_x(t)}{dt} = \gamma(M_y(t)B_z(t) - M_z(t)B_y(t)) - \frac{M_x(t)}{T_2} \tag{2.12}$$

$$\frac{dM_y(t)}{dt} = \gamma(M_z(t)B_x(t) - M_x(t)B_z(t)) - \frac{M_y(t)}{T_2} \tag{2.13}$$

$$\frac{dM_z(t)}{dt} = \gamma(M_x(t)B_y(t) - M_y(t)B_x(t)) - \frac{M_z(t) - M_0}{T_1} \tag{2.14}$$

where T_1 and T_2 are the relaxation constants for the T1 and T2 relaxation processes, respectively. The T1 relaxation occurs when spins exchange energies between each other, as they come close together, which causes dephasing of the individual spins of the nuclei and hence reduces M_{xy}. The longitudinal relaxation occurs due to the loss of energies associated with the spins of the nuclei to its surroundings. As examples, the T1 and T2 of white matter are 600 ms and 80 ms [49], respectively, peripheral nerves are 700 ms and 70 ms [50], respectively, and water is $\approx$ 3000 ms [51].

The precession of M_{xy} (subjected to T2 relaxation) around the main magnetic field generates a free induction decay (FID) signal. The signal is received by the RF receiver coils and induces an alternating voltage that can be recorded.

However, in reality, the signal decays much faster because the decay in M_{xy} is also affected by magnetic inhomogeneity in the surrounding environment of the nuclei. If we call this apparent relaxation time T_2', then the effective T2 relaxation, which is usually referred to as T2* can be described using Equation 2.15.

$$\frac{1}{T_{2*}} = \frac{1}{T_2} + \frac{1}{T_{2'}} \tag{2.15}$$

The effect of inhomogeneities can be reversed by using a technique known as spin echo. At the start of the experiment, a 90^oRF excitation pulse is used to flip the macroscopic magnetization of the ensemble of spins on the xy axis. As time increases, the spins dephase (as shown by circles on the top of Figure 2.8) due to T2 relaxation, and especially due to T2*, which reduces the signal M_{xy}. At time TE/2, a second refocusing 180^oRF pulse flips the spins, so that the spins with faster precession are behind the spins that precess slowly. At time TE, the spins rephase to form a signal echo. This is known as spin-echo.

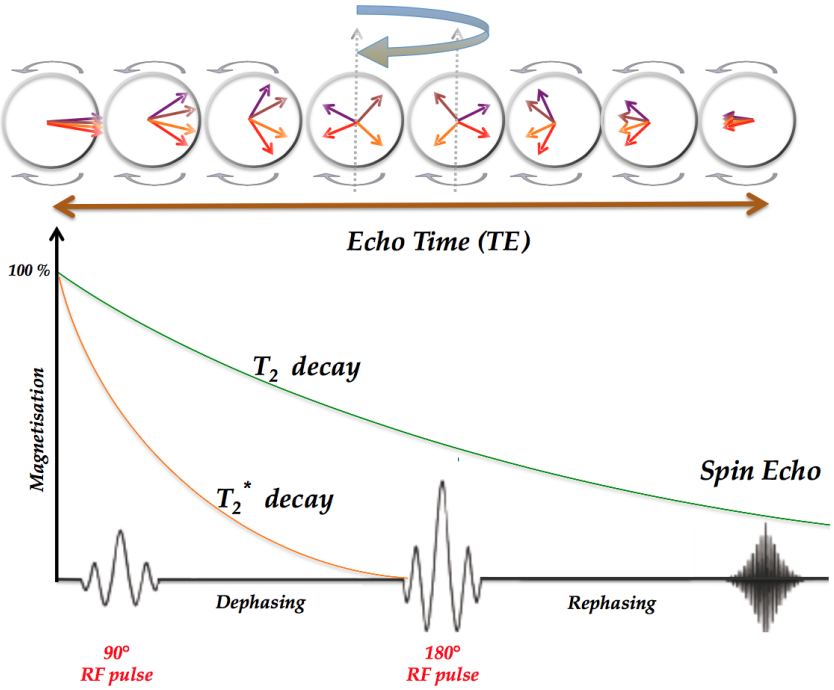

Figure 2.8: The spin-echo sequence. Diagram as featured in [52]

.

2.2.3 Spatial encoding

The acquired NMR signal is an average signal over the whole volume of the sample [49]. In order to create an image, the signal needs to be spatially localised. This is achieved during MR acquisition by using additional magnetic field gradients, **G**(t) = (G_x, G_y, G_z), which are applied along the x, y and z scanner axes. The role of the gradients is to modify the effective magnetic field strength, B_{eff}:

$$B_{eff} = B_0 + \mathbf{G.r} \tag{2.16}$$

The gradients cause B_{eff} to spatially vary as a function of position, **r** = (x, y, z). Consequently, the precession frequency of the spins within the sample being scanned and the phases accumulated by the spins also vary spatially (as in Equation 2.2). This enables direct encoding of spatial information into the measured signal.

For a 3D volume, spatial localization is usually achieved through three main steps: (1) slice encoding (2) frequency encoding and (3) phase encoding.

Slice encoding involves the use of a slice select gradient to ensure that only a two dimensional plane within the 3D volume is imaged. The slice selection gradient, which is applied simultaneously with an RF excitation pulse, linearly varies the resonant frequencies of the spins as a function of the position along the gradient direction (slice direction). The RF pulse usually has a narrow distribution of frequencies, known as the bandwidth, and therefore, only the frequencies of spins that are within the RF bandwidth are excited and produce a signal. Different slices can be excited by varying the frequencies of the RF pulse.

Once the slice is selected (for example, along the z-axis), spatial encoding is required to localise the signals within the two dimensional plane using frequency encoding (for example, along the x-axis) and phase encoding direction (for example, along the y-axis). First, the phase encoding gradient (G_y) is briefly switched on for a time, τ_{PE}. During this time, the precession frequencies of the spins vary with their position. When the gradient is switched off, all of the spins revert back to the Larmor frequency, however with different phases along the y position, which is given by:

$$\phi(y) = y \int_0^{\tau_{PE}} \gamma G_y(t) dt \tag{2.17}$$

Subsequently the frequency encoding gradient is then applied along the x-position for a time τ_{FE} at time TE. The frequency encoding gradient alters the

precession frequency of the spins along the x position to be:

$$\omega(x) = \omega_0 + x\int_{TE}^{TE+\tau_{FE}} \gamma G_x(t)dt \tag{2.18}$$

After carrying out the spatial encoding in the 2D plane, the total MR signal, S(t), is:

$$S(t) = \int\int I(x,y)e^{-i2\pi y\int_0^{\tau_{PE}}\gamma G_y(t)dt}e^{-i2\pi x\int_{TE}^{TE+\tau_{FE}}\gamma G_x(t)dt}dxdy \tag{2.19}$$

where I(x,y) is the image function. S(t) can be further simplified to:

$$S(t) = \int\int I(x,y)e^{-i2\pi k_y y}e^{-i2\pi k_x x}dxdy \tag{2.20}$$

where, k_x and k_y are defined as the spatial frequencies:

$$k_x = \int_{TE+\tau_{FE}}^{TE} \gamma G_x(t)dt \qquad\qquad k_y = \int_{\tau_{PE}}^{0} \gamma G_y(t)dt \tag{2.21}$$

There is a Fourier relation between the image function I(x,y) and the signal S(k_x, k_y). Therefore by measuring the signal at many points of k_x and k_y, often called the k-space, the image function can be recovered.

A standard method to fill up k-space is using a linear scheme. At each phase encoding step, frequency encoding is carried out to fill one line of k-space. Repeating this process of phase and frequency encoding multiple times (for example 64 times) results in acquiring the data for all values of k_x and k_y (as shown on the right panel of Figure 2.9).

The current method of filling up the k-space takes a long time. One line of k-space is read per TR, and therefore to cover 64 points in the k_y-direction, 64*TR is required. In diffusion imaging, image acquisition needs to fast to allow time for measuring diffusion in many directions. In this thesis, the majority of methods use a technique called single-shot spin echo imaging (SS-EPI) or multi-shot spin echo imaging (MS-EPI) to speed up image acquisition.

In SS-EPI, once the slice of interest is excited, phase encoding for the whole slice is carried out within one TR. In order to achieve this, the k-space is traversed from the centre ((k_x,k_y)=(0,0)) to the bottom left corner of k-space by using large negative gradients G_x and G_y. Subsequently, the oscillating G_x and the 'blipped' G_y pulses allow the k-space to be sampled in a linear zig-zag pattern as illustrated in Figure 2.9 until the whole k-space is filled. On the other hand, MS-EPI involves multiple phase encoding per TR, until all the k_y-space is filled.

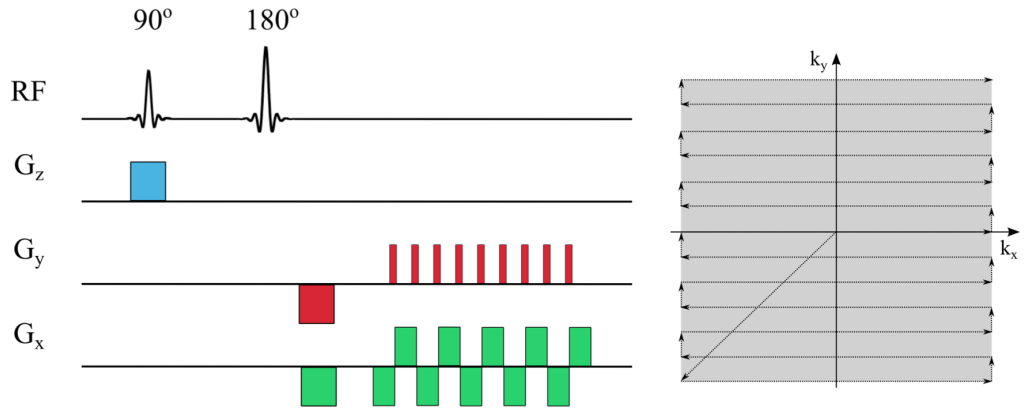

Figure 2.9: Schematic representation of a single shot echo planar imaging (SS-EPI) sequence (left). Diagram as featured in [53]

.

Once the k-space is filled, the image I(x,y) can be reconstructed from the raw k-space data using a 2D inverse Fourier transform. I(x,y) is a complex image function which can be used to form both magnitude and phase images [49].

2.2.4 Summary

Overall, in this section, we have described the basics of MR signal generation, signal excitation and signal detection. The mechanisms of signal decay (T1, T2 and T2*) are also briefly outlined. We then describe the principles behind spatial encoding of the signal to generate an MR image, and end with a very brief description of the fast MR acquisition methods that will be used in thesis.

2.3 Theory of diffusion MRI

The method of axon diameter imaging that we focus on in this thesis is related to a specific modality of MRI called diffusion weighted MRI. In this section, we will describe the principles behind diffusion MRI, the different types of waveforms used to measure diffusion as well as analytical expressions used to calculate free and restricted diffusion signal.

2.3.1 Diffusion of water molecules

Diffusion is the random motion of particles from an area of high concentration to an area of low concentration and is described by Fick's first law:

$$\mathbf{J}(\mathbf{r}) = -D.\nabla c(\mathbf{r}) \tag{2.22}$$

where D is the diffusion coefficient (with units of μm^2/ms) which is a property of the sample and is dependent on the size of the sample, temperature of the sample and microscopic structures surrounding the sample. c($\mathbf{r}$) is the particle concentration along a position $\mathbf{r}$ and $\mathbf{J}(\mathbf{r})$ describes the net flux of particles (with units of number/μm^2/ms) from high to low regions of concentration (hence the negative sign) in a system where concentration does not change with time [54].

In practice, the concentration of particles change with time and Fick's second law describes this :

$$\frac{\partial c(\mathbf{r},t)}{\partial t} = -\nabla \mathbf{J}(\mathbf{r},t) = D.\nabla^2 c(\mathbf{r},t) \tag{2.23}$$

This is known as the diffusion equation [54].

In a medium with no net concentration gradient, self diffusion of particles, termed "Brownian motion" occurs. The random thermal motion of particles was first observed by Robert Brown and later on mathematically described by Albert Einstein in terms of diffusion under probability gradients. The rewritten Fick's

second law by Einstein is:

$$\frac{\partial P(\mathbf{r}_1,t_1|\mathbf{r}_0,t_0)}{\partial t_1} = D.\nabla^2 P(\mathbf{r}_1,t_1|\mathbf{r}_0,t_0) \tag{2.24}$$

where P($\mathbf{r}_1$,t_1|$\mathbf{r}_0$,t_0) is the diffusion propagator and describes the likelihood of a molecule freely diffusing from an initial position $\mathbf{r}_0$ at time t_0 to a new position $\mathbf{r}_1$ over a time $t_1 - t_0$ and with a diffusion coefficient D. For a medium with a large ensemble of freely diffusing particles with no net concentration gradient, no barriers and with initial condition P($\mathbf{r}_1$,0|$\mathbf{r}_0$,0) = δ($\mathbf{r}_1$-$\mathbf{r}_0$) (where $\delta(\mathbf{r})$ is the Dirac delta function) and boundary condition P $\to$ 0 as $\mathbf{r}_1 \to \infty$, the solution (the diffusion propagator) to Equation 2.24, is defined by the Gaussian probability density function (PDF):

$$P(\mathbf{r}_1,t_1|\mathbf{r}_0,t_0) = \frac{1}{(4\pi D(t_1-t_0))^{3/2}} e^{-\frac{(\mathbf{r}_1-\mathbf{r}_0)^2}{4D(t_1-t_0)}} \tag{2.25}$$

The mean square displacement can be calculated from Equation 2.25 for particles undergoing free diffusion as:

$$\langle(\mathbf{r}_1-\mathbf{r}_0)^2\rangle = \int_{-\infty}^{\infty} (\mathbf{r}_1-\mathbf{r}_0)^2 P(\mathbf{r}_1,t_1|\mathbf{r}_0,t_0) d\mathbf{r}_0 d\mathbf{r}_1 = nD(t_1-t_0) \tag{2.26}$$

where n = 2, 4 or 6 for one, two or three dimensions.

In the presence of a boundary, such as the cell wall, diffusion of particles (water molecules) are restricted within the cell and diffusion is no longer free. Here, given that initial condition is P($\mathbf{r}_1$,0|$\mathbf{r}_0$,0) = δ($\mathbf{r}_1$-$\mathbf{r}_0$) and boundary condition, D$\hat{\mathbf{n}}\nabla_{\mathbf{r1}}$P($\mathbf{r}_1$,$t_1$|$\mathbf{r}_0$,$t_0$) = 0 (where $\hat{\mathbf{n}}$ is the outward flux perpendicular to the boundary and $\nabla_{\mathbf{r1}}$P($\mathbf{r}_1$,t_1|$\mathbf{r}_0$,t_0) is the probability gradient), shows no flux through the cell wall, the general solution to Equation 2.24 has the form:

$$P(\mathbf{r}_1,t_1|\mathbf{r}_0,t_0) = \sum_{n=0}^{\infty} e^{-D\lambda_n|t_2-t_1|} u_n(\mathbf{r}_0) u_n*(\mathbf{r}_1) \tag{2.27}$$

where $u_n(\mathbf{r})$ are orthogonal functions and λ_n are the coefficients [55] that are specific

to the geometry of the boundary. Analytical solutions for planar, cylindrical and spherical geometries are given in [55].

2.3.2 Diffusion weighted imaging

Diffusion of molecules can be probed using MR measurements. This method is termed Diffusion MRI. A standard method of measuring diffusion was developed by Stejskal and Tanner in 1965, which is often known as 'single pulsed field gradient (sPFG)', 'pulsed gradient spin-echo (PGSE)' or 'single diffusion encoding (SDE)'. In this thesis, we refer to them as SDE.

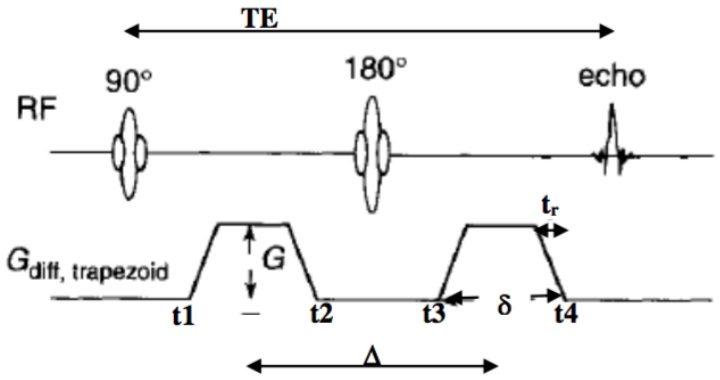

Figure 2.10: A basic SDE sequence for diffusion imaging. Diffusion gradients (symmetrical about the 180 RF pulse) are placed in a spin-echo sequence. δ denotes the duration (ms) of the gradient waveform, t_r denotes the slope duration (ms) and denotes the centre to centre time spacing (ms) for the two gradients and is known as the diffusion time. **G** is the gradient strength usually in mT/m and TE is the echo time (ms). t_1-t_4 are time points showing the start and end times of each gradient waveform. Figure adapted from [49]

The SDE sequence, illustrated in Figure 2.10, include two symmetrical gradients, with time duration δ, rise time t_r and gradient strength **G**(t), placed on either side of the RF 180^o pulse, such that the time between the start of the two gradients is Δ. The gradients, known as diffusion encoding gradients, are similar to those used for imaging but are much higher in gradient strength. For instance, in clinical scanners, the diffusion sensitizing gradients have gradient strength of $\mathbf{G} \geq 30$ mT/m, whereas imaging gradients usually tend to have $\mathbf{G} \leq 5$ mT/m [56].

Initially, when a sample is placed in a homogeneous magnetic field, B_0, their spins precess at the Larmor frequency and accrue a phase, $\phi = \omega_0 t = \gamma B_0 t$, which

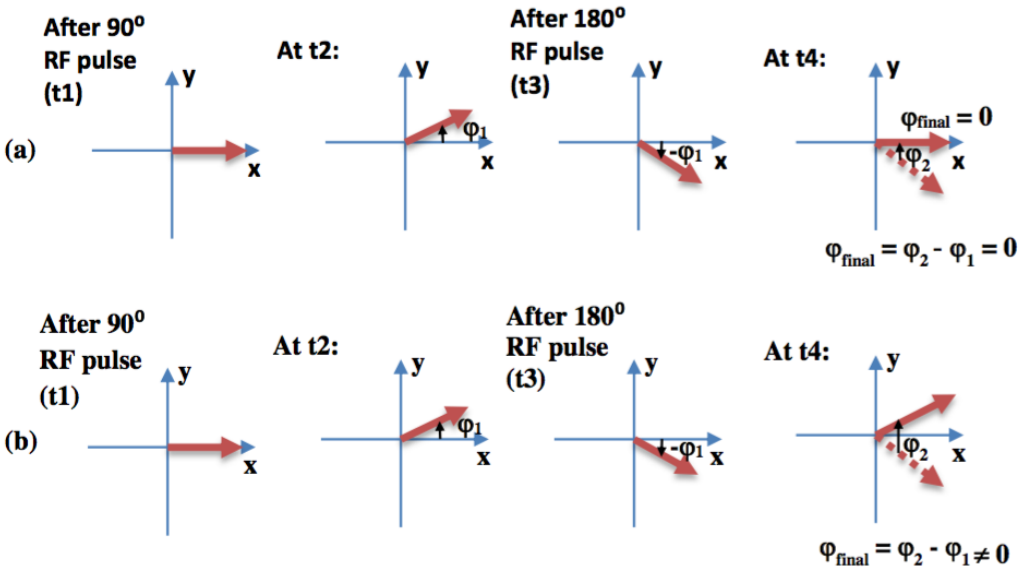

Figure 2.11: Diagram depicting the net phase accumulation for the case when (a) water molecule is stationary and (b) when water molecule diffuses.

is independent of their positions. On application of the first gradient waveform (at time t_1 in Figure 2.10 and Figure 2.11), the spins experience different precession frequencies depending on their position, $\mathbf{r}$, with respect to the gradients. By the end of the first waveform (at time t_2 in Figure 2.10 and Figure 2.11), they will have accumulated a net phase ϕ_1. The application of the 180^o RF pulse inverts the phases of all the spins. Following this, the second gradient pulse (by time t_4 in Figure 2.10 and Figure 2.11), induces a phase shift ϕ_2 that is opposite to the first gradient pulse. The resultant phase, ϕ_{final}, induced by two identical diffusion gradient pulses placed either side of a 180^o RF pulse is therefore:

$$\phi_{final} = \phi_1 + \phi_2 = -\gamma\Big(\int_0^{\delta} \mathbf{G}(t)\mathbf{r}(t)dt + \int_{\Delta}^{\delta+\Delta} \mathbf{G}(t)\mathbf{r}(t)dt\Big) \tag{2.28}$$

If the spins are stationary, the phases gained (ϕ_1 and ϕ_2) are equal in magnitude and therefore ϕ_{final} = 0 (Figure 2.11a). If movement of the spins occur, spins are not completely refocused ($\phi_1 \neq$ -ϕ_2) and therefore $\phi_{final} \neq 0$, which results in an attenuated MR signal (Figure 2.11b). The attenuated signal, known as the diffusion

signal, characterises the amount of diffusion within the sample along the direction of the applied gradient waveform.

Repeating this procedure along many gradient directions provide the attenuated measurements along these directions and builds up a 3D picture of water diffusion within the sample.

2.3.3 Oscillating gradient spin echo (OGSE) sequences

Diffusion weighted imaging is not limited to SDE sequences, where gradient pulses have a constant gradient strength across the gradient duration δ. In the literature, a wide range of diffusion gradient pulses have been used to induce diffusion weighting. For example, double diffusion encoding (DDE) sequences [18, 57] helps to differentiate between signals from compartments with different shapes. Dual spin echo sequences (DSE) [58] reduce eddy current distortions and are sensitive to compartments with different sizes. Generalised gradient waveform sequences are flexible and can be optimised for high sensitivity to microstructure parameters [59, 60]. However, generalised gradient waveforms are limited by their difficult implementation on the scanner and the long times required for parameter fitting since the signal calculations have to be done numerically.

OGSE sequences [24, 61, 62] have oscillating gradient waveforms that reduce the diffusion time of the experiment from Δ (time between the two pulses in the SDE) to approximately half period of the oscillation depending on the type of oscillating gradient waveform. By changing the frequency of the oscillations, the OGSE sequence can be tuned to probe a range of different diffusion times including the short time limit which can improve estimation of the intrinsic diffusivity. Figure 2.12 illustrates different types of OGSE sequences that are currently used in literature. Here we consider only trapezoidal OGSE sequences as it was shown previously [59, 63] that they maximize the sensitivity to microstructure parameters by maximizing the diffusion weighting for fixed time. We constrain N, the number of half oscillations, to be an integer number as is most typically used for OGSE methods [61, 62, 64]. When N=1, the trapezoidal oscillating gradient reduces to a SDE sequence.

In comparison to the different types of diffusion weighted sequences that require implementation of two RF pulse (DDE, DSE, generalised waveforms, etc), trapezoidal OGSE sequences are very simple to implement on a scanner and help reduce eddy current distortions [24]. Furthermore, the OGSE sequence itself requires only one extra parameter in comparison to SDE sequences, and that is the number of half oscillations. The simplicity of OGSE and its potential for higher sensitivity towards microstructure parameters are the reasons we focus on using OGSE sequences in this thesis, along with the standard SDE sequences.

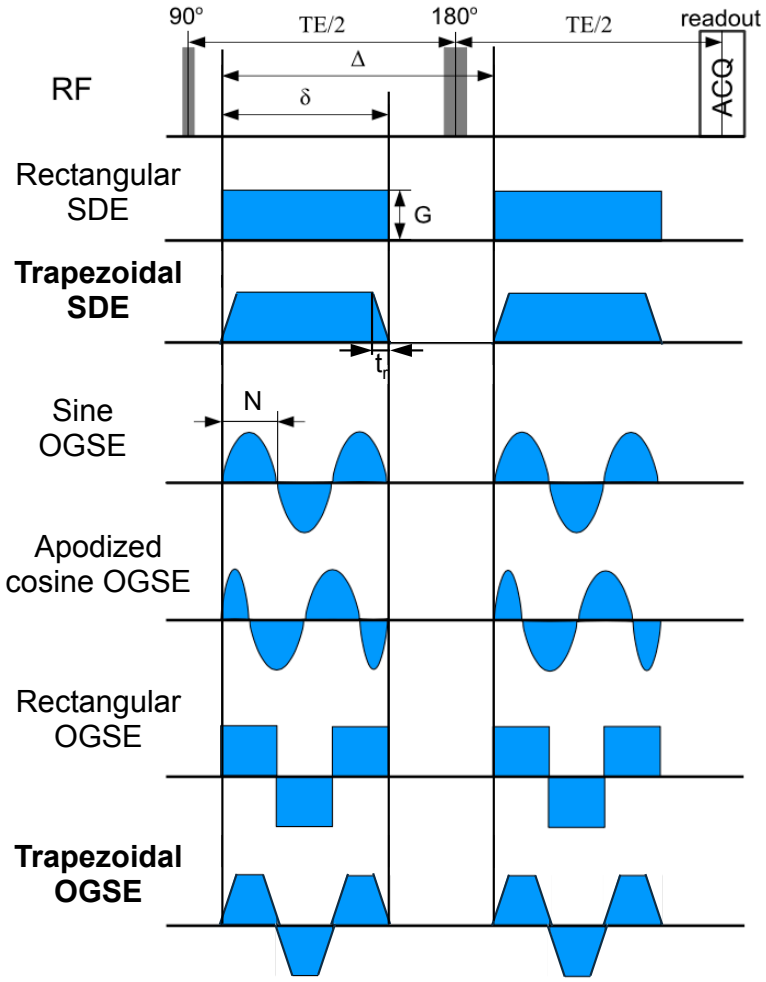

Figure 2.12: Schematic of different types of oscillating diffusion gradient waveforms and their location in a standard diffusion sequence. The sequences highlighted in bold are our sequences of interest. Figure adapted from [53]

2.3.4 Safety issues related to diffusion MRI

A part of this thesis will also involve implementation of OGSE sequences on a clinical scanner, safety issues regarding the diffusion gradient waveforms have to be considered.

Figure 2.13 gives a brief overview of a standard MR system and their components to demonstrate their roles in MRI.

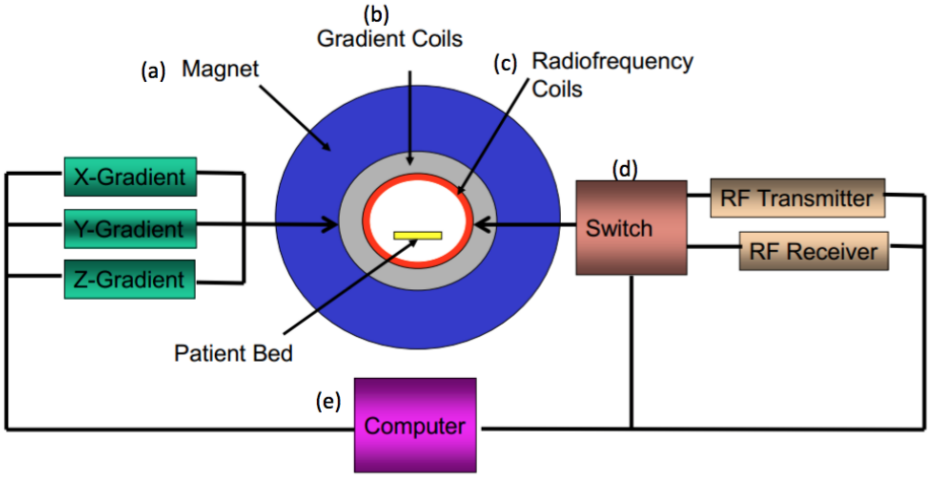

Figure 2.13: Simple block diagram of the main components in a standard MRI system. (a) Magnet which provides the static magnetic field used for generating the MR signal. (b) Gradient coils in the x, y and z directions of the scanner coordinates used for diffusion MRI and for imaging, where the power is supplied by their individual amplifier (shown in green). (c) Radiofrequency coils to generate the alternating B1 field required for MR signal excitation. The switch (d) can be used to change between the transmitting RF and receiving MR signal from patient. (e) Computer controls the scanner sequences and carries out image processing. This diagram was extracted from [47].

Diffusion gradient waveforms (and even imaging gradients) require the use of gradient coils. The gradient coils have specific inductance and resistance and are mounted inside the bore of the magnet (Figure 2.13). Each of these coils have their own independent gradient amplifier, which drives current through their own gradient coil and thus the coils produce a proportional gradient strength in the presence of the large static magnetic field within that coil.

In standard diffusion MRI, there are two major issues, regarding time varying gradients, such as those used in EPI readout or diffusion waveforms, that constrain the maximum performance of gradients. (1) Peripheral nervous stimulation (PNS)

and (2) gradient coil heating. These constraints are typical in EPI sequences due to the rapid gradient switching during the fast k-space readout. However, safety can potentially be a bigger issue when introducing oscillating gradients because it also means further addition of much stronger and rapidly switching gradients in comparison to the EPI imaging gradients [56].

2.3.4.1 Peripheral nervous stimulation (PNS)

Peripheral nervous stimulation (PNS) describes the electrochemical process of signal transfer from a dendrite to the tail end of the axon. It is an important concept because artificial PNS stimulation from imaging gradients can cause tingling sensation, muscle twitching or in the worst case scenario, cardiac stimulation.

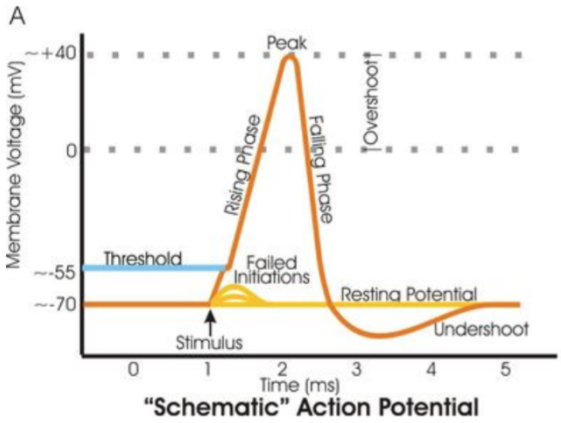

Figure 2.14: A typical action potential in a neuron. Nerve cells contain intracellular potassium ions and extracellular sodium ions. A nerve cell will initially be in a resting state (-70mV). Inflow of sodium ions will cause the axon region to become more positive. Activation will occur by depolarization (by further inflow of sodium ions), if its PNS threshold potential is achieved (-40mV to -55mV). Once this threshold is reached, the region will be automatically further depolarized, after which a peak is reached and hyper-polarization (outflow of potassium ions) occurs. This returns that region back to the resting state (after a brief further drop in its potential). The sodium ions will then flow along an electrochemical gradient inside the axon to the next node because the myelin sheath prevents any sodium/potassium influx/outflux. Arrival of sodium ions at the adjacent node of Ranvier is referred to as an electrical impulse or an action potential. This activates the whole process of depolarization, and the electrical impulse is effectively passed on. Figure as featured in [65].

Different types of nerve cells will have different action potential duration (see Figure 2.14), also known as time-constants. If a PNS stimulus is applied to a nerve

cell that has crossed the threshold potential and is undergoing an action potential, the nerve cell will not be affected by this stimulus. However, if the stimulus is applied straight after the time-constant, nerve fibre will be activated. Peripheral nerves fibres have time-constants of approximately 120 μs, compared to the longer time-constants of cardiac nerve fibres (3 ms) [66]. Hence peripheral nerve fibres can be activated more frequently than cardiac nerve fibres.

2.3.4.2 PNS thresholds in MRI

PNS occurs in MRI because the threshold energy can be provided by the gradient switching in the imaging gradients or in the diffusion gradients. The change in magnetic field with time, dB/dt of the waveform, generates an electric field within the body. If this exceeds the threshold dB/dt (threshold PNS), it will cause peripheral nerve stimulation [67].

Safety regulations [66] use dB/dt and $t_{s,eff}$ (which is maximum change in gradient strength divided by the slew rate) to estimate PNS threshold in humans in whole body MR equipment using trapezoidal waveforms of EPI readouts. The different limits of PNS for varying operation levels in whole body gradients are:

1. L01: Limit of dB/dt for normal operation mode (80% of dB/dt that will cause PNS)

2. L12: Limit of dB/dt for first level controlled operation mode (100% of dB/dt that will cause PNS)

3. Cardiac stimulation: Limit of dB/dt for cardiac stimulation (threshold above which ventricular fibrillation occurs).

Fortunately, nerve stimulation thresholds of cardiac tissue are greater than 100 T/s at the $t_{s,eff}$ commonly used in MRI (below 1 ms) and hence chances of cardiac stimulation are very low. However, for nerve tissue, at the clinically used $t_{s,eff}$, PNS thresholds are much lower and PNS stimulation can be possible [66] if lower $t_{s,eff}$ (i.e. high slew rates) are used.

One method of preventing the MR scanners from exceeding the PNS threshold is using an empirical method called SAFE (Stimulation Approximation by Filtering

and Evaluation) [68] to relate the PNS threshold to the gradient waveforms and the rise time, regardless of the shape of the waveform [66]. Generally, the output from the model is compared to the given limits of stimulation thresholds and exceeding this should stop the scanner to prevent PNS stimulation.

2.3.4.3 Gradient heating

Gradient amplifiers, associated with the gradient coils, contain transistors that allow amplification of current. High levels of current inputted into the transistor for an extended period of time can cause the temperature of the transistor to rise and exceed the limit set by the manufacturer [69].

Gradient coils that transform current generated by the amplifiers into magnetic gradients can also be overheated in the presence of a large static magnetic field. This is because of the eddy current that are generated during this procedure, which in turn generates Lorentz force that causes the gradient coils to vibrate producing loud acoustic noise and heat. Additionally, coil resistance will also lead to heat generation. Thus hot-spots (regions with high local current density) within the gradient set in the MR scanner contain the highest temperatures and hence must not exceed the given manufacturer‘s temperature limits.

In both cases of gradient amplifiers and coils, reduction in temperature are carried out through a cooling system, which uses water or air. In addition to this, the scan time is also lengthened by introducing ‘dead-time’ to prevent any further use of gradient amplifiers and coil [70].

2.3.5 Gaussian phase distribution (GPD) approximation

Safe implementation of time varying gradient waveforms, specifically OGSE sequences, have recently been demonstrated in clinical scanners by [71, 72] for diffusion imaging of the human brain. Once diffusion images are acquired, it is important to characterize the type of diffusion in tissue from which potential biomarkers could be inferred. This is possible by matching the measured diffusion signal to a theoretical diffusion signal. In the literature there are several approaches for approximating the restricted and free diffusion signal analytically or numerically.

One analytical approach is known as Single Gradient Pulse (SGP) approximation. It relates the diffusion signal to the diffusion propagator ($P(\mathbf{r}_1|\mathbf{r}_o,\Delta)$) and assumes that diffusion does not take place during the application of gradients and therefore is only valid when $\delta << \Delta$. When SGP is satisfied, we can also establish a Fourier relation between the average propagator ($P(\mathbf{R},\Delta)$, the probability of an ensemble of spins to be displaced by $\mathbf{R}$ in time Δ, and the measured signal - a technique known as q-space imaging [73, 74]. However, in practice, the condition $\delta << \Delta$ is not usually satisfied due its requirements for high gradient strengths coupled with very short gradient duration.

The diffusion signal can also be numerically calculated for generalised waveforms using a method known as matrix formalism [75]. However the method has been known to be computationally expensive [53].

Another analytical approach, and the one we are interested in, is known as the Gaussian phase distribution (GPD) approximation. Unlike SGP approximation and matrix method formalism, GPD approximation can be used in practical situations because it is valid for a finite δ and is also computationally fast, respectively. Hence, throughout this thesis, for both SDE and OGSE sequences, we use GPD approximation described below.

GPD approximation involves expressing the signal attenuation in terms of phase accrual at TE.

$$E(\mathbf{G},\Delta) = \int_{\infty}^{-\infty} P(\phi,\Delta)e^{i\phi}d\phi = \int_{\infty}^{-\infty} P(\phi,\Delta)cos(\phi)d\phi \tag{2.29}$$

where P(ϕ,Δ) is the probability distribution of phases at the end of time, Δ. The GPD approximation assumes that when the number of spins in sample is large compared to the displacement of the spins during time Δ, the probability distribution of the phases is Gaussian [76] and the signal attenuation can be derived to be [77]:

$$E(\mathbf{G},\Delta) = e^{-\frac{<\phi^2>}{2}} \tag{2.30}$$

where $<\phi^2>$ is the mean squared phase change.

The signal attenuation, $E(\mathbf{G},\Delta)$, can be calculated by evaluating $<\phi^2>$. In the case of free diffusion, under the application of rectangular SDE gradient waveforms, $E(\mathbf{G},\Delta)$ becomes [77]:

$$E(\mathbf{G},\Delta) = e^{-\left[\gamma^2\delta^2G^2(\Delta-\frac{\delta}{3})\right]D} \tag{2.31}$$

where D is the diffusion coefficient and the rest of the diffusion gradient parameters inside the brackets [..] are defined as the *b*-value. The higher the *b*-value, the stronger the degree of diffusion weighting and hence lower the measured signal attenuation.

For a trapezoidal SDE, with rise time t_r, the *b*-value is given by [78]:

$$b = G^2\gamma^2\left[(\delta-t_r)^2\left(\Delta-\frac{1}{3}(\delta-t_r)\right)-\frac{1}{6}(\delta-t_r)t_r^2+\frac{1}{30}t_r^3\right] \tag{2.32}$$

For a trapezoidal OGSE with rise time t_r, the *b*-value is given by [64]:

$$b = \frac{2G^2\gamma^2\delta^3}{15N^2}(5-\frac{15t_rN}{2\delta}-\frac{5t_r^2N^2}{4\delta^2}+\frac{4t_r^3N^3}{\delta^3})+G^2\gamma^2(\Delta-\delta)\left(\frac{(1-(-1)^N)(\delta-N\cdot t_r)}{2N}\right)^2 \tag{2.33}$$

where N is the number of half oscillations in the waveform, which we will call 'lobes'.

The GPD approximation is only fully accurate in the limit of free diffusion [76]. Free diffusion can also include the presence of restriction but provided Δ is very short compared to the time required by the spins to reach the boundary [79]. Additionally, the approximation is also valid for when Δ is long ($\Delta\rightarrow\infty$) because the positions of the spins and their phases become independent of the start position, which results in a Gaussian distribution [79].

In the presence of restriction at intermediate times, the mean squared phase distribution is *almost* Gaussian. [80] showed in simulation that GPD approximation of restricted diffusion inside spheres and parallel planes for rectangular SDE waveforms are accurate enough for practical cases. [64] later also validated GPD

approximations using simulations for rectangular and trapezoidal waveforms. Assuming GPD approximation and using the diffusion propagator from Equation 2.27, the restricted diffusion signal from a gradient waveform is given by [55, 64]:

$$E(\mathbf{G},\Delta) = e^{\Big(-\frac{2\gamma^2}{D^2}\sum_{n=0}^{\infty}\frac{B_n}{\lambda_n^2}\Gamma_n\Big)} \tag{2.34}$$

where B_n and λ_n depends on the underlying geometry and gradient directions.

In this thesis, we use a model of cylinders to represent axons. B_n and λ_n for restricted diffusion within a cylinder with gradient perpendicular to the main axis of the cylinder is:

$$B_n = \frac{2(R/\mu_n)^2}{\mu_n^2 - 1} \qquad\qquad \lambda_n = \Big(\frac{\mu_n}{R}\Big)^2 \tag{2.35}$$

where μ_n is the n^{th} root of the equation J_1' and J_1 is a Bessel function of first kind [64]. The parameter Γ_n in Equation 2.34 defines the contribution of the gradient waveform to the mean squared phase distribution and in the case of rectangular SDE waveforms is [81]:

$$\Gamma_n = G^2\{\lambda_n D\delta - 1 + e^{-\lambda_n D\delta} + e^{-\lambda_n D\Delta}(1 - cosh(\lambda_n D\delta))\} \tag{2.36}$$

In the case of trapezoidal SDE (N=1) and OGSE (N>1) sequences, Γ_n is given by [64]:

$$\begin{aligned}\Gamma_n =& \frac{G^2}{2D^2\lambda_n^2 t_r^2}\Bigg[\frac{(-1)^N}{E_{1+}^2}(e^{\tilde{t_r}}-1)^2(e^{\tilde{t_r}} - e^{\lambda_n D/2\nu})^2 e^{-\tilde{\delta}-2\tilde{t_r}}\Big(e^{-\tilde{\Delta}}\big(-1+(-1)^N e^{\tilde{\delta}}\big)^2 - \\ & 2\big(1+(-1)^N e^{\tilde{\delta}}(N-1+Ne^{-\lambda_n D/2\nu})\big)\Big) + N\Big(2e^{-\lambda_n D/2\nu}\big(e^{\tilde{t_r}}-1\big)^2 - \\ & 4(e^{-\tilde{t_r}} - 1 + \lambda_n D t_r) + \lambda_n^3 D^3 t_r^2(1/\nu - 8t_r/3)\Big)\Bigg],\end{aligned} \tag{2.37}$$

where $\nu = N/(2\delta)$, $\quad \tilde{\delta} = D\lambda_n\delta$, $\quad \tilde{\Delta} = D\lambda_n\Delta$, $\quad \tilde{t_r} = D\lambda_n t_r$, $\quad E_{1+} = e^{D\lambda_n/(2\nu)} + 1$

2.3.6 Summary

Overall, in this section, we have described the main theory behind diffusion MRI. This includes analytical expressions for the diffusion propagator, i.e. the probability distribution function, for both free and restricted diffusion. Following this we introduced the concept of diffusion weighted imaging and the range of sequences that can be used to carry out the measurements, SDE and OGSE sequences being the main focus. We also discuss the patient and scanner hardware safety that are related to using time varying diffusion gradient waveforms (such as OGSE). We also described the process of analytically approximating the diffusion signal using the Gaussian phase distribution approximation for both SDE and OGSE sequences for both cases of free and restricted diffusion.

2.4 Models in diffusion MRI

Analytical models of diffusion MR signal can be fitted to the diffusion measurements for estimating tissue-specific parameters by matching the resultant analytical signal to the measured diffusion signal. Repeating this procedure over all voxels builds up a map of the parameter of interest. This section presents some common models used to analyse the diffusion MR data. In the first part, we will describe the popular method of modelling diffusion MR data, which is known as diffusion tensor imaging (DTI). DTI gives parameters estimates that reflect the measured diffusion signal, however, due to the simplicity of tensor model, DTI parameters can be non-specific to actual tissue microstructural features. For this reason, in the second part, we focus on 'biophysical' tissue models that geometrically represent the underlying tissue. More specifically, we focus on tissue models for axon diameter imaging, which is the main focus of this thesis.

2.4.1 Diffusion tensor imaging (DTI)

Diffusion tensor imaging is a popular method of analysing diffusion MR data of the brain [4]. The method uses a 3D Gaussian model of spin displacements to acknowledge that diffusion in an anisotropic environment varies along different directions. In this case, the scalar diffusion coefficient, D, in Equation 2.25, is defined instead

by a 3×3 symmetric matrix known as the diffusion tensor, **D**:

$$\mathbf{D} = \begin{pmatrix} D_{xx} & D_{xy} & D_{xz} \\ D_{yx} & D_{yy} & D_{yz} \\ D_{zx} & D_{zy} & D_{zz} \end{pmatrix} \tag{2.38}$$

where D_{xx}, D_{yy} and D_{zz} are the diffusivities in the x, y and z directions and D_{xy}, D_{yz} and D_{xz} are the correlation between the given directions [82].

The measured diffusion signal accounting for changes due to gradient directions is written as:

$$S = S_0 e^{-b\hat{\mathbf{G}}^T \mathbf{D} \hat{\mathbf{G}}} \tag{2.39}$$

where S_0 is the MR signal without any diffusion weighting, b is the diffusion weighting factor and $\hat{\mathbf{G}}$ is a unit gradient vector along which the diffusion is measured. To find the 7 unknowns parameters (S_0, D_{xx}, D_{yy}, D_{zz}, D_{xy}, D_{yz} and D_{xz}), at least 7 measurements, one b=0 s/mm^2 and six diffusion measurements acquired using non-collinear gradient directions are required. In practice, 20-30 gradient directions are optimal to reduce the effect of noise in the estimates and to ensure oriental invariance [83]. Additionally, standard b-values for DTI in clinical scenarios tend to be between b = 600-1200 s/mm^2 [84].

Once the diffusion tensor is estimated, an eigenvalue decomposition of **D** is carried out to find the eigenvectors ($\mathbf{e}_1$, $\mathbf{e}_2$ and $\mathbf{e}_3$) and their corresponding eigenvalues ($\lambda_1 \geq \lambda_2 \geq \lambda_3$). The largest eigenvalue and its corresponding eigenvector, denotes the direction of fastest diffusivity, and hence the main fibre direction.

The eigenvalues can be used further to compute some common rotationally invariant indices such as fractional anisotropy (FA):

$$FA = \sqrt{\frac{3}{2}} \frac{\sqrt{(\lambda_1 - \langle\lambda\rangle)^2 + (\lambda_2 - \langle\lambda\rangle)^2 + (\lambda_3 - \langle\lambda\rangle)^2}}{\sqrt{\lambda_1^2 + \lambda_2^2 + \lambda_3^2}} \tag{2.40}$$

where FA = 0 corresponds to isotropic diffusion and FA = 1 corresponds to diffusion occurring along one specific direction. However FA cannot distinguish between

different shapes of diffusion tensors. For instance, FA is high for cases when $\lambda_1 > \lambda_2 = \lambda_3$, where diffusion is 'cigar' shaped and when $\lambda_1 = \lambda_2 > \lambda_3$, where diffusion is 'pancake' shaped. [85] introduced an alternative approach to visualising the shape of the diffusion tensor. The newly introduced indices are 'linearity' (C_l), 'planarity' (C_p) and 'sphericity' (C_s):

$$C_l = \frac{\lambda_1 - \lambda_2}{\sqrt{\lambda_1^2 + \lambda_2^2 + \lambda_3^2}} \qquad C_p = \frac{2(\lambda_2 - \lambda_3)}{\sqrt{\lambda_1^2 + \lambda_2^2 + \lambda_3^2}} \qquad C_s = \frac{3\lambda_3}{\sqrt{\lambda_1^2 + \lambda_2^2 + \lambda_3^2}} \tag{2.41}$$

A tensor with a 'cigar' shape therefore will have high linearity and low planarity, whereas a tensor with a 'pancake' shape will have low linearity and high planarity. Although indices estimated from DTI reflects the measured signal, the indices are non-specific to microstructural changes in tissue. For instance, axon diameter, axon density and myelination are some of the factors that could effect estimates of the DTI indices [83]. As a result, biophysical tissue models were introduced to provide more specific microstructure parameters.

2.4.2 Biophysical tissue models for axon diameter imaging

Biophysical tissue models provide a geometrical representation of the underlying tissue microstructure. The analytical diffusion signal are calculated for the specific model and then the inverse problem can be solved to estimate the tissue model parameters given the measured diffusion data.

The first such model was introduced by [46] for modelling the bovine optic nerves in the brain. The total signal from SDE sequences was modelled as a weighted sum of signals that came from three different compartments: restricted diffusion within spherical glial cells, restricted diffusion within prolate ellipsoidal axons and hindered diffusion in the extra-cellular space. The analytical signal for each compartment was calculated using the SGP approximation in the parallel and perpendicular direction with respect to the main direction of the ellipsoidal axons. The model fitting was then carried out to match the analytical signal to the measured diffusion signal. Tissue parameters such as the weighting, also known as the

volume fraction, of the compartments, diffusivity of intracellular and extracellular compartments, sizes of glial cells (sphere radius) and axons (short and long axis of the ellipsoids), as well as membrane permeabilities were then extracted. Due to the large number of parameters, a high quality dataset had to be acquired with multiple gradient strengths and diffusion times. Although the extracted parameter estimates were found to agree with histology, the long acquisition times and high gradient strengths associated with the dataset prevents the translation of this model *in vivo*. Hence simpler tissue models are essential for the possibility of *in vivo* microstructure imaging.

A particularly simple tissue model is the ball and stick model [86]. It is a two compartment white matter model, where intra-axonal diffusion occurs only in the parallel direction, i.e. stick, and the extra-axonal diffusion is isotropic, i.e. ball, and both compartments have the same diffusivity, d. The total signal is then the weighted sum of the signals from the two compartments:

$$S = S_0(fe^{-bd(\hat{\mathbf{n}}.\hat{\mathbf{G}})} + (1-f)e^{-bd}) \tag{2.42}$$

where f is the intra-axonal volume fraction and $\hat{\mathbf{n}}$ is the fibre direction and $\hat{\mathbf{G}}$ is the direction of the diffusion gradient.

Although, the simplicity of ball and stick model makes it clinically feasible, the model does not account for other important microstructures parameters such as axon diameter, which as pointed out in Section 2.1.3 is a potential biomarker for changes within CNS and PNS. As the focus of the thesis is axon diameter imaging, a brief review of the current techniques developed for axon diameter imaging is given in the following sections. The techniques include q-space imaging (Section 2.4.2.1), angular double diffusion encoding (Section 2.4.2.2), temporal diffusion spectroscopy (Section 2.4.2.3), CHARMED & AxCaliber (Section 2.4.2.4), and ActiveAx (Section 2.4.2.5). In Sections 2.4.2.6 and 2.4.2.7, specific advances of ActiveAx will be discussed.

2.4.2.1 q-space imaging

One method of imaging axon diameter is q-space imaging (QSI). When conventional SDE sequences are used the dependence of the signal attenuation, $E(q,\Delta)$, on the wave vector, $q = (2\pi^{-1})\gamma G\delta$, exhibits a diffraction pattern when using Δ ranging from $\Delta = 0$ to $\Delta >= a^2/D$, where $a/2$ is the distance from the boundary to the centre. This is a signature of restriction [87]. When no restriction is present, the diffraction patterns disappear. Hence the diffraction pattern can be used to characterize difference types of diffusion and restriction sizes. However, [88] showed that heterogeneity in restriction sizes causes the diffraction pattern to diminish.

[73] used Fourier transform of the measured signal (E(q,Δ)) acquired in q-space to estimate the average propagator, also known as the displacement probability distribution function (PDF) in heterogeneously sized yeast cells. By assuming a Gaussian-shaped displacement distribution, the diameter of the yeast cells were then inferred from the full width half maximum (FWHM) of the displacement PDF. Unlike in the cases of isotropic diffusion in yeast cells, axons tend to have anisotropic diffusion. [74] demonstrated that the FWHM of the PDF of unrestricted diffusion increase in width as the diffusion time is increased. However, they showed that when diffusion measurements are perpendicular to the main axon axis in the white matter of a rat spinal cord, i.e. under anisotropic restricted diffusion, the FWHM is independent of diffusion time and is correlated with the size of restrictions. Although this was encouraging, when [89] carried out simulations and white matter tissue experiments, their axon diameter estimates were overestimated (i.e. width of FWHM was large). They then suggested that multi-compartment models may help improve the accuracy of axon diameters estimates because larger width of FWHM could be attributed to hindered diffusion in the extra-cellular space.

A two-compartment model (restricted diffusion in the intra-axonal space and free diffusion in the extra-axonal space) using QSI was experimentally explored by [16] to accurately estimate axon diameters in the *ex vivo* mouse spinal cord. The displacement PDFs for both compartments were estimated and the diameter of axons were determined from the FWHM of the intra-axonal PDF. However, the main

limitation of the method comes from the requirement for high and commercially unavailable gradient strengths (G $>$ 3000 mT/m) to fulfil the SGP approximation. On current state-of-the-art MR scanners in clinical research such as the *Connectom* scanner, gradient strengths only reach up to G $\leq$ 300 mT/m [90, 91]. Hence, *in vivo* axon diameter imaging using QSI at currently available clinical gradient strengths is not a promising method [92].

2.4.2.2 Angular double diffusion encoding (DDE)

Another approach used to estimate restriction size is using angular double diffusion encoding (DDE) sequences (Figure 2.15). The signal attenuation profile from the DDE sequence is a function of ϕ, $E(\phi)$ and probes the correlation between displacement of water molecules in different time scales and different directions, giving more sensitivity to microstructure parameters such as axon diameter.

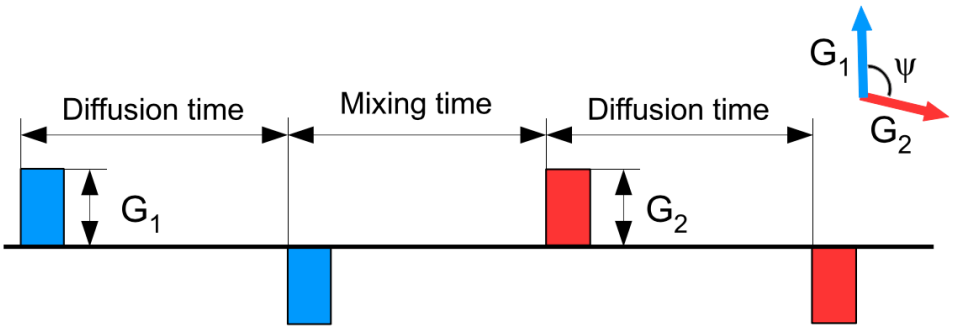

Figure 2.15: Schematic representation of a double diffusion encoding (DDE) sequence. Two pairs of SDE pulses, separated by a mixing time, are used. The first pair of diffusion gradients, G_1, in the direction of restriction, is fixed, while the second pair of diffusion gradients, G_2, is varied by an angle ψ, in the same plane, with respect to G_1. Figure as featured in [53].

Angular DDE for axon diameter imaging uses very little or no mixing time [93] and unlike SDE sequences, at high q-values, can extract the diffraction pattern of heterogeneous sizes. The sizes of restriction can then be extracted. However, as sizes become smaller, higher q-value is required to extract the diffraction pattern and with the short δ requirement of SGP approximation, this results in unattainable high gradient strength [93, 94]. [95] later theoretically demonstrated that high q-values are not required to extract sizes and [57] validated this later in experiments by using

cylinders with diameters of 10 μm and comparing the signal attenuation profiles from the SGP approximation [93] to the low q-value method [95] for various δ.

Using the low q-values, the potential to translate the method to clinical research arose. Hence two compartment tissue model with low q-value angular DDE were then applied to a range of cases of axon diameter imaging, such as water filled micro-capillaries [17], *in vivo* rat corpus callosum and *ex vivo* porcine spinal cord [18] and even *in vivo* human corpus callosum [96].

Although DDE has shown encouraging results on estimating axon diameters, one disadvantage of the method is that in cases of unknown orientation and anisotropic sample, such as the white matter, DDE is unsuitable. After acquiring a separate DTI to calculate the fibre orientations at each voxel, the DDE sequence (G_1, which is fixed and is perpendicular to the fibre orientation and G_2 which is varied across angles), has to be repeated as many times as the calculated number of different orientations to ensure orthogonality and hence accuracy of diameter estimate. This in the long run would not be clinically feasible. On a different note, recent work by [21, 22] theoretically demonstrated that at low q-values, DDE provides the same information on restriction size as SDE when assuming GPD. In fact, the main advantage of DDE over SDE sequences is their higher sensitivity towards microscopic anisotropy, especially at high q-values [21, 22, 97].

2.4.2.3 Temporal diffusion spectroscopy

A different approach to measuring axon diameter is using temporal diffusion spectroscopy. This is a method based on sampling the diffusion spectrum, $D(\omega)$, of a substance. In general, spins undergoing free diffusion have $D(\omega) = D$ (from Equation 2.24). In the case of restriction, $D(\omega)$ is dependent on the frequency of the waveform, where $D(\omega)$ is constant at high frequencies but underestimated at low frequencies. The temporal diffusion spectroscopy approach involves sampling the diffusion spectra using OGSE sequences with a range of frequencies, each with a range of b-values [23, 61].

[98] estimated restriction sizes in *ex vivo* rat brain using the cosine modulated OGSE waveforms. They modelled the diffusion spectrum as a function of dis-

tance between two parallel planes. They then modelled the diffusion signal using a kurtosis model (Kurtosis, K_{app}, is a measure of the deviation of diffusion from a gaussian) over a range of diffusion times and b-values.

$$S(b) = S_0 e^{-b.ADC + \frac{1}{6}b^2.ADC^2.K_{app}} \tag{2.43}$$

ADC was then estimated at various frequencies by fitting the corresponding diffusion signal to the kurtosis model. The restriction size was then computed from the analytical diffusion spectrum that best fits the estimated ADC spectrum from the raw dataset.

Another approach of using temporal diffusion spectroscopy for imaging axon diameters was demonstrated recently by [99]. They measured axon diameters by fitting a biophysical model to the acquired OGSE dataset using an analytical signal model for apodized cosine modulated OGSE sequences. The tissue model, itself, is a two compartment model similar to the ball & stick model with modelling assumptions that are similar to the modelling frameworks based on the CHARMED model [100], i.e. AxCaliber [19] and ActiveAx [101]. Details on the CHARMED models are provided in later sections. The restricted diffusion of the intra-axonal compartment is modelled as randomly packed identical parallel cylinders, each with a volume weighted diameter α (identical to ActiveAx [20]). The hindered diffusion within the extra-axonal compartment are represented by a 'zeppelin' compartment (referring to the taxonomy by [102] and similar to the models based on the CHARMED model [100]). The signal model for apodized cosine modulated OGSE sequences assumes GPD approximation to describe restriction within cylinders provided the diffusion measurement is perfectly perpendicular to the main axon orientation and has been validated theoretically in Monte Carlo simulations [103] and then experimentally in phantoms [104] and *in vivo* perfused rat brains [99]. Excellent agreement between the estimated axon diameters and histology were observed in all cases.

A key disadvantage of temporal diffusion spectroscopy is its requirement for

large gradient strengths (to enable fixed b-values and a range of frequencies) and perfect gradient alignment with fibre orientation, which limits the method to pre-clinical settings only. Furthermore, although temporal diffusion spectroscopy is extremely useful for characterising the tissue microstructure by estimating the diffusion spectrum, in cases where the model of the underlying tissue is well known, it is equivalent to simply using model-based fitting of the diffusion MRI signal directly. This direct fitting approach is a standard method of estimating axon diameter in [19] (see Section 2.4.2.4) and [20] (see Section ActiveAx) and is the method we use in this thesis.

2.4.2.4 CHARMED and AxCaliber

Similar to the ball & stick model, CHARMED (composite hindered and restricted model of diffusion) is also a two-compartment tissue model [100]. However, it represents the restricted diffusion of the intra-axonal compartment as cylinder(s) and hindered diffusion within the extra-axonal compartment as a symmetric diffusion tensor compartment (also known as the 'zeppelin' compartment according to the taxonomy in [102]). By fixing the axon diameter of the cylinders to some typical values in the spinal cord, CHARMED allows the estimation of the cylinder orientation, diffusivity parallel to the main axis of the cylinder, $d_{||}$ (which is the same for both intra- and extra-axonal space), perpendicular diffusivity of the hindered compartment, d_h or $d_{\perp}$, as well as the intra- and extra-axonal volume fractions, f and (1-f), respectively. Figure 2.16 illustrates the two compartment CHARMED model from which the total signal can be described as:

$$S = S_0(fS_r + (1-f)S_h) \tag{2.44}$$

where S_r and S_h are the restricted and hindered diffusion signal arising from the intra- and extra-axonal compartments, respectively.

The importance of imaging axon diameter is evident in Section 2.1.3 and so CHARMED was later extended by the same group to estimate a distribution of axon diameters, but assuming a fixed fibre orientation. The modelling framework is

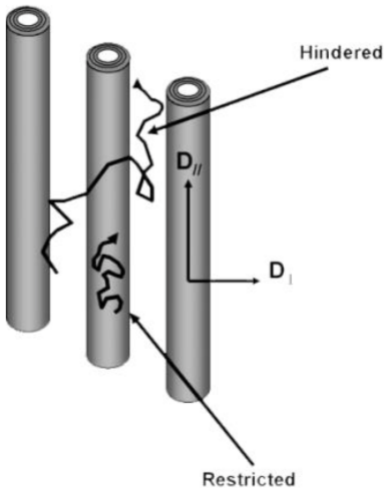

Figure 2.16: The CHARMED tissue model developed by [105]. This figure was extracted from [105].

known as AxCaliber [19]. Here, a gamma distribution describes the axon diameter distribution, consistent with histological work [29].

Several papers based on the AxCaliber approach have been published, which provide estimates of axon diameter in *in vitro* porcine spinal cord tissue [19], *in vivo* rat CC [106], *in vivo* and *ex vivo* human CC [91, 107]. In some cases, an additional compartment ('Ball' in accordance to the taxonomy of models by [102]) is added to account for the isotropic diffusion of the cerebral spinal fluid [106, 107]. Across all cases, high gradient strengths, $G \geq 150$ mT/m, are employed to image the axon diameters.

Although, the animal studies showed excellent agreement with histology, *in vivo* human data showed overestimated axon diameters, even at very high q-values. Furthermore, AxCaliber requires fibre orientation to be known [108], and so can only be applied for gradients perpendicular to the fibres. Lastly, due to the number of parameters, the method also requires many measurements (by varying diffusion time and gradient strengths) to the nerves to enable stable parameter estimates, which significantly lengthens acquisition time (more than 50 minutes [91, 107]).

2.4.2.5 ActiveAx

ActiveAx [20, 101] is also based on the CHARMED model and was developed at the same time as AxCaliber. The ActiveAx framework models the axon populations using randomly packed identical and parallel cylinders with a diameter, α. The extra-axonal compartment is the same as in the CHARMED model but the perpendicular diffusivity, d_h, is constrained by a simple tortuosity model [109]. An additional compartment to account for the isotropic diffusion of CSF is also added for *in vivo* brain imaging [101] and a further isotropic restricted compartment to represent trapped water for *ex vivo* brain imaging [110].The model has also been referred to as the minimal model of white matter diffusion (MMWMD) [110].

Minimal model of white matter diffusion (MMWMD)

The different compartments of MMWMD are visualised in Figure 2.17. No exchanges between the water populations of the four compartments are assumed. Henceforth, the full model for the diffusion MRI signal, S, is:

$$S = S_0 \sum_{i=1}^{n} f_i S_i \tag{2.45}$$

where, S_0 is the non-diffusion weighted signal, n is the number of compartments (n=4), S_i are the signals from these compartments and f_i corresponds to the volume fraction of water from the resulting compartments. In the rest of the chapter, f_1 is known as the intra-axonal volume fraction (f_{icvf}), f_2 is known as the extra-axonal volume fraction (f_{extra}), f_3 is known as the CSF volume fraction (f_{CSF}) and f_4 is known as the dot volume fraction (f_{dot}).

The analytical diffusion signal from the four compartments are described below:

1. Intra-axonal compartment models the signal S_1 coming from a population of parallel cylinders (to represent axons), each with the same diameter a. The parameter $d_{||}$ defines the intrinsic diffusivity within this compartment. S_1 is

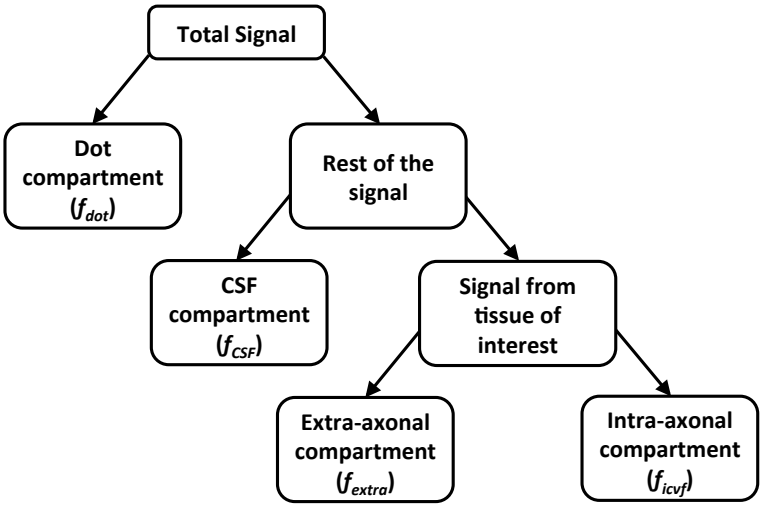

Figure 2.17: Schematic representation of the compartmentalisation of the four compartment white matter tissue model and their corresponding volume fractions. Intra-axonal compartment refers to water population within the axon. Extra-axonal compartment refers to water population outside the axon. Cerebrospinal fluid (CSF) compartment refers to the fast flowing free water population in the brain, where the axons do not affect diffusion. Dot compartment accounts for signal coming from water population trapped in very small structures like glial cells and cell membranes of fixed tissues.

defined by:

$$S_1 = S_{1||}(d_{||})S_{1\perp}(a, d_{||}) \tag{2.46}$$

The diffusion is assumed to be free parallel to the axis of the cylinder(s), $S_{1||}$, and is defined by:

$$S_{1||} = e^{-(b\ \cos^2\theta\ d_{||})} \tag{2.47}$$

for a diffusion gradient parallel to the cylinder with strength $|\mathbf{G}|\cos\theta$, where θ is the angle between the cylinder's long axis and $\mathbf{G}$. b in Equation 2.47 is the b-value and is given by Equation 2.32 [64, 78].

$S_{1\perp}(a, d_{||})$ is the diffusion signal from the perpendicular direction to the main axis of the cylinder(s). This diffusion is restricted by the cylinder wall and the signal is approximated from the GPD approximation (Equation 2.30 [55] and Equation 2.33 [64, 81]).

2. Extra-axonal compartment models the signal S_2 as anisotropic Gaussian displacements [82] with diffusivity $d_{||}$ parallel to the cylinder and diffusivity of

d_h perpendicular to the axons. S_2 is defined by:

$$S_2 = e^{-(b\ cos^2\theta\ d_{||})} e^{-(b\ (1-cos^2\theta)\ d_h)} \tag{2.48}$$

where d_h is modelled by the tortuosity model [109]:

$$d_h = (1 - f_{icvf}) d_{||}). \tag{2.49}$$

3. Cerebrospinal fluid (CSF) compartment models the signal S_3 as isotropic Gaussian displacements with diffusivity d_{iso} and is defined by:

$$S_3 = e^{-bd_{iso}} \tag{2.50}$$

4. Dot compartment accounts for trapped water molecules inside cell membrane of fixed tissues or glial cells [101]. It does not contribute to the signal attenuation and is included to allow a fraction of the signal to remain constant, i.e.:

$$S_4 = 1 \tag{2.51}$$

Pulse sequence optimisation

An important aspect of ActiveAx is experiment design. This enables ActiveAx to be used for imaging axon diameters under tolerable times for live subjects. Simultaneously, it ensures that the diffusion sequences used for imaging are most sensitive to the parameters of interest given the tissue model and hardware constraints of the MR scanner (for example maximum gradient strength, maximum slew rate and maximum echo time).

The optimisation framework finds pulse sequence combinations (defined by G, δ and Δ) that minimize the sum of the expected variance of each model parameter. The objective function is:

$$F = \sum_{i=1}^{K} \frac{(J^{-1})_{ii}}{p_i^2} \tag{2.52}$$

where p_i is the i^{th} model parameter and $(J^{-1})_{ii}$ is the corresponding Cramer-Rao

lower bound (CLRB) for the parameter and is calculated assuming a Rician noise model [20]. The CRLB provides the lower bound on the variance of the parameter estimates and is known to correlate with the true variance. The optimisation to find the minimum objective function is carried out using a stochastic algorithm, known as SOMA (self-organising migratory algorithm) with population size of 50, 500 migrations and other default settings.

Axon diameter index

One of the main traits of ActiveAx is the description of the axon diameter index as a single summary statistic to quantify the range of axon diameters present in tissue. The model description of MMWMD above states that there is only a single axon diameter, a in tissue, however in reality, tissue contains a range of axon diameters. The estimated axon diameter produces fitted diffusion signal that best match the measured diffusion signal, where the measured signal contains signal contribution from all of the axons. Each contribution is proportional to the volume of water within the axons, and in turn proportional to the diameter squared of the axons. Therefore, we expect and indeed [101] has shown that the estimated axon diameter correlates with the volume weighted axon diameter in tissue as demonstrated by the equation below:

$$\alpha = \frac{\sum_{i=1}^{n} a_i^2 . a_i}{\sum_{i=1}^{n} a_i^2} \tag{2.53}$$

where the numerator is the volume weighted axon diameter calculated across n axons and the denominator is used for normalization. We refer to this estimated axon diameter, α, as the "axon diameter index" from here onwards to indicate the range of axon diameters present in tissue.

Previous work based on the ActiveAx framework

[20] developed and applied the sequence optimisation for a simplified MMWMD model (where $S_3 = 0$ and $S_4 = 0$) and used the optimised protocols to estimate diameters of various synthetic cylinders (2-40 μm). They demonstrated that a-priori diameters in the range of 10-40 μm can find optimised protocols that minimise the CRLB very easily. They also showed that diameters in the range of 10-20 μm are

easiest to estimate using the optimised protocols.

Later, on they experimentally demonstrated the use of the ActiveAx framework to map the axon diameters in an *in vivo* human brain at a low gradient strength of only 60 mT/m. The work highlighted that ActiveAx framework is simple, requires reduced number of measurements (due to pulse sequence optimisation) and is orientationally-invariant to enable whole-brain mapping. However, axon diameters were found to be overestimated but at the corpus callosum, the 'low-high-low' pattern of axon diameters was consistent. [111, 112] later suggested that overestimation can occur from fibre dispersion (fanning and bending of fibres) in the brain. [111] modelled dispersion and showed slight improvements on the accuracy of axon diameters but the overestimation still persisted. Recently, [110] used the ActiveAx framework on a pre-clinical scanner with a gradient strength of G = 300 mT/m to measure axon diameters across an *ex vivo* monkey corpus callosum. They suggested that use of SDE sequences would require high gradient strengths than those offered currently by conventional clinical scanners, which is also the same conclusion that was later reached by two studies using the *Connectom* scanner equipped with G = 300 mT/m: [113] using ActiveAx and [91, 107] when using AxCaliber. Additionally, the ActiveAx framework has also been extended to different forms of diffusion sequences, such as double spin echo [58] and OGSE sequences [59, 60, 63], in the hope to discover diffusion sequences that are more sensitive towards the microstructure parameters.

2.4.2.6 Advances of modelling in ActiveAx

For modelling frameworks based on the CHARMED model such as AxCaliber and ActiveAx, the consistent overestimated axon diameters, even at G = 300 mT/m, have proved to be highly challenging and has thus attracted a lot of interest. It is possible that finding the tissue model that could best represent tissue microstructure could potentially improve accuracy of axon diameters. [102, 113, 114] have carried out extensive studies using a range of SDE waveforms to generate high a quality dataset and added additional compartments to represent the main pools of water in tissue (corpus callosum of an *ev vivo* rat and of an *in vivo* human) such as intra-

axonal space, extra-axonal space, CSF and glial cells. Some of the representative compartments are summarised in Figure 2.18. Their work collectively found that the best model for white matter tissue is a three compartment model with either the restricted diffusion being modelled as a distribution of 'sticks' with anisotropic dispersion or as parallel cylinders. However, axon diameter was still found to be significantly overestimated ($\geq 3\mu$m) when using the best model with cylinders to represent the white matter [113]. It is possible that using waveforms such as OGSE sequences could potentially improve axon diameter estimates.

2.4.2.7 Axon diameter imaging using OGSE ActiveAx

There is evidence that OGSE can improve axon diameter estimates [23–25, 99]. Oscillating gradient waveforms reduce the diffusion time of the experiment from the Δ (time between the two pulses in the SDE) to half period of the oscillation. Therefore, frequencies of the oscillations can be tuned to make OGSE sequences more sensitive to intrinsic diffusivity and leading to improved sensitivity towards diameters.

Initially, [59] used the optimisation framework to find the optimal waveform shape for probing diameter and diffusivity when the diffusion measurement direction is orthogonal to the main axis of the cylinder. Square oscillating gradient waveforms with maximum gradient strength emerged from the optimisation. Their frequencies also increased as the diameter reduced. Later on, [60] explored the effects of varying the diffusion measurement direction on the shape of the optimal waveforms and demonstrated that diffusion measurements parallel to the main axis of the cylinder provides a robust estimates of intrinsic diffusivity, which otherwise would be harder to estimate from perpendicular measurements. They also demonstrated that diffusion measurements in the parallel direction also help to reduce the overall oscillation frequency of the optimised gradient waveforms because intrinsic diffusivities are calculated through the measurements in the parallel directions, which is then used, along with lower frequency OGSE sequences, to estimate diameters that could not be accessed previously in [59]. Later on [62] experimentally demonstrated axon diameter imaging in an *ex vivo* corpus callosum of a rat using a range

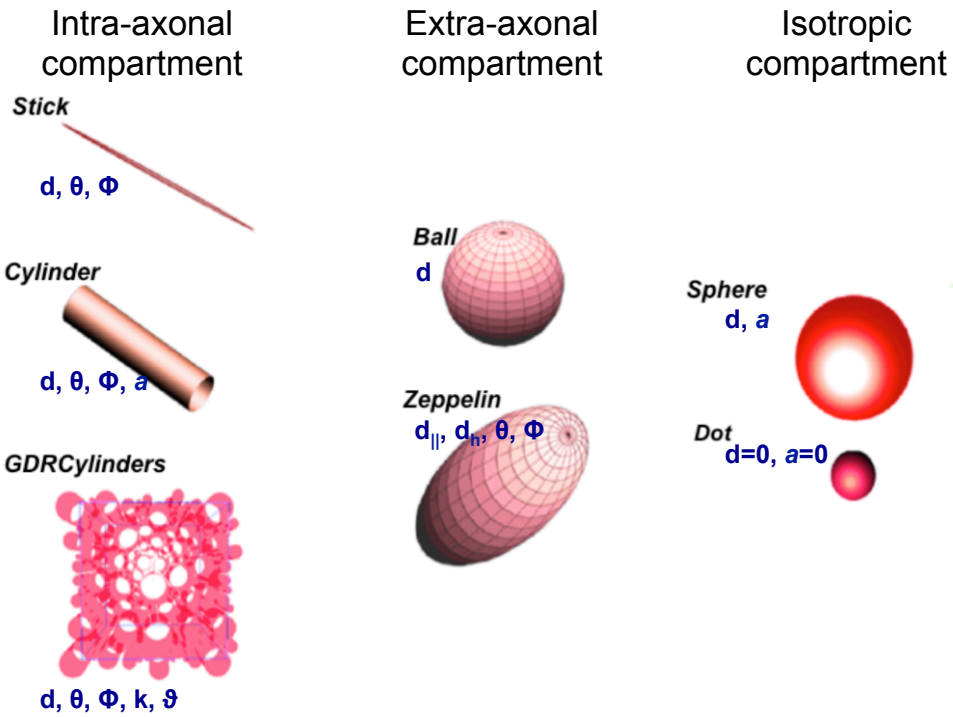

Figure 2.18: Some of the compartments used to represent diffusion in tissue and their associated model parameters (in blue). The intra-axonal compartments ('stick', 'cylinder', and 'GDRcylinders' (cylinders with gamma distributed radii) in the order of top to bottom in the first column) model restricted diffusion. The parameter d is the intrinsic diffusivity of the cylinders and a is their diameter. In terms of GDRcylinders,the parameters, k and ν are the shape and scale parameter respectively. The extra-axonal compartments ('ball' and 'zeppelin' in the order of top to bottom in the second column) model the hindered diffusion in the extra-axonal space. Here the diffusivity within the compartment is either given by d or $d_{||}$ and d_h, which are the parallel and perpendicular diffusivities of the zeppelin compartment. Lastly, the other compartments ('sphere' and 'dot' in the order of top to bottom in the third column) model isotropic restricted diffusion. For the sphere compartment, the intrinsic diffusivity is again described as d and the size of the restriction is define by a. Both d and a are zeroed for the dot compartment, which can be used to define trapped water. Note that although the 'ball' and 'sphere' compartment look similar, the prior models Gaussian diffusion while the latter models restricted diffusion. θ and ϕ define the fibre orientation. According to the taxonomy by [102], the MMWMD model is comprised of cylinder, zeppelin, ball and dot compartments. Figure adapted from [102].

of optimised gradient waveforms, which included OGSE and SDE sequences, with gradient strength fixed at G = 400 mT/m. The findings showed that OGSE provided the lowest axon diameter estimates consistent with findings from [60]. However, largely overestimated diameter up to 10 μm are observed in the dataset suggesting the method was not fully refined. Additionally, the automatic optimisation framework gave the final acquisition protocol and the results showed that OGSE sequences improved the estimates of diffusion coefficient and hence in turn that of the axon diameter [60], however, it was unclear whether OGSE sequences provide better sensitivity than SDE sequences to the axon diameter itself.

A very recent study by [24] explored the signal sensitivity of SDE and OGSE sequences to axon diameters under a range of situations, which included looking at the ideal case of parallel cylinders with known orientation and realistic cases of unknown orientation and dispersion within fibres. They empirically demonstrated that under ideal conditions, SDE sequences with long gradient duration and maximum available gradient strength give the highest sensitivity to small axon diameters ($a \in \{0,10\}$ μm), while under realistic cases, low frequency OGSE sequences are preferred for $a < 7$ μm, with the frequency increasing as the diameter is reduced. Under realistic cases, the low b-value is able to retain signal sensitivity by avoiding excessive signal attenuation from the freely diffusing water along the length of the fibre. More importantly, [24] introduced the concept of the diameter resolution limit, which is the smallest diameter that can be distinguished from zero. They outlined the diameter resolution limits after considering T2 of white matter and different levels of SNR under idealistic and realistic cases. At current clinical gradient strengths of G $\geq$ 80 mT/m, the resolution limit is approximately 5 μm whereas at high gradient strength that are achievable on the *Connectom* scanner, the resolution limit is around 2.5 μm. The very recent theoretical work by [25] also agrees with the findings from [24].

2.4.3 Summary and motivation for the thesis

In this section, we have introduced microstructure imaging using diffusion MRI, with a focus on axon diameter imaging. We have presented the different methods of measuring axon diameters, ranging from q-space imaging, angular double diffusing encoding sequences, temporal diffusion spectroscopy methods and most importantly models based on the CHARMED model which are AxCaliber and ActiveAx. The review so far suggests that ActiveAx is the most practical framework to use because it requires reduced number of measurements and is orientationally invariant - two factors that are essential for *in vivo* imaging. The review also suggests that OGSE and SDE sequences are the best waveforms for estimating axon diameters [24, 25] because, theoretically, they have the highest sensitivity towards small axon sizes. The theory also suggests that under practical scenarios, such as when fibre orientation is unknown or when fibres are dispersed, OGSE sequences show additional sensitivity towards axon diameters, which increases further when higher gradient strengths are used. In this thesis, we verify the theoretical findings experimentally.

Although a previous attempt has been made to compare OGSE and SDE sequences [62], the work showed largely overestimated axon diameters which were not validated with histology. Overestimated axon diameters are a common issue in ActiveAx, as well as in AxCaliber. Two potential reasons that have been mentioned so far in the review are fibre dispersion and insufficient gradient strengths. The prior reasoning has been investigated by [111] but were shown to have very small effects in reducing the overestimation. On the other hand, the latter case of using low gradient strength ($G \leq 80$ mT/m) in clinical settings, has been shown to limit the smallest axon diameter that can be detected [91, 101, 107, 110, 113], leading to largely overestimated diameters. In this thesis, we will carry out extensive experiments to compare axon diameter imaging using OGSE and SDE sequences across a range of gradient strengths, including at the maximum available clinical gradient strength. We use simulations, phantoms and animal models to test the performance of these sequences across substrates ranging from simple to complex environments.

More importantly, we will directly validate the resultant microstructure estimates across most of the substrates using ground truth values, such as manufacturer provided diameters for phantoms and histology for tissue.

Ultimately, the thesis will provide the answer to whether OGSE is preferred in practice for axon diameter imaging. In the big picture, the findings from this thesis can contribute towards using axon diameters as biomarkers for neurodegenerative diseases, such as amyotrophic lateral sclerosis (ALS), and for peripheral nerve regeneration studies.

Chapter 3

Clinical scanner: Implementation and validation of OGSE sequences

The main purpose of this chapter is to implement and validate the performance of OGSE sequences on a typical hospital clinical scanner. In the first section, we implement trapezoidal OGSE sequences with a sine profile onto the clinical scanner and test the implementation using an MR scanner simulator. In the second section, we validate the implementation using gelatine phantoms. The implementation and validation in this section are carried out under the supervision of David Atkinson and Rachel W Chan (Centre of Medical Imaging, University College London).

3.1 Implementation

The purpose of this section is to describe the implementation of the oscillating gradients onto the MRI scanner. The hardware specifications and the software of the MRI system will be explained in general terms to protect proprietary information. The layout of the Philips source code and the procedure of building a diffusion-weighted sequence will also be described. After which, the implementation of the new gradient waveform will be explained in detail, including tests carried out for safety checks to ensure the safe implementation of the OGSE sequences.

3.1.1 Materials and methods

3.1.1.1 Philips Achieva 3.0T TX and source code

The MRI scanner used in this chapter is the Philips Achieva 3.0T TX located at the University College London Hospital (UCLH). This is a standard clinical scanner, which is also used for research purposes. The maximum gradient strength available for this scanner in clinical mode is 62mT/m with a maximum slew rate of 100mT/m/s. The Philips Achieva 3.0T TX has a pulse programming environment (PPE) to allow low-level control of the MRI scanner, which enables customisation of default MRI sequences. The Philips source code contains a massive library of functions involving functions that create basic sequences, add or modify objects such as diffusion-weighted gradients and spoilers into these sequences, as well as functions that carry out patient-related and MR hardware-related safety checks relating to these particular sequences, such as peripheral nervous stimulation and gradient heating.

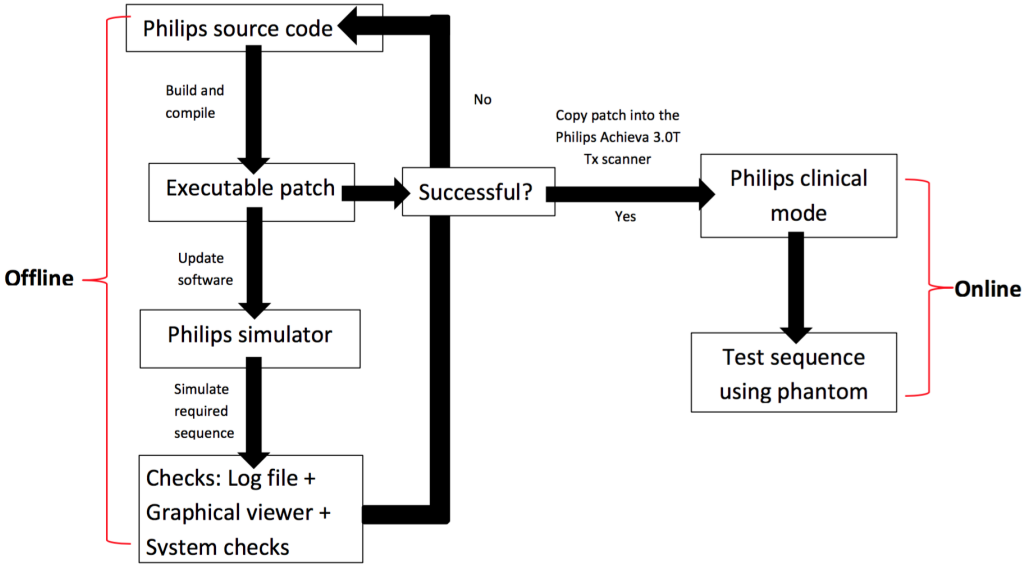

Figure 3.1: Overall process used to create a modified sequence

Figure 3.1 shows the overall process that is used to create the modified MRI pulse sequences. When a modified source code is compiled, it creates an executable patch file, which is used to update the interface of the Philips simulator. This in-

terface is the same user interface that will be displayed in the Philips Achieva 3.0T Tx scanner. The amended sequence can then run in this modified Philips simulator, which is shown in Figure 3.2. Any modifications of a default Philips sequence requires checks in the appropriate areas of the Philips library. These modifications must be ensured to have been registered by the required safety checks by debugging the source code and viewing the whole simulated pulse sequence in a graphical viewer. This newly modified sequence can only be inserted into the actual Philips MR scanner when this whole process is completed successfully and the modified source code has been heavily reviewed by another experienced individual (as an additional safety check). Validation of the sequence using the MRI scanner can be then carried out.

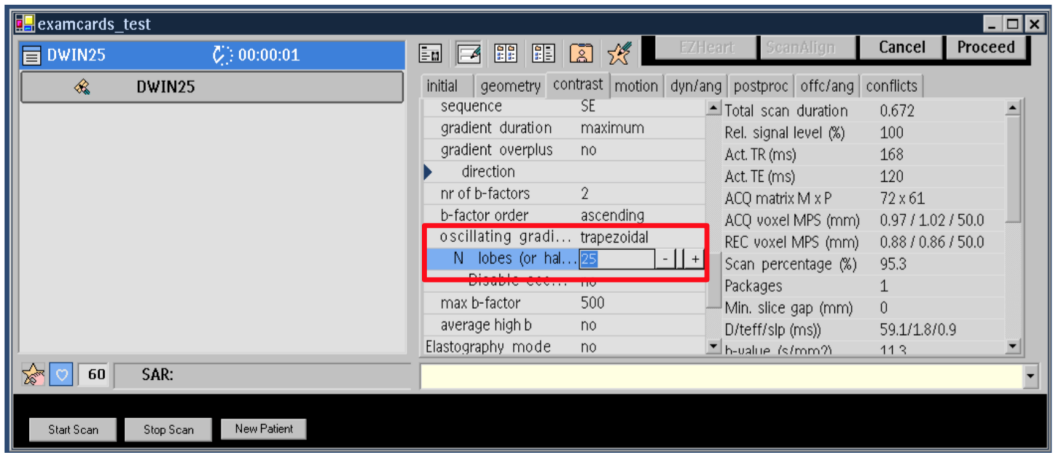

Figure 3.2: Snapshot of the Philips simulator containing the newly introduced oscillating gradient parameters outlined in red.

3.1.1.2 Philips basic diffusion code

In order to understand the process of implementing a diffusion-weighted oscillating gradient sequence, Figure 3.3 illustrates the implementation of the standard Philips SDE diffusion sequence.

In Philips and most other scanners, diffusion waveforms are trapezoidal in shape, which can be defined by their rise-time or slope (units of ms), gradient strength (units of mT/m) and gradient duration (units of ms). Prior to adding the diffusion gradients to the sequence, the required diffusion weighting (b-value (s/mm^2)

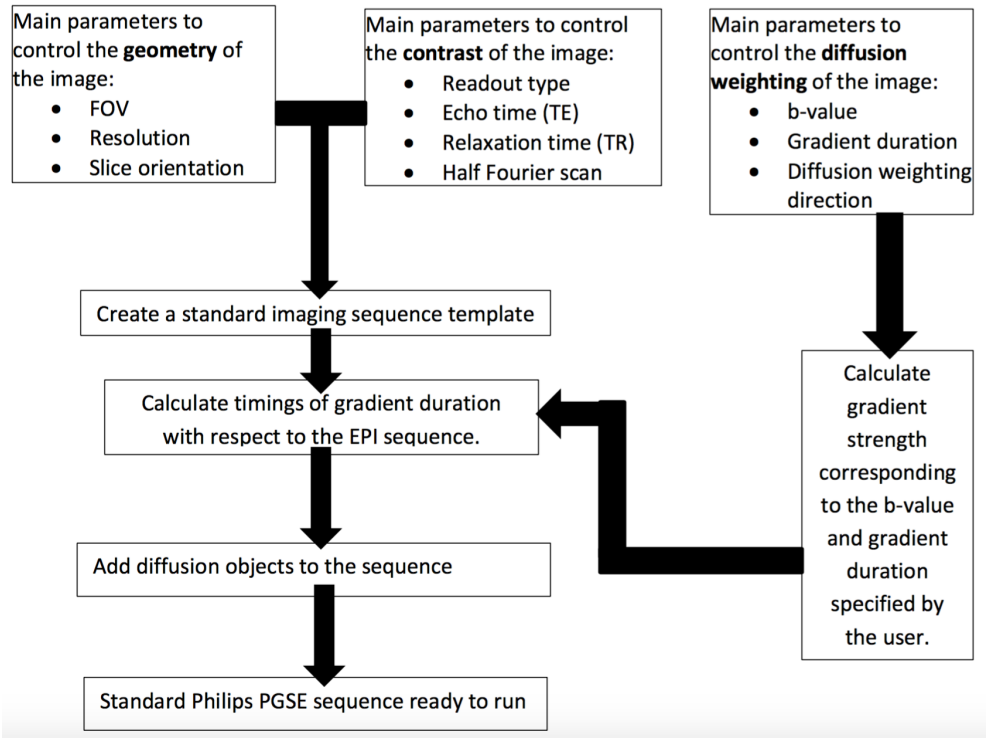

Figure 3.3: Overview of the processing pipeline for the creation of a standard SDE sequence.

is inputted by the user. The gradient duration time (δ) is also specified by the user. The slope (t_r) for the gradients is pre-determined automatically by the existing Philips software and is set to 0.9 ms. The standard relationship for b-value of trapezoidal gradients with respect to the diffusion gradient duration (δ) diffusion time (Δ) and the diffusion gradient strength (G) is given by Equation 2.32 in Chapter 2. Using Equation 2.32, the G and Δ required for the specific b-value can be automatically calculated. The timings of the gradients are then calculated with respect to the imaging sequence template. The diffusion gradients are then fully defined and therefore placed in the imaging sequence template to create a diffusion weighted imaging sequence.

3.1.1.3 Implementation of OGSE sequences

In order to implement OGSE sequences, a similar procedure to the previous section is carried out. Here, we replace the two large trapezoidal blocks of pulsed gradients with trapezoidal waveforms with multiple half oscillations. From here onwards we will refer to the half oscillations of the OGSE sequences as number of lobes (Figure

3.4).

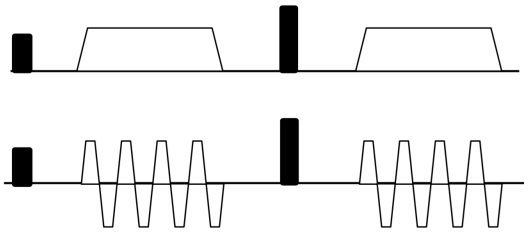

Figure 3.4: The top diagram shows a standard SDE sequence with two blocks of trapezoidal gradients placed on either sides of the RF180 pulse. The bottom diagram shows the OGSE sequence with 8 lobes that replaces the standard single gradient blocks.

The δ and TE parameters, which control Δ, are specified by the user as before. Figure 3.5 shows the new parameters that are introduced during this study. The user now has to define the number of lobes, N, of the OGSE diffusion sequence. The second new parameter that is introduced is the way in which we control b-value.

The first option of the new parameter uses b-value inputted by the user to decide the gradient strength. To do this, the standard SDE b-value equation (Equation 2.32) is replaced with the OGSE b-value equation, Equation 2.33 in Chapter 2 [64].

The second option is to use the maximum gradient strength available to maximise the b-values. The gradient strength, in this case, is set to G_{max} (62 mT/m) instead of determining the gradient strength from Equation 2.33. Figure 3.6 demonstrates that the introduction of OGSE sequences cause a fast decay in b-value with respect to the number of lobes N $\in$ [1,25] used, for a fixed δ=45.5 ms, Δ=59.1 ms and TE=120 ms.

3.1.1.4 Safety considerations

There are two major issues associated with the modification of the diffusion gradient waveform in standard diffusion MRI which prevent maximum performance of gradients: (1) patient safety (peripheral nervous stimulation (PNS)) and (2) hardware safety (gradient coil and amplifier heating). These are also typical in EPI sequences due to the rapid gradient switching during the fast k-space readout by the imaging gradients. However, safety can potentially be a bigger issue when introducing oscillating gradients for diffusion MRI because much stronger gradients are used in

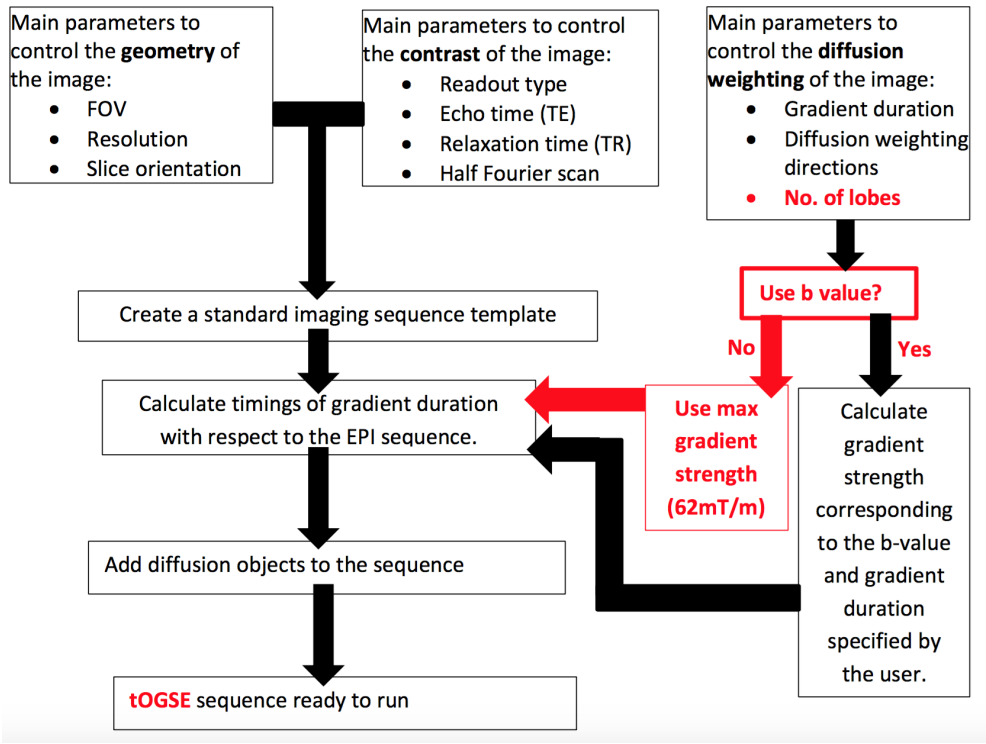

Figure 3.5: Overview of the processing pipeline implementing the new OGSE sequence.

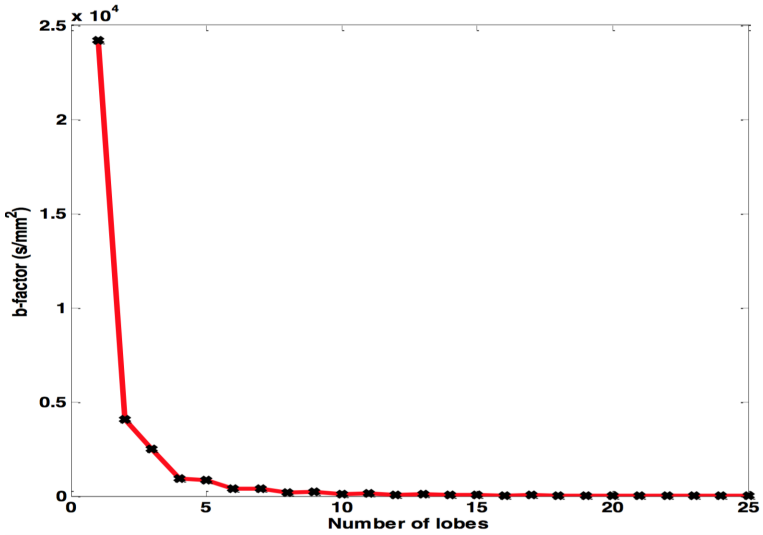

Figure 3.6: Graph showing the reduction of b-value, of an OGSE sequence with fixed Δ and δ, as a function of the number of lobes when maximum gradient strength is used.

comparison to the EPI imaging gradients. In the next three sections, we check the performance of our sequences and ensure that they do not override the manufacturer's safety checks. It must be clarified here that all work that is carried out in this section is on the Philips simulator.

3.1.1.5 Test 1 - Patient safety: Peripheral nervous stimulation (PNS)

Philips use an empirical method called SAFE (Stimulation Approximation by Filtering and Evaluation) [68] to relate the PNS threshold to the gradient waveforms and the rise time, regardless of the shape of the waveform.

Here we check whether our implemented oscillating gradients (which are new objects that were created and added to the diffusion sequence) are being accounted for. In Philips, amplitudes and time points of all involved gradient waveforms within a sequence are logged. Hence to ensure that the new gradient objects are accounted for, we check the logged PNS calculations. Furthermore, the implemented oscillating gradients and the oscillating gradients used in normal EPI readouts only differ in terms of maximum gradient strength and duration of the gradient. The similarities between the two types of oscillating gradients are in their slew rates and approximate frequencies of oscillations. Hence the SAFE model should still be valid for our OGSE sequences.

In this experiment, we use three different diffusion sequences applied in the x-axis only to ensure that the PNS limit set by Philips is pushed to its limits when using OGSE sequences. Figure 3.7 illustrates the following sequences:

- A standard diffusion sequence, with parameters N=1, b=500 s/mm^2, G=9 mT/m, which we call OGSE1$_{lowG}$.

- A diffusion sequence with a very large b value, with parameters N=1, b=25000 s/mm^2, G=62 mT/m, which we call OGSE1$_{maxG}$.

- A diffusion sequence with the maximum number of lobes possible for the specified TE, with parameters N=25, b=12 s/mm^2, G=62 mT/m, which we call OGSE25.

We also repeat the OGSE25 by choosing the diffusion encoding direction to involve an equal combination of the x, y and z axes gradients to ensure that a combination of gradient waveforms does not exceed the PNS limit. We refer to this sequence as 'OGSE25$_{oblique}$'. It must also be clarified here that the OGSE1 sequences mentioned above are simple SDE sequences but are run using the new implementation developed above. We expect that OGSE25 and OGSE25$_{oblique}$ will generate the

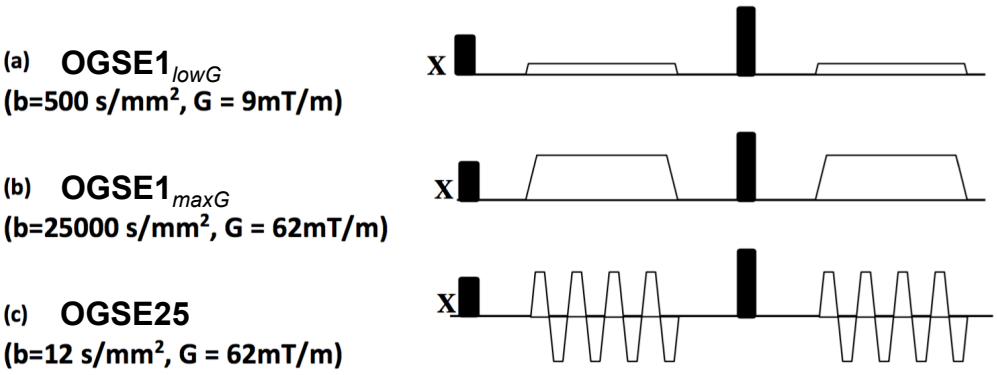

Figure 3.7: Diagram showing the 3 different diffusion sequences used to check the gradient heating model. (a) OGSE1$_{lowG}$, (b) OGSE1$_{maxG}$, (c) OGSE25 (although only N=8 are shown here for clarity). The gradient strength are not scaled. Also, the X corresponds to the gradients axis in the scanner coordinates.

higher PNS value as they have the maximum number of lobes possible for TE=120 ms, and in the case of OGSE25$_{oblique}$ a combination of gradients is used. If the PNS limits for these sequences are satisfied, then the PNS limits should also be satisfied for all other sequences.

3.1.1.6 Test 2a - Hardware safety: Gradient heating

Here we verify that our OGSE implementation is registered by the Philips gradient heating model and is not inadvertently ignored. We test the model by changing the parameters of the oscillating gradients (such as the number of lobes used), and check that resultant changes in the predicted temperature from the Philips simulator does occur. The predicted temperature of the transistors within the gradient amplifiers and the hotspot regions within the gradient coils are obtained from the Philips simulator's log file. Similar to the previous section, it is important to clarify here that this is carried out on the simulator and that we are not changing the gradient

heating model that is incorporated into the Philips scanner.

We record the temperature of the transistors and the hot spot regions from the log file for the same three sequences in Figure 3.7. Additionally, instead of using the OGSE25 sequence from the section above, here we use OGSE1_{maxG} with a combination of the x, y and z axes gradients and refer to this particular sequence as $\text{OGSE1}_{maxG,oblique}$. We expect the last two sequences in Figure 3.7 and $\text{OGSE1}_{maxG,oblique}$ to generate the maximum heat possible for TE=120ms because they require maximum b-value, maximum number of lobes and use of a combination of gradients, respectively. Hence if these sequences pass the test, the less extreme sequences should pass as well.

3.1.1.7 Test 2b - Hardware safety: Capacitor drain of the gradient amplifier's power supply

In Philips, a function is available to check whether the implemented diffusion gradients will drain the capacitor voltage of the gradient amplifier's power supply to below minimum. The gradient strength and the total gradient duration time (see Figure 3.8) are used to calculate the present power drawn from the power supply by the gradient amplifier in the Philips simulator. This function had to be modified because the total gradient duration time of the oscillating lobes is initially interpreted as the gradient duration time in Figure 3.8. Thus the function is modified for OGSE sequences to include the total time duration of the oscillating gradient waveforms. We then use the log file to check the capacitor voltage for OGSE1_{maxG} and OGSE25 from Figure 3.7 to ensure that the changes have been registered.

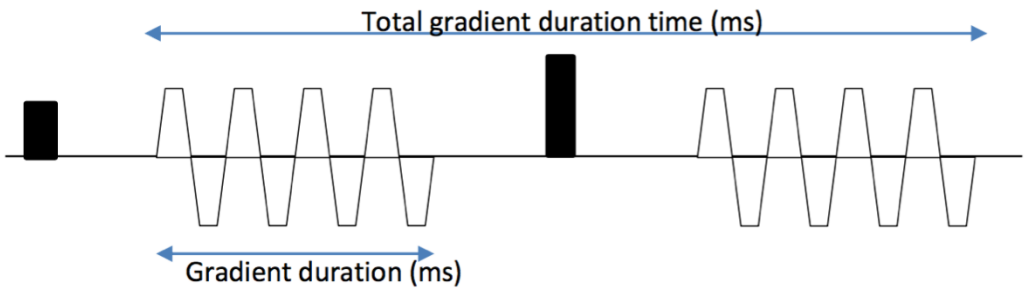

Figure 3.8: Illustration of the gradient duration and total gradient duration time used in calculation of capacitor voltage of the power supply of the amplifier.

3.1.2 Results and discussion

3.1.2.1 Test 1 - Patient safety

For each gradient waveform, we follow the available log file of the simulator and plot the amplitudes and time points. The PNS limit set by Philips at any time point is 84.69 T/s, which is the first operation mode. For a standard SDE, ($OGSE1_{lowG}$) a maximum PNS of 18.7 T/s is attained. On the other hand, Figure 3.9 shows that a higher PNS of 53.6 T/s and 68.4 T/s is reached for $OGSE1_{maxG}$ and OGSE25, respectively. Furthermore comparison of the PNS for $OGSE25_{oblique}$ shows a maximum PNS value of 77.1 T/s. This confirms that the simulated PNS data obtained from the OGSE sequences is accounted for and does comply with the safety regulations set by Philips (which can vary between the EU and USA).

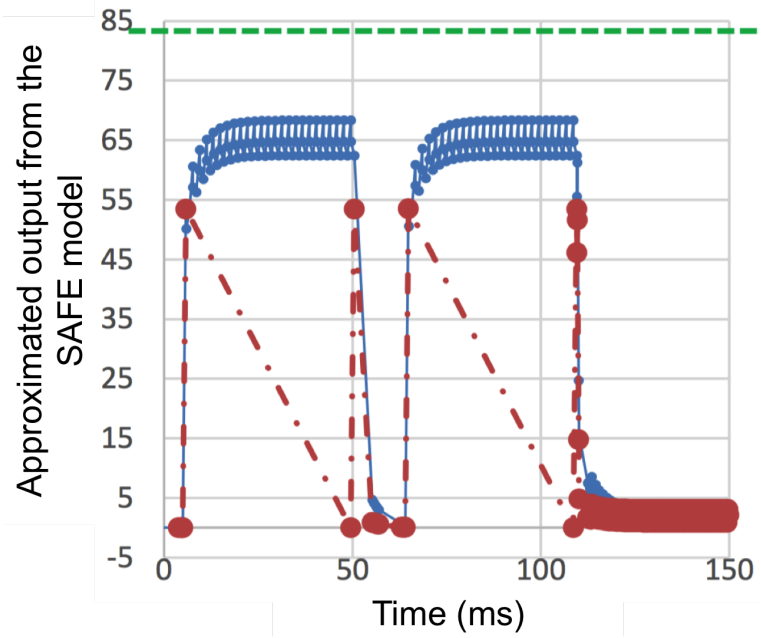

Figure 3.9: The outputs from the SAFE model of the $OGSE1_{maxG}$ (red) and OGSE25 (blue) sequence are shown here with respect to the duration of the gradient waveform applied. Diffusion weighting is applied only in the x-direction of the scanner coordinates. The PNS threshold is 84.69 T/m and is plotted in green.

3.1.2.2 Test 2a - Hardware safety

Hotspot temperatures within gradient coils were recorded but were found to vary by a maximum of 1^{o}C for the sequences with high b-value and high number of lobes and thus graphs for this case have not been generated. This is good because,

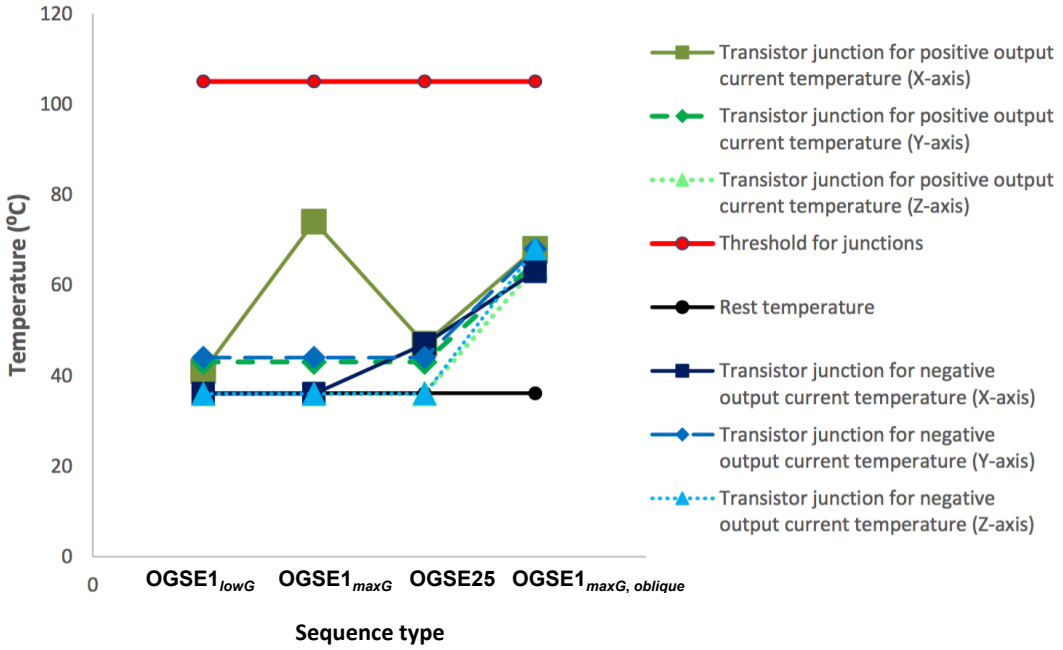

Figure 3.10: Graph to show the temperature of the transistor for the sequences in Figure 3.7. The threshold and rest temperature for the transistors are also shown.

otherwise, increases in the temperature of the hotspot regions could indicate local heating due to our implemented oscillating gradients.

Figure 3.10 shows temperatures of the transistors within the gradient amplifier for the sequences defined in Figure 3.7. For all cases, the temperatures lie below the threshold (red line). Exceeding this threshold by the transistor may cause MR hardware failure. The rise in temperature for the transistor junction for positive output current corresponds to when a positive gradient amplitude is used in the diffusion sequence and vice versa for the transistor for negative output current. For example, temperature increases are only observed for the transistor for the negative output current in the cases of OGSE25, where oscillating lobes occur, and $\text{OGSE1}_{maxG,oblique}$, where combination of gradients are used.

We only apply the diffusion encoding gradient in the x-axis for most sequences, and therefore, we expect and also observe maximum gradient heating occurring only in the x-axis for majority of the sequences. However, two exceptions occur. First is the $\text{OGSE1}_{maxG,oblique}$ sequence where gradient heating occurs on all axes due to the combination of axes used. Second is the OGSE1_{lowG}, where the very

low gradient strength results in minimal temperature increase in the x-axis. Interestingly, we also observe an increased but constant temperature in the transistor junction for positive output current in the y-axis across all sequences with diffusion encoding gradient in the x-axis. We believe this temperature increase in the y-axis is not due to the diffusion encoding gradients as the temperature is stable across all sequences.

We also observe from the sequences using maximum gradient strengths that OGSE1$_{maxG}$ and OGSE1$_{maxG,oblique}$ had much higher increases in temperature than OGSE25, which had the same gradient duration time. This is probably because both of the OGSE1$_{maxG}$ and OGSE1$_{maxG,oblique}$ sequences require continuous current input at maximum power, whereas the OGSE25 sequence requires maximum power in intervals of 1.8 ms (2 $\times$ slope of the diffusion gradient waveform).

For the cases where temperature rises, the gradient heating model adds some 'dead time' to the sequence, which allows time for the gradient amplifiers to cool down [70]. Hence for OGSE25 and both cases of OGSE1$_{maxG}$ and OGSE1$_{maxG,oblique}$, extra time that correlates with the temperature of the transistors of the amplifier, as shown in Table 3.1, is added into the sequence.

Table 3.1: Table to show the additional time extension added to the end of the diffusion sequence to allow the gradient amplifiers to cool down after heating up. These time values are recorded from the Philips log file.

	OGSE1$_{lowG}$	OGSE1$_{maxG}$	OGSE25	OGSE1$_{maxG,oblique}$
Time extension (ms)	0.0	75.2	47.4	74.4

This section has checked that the Philips gradient heating model does include the implemented oscillating gradients in the system checks.

3.1.2.3 Test 2b - Hardware safety

The maximum available capacitor voltage of the gradient amplifier's power supply is 4.7 kV. The voltages calculated for both the OGSE1$_{maxG}$ and OGSE25 from Figure 3.7 are 1.8kV and 0.59 kV, respectively. This makes sense because the positive to negative gradient strength for OGSE (+62 mT/m to -62 mT/m) requires double

the voltage from the capacitor than the OGSE1$_{maxG}$ case. Thus it can be stated that the threshold capacitor voltage of the power supply of the gradient amplifiers is not exceeded.

Overall, all of the safety checks that have been conducted in this section suggests that the implemented OGSE sequences are safe to use. This, therefore, allows us to move onto the validation of these implemented sequences using phantoms.

3.2 Validation

The previous section ensured that the newly added oscillating diffusion gradient waveforms do run through the main software checks that all standard Philips SDE diffusion gradients experience. The aim of this section is to validate the implementation of the oscillating diffusion gradients onto the actual Philips Achieva 3.0T Tx MR scanner using a gelatine phantom to check the image quality.

A gelatine phantom is commonly used in quality assurance of MR scanners. Their advantages over water phantoms are that (1) they have a lower T2 (40-150 ms) similar to those found in tissue, (2) they do not require settling time and (3) they prevent issues regarding physical vibrations, which could vary depending on the extent of the oscillating gradients [115]. The last advantage is the most important in our case because otherwise non-uniform images of the phantom could be acquired, preventing any conclusion on the implementation of the OGSE.

3.2.1 Methods

3.2.1.1 Gelatine phantom preparation

In order to prepare the homogeneous phantom for MR scanning, a set procedure is used. A large plastic container is filled with 1 l of boiling water. 132 g of Dr Oetker‘s beef gelatine are then placed in the container and this gelatine mixture is simultaneously stirred gently with a plastic spatula.

Once all the required gelatine is dissolved, the gelatine mixture is transferred by pouring slowly into a standard plastic food container (NMR invisible) that is going to be used as a phantom (Figure 3.11).

The container, with dimensions of 220 mm $\times$ 160 mm $\times$ 60 mm, is roughly

Figure 3.11: Photograph of the gelatine phantom, which is essentially a food container containing two smaller plastic containers inside.

the size of the head in the Head-Foot and Left- Right directions. It also has an air tight lid to prevent any future substance leakage. Two smaller plastic containers (with dimensions of 140 mm $\times$ 105 mm $\times$ 50 mm and 105 mm $\times$ 75 mm $\times$ 50 mm), are also contained within this large food container, where the smallest container is stacked on top of the medium sized container. Hence this provides a three compartment gelatine phantom. Any bubbles on the surface are removed with the plastic spatula. The air tight lid is then locked onto the food container, and the whole phantom is slowly transferred to a refrigerator (which is at a temperature of $+3^{o}$C), and is placed on an even surface. The phantom is left for 24 hours to fully set. It is then transported with caution, to prevent movement causing de-gelatinisation of the phantom, into the MR scanning room and is left for 4 hours to reach the room temperature of the scanning room. This approach is taken to ensure that the temperature changes in the phantom, which can further cause T1 and T2 lengthening along with changes to diffusivity, do not occur during the experiment itself.

3.2.1.2 Image acquisition

Gelatine phantom is placed on an MR head coil (SENSE Head coil 8 elements) and secured in place with NMR invisible wedges. One standard Philips SDE sequence (N=1 run using the standard implementation) and two trapezoidal OGSE sequences (N=2, N=3), with TE/TR = 120 ms/1000 ms , δ/Δ=45 ms/59 ms and G=9, 19, 26 mT/m, respectively, and with equal b-values (500 s/mm^2) are applied on the gelatine phantom in three directions (readout, phase-encoding and slice-encoding

directions). The imaging matrix is 115 × 36 × 24 with a resolution of 2 mm × 2 mm × 5 mm. Other sequence parameters are: Half Fourier=0.618, repetitions=10 and total acquisition time is 30 minutes.

Only one transverse slice at the phantom centre, averaged over 10 repetitions, is used to analyse the gelatine phantom to validate the OGSE sequence implementation.

3.2.2 Results and discussion

Figure 3.12 shows the images of the gelatine for the three trapezoidal OGSE sequences over the three gradient directions. It also shows the corresponding b=0 image for each sequence. No systematic artefacts or distortions are observed in the images. The signal intensity for all diffusion-weighted images also look the same and are quantified in Figure 3.13.

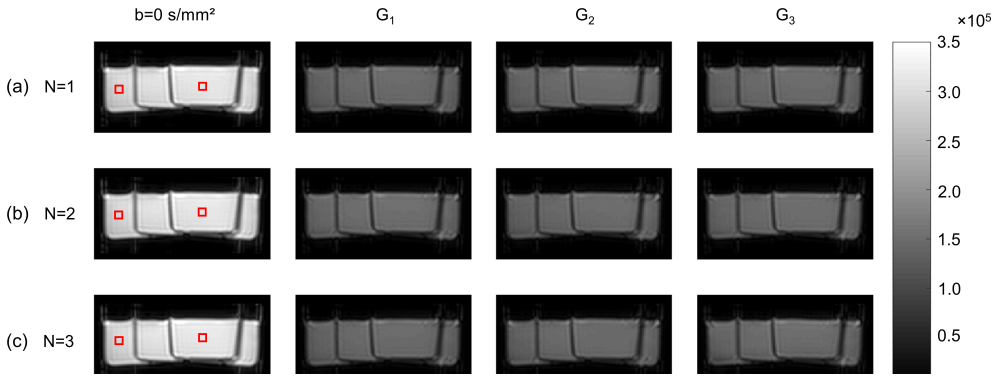

Figure 3.12: Images of a single slice of the gelatine phantom acquired for three trapezoidal OGSE sequences (a) N=1 (b) N=2 and (c) N=3, all with b = 500 s/mm^2. The first column shows the b=0 s/mm^2 measurements and the subsequent columns display the diffusion weighted images in the readout (G_1), phase-encoding (G_2) and slice-encoding (G_3) directions. The two red boxes indicated on each of the b=0 images are regions of interest (ROI 1 (left) and ROI 2 (right)) used in Figure 3.13.

Figure 3.13 shows the mean and standard deviation of the MR signal calculated for each measurement at the two ROIs (indicated by the red boxes in the b=0 images in Figure 3.12). The MR signal across all diffusion weighted measurements are the same because the gelatine phantom has isotropic diffusion. Therefore, the signal attenuation is independent of gradient directions, as visually observed in Figure 3.12. The results demonstrates that the OGSE sequences used here are comparable

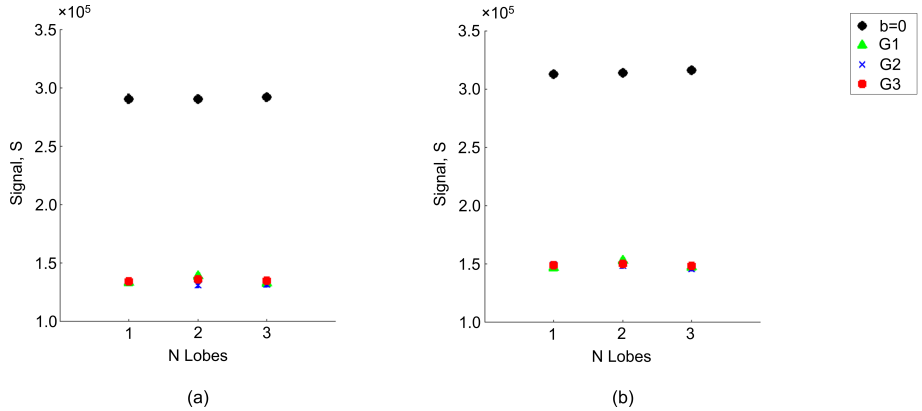

Figure 3.13: The graph shows the mean and standard deviation in (a) ROI 1 and (b) ROI 2 across all measurements of the three trapezoidal OGSE sequences displayed in Figure 3.12. Black circle data points represent the signal from the b=0 images, while the green triangles, blue crosses and red squares represent the diffusion weighted signal from the readout (G_1), phase-encoding (G_2) and slice-encoding (G_3) directions, respectively. As the images are highly homogeneous, the standard deviations are too small to be seen on the graphs.

to the standard SDE sequences (i.e N=1).

In general, the sensible images of the gelatine phantom suggest that the scanner implementation of the oscillating diffusion gradients is successful and that the gradients are applied as expected.

3.3 Conclusion

Overall in this chapter, we implement and validate trapezoidal OGSE sequences on a clinical scanner. We test the implementation of the sequences on the Philips simulator and ensure that the safety limits for both patients (in terms of peripheral nerve stimulation) and scanner hardware (in terms of gradient heating) are met by pushing the diffusion gradients to their limits on the simulator. We then validate the implemented sequences on the clinical scanner by imaging a gelatine phantom with isotropic diffusion using diffusion sequences with same b-values, over multiple gradient directions, but with varying number of lobes, N. As expected, the diffusion signal is independent of N and gradient directions, and therefore demonstrates successful implementation of the sequences on the clinical scanner.

In the next chapter, we attempt to use these newly validated OGSE sequences to carry out microstructure imaging in phantoms with restricted diffusion.

Chapter 4

Clinical scanner: Pore diameter mapping of micro-capillaries phantom

In chapter 3, we implemented oscillating trapezoidal OGSE sequences onto a clinical scanner. Here we explore the sensitivity of OGSE to various capillary diameters on a clinical scanner using the OGSE ActiveAx approach.

We use water-filled micro-capillaries array plates as a model for axons and OGSE ActiveAx [59, 60, 63, 64, 116] with a range of frequencies for the estimation of microstructure indices. The practical experiments in this section are carried out under the supervision of David Atkinson and Rachel W Chan (Centre of Medical Imaging, University College London).

The work in this chapter is published as:
L S Kakkar, D Atkinson, R W Chan, B Siow, A Ianus and I Drobnjak. Pore diameter mapping on a clinical scanner using orientationally-invariant OGSE ActiveAx, Computational Diffusion MRI, MICCAI Workshop 2016.

4.1 Methods

This section outlines the diffusion MR model for the micro-capillaries array plates representing the white matter axons. It then describes the preparation of the micro-capillaries array plates, specifies the imaging protocols and lays out the data pro-

cessing pipeline.

4.1.1 Phantom model

We use a single restricted compartment of unknown orientation as a model for our phantoms (i.e. a very simplified MMWMD model from Chapter 2, Section 2.4.2.5, where $S_2 = 0$, $S_3 = 0$ and $S_4 = 0$). All microcapillaries (representing axons) are parallel and non-abutting cylinders, with equal radii and impermeable walls. The parameters of the model are (1) microcapillary diameter, a, (2) intrinsic diffusivity, $d_{||}$, and (3) microcapillary direction, $\mathbf{n}$.

4.1.2 Phantom experiments

4.1.2.1 Sample preparation

The microcapillaries array plates (as shown in Figure 4.1a) are thin square plates (each of dimensions 20 mm $\times$ 20 mm $\times$ 1 mm) made up of borosilicate glass (Incom, inc). The microcapillaries array plates will simply be referred to as 'plates' from here onwards. Each plate consists of many microcapillaries. This study uses three pairs of plates with ground truth microcapillary diameters of 5, 10 or 20 μm, and an open area fraction between 60 and 65 % (Figure 4.1b, c and d). The ground truth diameters of the microcapillaries are provided by the manufacturer and these are the only available sizes which broadly mimic the possible *in vivo* axon diameters that are encountered in the central nervous system [5].

The 3 pairs of plates are slotted into a 3D printed phantom holder (using Objet VeroBlue (Stratasys Ltd) as the material) containing distilled water such that the microcapillaries are aligned parallel to the main magnetic field. Since there are differences in the susceptibility of the water (susceptibility of -9.03 ppm [117]) and plates that are made up of borosilicate glass (susceptibility of -11.05 ppm), the alignment helps to reduce the inhomogeneity in the main magnetic field, which otherwise can lead to artefacts such as image distortion and signal loss. Afterwards, the plates are also soaked in the distilled water for one week to remove air bubbles at the plate surface.

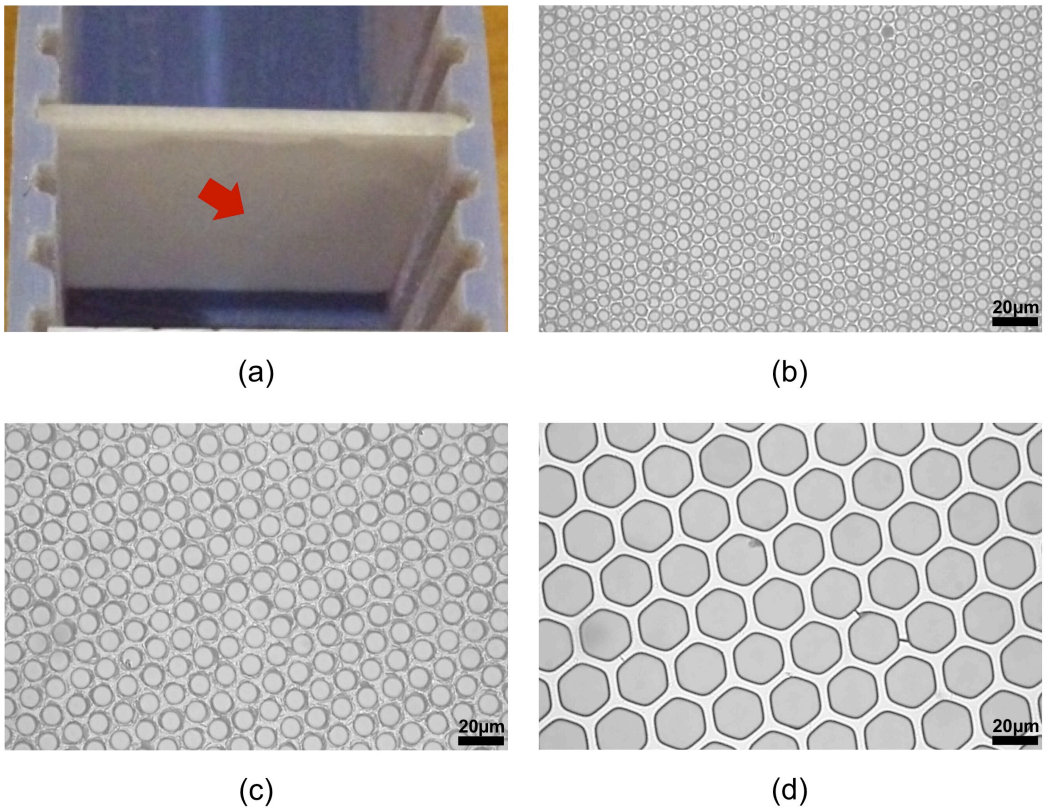

Figure 4.1: (a) Photograph of an example microcapillaries array plate with microcapillary diameters of 5 μm (plate 1). Each plate is vertically slotted into a phantom holder containing distilled water. Magnified light microscopy images of (b) 5 μm (plate 1), (c) 10 μm (plate 1) and (d) 20 μm (plate 1), at the approximate point indicated by the red arrow, to show the cross-section of the microcapillaries array plate.

4.1.2.2 Image acquisition

Trapezoidal OGSE diffusion sequences, as shown in Figure 4.2, are implemented on a Philips Achieva 3.0T TX MRI system (University College London Hospital, London, UK). We choose trapezoidal OGSE waveforms with a fixed maximum gradient strength as it has been shown previously that these are the most sensitive to microcapillary diameters [59, 63]. The main user controlled parameters are echo time (TE), pulse duration (δ), diffusion time (Δ) and number of half period oscillations, referred to as 'lobes' (N). Gradient strength, G, and slew rate for the trapezoid waveforms are fixed at 62 mT/m and 68.9 mT/m/ms, respectively, to adhere to manufacturer set threshold for peripheral nervous stimulation (PNS). The b-value for the OGSE sequences with trapezoidal gradient are calculated as in [64].

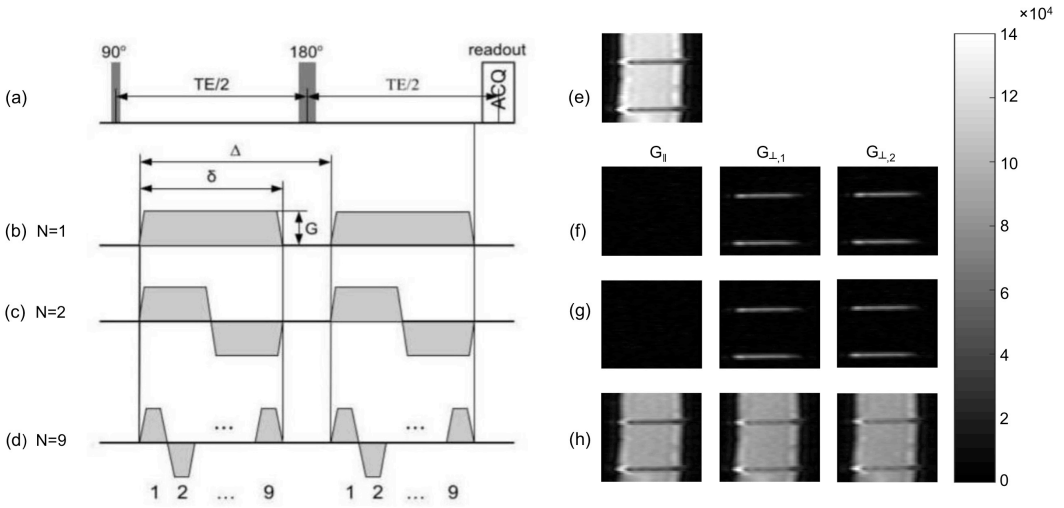

Figure 4.2: Schematic representation of the OGSE diffusion imaging protocols (left) and corresponding plate example images (right). The protocol included (a) the single shot echo planar imaging (SS-EPI) sequence containing the excitation, refocusing pulse and readout timings; and the OGSE sequences with (b) N = 1, (c) N = 2 and (d) N = 9. The parameters depicted here are: echo time (TE), pulse duration (δ), diffusion time (Δ), gradient strength (G) and number of lobes (N). The example plate images show the 5 μm pair (immersed vertically in water) scanned perpendicular to the plane of the plate. (e) is the non-diffusion weighted image. (f), (g) and (h) display diffusion weighted images for OGSE sequence shown in (b), (c) and (d) respectively. The diffusion weighted images are in the parallel and two nearly perpendicular directions relative to the long axis of the microcapillaries. These are only three example directions of the 32 gradient directions that were used in this study. High signal attenuation is seen in the parallel gradient direction indicating free diffusion of water along the long axis of the microcapillaries. Signal appears bright in the perpendicular directions which comes from the restricted diffusion of water across the long axis of the microcapillaries.

The plates are scanned during the same session using Philips SENSE Flex Surface coils. A room temperature of 20 ^{o}C is maintained throughout the experiment. The diffusion protocol consists of 9 HARDI shells with b-values 120-20000 s/mm^2, each with 32 gradient directions and one b=0 s/mm^2. The shells have a fixed pulse duration (δ = 39ms, Δ = 63ms) but the number of lobes varies from N = 1 to N = 9 (i.e. frequencies between 12.8 - 115 Hz), and consequently the b-values varied (see Figure 4.2). An additional, standard SDE diffusion sequence (N = 1, δ = 10 ms,Δ = 92ms) with a b-value of 1860 s/mm^2 is also included for comparison.

All diffusion protocols use single-shot-echo-planar imaging (SS-EPI). Each

acquired image has one slice of thickness 10 mm, which is orthogonal to the plane of the plate (see Figure 4.2). The imaging matrix is 76 $\times$ 19 with a resolution of 0.4 $\times$ 1.6 mm, which is used to ensure at least one row of the voxels does not contain partial volume effects. In order to obtain sufficient diffusion weighting for all N, we extend the diffusion gradient duration by using a long echo time (in terms of clinical scanning) TE = 120 ms for all shells. Other sequence parameters are: Half Fourier = 0.8, TR = 3 s, repetitions = 1 and acquisition time per protocol is 1.75 minutes.

4.1.3 Data analysis

4.1.3.1 Data processing

The acquired images are registered using FMRIB Software Library (FSL, FMRIB, Oxford) rigid-body registration [118] to account for any potential vibrations from the oscillating gradient waveforms. The SNR is calculated from the mean and standard deviation across 9 b = 0 images per voxel. The region of interest (ROI) is chosen from the b = 0 images by manually excluding edges of the plate to avoid voxels affected by partial volume effect. The ROIs of all plates has a mean SNR $>$ 45. Additionally, as the direction of the microcapillaries, **n**, is assumed to be unknown, **n** is estimated using OGSE diffusion tensor imaging and then is inputted into our model fitting procedure described below.

4.1.3.2 Model fitting

A voxel-wise two stage model fitting procedure, as defined in [101], is used to estimate diameter and diffusivity of the plate samples.

Grid search An initial search for the maximum likelihood parameter settings given a Rician noise model is carried out by iterating over a fixed grid of parameter values within a specified range of physically plausible values. The objective function (f_{Obj}) to be minimised is the negated Rician log likelihood of the model parameter values given the measured data (R_{log}) [20]:

$$f_{Obj} = -R_{log} = -2log(\sigma) - \frac{S^2 + A^2}{2\sigma^2} + log(A) + I_0(\frac{AS}{\sigma^2}) \tag{4.1}$$

where σ is the gaussian standard deviation, A is the measured signal, S is the predicted signal from the model described in Section 4.1.1 and I_0 is the Bessels function of the first kind order 0.

To reduce the search space, the axon orientation, **n**, which is assumed to be unknown, **n** is estimated using a Diffusion Tensor model. The results from the grid search are used as the starting points for the next stage.

Active-set method The active-set algorithm is used with the same Rician noise model as in grid search to refine the maximum likelihood parameter estimates. The algorithm is a non-linear constrained optimisation method and more details can be found in [119]. It uses a line search procedure to find the direction in which the objective function is decreases. Subsequently, the objective function moves a certain distance provided the constraint boundaries are satisfied. This step is iterated until the direction does not changes and the objective function reaches a minima. Constrained optimisation such as this increases the speed of convergence and is a disadvantage in un-constrained algorithms like Levenberg-Marquardt which is used in [101, 102]. The active-set user-defined constraints for all parameters, lower and upper bound limits, are a = 0.002 and 30.0 μm, and $d_{||}$ = 0.002 and 3 μm^2/ms, respectively. Once the microcapillary diameters and diffusivities with the highest log-likelihood are found for each voxel for each plate across the given ROI, their mean and standard deviation are calculated across this region.

4.2 Results

First we test whether the microcapillary diameter and the intrinsic diffusivity can be estimated based on the entire trapezoidal OGSE imaging protocol in Figure 4.2. We then test which of the OGSE sequences out of those in Figure 4.2 provide the most accurate parameter estimates by analysing each shell separately, and we compare the results with the parameters obtained from the standard SDE with long diffusion time.

Figure 4.3a and b display the parameter maps (diameter and diffusivity, respectively) for the ROIs of our plates. Both pairs of 10 and 20 μm plates have

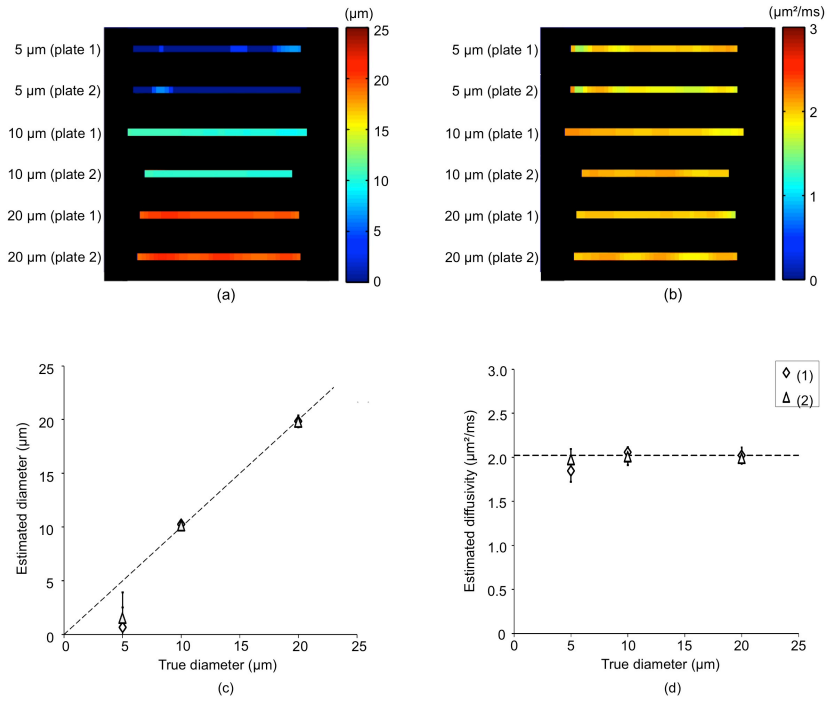

Figure 4.3: The (a) diameter, a, and (b) diffusivity, $d_{||}$, maps, respectively, across the ROIs of the 5 μm (plates 1 & 2), 10 μm (plates 1 & 2) and 20 μm (plates 1 & 2) plates. All images have been cropped and magnified by the same amount for visual clarity. The graphs show the mean and standard deviation of the (c) diameters of the microcapillaries (μm) and (d) intrinsic diffusivities (μm^2/ms), which are calculated over the ROIs. The diamond and triangle data points represent the first and second set of plates, respectively. The dashed line represent the line of equality for (c), and for (d) it represents the theoretical water diffusivity calculated using [120] for water at 20 ^{o}C.

accurate and precise (indicated by the homogeneous maps) estimates. The parameter maps for the 5 μm plates are partially inhomogeneous and they significantly underestimate the diameter. Figure 4.3c and d reflect the accuracy and precision of the parameters, displayed in Figure 4.3a and b, as the mean and standard deviation of the estimated a and D_i calculated across the ROI. The figure also shows very similar parameter estimates within each pair of plates suggesting that the results are reproducible. For the first set of 5, 10 and 20 μm plates, the estimates of mean$\pm$standard deviation for [a,$d_{||}$] are [1.5 $\pm$ 2.4 μm, 2.0 $\pm$ 0.1 μm^2/ms], [10.1 $\pm$ 0.5 μm, 2.0 $\pm$ 0.1 μm^2/ms] and [19.8 $\pm$ 0.4 μm, 2.0 $\pm$ 0.1 μm^2/ms], respectively. For the second set of 5, 10 and 20 μm plates, the values of [a,$d_{||}$] are: [0.7 $\pm$ 1.9 μm, 1.9 $\pm$ 0.1 μm^2/ms], [10.3 $\pm$ 0.2 μm, 2.1 $\pm$ 0.1 μm^2/ms] and [19.8 $\pm$ 0.6 μm,

2.0 ± 0.1 μm^2/ms], respectively. We observe the highest accuracy and precision for 10 μm plate pairs, and the worst for 5 μm plate pairs. A possible reason for the diameter index estimates of 5 μm plates hitting the lower bound, 0.0 μm, is due to model instability. Fitting errors caused by model instability usually occur when there are insufficient diffusion measurements for the given model or when the model has too many parameters [121, 122]. However, in our case, neither reasons justify the lower bound estimate as a fitting error because our simple model has only two parameters and a large number of measurements (9 shells each with 30 measurement directions). In addition to this, the accurate measurements of 10 and 20μm plates also suggest that the model is stable. This suggests that the current set of diffusion measurements may not be sensitive to diameters of 5 μm plates.

Figure 4.4 shows the quality of fit by comparing measurements with predictions from the fitted model (dashed line) and the ground truth (solid line) in the central voxel of each plate ROI. The ground truth curve was generated using the manufacturer provided diameters and a diffusivity constant (2.0 μm^2/ms) calculated for the free water compartment at 20 ^{o}C ([120]). The representative voxels chosen here are typical for the ROIs. A good agreement can be observed between the measurements and the fitted curve across all plates and the quality of fit can be quantified using R_{log} (see Equation 4.1). The R_{log} for 5, 10 and 20 μm plates are 1.4×10^5, 1.1×10^5, and 1.7×10^5 for the first pair of plates, respectively, and 1.3×10^5, 1.3×10^5 and 1.4×10^5 for the second pair of plates, respectively. A good agreement is also observed between the fitted curve and the ground truth curve for the first pair of 10 μm and 20 μm plates. However, slight differences between the fitted curve and the ground truth curve can be observed in the second plates of 10 and 20 μm. This can be due to the overestimated diffusion constant caused potentially by partial volume effects. For this central voxel, in the case of 5 μm plates (Figure 4.4a and b), the differences between signals predicted using the known parameters [a,$d_{||}$] = [5.0 μm, 2.0 μm^2/ms] and model estimates [a, $d_{||}$] = [0.0 μm, 2.0 μm^2/ms] for the first 5 μm plate are small, despite the model estimates of diameter being so different. The difference is slightly larger in the second 5 μm plate ([a,$d_{||}$]

= [0.0 μm, 1.8 μm^2/ms]) but this is most likely due to an underestimation in the diffusion constant. These results suggest the change in measured signal is negligible for microcapillaries with diameters at or below 5 μm, i.e the measured signal is not very sensitive to diameters at or below 5 μm.

Figure 4.5 shows the mean and standard deviation of the estimated diameter and diffusivity obtained by separately analysing each individual shell with N lobes (from Figure 4.2). Here, results from a standard SDE sequence (N = 1,δ = 10 ms) are also included for comparison. 10 and 20 μm plate diameter estimates are close to the ground truth values for the majority of N, whereas 5 μm estimates are largely underestimated for all N. Focusing on 10 and 20 μm plates, N $\in$ 2,3,4} perform very well, while for N $\geq$ 5, the estimates are progressively less accurate and precise as N increases. This may be due to insufficient diffusion weighting as N increases. At low N (N = 1 (δ = 39ms)), the fitting fails to correctly estimate the parameters for 20 μm plates because of the strong diffusion attenuation, forcing the model to fit to the noise floor. As a sanity check we compare the results to (N = 1,δ = 10ms) and find that diameter and diffusivity of microcapillaries with diameter of 20 μm are estimated accurately for this SDE sequence, however, 10 μm plates are poorly estimated. Hence, for this particular TE and diffusion gradient duration, we find that N>1 gives better results overall.

N = 3 gives the best estimates for both 10 and 20 μm plates. N = 3 outputs [a,$d_{||}$] of [9.7 $\pm$ 0.5 μm, 2.0 $\pm$ 0.0 μm^2/ms] and [20.1 $\pm$ 0.5 μm, 1.9 $\pm$ 0.1 μm^2/ms] for the first pairs of 10 and 20 μm plates, respectively. We also see consistency in our estimates because the estimates ([a,$d_{||}$]) for the second pair are [9.9 $\pm$ 0.3 μm, 2.1 $\pm$ 0.0 μm^2/ms] and [20.1 $\pm$ 0.8 μm, 1.9 $\pm$0.1 μm^2/ms]. The diameter estimates from N = 3 are close to the ground truth and are also within the confidence limits of the estimates from the combined OGSE protocol shown in Figure 4.3. The diffusivity estimates have slightly higher accuracy and slightly lower precision for both pairs of 10 and 20 μm plates in comparison to the combined OGSE protocol. The diffusivity estimates are also very close to the estimates from the combined OGSE protocol. These results suggest that, for the case of idealised systems, one

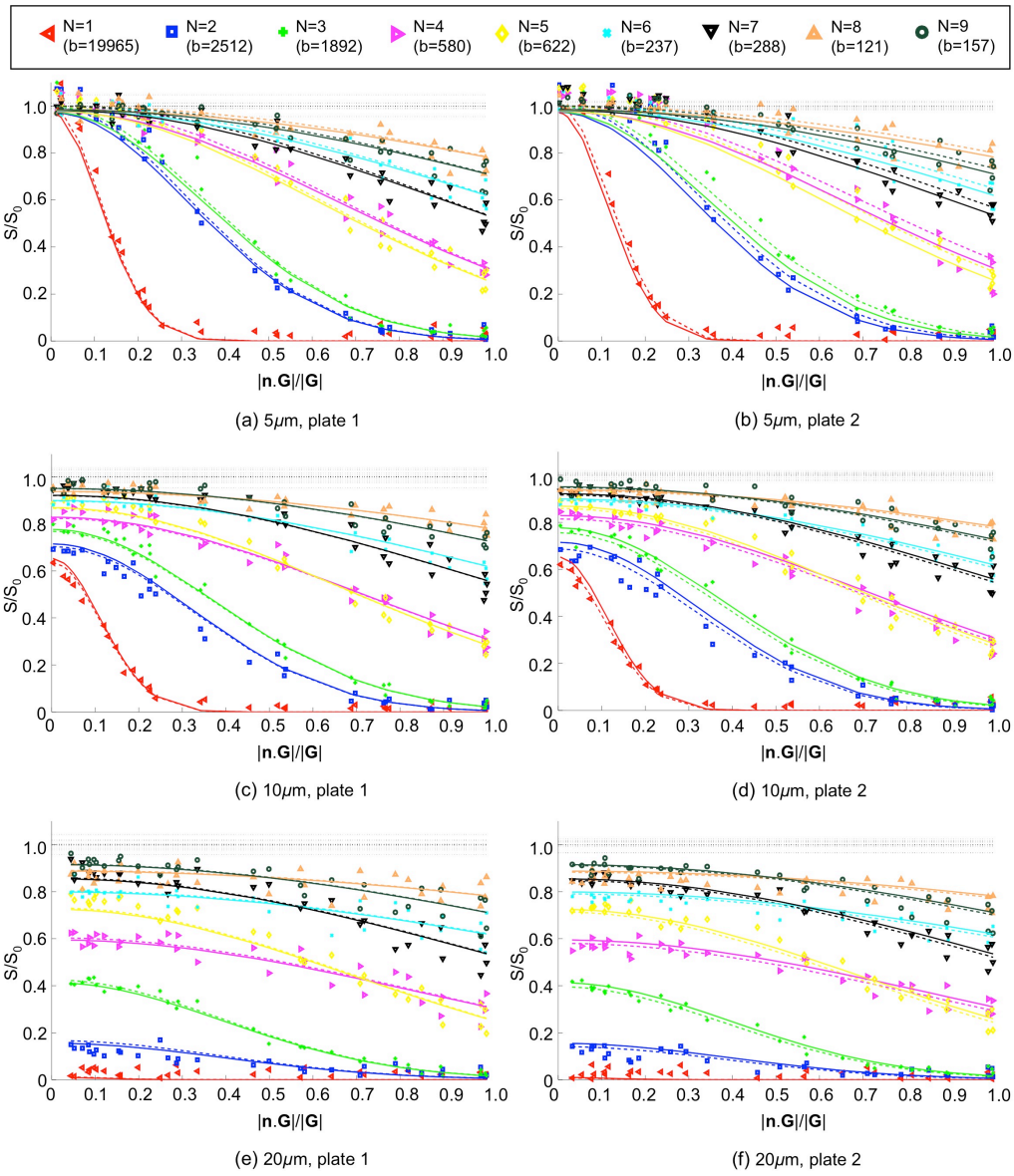

Figure 4.4: Plots of normalised signal from central voxel of each ROI in Figure 4.3a against absolute dot product between the gradient directions and the estimated direction of the microcapillaries; signals from perpendicular gradient direction are towards 0 on the x-axis, and from parallel directions towards 1. The measurements are represented by markers, while the solid (−) and dashed (- -) lines show the predicted signal from the ground truth and estimated parameters, respectively. The colours indicate the different N of the imaging protocol. The black horizontal dotted lines around $S/S_0 = 1$ show the b=0 measurements. All measurements are normalised by the averaged b0 signal per voxel. The parameter estimates for the representative voxels here are: $[a,d_{||}]$ = [0.0 μm, 2.0 μm^2/ms],[10.2 μm, 2.0 μm^2/ms] and [20.1 μm, 2.0 μm^2/ms] for the first pair of 5, 10 and 20 μm plates, respectively. For the second pair, the respective $[a,d_{||}]$ are [0.0 μm, 1.8 μm^2/ms], [10.4 μm, 2.1 μm^2/ms] and [20.5 μm, 2.1 μm^2/ms]. The R_{log} for 5, 10 and 20 μm plates are 1.4×10^5, 1.1×10^5, and 1.7×10^5 for the first pair, respectively, and 1.3×10^5, 1.3×10^5 and 1.4×10^5 for the second pair of plates respectively.

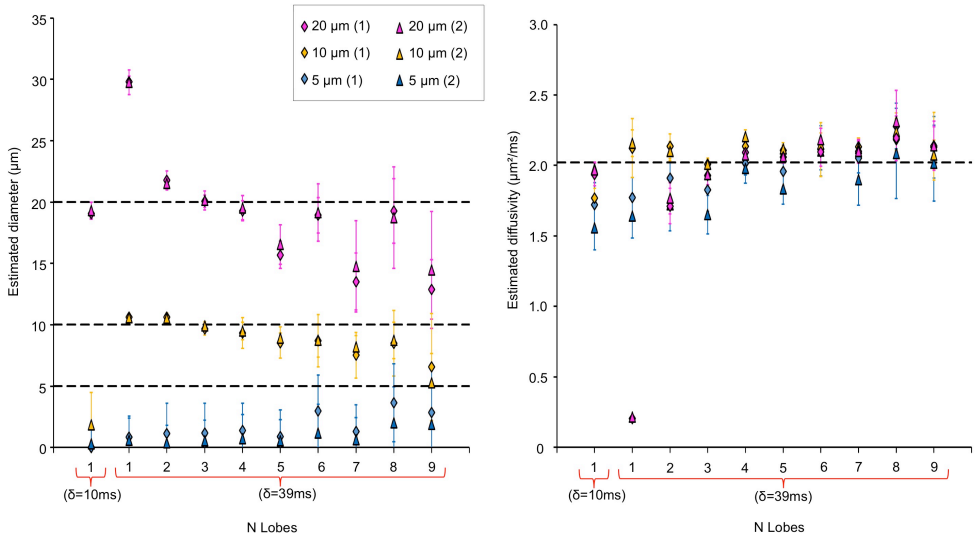

Figure 4.5: Mean diameter (a) and diffusivity (b) estimates calculated for each N from Figure 4.2 (labelled as 1 to 9 (39ms), where δ = 39ms) and also from the standard SDE sequence (labelled as '1 (10ms)', where δ = 10ms), for all plates. The same central row of voxels, as in Figure 4.3, is used to calculate the mean and the standard deviation. The dashed lines represents the real ground truth diameters in (a), and the calculated diffusivity from [120] in (b). N = 3 produces the best diameter and diffusivity for both pairs of 10 μm and 20 μm plates.

OGSE shell can perform similarly compared to a combination of OGSE shells.

4.3 Discussion

In this chapter we explore the sensitivity of OGSE to microstructural dimensions of microcapillaries of unknown orientation on a clinical scanner. We find that 10 and 20 μm micro-capillary diameters can be accurately and precisely estimated whereas 5 μm estimates are neither accurate nor precise. We also find that low frequency OGSE sequences give the best results and are optimal for parameter estimation. In particular, N = 3 OGSE sequence can be used on its own to give estimates that are very similar to those of the combined OGSE frequencies (N = 1 to N = 9).

Our observations support the theoretical findings in [24, 123] regarding the clinical scanner diameter resolution limit which, based on their calculations, for gradient strength of G = 62 mT/m, is approximately 6 μm for SNR $\approx$ 50. We get excellent estimates for 10 and 20 μm plates and can assume that the same would be true for the diameters of microcapillaries within this range ($a \in$ 10,20 μm). On the other hand, 5 μm diameters cannot be estimated as they fall below the resolution

limit. In our study, we used idealised phantom plates (homogeneously and densely packed with microcapillaries), which were imaged with a HARDI type acquisition, pushed to the clinically feasible limits. We used a 'long' TE = 120 ms (in terms of standard clinical settings) in order to allow for larger diffusion weighting which is necessary to improve the sensitivity to the smaller diameter microcapillaries (5 μm). We also maximised SNR ($\geq$ 45) on the clinical scanner by imaging the phantom ensemble with a surface coil and using water as the substrate (long T2 relaxation time $\approx$ 1500 ms). Yet for a gradient strength of 62 mT/m, the diffusion weighted signal for the 5 μm microcapillaries could not be differentiated from a diffusion signal for 0μm microcapillaries. This highlights that diameters of 5 μm cannot be estimated on clinical scanners even under idealised conditions. Moreover, this is also further evidence for the validity of models of brain nerve tissue where axons can be represented as sticks and not as cylinders at G $\leq$ 62 mT/m [86, 124]. On the other hand, when we place the same 5 μm plates in a pre-clinical scanner with 800 mT/m gradients we estimate 5 μm almost perfectly (see Chapter 6, suggesting that the reason is the insufficient gradient strength).

Our analysis of individual OGSE sequences shows that there is an optimal range of OGSE lobes, for estimation of diameters of microcapillaries and intrinsic diffusivity. The optimal OGSE shells are with low number of lobes, (N $\in \{2, 3, 4\}$) and their parameter estimates are accurate and precise, especially for N = 3. Our experimental findings are consistent with the recent ActiveAx simulation study [24] and spectroscopy study [104], which show that OGSE sequences with lower N are optimal for the measurement of fibre diameters. The result highlights the importance of optimisation for microstructure indices estimation.

In this work we analysed the sensitivity of OGSE sequences to fibre diameter in micro-capillaries. Based on theoretical studies which compare OGSE and SDE sequences [24, 25], we do not expect SDE based techniques to provide better diameter estimates, with the same gradient constraints. Although we have not directly compared the sensitivity of other more complex sequences (e.g. DDE [53, 57]), similar conclusions hold, as the sensitivity and resolution limit is driven by the maximum

gradient strength and pulse duration [25].

The phantom we use in this study is much simpler than *in vivo* nerve tissue. However, the purpose of this work is to test the innate sensitivity of OGSE sequences to fibre diameters on a clinical scanner, which requires ideal diffusion substrates. We expect that results for *in vivo* nerve tissue to be similar or worse. For instance, resolution limit would be lower, i.e. since 5 μm diameter can not be estimated in an ideal phantom with extremely long T2 of pure water and simple parallel cylindrical capillaries, then its potential to be estimated *in vivo* is further reduced. As for the optimal frequency of the OGSE, the exact value would be different, however it is predictable that it would be of low frequency [24].

A potential drawback of using the phantoms in the study are possible artefacts such as signal loss and image distortions that could arise from inhomogeneous magnetic field which are further caused by the differences in the susceptibility between the plates and water. These artefacts could be reduced in the future by using microcapillaries that are longer than the sensitive length of the RF coil (50mm in length) and ensuring that they continue to be aligned parallel to the main magnetic field [116].

Unlike the drawbacks, there are numerous benefits of using physical phantoms with known geometry and microstructural characteristics. They are not degradable over time and are easy to use in validating microstructure imaging protocols [17], even over multiple clinical trial sites. There are other ongoing development of more complex phantoms such as biomimetic phantoms [125] being developed for validating diffusion MR imaging with a focus on materials that are have similar susceptibility to tissue. However, the simplicity of the plates used in this study is also ideal for validation and calibration purposes. Additionally, there is also potential here to develop an integrated phantom with a more finely graded range of microcapillary diameters to explore the resolution limit with more accuracy.

4.4 Conclusion

Overall, our results suggest that imaging axon diameter in the brain on a standard clinical scanner with gradient strength of 60-80 mT/m is extremely challenging. This was demonstrated by the insensitivity of the sequences towards diameters at or below 5 μm, which is the majority of axon diameters in the brain [29, 30]. Using stronger gradient strengths could potentially increase the sensitivity of the pulse sequences to axon diameter. With the increasing practice in the community to build clinical scanners with stronger gradients, for instance the *Connectom* scanner [90, 91, 107], *in vivo* axon diameter mapping could also be a possibility in the near future. In the following chapters we focus our research on exploring the potential of axon diameter mapping, and evaluate both OGSE and SDE sequences, using stronger gradients.

Chapter 5

Preclinical scanner: Axon diameter mapping in *ex vivo* monkey brain

In chapter 4, we experimentally demonstrate that OGSE sequences with low frequency provide more accurate and more precise diameter estimates of pores in idealised phantoms at clinical gradient strengths (G = 62 mT/m) than standard SDE sequences. We also show that the sequences were insensitive to diameters below 5 μm in these simple phantoms with no extra-axonal space. Previous theoretical work by [24, 25] support these results and suggest that smaller diameters can only be accessed with higher gradient strengths (G>100 mT/m).

This chapter focuses on using higher gradient strength to experimentally demonstrate axon diameter mapping in a biological tissue, an *ex vivo* monkey brain.

The work is carried out in collaboration with Tim Dyrby (from the Danish Research Centre For Magnetic Resonance), who acquired the experimental dataset required for this study, and the manuscript is in preparation.

5.1 Motivation

In CNS and PNS tissues, most axon diameters are far below 5 μm [29, 30, 126]. Accurate axon diameter imaging is therefore extremely difficult on standard clinical scanners with gradient strengths below 80 mT/m, although some attempts have been made [58, 101, 111]. Recent developments of human MR systems equipped with much higher gradients of 300 mT/m, such as the *Connectom* scanner [90], have

been shown to benefit axon diameter imaging in *in vivo* [91, 107, 114] and in *ex vivo* [110] white matter tissue using SDE sequences.

In this chapter, we use stronger gradient strengths, G = 300 mT/m, to experimentally demonstrate axon diameter mapping in an *ex vivo* monkey brain. Here we overcome the limitations presented by the simplicity of the plates, mainly the presence of extra-axonal space that was absent in the plates. This chapter is further motivated by previous work from [110], in which optimised SDE sequences at G = 300 mT/m were used but overestimated axon diameters were measured. Here, we investigate whether using OGSE can provide estimates close to the histological values that are found in literature [29, 30] and compare their performance to newly optimised SDE sequences.

The comparison for axon diameter mapping is carried out by calculating axon diameter index maps using the minimal model of white matter diffusion (MMWMD). This white matter model is orientationally invariant, but it does assume that axons are straight and parallel throughout each voxel. It is therefore important to ensure that we only apply the model of white matter where we believe this to be the case. Hence the white matter of interest in this study is the corpus callosum (CC). Furthermore, we also carry out simulation experiments to support our imaging experiments by using synthetic substrates that mimic axons in biological tissues.

5.2 Methods

This section starts by outlining our procedure for the preparation of tissue sample, i.e. the monkey brain, for imaging. It then describes the tissue model used to represent the microstructure of the region of interest, corpus callosum, in the monkey brain. This is followed by a description of the optimisation of the diffusion imaging protocols, the MRI scanner hardware and imaging sequence parameters used to acquire the raw data. The pre-processing steps for the raw data and the model fitting procedure that generates the final parameter maps using the full tissue model are then outlined. Following this, the details of the segmentation of CC is outlined,

which is used to carry out an in-depth analysis of the dataset. In the last section simulation experiments, which are used to support the tissue results, are described.

5.2.1 Tissue samples

The tissue sample used in our MRI experiments is from the brain of a male Vervet monkey (Chlorocebus pygerythrus), who is obtained from the Montreal Monkey Brain Bank. We follow the optimised *ex vivo* imaging pipeline guidelines on preparation of subjects and scanning outlined by [127]. Briefly, the live monkey is handled and cared for on the Island of St. Kitts according to a protocol approved by the local ethics committee (The Caribbean Primate Centre of St. Kitts). The brain is excised and then perfusion fixated in 4% formaldehyde and post-fixed for at least 3 weeks in 1% formaldehyde. The tissue is then placed in phosphate buffer saline (PBS) and kept at 5^oC for long-term storage to restore T_2-relaxation. Prior to the experiment, the monkey brain is kept at a temperature close to that of the inside of the MR magnet for $\approx$6 hours to ensure temperature stabilisation during scanning.

5.2.2 Tissue model

The minimal model of white matter diffusion (MMWMD) [101], as used by [101] and [110], is chosen to represent the CC microstructure for our study. The model is based on the simplified CHARMED model [100, 105] and is detailed in Chapter 2, Section 2.4.2.5. The parameters of the model are (1) axon diameter, α, (2) intrinsic diffusivity, $d_{||}$, (3) CSF diffusivity, d_{iso},(4) intra-axonal volume fraction, f_{icvf}, (5) CSF volume fraction, f_{CSF}, (6) trapped water volume fraction, f_{dot} and (7) axon direction, $\mathbf{n}$.

5.2.3 Protocol optimisation and imaging protocols

The OGSE and SDE diffusion imaging protocols are both optimised for a simplified MMWMD, where $S_3 = 0$ and $S_4 = 0$ (i.e. the CSF and dot compartment are excluded), using the optimisation framework from [20, 59] (see Chapter 2 Section 2.4.2.5 for more details). The optimisation seeks the diffusion sequence parameters: gradient strength (G), diffusion time (Δ), gradient duration (δ) and also, in the case of OGSE, the waveform frequency (ω); that maximise sensitivity to the tissue

model parameters.

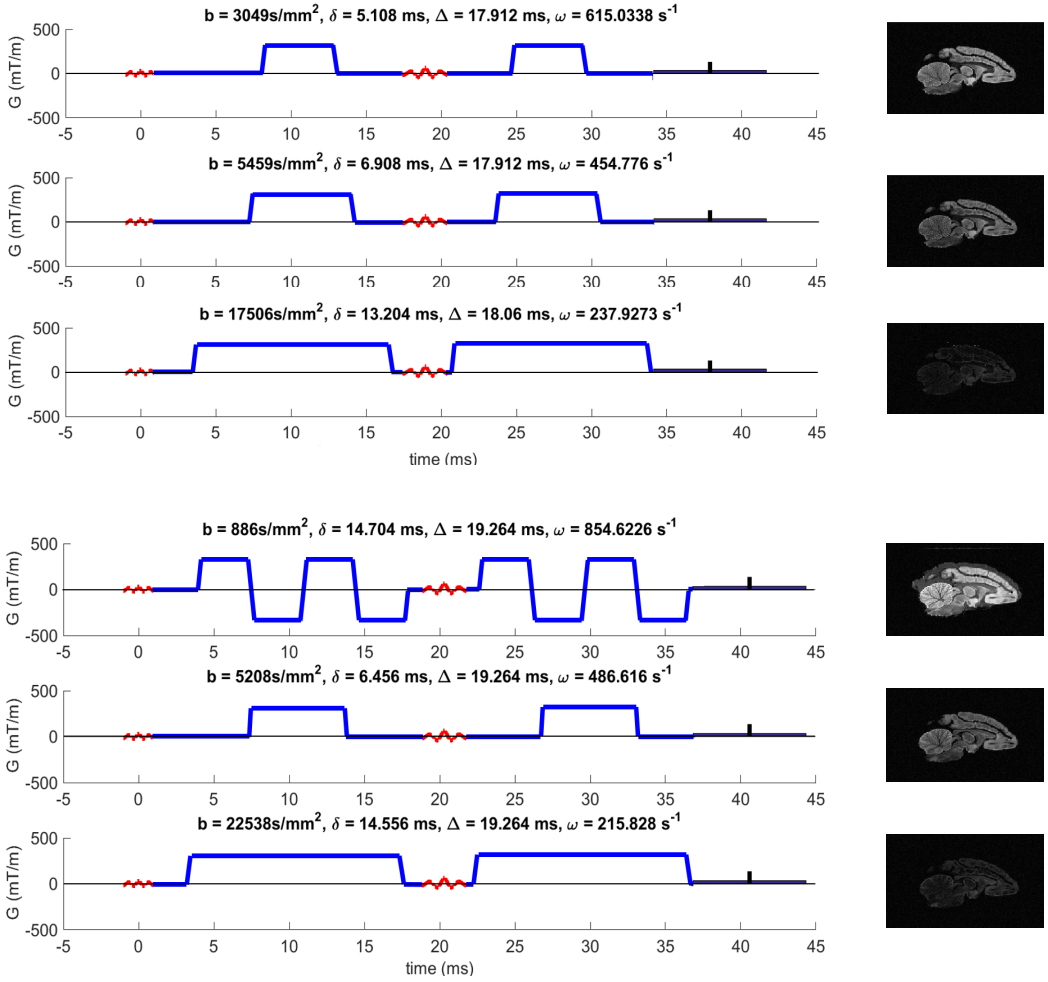

Figure 5.1: Schematic representation of the optimised SDE (top) and OGSE (bottom) 3-shell diffusion imaging protocols with a single-line readout 2D spin echo sequence containing the excitation, refocusing pulse and readout timings. The corresponding instance of a diffusion weighted image of the mid-sagittal slice of the monkey brain is also displayed next to each sequence. All images are at the same grayscale level.

We optimise both OGSE and SDE protocols using a priori model parameters settings (similar to [101]) of $f_{icvf} = 0.70$, $d_{||} = 0.60\ \mu m^2/ms$, $d_h = 0.18\ \mu m^2/ms$, and for axon diameter indices of 1.5, 3.0, and 6.0 μm. The diffusion imaging scanner settings for the optimisation are: G_{max} = 300 mT/m, number of gradient directions = 60, slew rate = 2000 T/m/s and maximum echo time (TE) = 40ms. SDE protocols are constrained to non-oscillating gradient waveforms, while OGSE protocols are

allowed to have both non-oscillating gradient waveforms and oscillating gradient waveforms. The final optimised protocols for SDE and OGSE are displayed in Figure 5.1, each with 3 HARDI shells and unique b-values.

We use a 4.7 T Varian Imaging System with 120 mm bore size and a maximum gradient strength of 300 mT/m with a slew rate of 2000 T/m/s to acquire our diffusion images. All sequences use a single-line readout 2D spin echo (SE) sequence, in-plane image matrix $256 \times 128 \times 10$, resolution $0.5 \times 0.5 \times 0.5$ mm^3, constant TE (40 ms) and TR (2500 ms).

Our final dataset consisted of 360 measurements per protocols (two repetitions of each protocol) and an additional 48 b=0 measurements that were acquired separately.

5.2.4 Data preprocessing

We carry out preprocessing on the raw dataset to identify our region of interest, the corpus callosum. OGSE and SDE image volumes with b < 3050 s/mm^2 are first concatenated together to make a large volume and then a set of rules are applied to extract the appropriate voxels.

1. Visual inspection of data sets suggests that no preprocessing is needed to correct subject motion before fitting. Some voxels across the CC have much larger attenuated diffusion signal than the non-diffusion weighted signal and such voxels are removed.

2. We apply an initial threshold mask to exclude all voxels where S_0 (the b=0 measurement) is more than twice the average S_0 across all voxels. This helps to avoid large partial volume effects with CSF in the white matter.

3. A Diffusion Tensor model is fitted to the remaining voxels and the linearity and planarity are calculated (see Equation 2.41 [85]). Voxels with linearity less than 0.55 or planarity greater than 0.25 are removed from the threshold mask.

4. The SNR (signal to noise ratio) image of our b=0 measurements is calculated by dividing the mean voxel values across the 48 b=0 images by its standard

deviation. All voxels with SNR < 10 are excluded from the threshold mask to avoid fitting to noise.

5. The final threshold mask is applied separately to the SDE and OGSE volumes. A box filter is then used to smooth the data. The filter takes the mean signal values in a 5×5 voxel square for all voxels, independently across all images in the volume. We considered only voxels that are present in the final mask to calculate the smoothed value of the voxel.

5.2.5 Model fitting

We carry out model fitting for each voxel in the final region of interest using a two stage procedure (similar to that described in Chapter 4, Section 4.1.3.2 and described by [101]) and the tissue model, MMWMD.

Grid Search Grid search as in Chapter 4, Section 4.1.3.2 is performed. Additionally, to reduce the search space, fixed values are used for the intrinsic diffusivity parameter $d_{||} = 0.6\ \mu m^2/ms$. For the monkey data, due to its CSF compartments, $d_{iso} = 2.0\ \mu m^2/ms$ is also fixed. These are the values recommended in the literature for diffusivity in fixed *ex vivo* samples [101, 110]. The results of the grid search are used as the starting points for the next stage.

Active-set algorithm For the non-linear fitting, $d_{||}$, d_{iso} and $\mathbf{n}$ are fixed and all other parameters are treated as free parameters. The active-set algorithm is as in Chapter 4, Section 4.1.3.2. The algorithm is run 10 times, first using the starting point found in the grid search, and then 9 further times from starting points randomly perturbed from that original starting point. The parameter values with the highest log-likelihood are chosen as the final fitted model parameter estimates.

We then visually display the generated microstructure parameter maps by overlaying them on top of the b=0 measurements.

5.2.6 Analysis

In order to analyse the parameter patterns across CC, we segment the monkey CC into 10 different in-plane regions. We first fit a Diffusion Tensor model to all measurements below b = 3050 s/mm^2. The resultant fractional anisotropy (FA) map is

used to segment out the CC by only considering voxels with FA ≥ 0.3. As suggested by [128], at the mid-sagittal slice, we draw a midline stretching from the genu to the splenium and then divide the CC into 10 specific anatomical regions. The same regions are then translated to all other slices. The corresponding mean parameter values per regions are then calculated and compared across the CC and slices for OGSE and SDE protocols.

5.2.7 Simulations

Prior to using the monkey corpus callosum, simulations are carried out to investigate the sensitivity of the optimised OGSE and SDE protocols to axon diameter in a controlled environment. Two experiments are carried out to investigate the sensitivity of the optimised OGSE and SDE protocols to axon diameters in simulations.

5.2.7.1 Simulation experiment 1

Experiment 1 tests the performance of the optimised OGSE and SDE protocols shown in Figure 5.1 for estimating axon diameters.

5.2.7.2 Simulation experiment 2

Experiment 2 tests the importance of oscillating gradient waveforms in estimating axon diameters. In this case, we replace the oscillating gradient sequence in the optimised OGSE protocol with equivalent b-value SDE sequences. The parameters of the different SDE sequences are calculated by constraining the sequence parameters (gradient strength, slope time and b-value) using the trapezoidal b-value equation [78], where only Δ and δ are allowed to vary. A total of three protocols are generated and are shown in Figure 5.6. The new SDE sequences for OGSE equivalent protocol (1), OGSE equivalent protocol (2) and OGSE equivalent protocol (3) have (Δ, δ) as (29.76 ms, 2.30 ms), (13.91 ms, 3.30 ms) and (8.59 ms, 4.30 ms),respectively.

5.2.7.3 Data synthesis for simulations

For both experiments, we use Monte-Carlo diffusion simulations via the CAMINO framework [20, 129, 130] and generate synthesised data using 3D digital phantoms representing the white matter tissue substrates. Each phantom is characterised as a

unique combination of four parameters: the shape k and the scale parameter θ of the axon radius distribution, the intrinsic diffusivity of spins $d_{||}$ and the intra-axonal volume fraction f_{icvf}. To mimic the structure of the monkey corpus callosum, we model the tissue as a collection of non-abutting parallel cylinders, which are randomly packed as in [130], with radius drawn from a gamma distribution. The shape and the scale parameters of the gamma distribution are obtained from [101]. [101] predetermined the parameters from 11 histograms of axon diameters from histology studies of human [29] and monkey [39] corpus callosum. [101] also accounted for potential shrinkage and two different f_{icvf} (maximum volume fraction that can be achieved and volume fraction that is 0.1 less than the maximum) to bring the total number of synthetic substrates to 44. 22 of the substrates (i.e. for one volume fraction) are shown in Figure 5.2. Lastly, a $d_{||} = 0.6$ μm^2/ms is used.

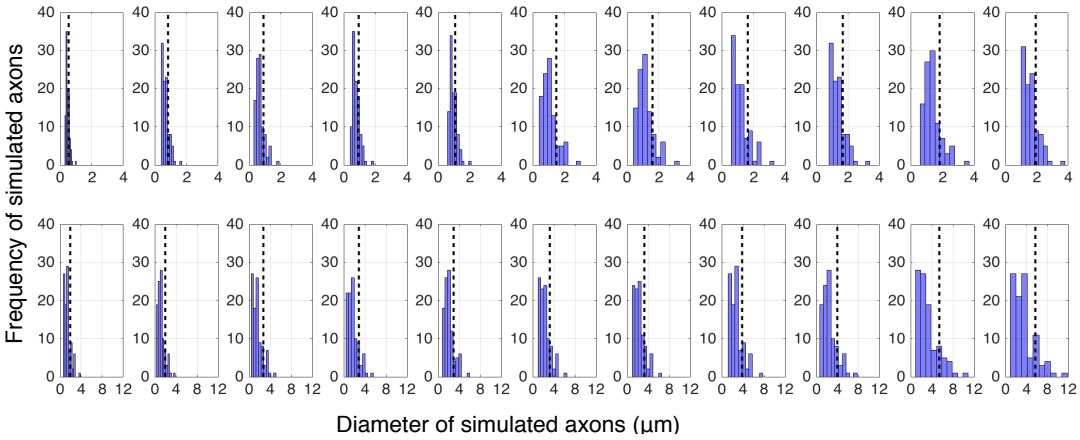

Figure 5.2: Histograms of axon diameter distributions we use to generate digital substrates for the Monte Carlo simulations are shown here. Although, there are 44 substrates in total (22 gamma distributions, each with two intra-axonal volume fractions), only 22 of those substrates are shown here (i.e. only one intra-axonal volume fraction) in the order of increasing axon diameter indices (shown as black dashed lines on each histogram) from left to right. Note that the first and second rows have different scales.

All simulations are performed using 50000 spins, 20000 time steps and 100 cylinders, similar to the study by [101]. The noise-free dataset is referred to as SNR = ∞. In order to make the synthesised dataset more realistic, 100 different instances of random Rician noise (SNR = 20) are introduced to the final dataset. This noisy dataset is referred to as SNR = 20. Finally the tissue model described in Section

5.2.2 is fitted to the noise-free and noisy dataset to estimate the model parameters using the model fitting procedure in Section 5.2.5.

5.3 Results

In this section, we first present the results from experiment 1 and 2 from our simulation study, and then present the results from the monkey dataset.

5.3.1 Simulation experiment 1

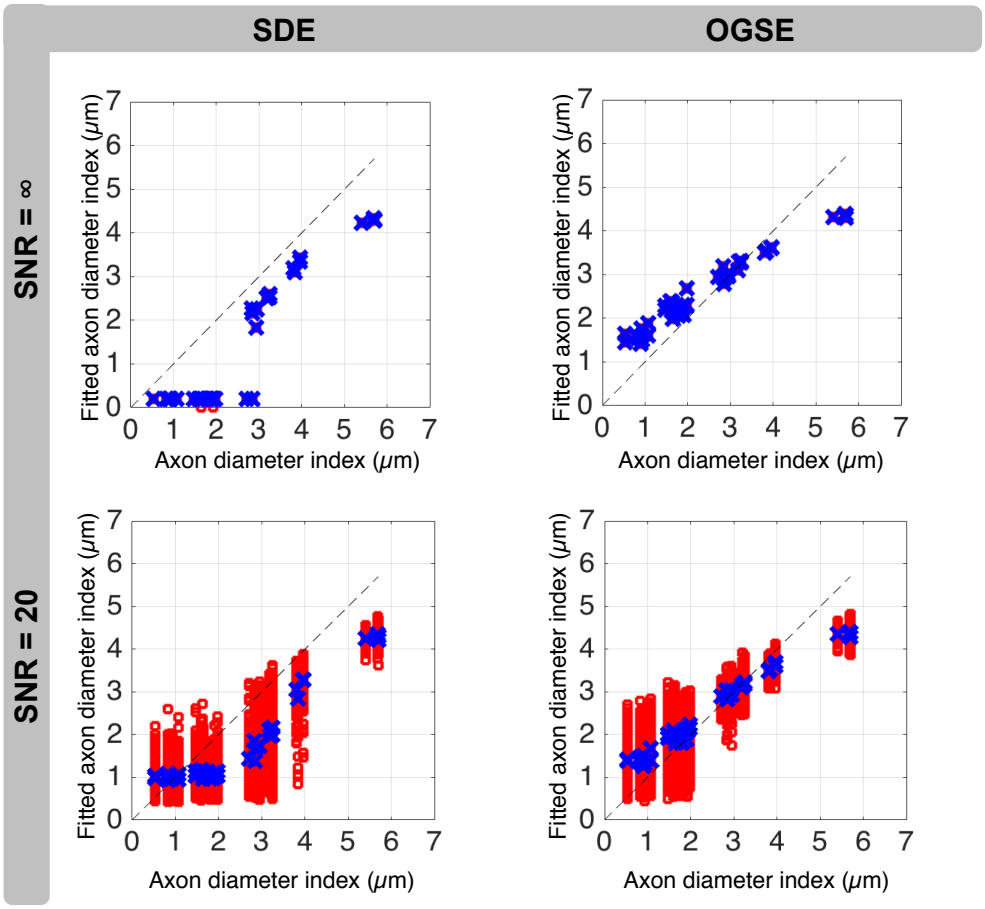

Figure 5.3: Graph shows the axon diameter index estimates plotted against the true axon diameter index for a series of voxels simulated with the CAMINO Monte Carlo simulator using the optimised SDE (left column) and OGSE (right column) protocol. Results from two datasets: noise free (top) and noisy (SNR = 20, bottom) are shown.The noisy dataset contains 100 different instances of random Rician noise (SNR = 20) for each substrate, and the estimates for each of these instances are displayed as red squares. The blue crosses indicate the mean estimated axon diameter index across the 100 runs. The dashed line is the identity line.

Figure 5.3 compares the fitted axon diameter index with the ground truth diameter index (from Figure 5.2) for the optimised SDE and OGSE protocols in noise free and noisy cases. In the noise free case, SDE and OGSE perform similarly for $\alpha \geq 4$ μm. Both protocols underestimate large axon diameter indices as the diffusion time of our protocols may not be long enough to probe restriction of large diameters. However, OGSE outperforms SDE for $\alpha < 4$ μm and moreover the OGSE protocol is sensitive to $\alpha < 3$ μm unlike the SDE protocol. Overall, OGSE estimates the axon diameter index more accurately than SDE in noise free and, more importantly, in noisy cases, suggesting the robustness of OGSE sequences to realistic data.

Similar to Figure 5.3, Figure 5.4 shows the estimated intra-axonal volume fraction plotted against the ground truth intra-axonal volume fraction. As indicated by the close proximity of the data points to the identity line, there is high correlation between the estimates and the ground truth for the optimised SDE and OGSE cases for both noise free and noisy cases.

Figure 5.5 compares the signals from three sample voxels from the simulation substrates where the ground truth diameter indices are 3.80 μm, 2.85 μm and 1.59 μm, respectively and the ground truth intra-axonal volume fractions are 0.68, 0.53 and 0.48, respectively. The almost perfect fits to the raw data for both SDE and OGSE are indicated by the high R_{log} values and suggests that the current model assuming tortuosity can roughly describe the signal from the gamma distributed axon diameter voxels.

5.3.2 Simulation experiment 2

Figure 5.6 shows the effect of replacing the oscillating gradient waveform in the optimised OGSE protocol, with different b-value equivalent SDE sequences, when generating and fitting for both noise free and noisy datasets. For each protocol, their corresponding graphs show the correlation between the fitted axon diameter indices with respect to the ground truth axon diameter indices for the noise free and noisy cases. The b-value equivalent SDE protocols do not maintain the axon diameter sensitivity of OGSE below 3 μm. We also consistently see that $\alpha < 2$ μm are only sensitive to the original optimised OGSE protocol. The same patterns

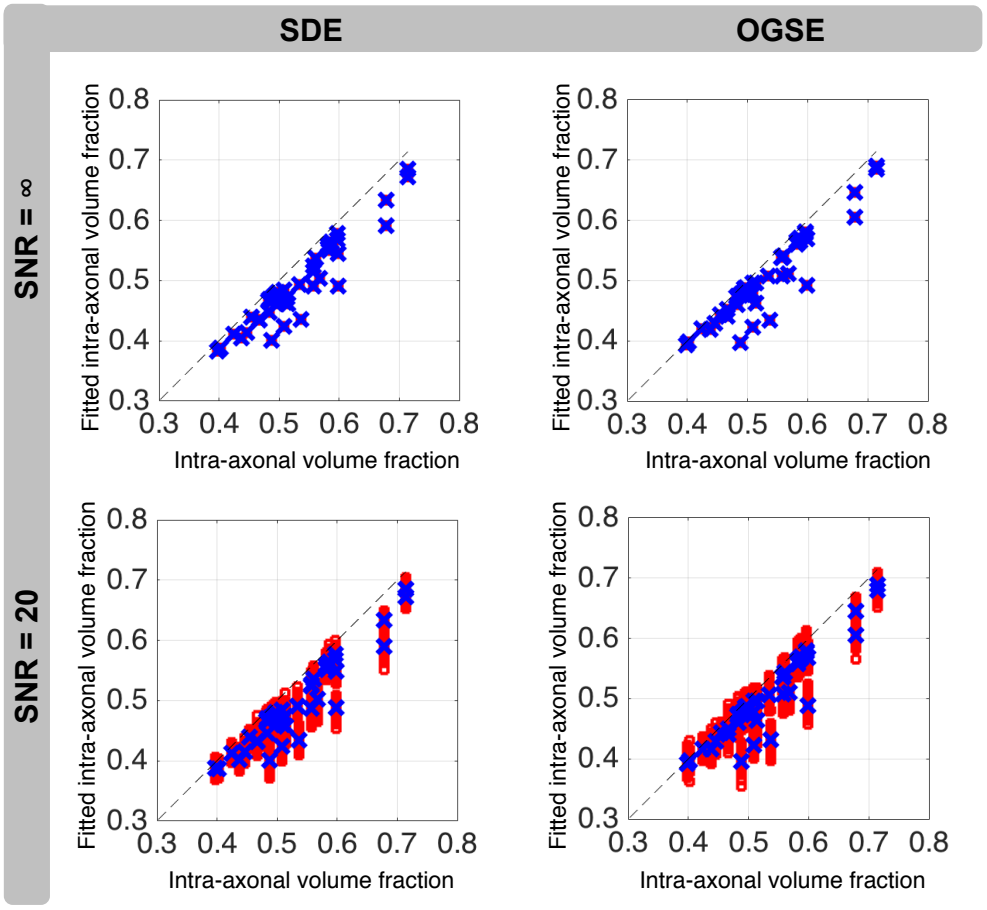

Figure 5.4: Graph shows the estimated intra-axonal volume fraction plotted against the true intra-axonal volume fractions for a series of voxels simulated using optimised SDE (left column) and OGSE (right column) protocol. The same description as Figure 5.3 applies.

are also true for the noisy signals even if we acknowledge the bias in all equivalent SDE protocols due to the noise floor for $\alpha < 2$ μm. This suggests the importance of oscillating gradient waveforms in probing small microstructures.

Figure 5.7 shows differences between the signal attenuation of the oscillating gradient waveform and the three b-value equivalent SDE sequences, all with b = 886 s/mm^2. The restricted signal is most attenuated for the oscillating gradient waveform.This is probably because the shorter diffusion time of the oscillating gradient waveform allows them to 'see' more of the diffusing particles and therefore the resultant signal cancels out the most. As all other measurements in each of the protocols in Figure 5.6 show almost identical attenuation, this suggests that the difference in restricted signal attenuation contributed to the higher sensitivity of

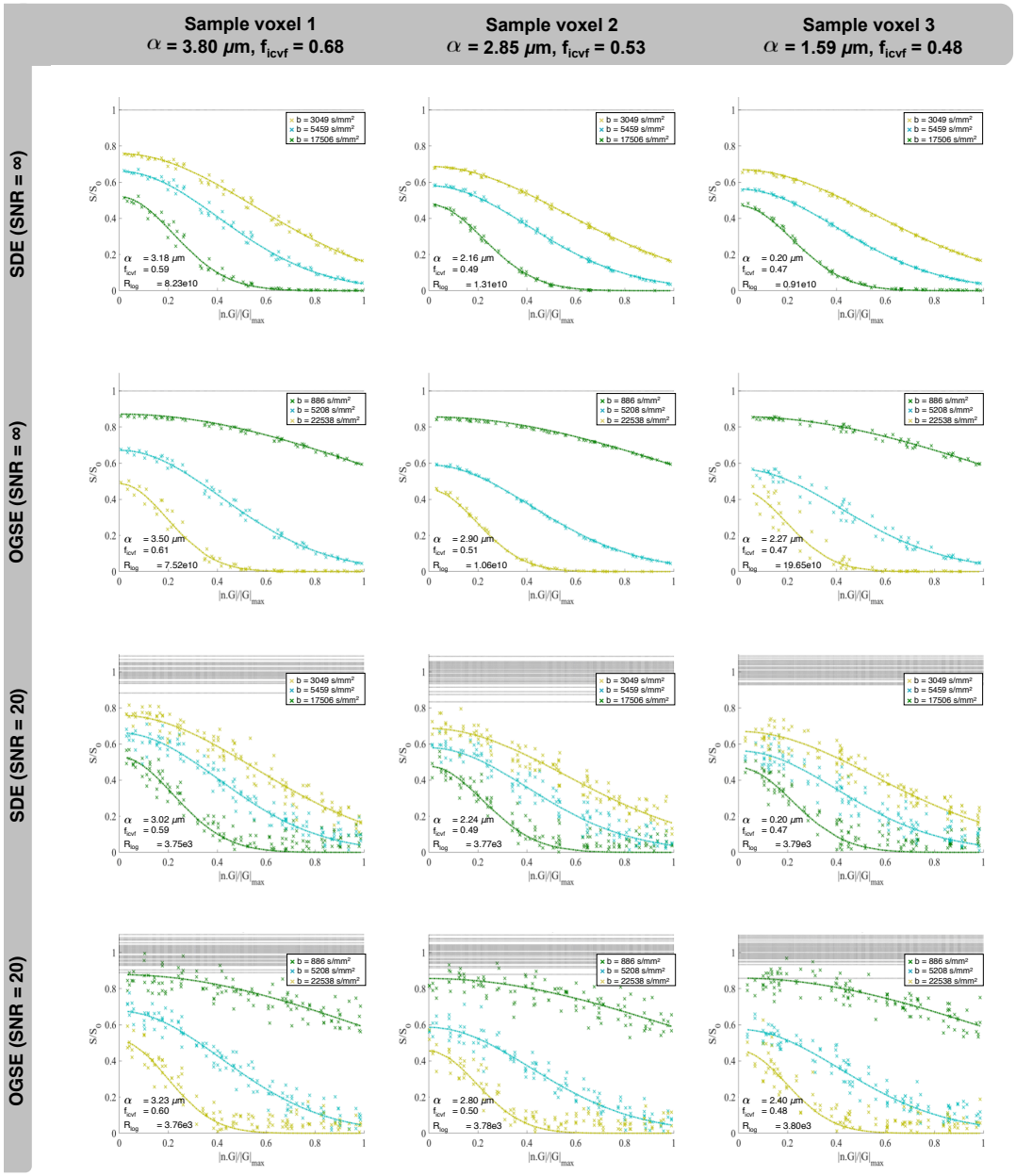

Figure 5.5: The signal attenuations of the simulated sample voxels 1, 2 and 3 (shown in columns) are plotted for OGSE and SDE cases with and without noise (rows). The signal attenuation is plotted against absolute dot product between the gradient directions and the estimated axon orientation; signals from perpendicular gradient direction are towards 0 on the x-axis, and from parallel directions towards 1. The measurements are represented by markers, while the solid lines show the predicted signal from the estimated parameters. The fitted parameter estimates (α and f_{icvf}) and R_{log} of the measurements given the model parameters for each voxel are also displayed on each graph. The colours on the graph indicate the different b-value of the imaging protocol. Note that the only oscillating gradient waveform in the OGSE protocol is b=886 s/mm^2. The black horizontal dotted lines near $S/S_0 = 1$ show the b=0 measurements. All measurements are normalised by the averaged b=0 signal per voxel.

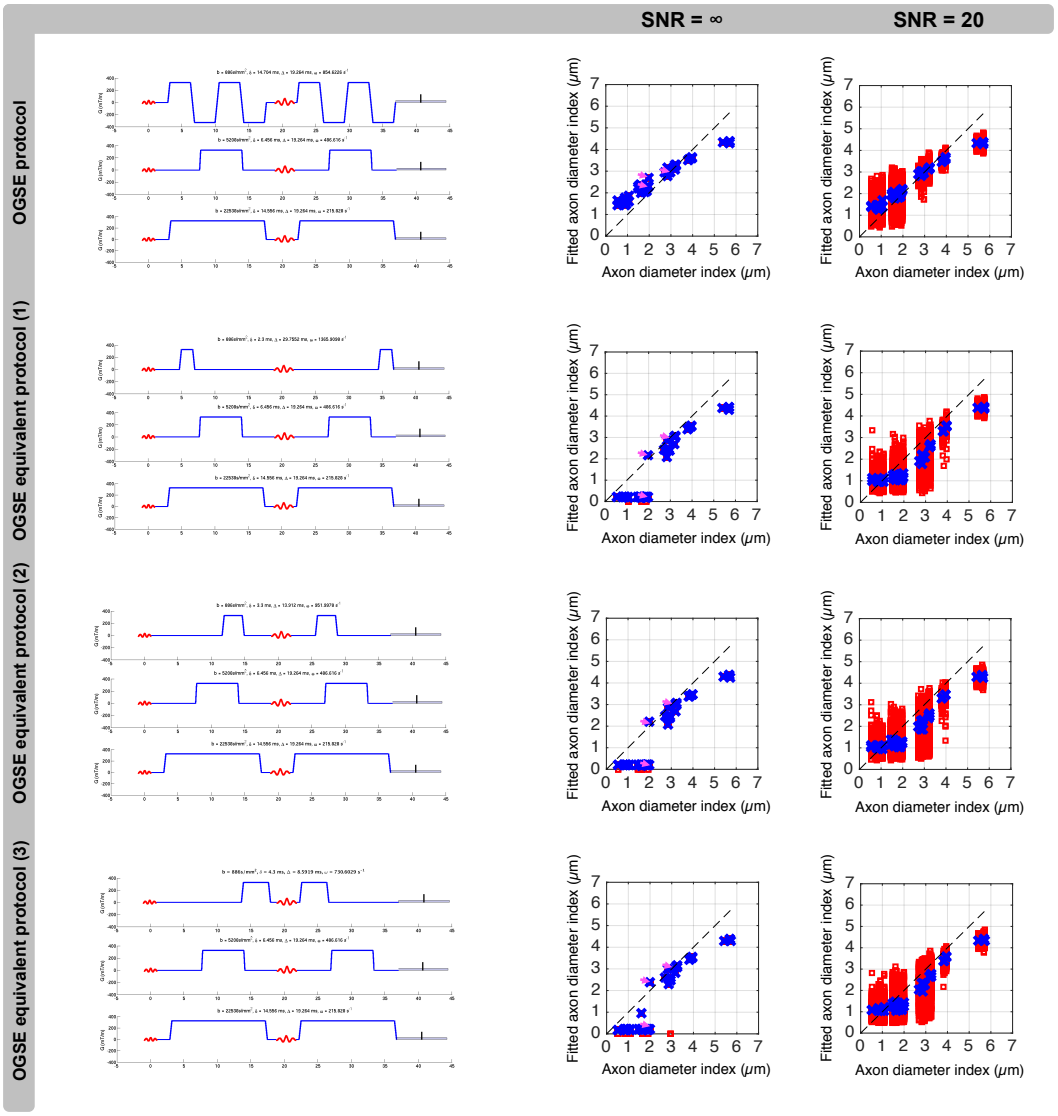

Figure 5.6: Optimised OGSE protocol (top row) and three instances of OGSE equivalent SDE protocols (2nd-4th row) are shown in the first column. Each protocol is used with CAMINO framework to simulate voxels containing axon diameter distributions obtained from literature [29, 39]. Similar to Figure 5.3, the 2nd and 3rd columns show the estimated axon diameter index plotted against the true axon diameter index for a series of voxels in the case of no noise (second column) and in the case of added Rician noise at SNR=20 (third column).

oscillating gradient waveforms to small diameters.

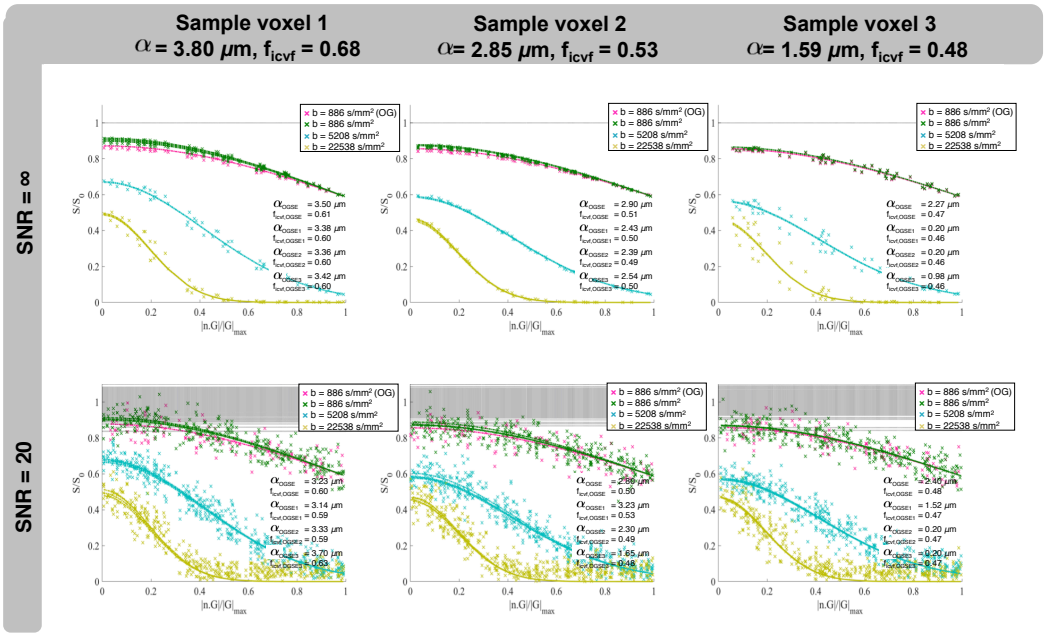

Figure 5.7: Signal attenuations from all protocols in Figure 5.6 are shown here overlapped on top of each other. The same sample voxels as in Figure 5.5 are used. The b=886s/mm^2 measurements for the SDE waveforms are in green and the OG waveforms are in pink. The fitted parameter estimates (α and f_{icvf}) for each voxel and each protocol are also displayed on each graph.

5.3.3 Monkey corpus callosum

The theoretical findings on the advantages of the OGSE protocol over SDE protocol under realistic conditions are encouraging. Here we show the results for the *ex vivo* monkey brain.

Figure 5.8 displays the fitted parameter maps of the axon diameter index (α), volume fractions of all the compartments (f_{icvf} ,f_{CSF} ,f_{dot}, f_{extra} (using 1-f_{icvf})) and calculated map of axon density, ρ, (using equation (5) from [101]). All maps are overlaid on top of the mid-sagittal slice of the monkey corpus callosum for both SDE and OGSE protocols. Figure 5.9 compares the trend of the axon diameter index across the corpus callosum and also across slices for SDE and OGSE protocols.

The maps of axon diameter index (in the top row of Figure 5.8) for both protocols show a low diameter distribution at the genu and splenium end and high diameter distribution at the mid-body and Figure 5.9 shows that this trend is consistent

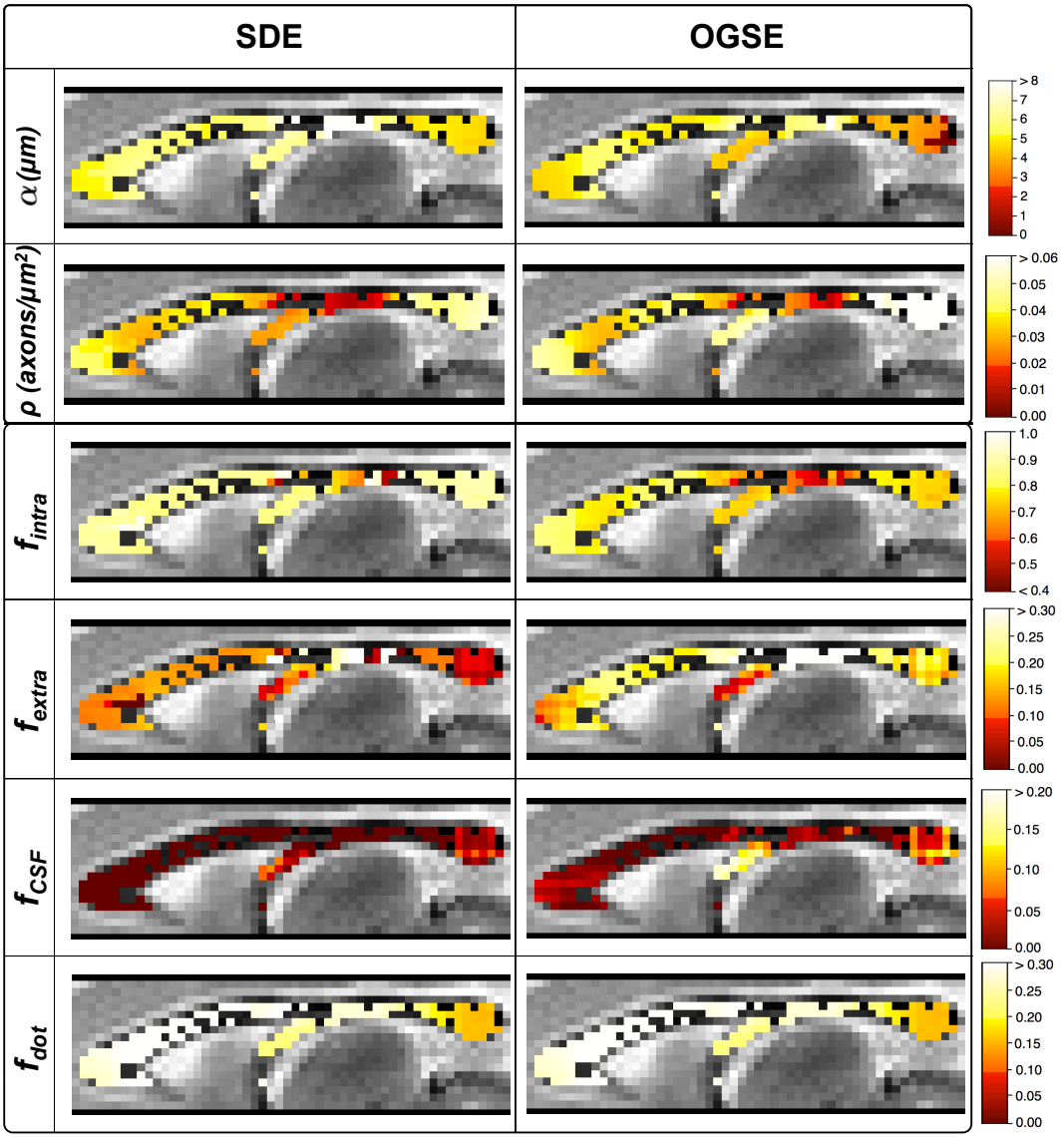

Figure 5.8: The fitted parameter maps of the mid-sagittal slice of the monkey corpus callosum are shown here superpositioned on top of the b=0 measurements. The maps were generated by fitting the four compartment model to the optimised SDE (left) and optimised OGSE (right) dataset. The parameters on display are axon diameter index (μm) (1st row), axon density (axons/μm^2) (2nd row, calculated from [101]), intra-axonal volume fraction (3rd row), extra-axonal volume fraction (4th row, calculated using 1-f$_{icvf}$), CSF volume fraction (5th row) and trapped water volume fraction (6th row). The corresponding legends are also shown.

across the CC slices. This low-high-low trend is in agreement with findings from previous studies [101, 110] but only in partial agreement with histological findings from [39].

Direct comparison between the protocols demonstrate the ability of OGSE pro-

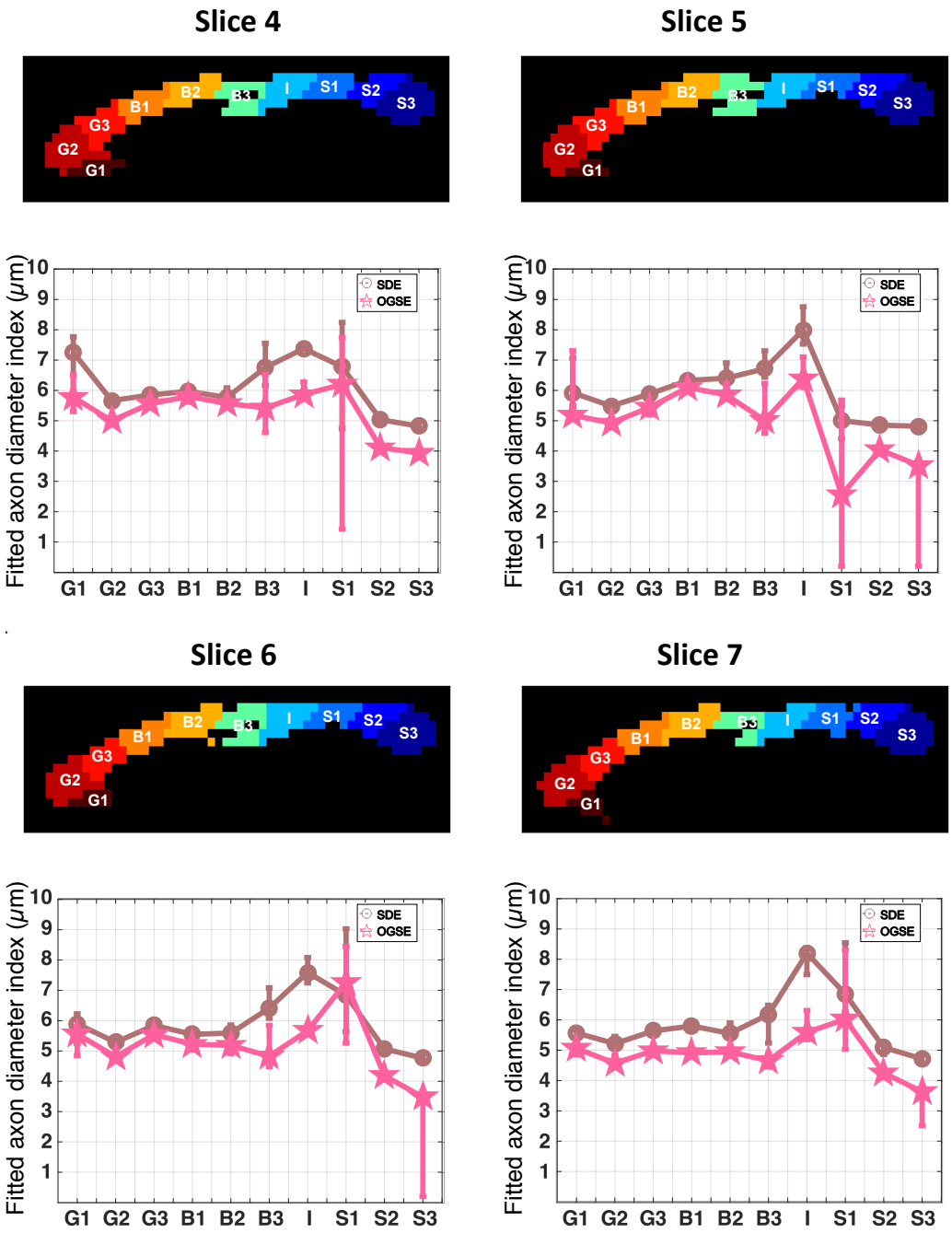

Figure 5.9: Comparison between the median axon diameter index trend estimated by SDE and OGSE protocols across the corpus callosum and across multiple slices. The error bars indicate the 25th and 75th percentile. The median values are calculated over the available voxels in each segmented region of the corpus callosum.

tocol to consistently estimate lower axon diameter indices. SDE protocols have estimates ranging from $\alpha \approx$ 5.4-9.2 μm at the genu, $\alpha \approx$ 5.8-9.2 μm at the mid-body and $\alpha \approx$ 4.4-9.0 μm at the splenium. OGSE protocol estimates lower axon diameter indices for the same regions; $\alpha \approx$ 4.8-9.7 μm at the genu, $\alpha \approx$ 4.0-9.4 μm at the mid-body and $\alpha \approx$ 0.2-9.0 μm at the splenium. For both protocols, areas, B3, I and S1 show more variability which we believe has been caused by Gibbs ringing present in the image.

Fitted parameters α, ρ, f_{icvf} and f_{extra} (in Figure 5.8) give a good indication of the axon topography within the CC as they show complementary patterns across the CC. Both OGSE and SDE protocols show occurrences of small axons, high axon density, high signal contribution from the intra-axonal compartment and low signal contribution from the extra-axonal compartment occurring at the splenium and genu. Similarly, larger axons, lower axon density, lower intra-cellular signal contribution and higher extra-cellular signal contribution occur in the mid-body region. The observation agrees with histological findings [39], where tightly packed small axons are found in the genu and splenium, and large axons with large extra-cellular spaces between them occur at the mid-body.

Figure 5.8 compares the f_{CSF} maps for the OGSE and SDE protocols. The SDE f_{CSF} map suggests very little contamination ($<$1%) occurs from the free water compartment within the CC except at the splenium end, where free water compartment can contribute to almost 5% of the total signal. OGSE f_{CSF} map indicates that the same voxels in the splenium suffer from partial volume effects that are twice as large in comparison to SDE ($\approx$ 10%), which causes the axon diameter estimates here to hit the lower diameter limit used as a fitting constraint. Furthermore, OGSE protocol also highlights the region of genu with free water signal contribution up to 3%, suggesting the potential likelihood of CSF contamination in the genu. It is possible that the low b-value ($\approx$ 900 s/mm^2) of the OGSE protocol preserves the fast decaying free water signal compared to the lowest b-value of the SDE protocol ($\approx$ 3050 s/mm^2), and thus makes the OGSE protocol more sensitive to the CSF compartment, allowing for more accurate estimates of f_{CSF}.

The f_{dot} maps shown on the sixth row of Figure 5.8 for both OGSE and SDE are almost identical. They show the lowest amount of trapped water ($\approx 15\%$) at the splenium end, while the higher amount of trapped water occurring at the rest of the CC can contribute to around 30% of the total signal. These large signal contributions have to be accounted for because [101] have highlighted the importance of not considering trapped water compartment in *ex vivo* data, which can otherwise result in bad fitting to the signal.

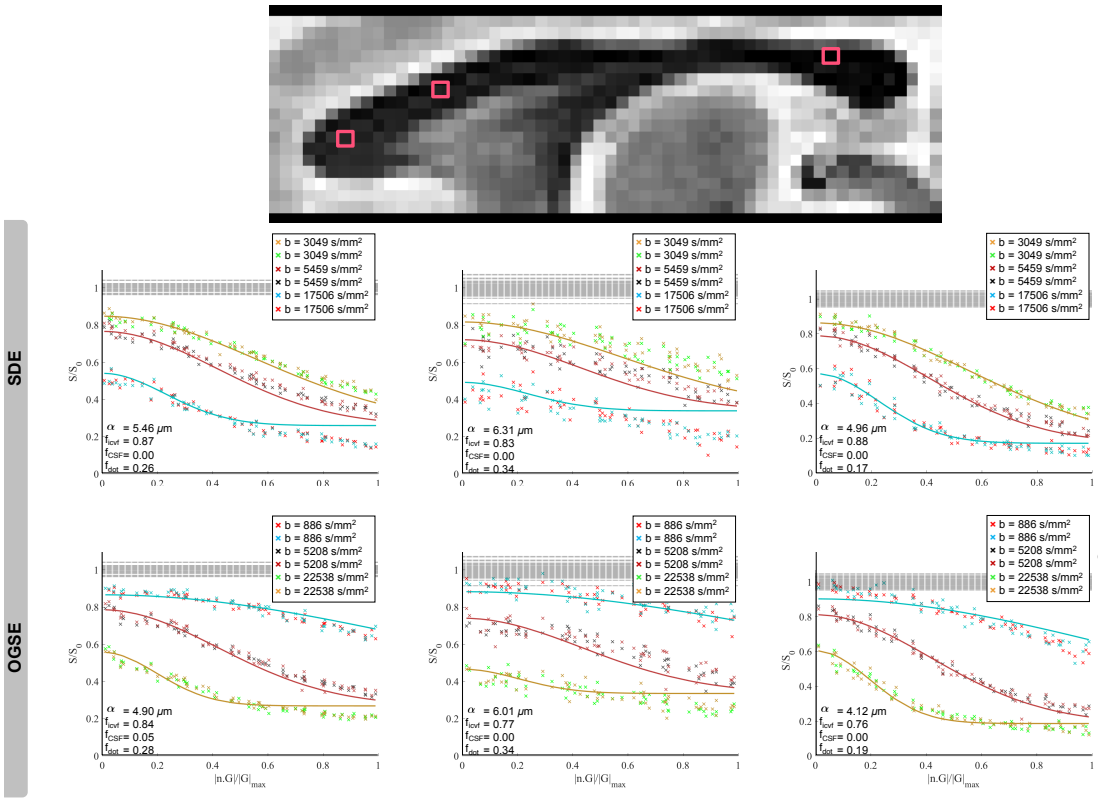

Figure 5.10: Example voxels across the mid sagittal slice at the genu (left), mid-body (middle) and splenium (right) and their corresponding signal attenuations for the SDE (second row) and OGSE (third row) protocols. The fitted parameter estimates (α, f_{icvf}, f_{CSF}, f_{dot}) for each voxel are also displayed on each graph. The quality of fit of the predicted data to the measured data is quantified using R_{log} of the voxels (from left to right). The R_{log} for the SDE protocol are 0.82×10^3, 1.65×10^3 and 0.30×10^3, respectively, and the R_{log} for the OGSE protocol are 0.33×10^3, 0.67×10^3 and 0.30×10^3, respectively.

Similar to findings from [101], we also observe that majority of the model parameters are independent of each other. Scatter plots (not shown) of all of the model parameters against each other confirm this. Also, as expected, there is interdepen-

dency between α and ρ, because ρ is proportional to α^{-2} by definition and this is reflected by strong negative correlations between the two parameters (data not shown).

Figure 5.10 shows the quality of fit by comparing measurements (data points) with predictions from the fitted model (solid line) in the voxels indicated by the red squares in the b=0 measurement of the corpus callosum. The red squares are chosen specifically to be in the genu, mid-body and splenium. Qualitatively, a moderately good agreement can be observed between the measurements and the fitted curve in most cases and this is further indicated by the calculated R_{log} values which are of a similar order for both SDE and OGSE protocols. However, similar to [101], signal fits of the large b-value SDE sequences are not perfect when S/S_0 is near 1.

5.4 Discussion

In this chapter we investigate axon diameter mapping in an *ex vivo* monkey corpus callosum using a gradient strength of G = 300 mT/m. We reproduce a well established study that applies optimised SDE sequence to estimate axon diameter [110] and similarly find that axon diameter is overestimated compared to the histological values from literature [29, 30]. We show that the results can be improved when using optimised OGSE sequence and although overestimation still occurs, OGSE achieves a lower resolution limit than SDE. Our results are consistent for both simulation and scanning data.

Key finding

A key finding in this study is that when the fibre direction is unknown and/or have multiple directions, the optimised OGSE protocol consistently shows higher sensitivity to small axon diameters than for the SDE protocol both in simulation experiments and in the *ex vivo* monkey corpus callosum scanning experiment. We also show that the oscillating waveform is a key component of the protocol. These results support previous simulation studies [24] and theoretical work [25], which states that in the presence of dispersed fibres or fibres with unknown directions, and

hence non-perpendicular angles between fibres and gradients, OGSE sequences are optimal for axon diameter imaging. This is because the optimal gradient waveforms for axon diameter sensitivity have long duration [24, 25] and in the case of SDE sequences that requirement results in extremely large b-values that can diminish the parallel component of the intra-axonal signal, and hence the total intra-axonal signal. On the other hand, low frequency OGSE sequences can have gradient waveforms with long duration at a relatively low b-value, which preserves the intra-axonal signal better.

Comparison with histology

Another encouraging outcome of this study is the reproducibility of the low-high-low axon diameter index trend across the corpus callosum. This is similar to the trend reported in previous studies on axon diameter [91, 101, 107, 110, 111, 131]. One difference between the diffusion MRI studies (including our study) and the histology studies [39, 45, 126] is that we report larger axons at the genu than at the splenium, which is opposite to the histological findings. A likely cause could be the dispersion of fibres at the genu [132]. Another difference with the histology studies is that we consistently get much larger diameter estimates. We show that OGSE sequence provides lower estimates than SDE, however these are still larger than the histology estimates. One possible reason for this could be the dispersion of the fibres, however studies that model dispersion [111] still report overestimation. The more likely reason is that the sequence lacks sensitivity to smaller axons, as we show in simulation, and that the signal change comes from a very small proportion of larger axons in the voxel. There is more ongoing work that involves studying the corpus callosum architecture as well as improvements in tissue models (discussed in Limitations) [111, 131, 133, 134] to better understand the reasons behind mismatch between histology and axon diameter imaging using diffusion MRI.

Similar to trends in histology with respect to tissue results, in simulation, we also expect axon diameters to be overestimated at smaller diameters ($\alpha < 3$ μm - range of axons in brain tissue). However, in simulation we observe that axons

down to $\alpha > 2$ μm are roughly estimated. Unlike in tissue, larger axons (>3 μm) can make up about $<1\%$ of the fibre population [31] whereas in simulations only $<0.05\%$ of the axon diameters are above 3 μm. Hence in tissue, it possible that the axon diameter index is weighted more by the larger diameters resulting in over-estimated diameters. Additionally, simulated substrates have parallel, non-abutting cylinders with impermeable walls and non-existent myelin, with the same diffusivity occurring in the intra-axonal and extra-axonal spaces. The simplicity of simulated substrates is matched by the tissue model used in this chapter, which potentially allows more accurate microstructure estimates in simulation.

We also expect that our simulation results will differ from previous work by [110] using SDE sequences. Software improvements in the CAMINO simulation framework for synthesizing substrates means that although we use the same parametrized gamma distributions as in [110] to simulate our substrates, our SDE results cannot estimate $\alpha = 2$ μm whereas in previous work it is estimated. Appendix A shows that this is due to improvements in the CAMINO simulation framework over the years to allow better sampling of the parametrized gamma distributions.

Limitations

A potential limitation of our work is that the protocol optimisation may not be the best. We find that SDE protocols from Section 5.3.2 with different b-values give lower axon diameter estimates than the optimised SDE protocol. It is possible that during protocol optimisation, the SDE protocol could have been in a local minima - a known problem in optimisation techniques [20]. This suggests that OGSE sequences could have been equally affected too. In the future, protocol optimisation will be run 10 times to ensure that the global minima is reached.

Another important limitation is that we use a very simple model of white matter tissue. The tissue is much more complex containing axons that are either undulated and/or dispersed and other microstructures such as glial cells, microfilaments within the axons. As our tissue model is unable to capture variations in axon ar-

chitecture, such as undulations [132] and dispersion [112] at the genu, this could potentially lead to overestimated diameters. Accounting for axon dispersion [111] could potentially resolve this issue to some extent. Recent studies have also shown that imaging multi-diameter substrates using a large range of diffusion times (such as the measurements in the OGSE protocol) can lead to time dependency of the hindered diffusion coefficient (d_h) and can cause overestimated axon diameters in simulations [133] and *in vivo* [131]. More over, even more recent work by [134] suggests that not only is the hindered diffusion coefficient time dependent, the intrinsic diffusion coefficient ($d_{||}$) also has some time dependency. In the future, it is possible to incorporate all of these effects into a complex tissue model if the new model can achieve significantly higher improvement in axon diameter estimates, however complex models usually require more number of measurements, which can significantly increase scan times, and are usually more unstable than simple models [113].

Finally, our validation was purely qualitative and we did not compare our results to the actual histology of the sample used. However there is ongoing work to make this possible.

Translation to in-vivo studies

Th results of this work can not be directly used for *in vivo* situations since there are differences in the intrinsic diffusivities between the two tissue types, which can easily influence the diameter estimates [24, 110]. *Ex vivo* tissue has low intrinsic diffusivity ($d_{||} \approx 0.6\ \mu\text{m}^2/\text{ms}$), caused by fixation [135, 136] and lower temperature used for *ex vivo* imaging, whereas *in vivo* tissue, which is usually at body temperature (37^oC) has intrinsic diffusivity that is almost three times higher. Higher diffusivity *in vivo* tissue means that smaller axons become difficult to detect and larger diameters are less difficult [24, 110]. [24] suggests that in this case, OGSE is even more advantageous over SDE, compared to that of *ex vivo* case, because the low b-values of OGSE sequences prevents fast signal loss from the high diffusivity of the tissue. Consequently, the significant differences between OGSE and SDE

protocols that are already observed in this *ex vivo* tissue study should be also be enhanced in *in vivo* tissue studies. In the next chapters, I will focus on experimentally demonstrating axon diameter mapping in *in vivo* tissue.

5.5 Conclusion

Overall, this chapter demonstrates that the OGSE protocols are more advantageous than SDE protocols for axon diameter mapping in the CNS white matter at G=300 mT/m. The work confirms that sensitivity of OGSE to small axon diameters are higher, by almost 1-2 μm, than for SDE in *ex vivo* tissue, and the results are supported by our simulation work. Additionally, our findings support other studies of axon diameter mapping on the benefits of using high gradient strength human MR scanners, such as the *Connectom* scanner [90, 91, 107, 113]. The combination of high gradient strength human MR scanners and the added advantage of OGSE protocols for axon diameter mapping could potentially contribute towards the development of axon diameter mapping techniques for diagnosis of CNS diseases which cause axonal degeneration leading to abnormal axon diameters, such as in amyotrophic lateral sclerosis [8, 9], autism [12, 13], and schizophrenia [10, 11].

Chapter 6

Preclinical scanner: Rat sciatic nerve - Sequence optimisation and phantom testing

In chapter 5, I demonstrate that OGSE protocols have higher sensitivity to small axons than SDE protocols. The finding is experimentally demonstrated in a fixated *ex vivo* corpus callosum from a monkey, which is further supported by Monte Carlo simulation experiments.

In order to evaluate the axon diameter mapping in close to *in vivo* conditions and to be able to quantitatively validate the work, we design experiments that use viable nerve tissue and perform a thorough histology that is then compared to the diameter estimates.

The experiments are done in three stages and presented in the three following chapters. The first stage (Chapter 6) presents optimisation of sequences and their testing using microcapillary array phantoms. The second stage (Chapter 7) presents a simulation study using the optimised sequences and model selection. Finally, the last stage (Chapter 8) presents a scanning experiment using the optimised sequences and the selected model, validated using histology experiments.

The overall purpose of the experiments will be to test the performance of OGSE waveforms and SDE waveforms. To compare the protocols, we evaluate them on three separate criteria: (i) Accuracy of model estimates compared to the

ground truth (for simulated data) or histology (for scanning data); (ii) Robustness of model estimates as the total number of diffusion measurements changes; (iii) Precision of model estimates.

The experiments here are carried out with help from Bernard Siow for fine tuning the imaging sequences to avoid artefacts. Parts of this work are featured in the recently accepted paper to *NeuroImage*:
L S Kakkar, O F Bennett, B Siow, S Richardson, T Quick, D Atkinson, J B Phillips and I Drobnjak. Comparison of OGSE and SDE ActiveAx for axon diameter mapping: An experimental study in viable nerve tissue.

6.1 Motivation

There are differences between *ex vivo* and *in vivo* tissues that directly prevent our findings from *ex vivo* tissue to be related to *in vivo* tissue. For instance, water diffuses much slower in *ex vivo* tissue than in *in vivo* tissue [135, 136], enabling smaller axons to be detected more easily in *ex vivo* tissue. Additionally, tissue fixation used to preserve the tissue causes axons to shrink resulting in diameter reductions of 30% or more [30]. As a result, the changes in the diffusion signal can lead to misleading diameter estimates that are different to those from *in vivo* samples. Thereby, it is necessary to validate biophysical models and advanced diffusion sequences *in vivo* [101, 131].

However, *in vivo* microstructure imaging can be difficult. There are issues such as subject motion, restricted scan duration and invasive tissue extractions for histology that hamper *in vivo* imaging. On the other hand, *ex vivo* tissue imaging does not have any of these disadvantages. To bridge this gap between the *in vivo* state and the more convenient but less realistic *ex vivo* tissue experiments, [137] introduced the viable isolated tissue (VIT) system. This is an experimental technique that allows tissue samples to be kept in a physiologically stable state during which the tissue is as close to *in vivo* as possible, maintaining the same diffusion properties and experiencing negligible amount of tissue degradation. The tissue can be kept in the VIT chamber for an extended period of time ($\approx$ 12 hours) and can therefore emulate *in*

vivo imaging experiments with extensive acquisition times.

The aim of this chapter is to assess the performance of diffusion imaging protocols, OGSE and SDE, to estimate microstructure parameters, especially axon diameters, in a viable rat sciatic nerve. The protocols are initially optimised for a rat sciatic nerve tissue and are tested for their innate sensitivity to diameters using simple idealised phantoms. Each phantom (referred to as 'plates' as in chapter 4) contains microcapillaries with a specific diameter (2, 5, 7, 10, 15 or 20 μm), and the range of diameters cover the range that are usually present in peripheral nerve tissues. The performance of the OGSE and SDE protocols are evaluated from their ability to recover the size of capillaries within the plates.

6.2 Method

This section introduces the optimisation of the diffusion imaging protocols that are used across the three chapters (Chapter 6, Chapter 7 and Chapter 8). It then briefly describes the protocol optimisation and outlines the scanning parameters used for imaging the plates. The section then outlines the steps for plates preparation, data preprocessing and model fitting used to acquire the microstructure parameter estimates of the plates.

6.2.1 Phantom model

In this chapter, the tissue model used for model fitting of the plates only uses a single restricted compartment of unknown orientation (i.e. a very simplified MMWMD model from Chapter 2, Section 2.4.2.5, where $S_2 = 0$, $S_3 = 0$ and $S_4 = 0$). It contains just the intra-axonal space to represent the capillaries within the plates. The parameters of the model are (1) microcapillary diameter, a, (2) intrinsic diffusivity, $d_{||}$, and (3) microcapillary direction, $\mathbf{n}$.

6.2.2 Protocol optimisation and imaging protocols

The purpose of our work in the future chapters is to image a peripheral nerve tissue. Hence the OGSE and SDE diffusion imaging protocols are both optimised for the peripheral nerve tissue model using the simplified MMWMD model, where $S_3 = 0$ and $S_4 = 0$ (i.e. the CSF and dot compartment are excluded), and the ActiveAx

optimisation framework [20, 59] (see Chapter 2 Section 2.4.2.5 for more details). Hence the apriori model parameters required are: (1) axon diameter, α, (2) intrinsic diffusivity, $d_{||}$, (3) hindered diffusivity, d_h, (4) intra-axonal volume fraction, f_{icvf} and (5) axon direction, **n**.

Both OGSE and SDE protocols are optimised using *a priori* model parameters settings from rat histological studies. The settings are α = (2.26, 4.50, and 6.74) μm (obtained from [15]), f_{icvf} = 0.60 (obtained from [138]), $d_{||}$ = 1.7 μm^2/ms (obtained from [101]), d_h = 0.68 μm^2/ms [109] and **n** is assumed to be unknown. The scanner settings for the optimisation are as follows: G_{max} = 800 mT/m, number of gradient directions = 8, 16 and 32, slew rate = 2000 T/m/s and maximum echo time (TE) = 40 ms. The gradient waveform shape in the OGSE protocol is constrained to sine-like trapezoidal waveforms. The final optimised protocols for SDE and OGSE, for the three separate gradient directions sets (8, 16 and 32), are displayed in Figure 6.1, each with 3 HARDI shells and unique b-values. An additional 9 b=0 measurements are also included in the final optimised protocols.

All MR measurements are conducted with a small bore 9.4T scanner (Agilent Inc., Santa Clara, CA, USA) equipped with 1000mT/m imaging gradients and a 33mm RF bird cage volume coil (RAPID, Biomedical GmbH, Rimbar, Germany). The diffusion protocol is read out using a multi-shot echo planar imaging sequence, with an echo train length = 16. Similar to Chapter 4, the images are acquired orthogonal to the plane of the plate. The imaging matrix is 128 $\times$ 64 with a resolution of 0.13 $\times$ 0.38 mm and a slice thickness of 10 mm. Other relevant parameters are: TR = 3 s, NSA = 2, acquisition time per protocol = 30 minutes and number of b=0 measurements = 6. An example of the b=0 image acquired using the imaging parameter is shown in Figure 6.3c.

6.2.3 Phantom preparation

Prior to imaging, we prepare the phantom. We insert plates with capillary diameters 2 μm, 5 μm, 7 μm, 10 μm, 15 μm and 20 μm (displayed in Figure 6.2), into a newly designed phantom holder shown in Figure 6.3a. The phantom holder is 3D printed and is made up of Objet VeroClear and Objet VeroWhite (Stratasys Ltd).

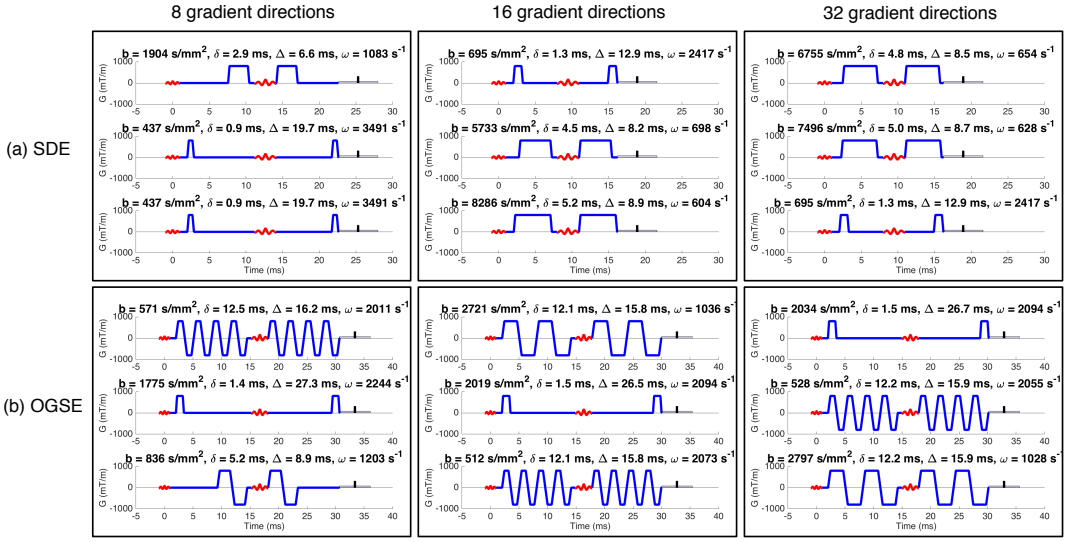

Figure 6.1: The optimised protocols for SDE (top row) and OGSE (bottom row). The diagrams show the diffusion weighting waveforms used in the three shells of the 8 (left column), 16 (middle column) and 32 (right column) direction protocols. The sequence parameters are also given for each measurement as: b-value (b), duration of the first gradient waveform (δ), time between the start of the first gradient waveform and start of the second gradient waveform (Δ) and frequency of the waveforms (ω).

The plates are surrounded by water and are separated by 1 mm thick hollow spacers, which allow the gaps between the plates to be filled with water, as demonstrated in Figure 6.3b. Similar to previous plate experiments in Chapter 4, we leave the sample immersed in water for a week before carrying out any experiments.

6.2.4 Data preprocessing

After data acquisition, we carry out preprocessing on the raw dataset to identify our regions of interest, the plates. As the voxel-wise SNR of the plates is very low (SNR = 3 to SNR = 11), we average across voxels to improve the SNR. To do this, each plate (which is 8 by 55 voxels) is initially assigned a 3 by 38 voxels ROI that is fully contained within the plate. The voxels within each ROI are averaged across the shorter axis of the ROI, which results in the final ROI for each plate - that is 38 voxels, each with almost double the SNR compared to the original data.

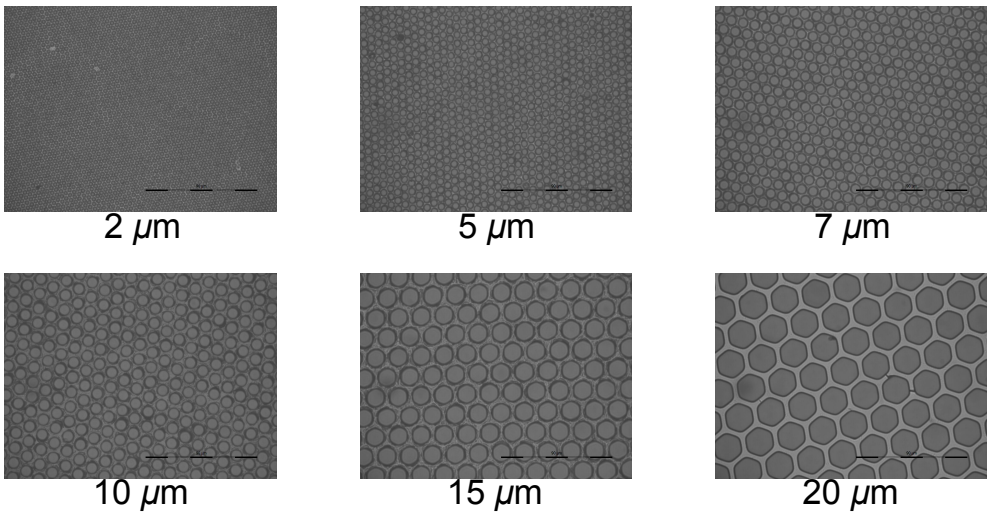

Figure 6.2: Light microscopy of the six plates with capillary diameters 2 μm, 5 μm, 7 μm (in the first row, left to right), and 10 μm, 15 μm and 20 μm (in the second row, left to right), which are used in this chapter. The scale bar = 90 μm.

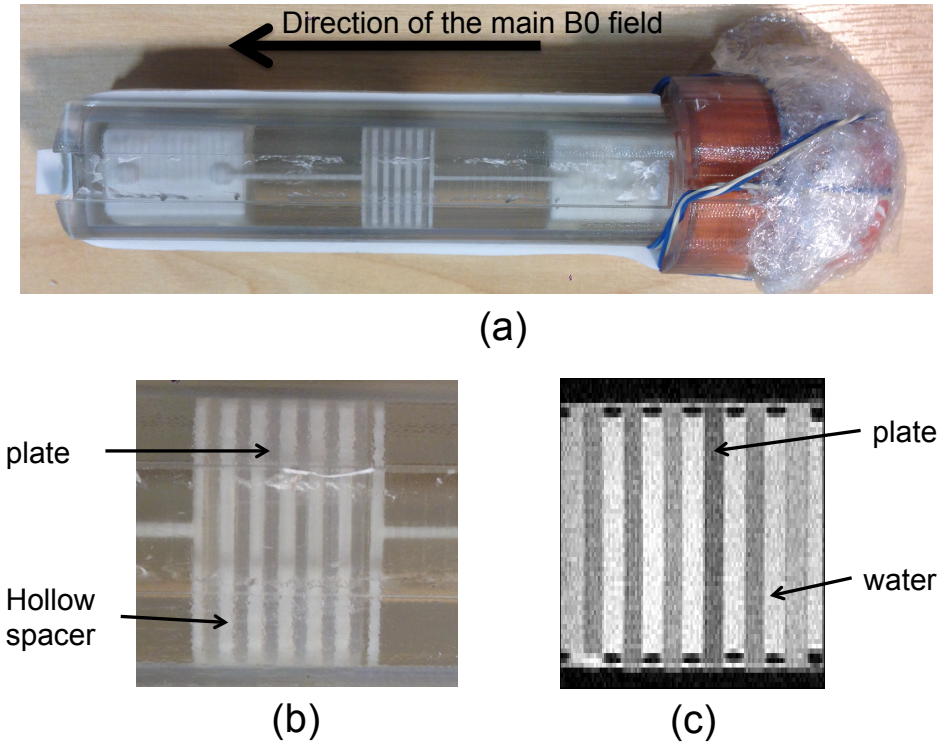

Figure 6.3: (a) The new phantom holder containing the plates with different diameters, where the plates are surrounded by water. (b) Magnified version of the plates ensemble to show the hollow spacers that ensure water filled gaps between the plates. (c) b=0 image of the plates. The plates are positioned in random order of diameter in the image: 5, 10, 7, 2, 15 and 20 μm, from left to right.

6.2.5 Sequence calibration

At the high gradient strengths, G = 800 mT/m, the diffusion encoding gradient waveforms inserted may not be the same as the gradient waveforms that play out during data acquisition [139]. Preliminary results showed that using uncalibrated sequences caused diffusivity of water to be overestimated up to 3 μm^2/ms. To prevent this from happening, we calibrate our sequences. Post data acquisition, the gradient strengths of SDE sequences are modified to match the gradient strength that are reverse calculated from the trace of the b-matrix in the image header file. This is not possible for newly implemented oscillating gradient sequences, and so they are calibrated using the plates dataset. Similar to [116], the analytical signal of the intra-axonal compartment is calibrated to match the measured signal from the capillaries in the plates by only varying the gradient strength. The gradient strength which maximises the log likelihood of the the measured signal given the analytical signal for the Rician noise model is chosen as the calibrated gradient strength for the sequence.

6.2.6 Model fitting

The pre-processed data is then fitted to a one compartment model to estimate the model parameters, $d_{||}$ and a, using an adapted voxel-wise model fitting procedure described by [101]. The same method as in Chapter 4, Section 4.1.3.2 is performed. First, in order to reduce the number of combination of parameters a diffusion tensor is fitted to the data to find the fibre orientation. Next, a two stage process that involves a grid search and then an active-set algorithm (which is run 10 different times with a different set of *a priori* parameters each time) is performed to estimate $d_{||}$ and a using the computed fibre orientation.

After the fitting procedure, noisy data (SNR $<$ 10) is removed. The data is then further filtered to remove any voxels that are not aligned in parallel with the ground truth direction of the capillaries within the plates. A dot product between the estimated fibre orientation for each voxel and the ground truth orientation is computed and voxels with a dot product below 0.99 are omitted.

6.3 Results

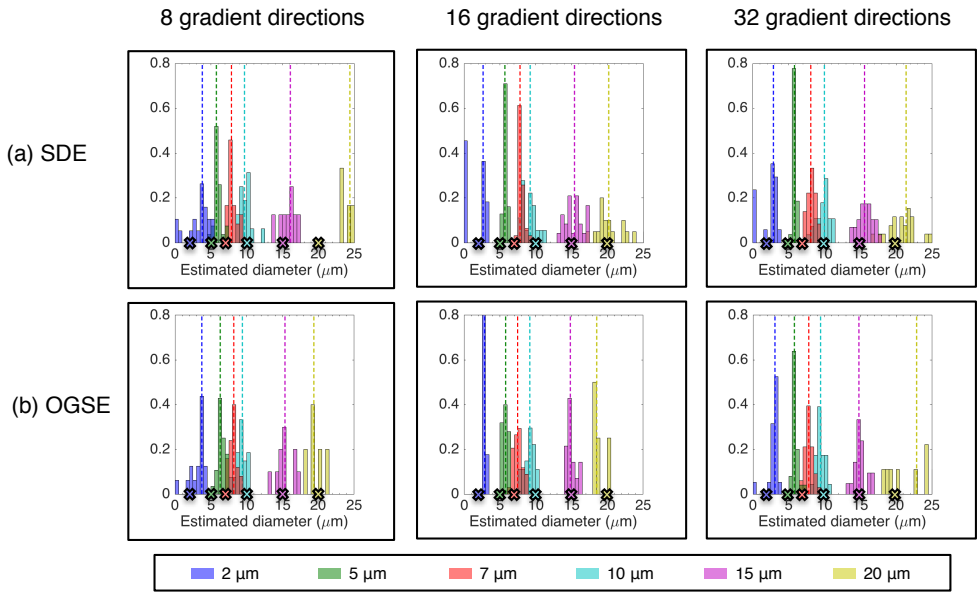

Figure 6.4: Histograms of the diameter estimates computed using the 8 (left), 16 (middle) and 32 (right) gradient directions SDE (top row) and OGSE (bottom row) protocols. Each histogram displays the voxel-wise estimates for all of the plates in different colours as shown in the legend below the figure (a = 2 μm (blue), a = 5 μm (green), a = 7 μm (orange), a = 10 μm (cyan), a = 15 μm (purple) and a = 20 μm (yellow)). The dashed lines indicate the median diameter estimate for each plate, and the markers at y=0 indicate the true diameter of the plates.

Figure 6.4 displays the histograms of the estimated diameter indices of the plates computed from the 8, 16 and 32 gradient directions of SDE and OGSE protocols. Each histogram contains the diameter estimates for each plate in different colours (a = 2 μm (blue), a = 5 μm (green), a = 7 μm (orange), a = 10 μm (cyan), a = 15 μm (purple) and a = 20 μm (yellow)). Visually, all protocols for OGSE and SDE can equally distinguish the range of diameters used here. However, a closer look at the histograms show that at a = 2 μm, many of the voxels for the SDE protocols hit the lower diameter limit used in model fitting, whereas most of the OGSE protocols show accurate estimates. This suggests that OGSE protocols show a higher innate sensitivity towards diameters of 2 μm than for SDE protocols.

Table 6.1 compares the relative accuracy of the diameter estimates between SDE and OGSE protocols. The accuracy is defined in terms of the average percentage difference between the voxel-wise diameter estimates and the true diameter for

each plate. The interquartile range is also displayed in brackets to demonstrate the spread in the data. A lower percentage difference refers to higher accuracy for that diameter. The most accurate diameter estimates across all protocols are for diameters $a = 10\ \mu$m and $a = 15\ \mu$m (3-10% difference from the true diameter), whilst the least accurate estimates are for $a = 2\ \mu$m ($> 40\%$ difference from the true diameter).

Table 6.1: Comparison between OGSE and SDE protocols on the relative accuracy of diameter estimates of each plate. The median, along with the interquartile range in brackets (), of the percentage difference (%) between diameter estimates from the ROI of each plate and its corresponding true diameter is shown. Two sided Wilcoxon rank test is carried out to test whether the difference between SDE and OGSE is statistically significant. The significance levels of $p < 0.01$ and $p < 0.005$ are indicated by * and **, respectively. Note that for $a = 2\ \mu$m, most of the SDE voxels hit the lower diameter limit as shown in Figure 6.4.

8 gradient directions		
Plates	SDE	OGSE
2 μm	90 (45)	87 (40)
5 μm	15 (12)***	25 (16)***
7 μm	13 (7.9)	17 (9.2)
10 μm	4.8 (6.4)	6.1 (7.3)
15 μm	7.5 (6.7)	3.7 (8.5)
20 μm	22 (8.2)***	3.6 (4.1)***

16 gradient directions		
Plates	SDE	OGSE
2 μm	70 (45)**	44 (11)**
5 μm	14 (7.2)	16 (11)
7 μm	12 (5.5)**	8.1 (10)**
10 μm	9.7 (12)	8.2 (10)
15 μm	6.2 (8.5)*	3.0 (4.3)*
20 μm	7.4 (13)	7.3 (4.5)

32 gradient directions		
Plates	SDE	OGSE
2 μm	53 (42)	54 (18)
5 μm	16 (7.0)	16 (7.0)
7 μm	16 (11.7)***	11 (8.9)***
10 μm	5.8 (8.5)	5.9 (6.0)
15 μm	6.5 (7.2)*	3.0 (5.3)*
20 μm	9.7 (11)	14 (19)

In terms of the OGSE and SDE performance for diameter estimation, across most plates, both types of protocols provide similar accuracy. The exceptions are at $a = 5\ \mu$m where there SDE protocols give significantly more accurate diameter estimate than the OGSE protocols. At 8 gradient directions, OGSE gives better estimates for $a = 20\ \mu$m than the SDE protocol. For $a = 2\ \mu$m, OGSE also has overall better accuracy across 32 and 16 gradient directions spread is much narrower at 17%.

Figure 6.5 shows the SDE (top row) and OGSE (bottom row) estimates of intrinsic diffusivity for each plate and for each set of gradient directions, similar to Figure 6.4. The median diffusivity estimates of plates at each protocol show a similar range of diffusivities, which range between 1.8-2.2 μm^2/ms. On average, the diffusivity estimates agree with the theoretical diffusivity of water at room temperature (20^{o}C), which is approximately 2.0 μm^2/ms [120]. Additionally, the comparison of the relative accuracy of diffusivity estimates (similar to that in Table 6.1 but data not shown) show no significant differences between the OGSE and SDE diffu-

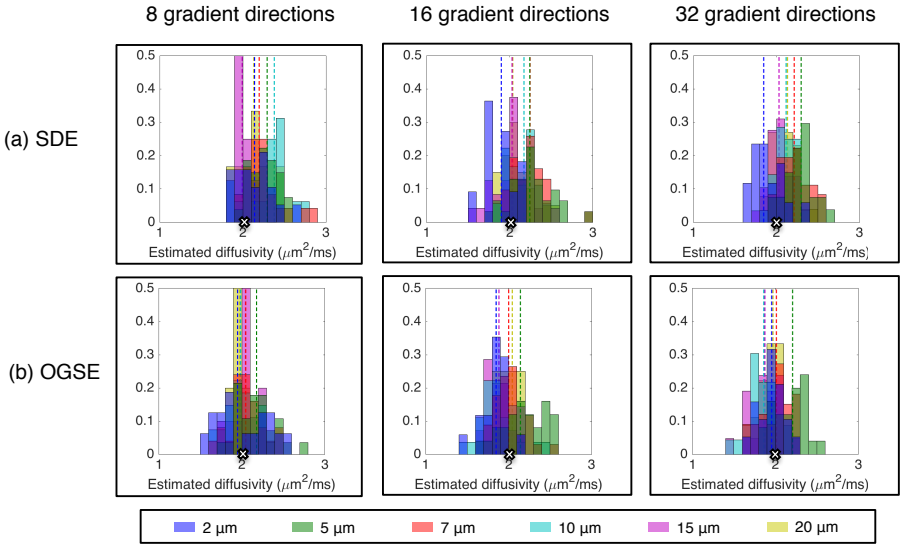

Figure 6.5: Histograms of the diffusivity estimates computed using the 8 (left), 16 (middle) and 32 (right) gradient directions SDE (top row) and OGSE (bottom row) protocols. Same caption as in Figure 6.4 applied here. The dashed lines indicate the median diffusivity estimate for each plate, and the white marker at y=0 labels the theoretical diffusivity of water at 20^{o}C [120].

sivity estimates for each plate at each gradient directions set. The only exceptions occur at 10 μm and 15 μm plates for the 8 gradient directions protocol and 5 μm, 10 μm and 15 μm plates for the 32 gradient directions protocol. At 8 gradient directions, OGSE shows significantly more accurate diffusivity estimates ($p < 0.05$), where the percentage difference in diffusivity estimates relative to the theoretical diffusivity for α = 10 μm is 9.5% compared to 19% for SDE. In contrast, for α = 15 μm OGSE is less accurate, with a percentage difference of 11% compared to 4.1% for SDE. In terms of 32 gradient directions, OGSE shows significantly more accurate diffusivity estimates ($p < 0.05$), where the percentage difference in diffusivity estimates relative to the theoretical diffusivity for α = 5 μm, α = 15 μm and α = 20 μm are 15%, 4% and 7%, compared to 21%, 11% and 22%,respectively, for SDE. Our results suggests that diffusivity estimates for each diameter case are stable and are independent of the type of waveform used in our diffusion protocols.

Figure 6.6 shows the fitted model signal for a voxel from each ROI of the plates for the 32 gradient directions SDE and OGSE protocols, only. As expected, both protocols show that the plate with the smallest capillary diameter (a = 2 μm) shows

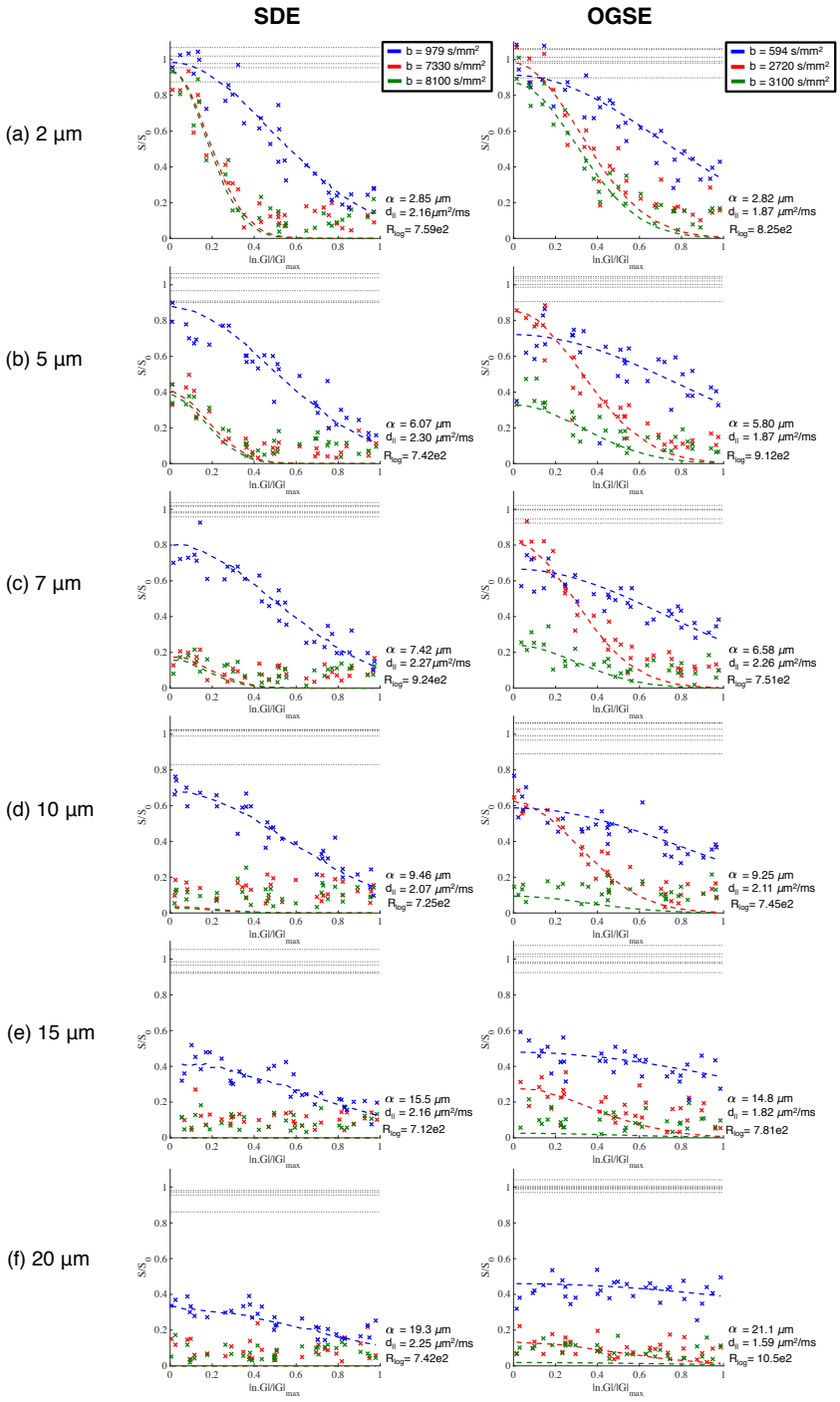

Figure 6.6: Graphs showing the model signals fitted (dashed lines) to the raw data (data points) of a voxel from an ROI of each plate in Figure 6.4. Signals from the 32 gradient directions SDE (left column) and OGSE (right column) protocols are shown. The x-axis is the absolute dot product between the gradient directions and the estimated fibre orientation. The three curves represent the model fit to each of the three measurement shells. The corresponding calibrated b-values of the measurements are displayed here, out of which b=594 and 3100 s/mm^2 from the OGSE measurements have oscillating waveforms. The estimated parameters (α and $d_{||}$), as well as the R_{log} to quantify the quality of fit are shown in the bottom right hand corner of each graph. The horizontal dashed lines around S/S_0=1 represent the spread in the b=0 measurements.

lower attenuation than the plates with the largest capillary diameter (a = 20 μm). This is because larger diameters allow diffusion to occur for a longer time without coming across any boundaries and as a result causes the signal to be attenuated. For similar reasons, the oscillating gradient sequences (b=594 and 3100 s/mm^2) also show much larger signal attenuation in the restricted direction (S/S_0=0) than for the SDE sequence (b=2720 s/mm^2). OGSE sequences have shorter effective diffusion times, which allows them to 'see' water molecules before the molecules come across boundaries, leading to signal attenuation. In addition to this, the high b-value (b $\geq$ 7000 s/mm^2) signals of the SDE protocol at $a \geq 10$ μm are completely attenuated to the noise floor and there is effectively only one measurement that is used for estimating the model parameters. Overall, however, the figure shows a good match between the raw data and the fitted signal.

6.4 Discussion

In this chapter, we have assessed the performance of optimised OGSE and SDE sequences to estimate microstructure parameters of simple idealised phantoms. We have estimated the diameter of capillaries and diffusivity within the capillaries of each plate using OGSE and SDE protocols that were optimised for 8, 16 and 32 gradient directions. In total 6 plates were used with capillary diameters 2,5,7, 10, 15 or 20 μm. Our results demonstrate that both OGSE and SDE protocols can easily distinguish between the whole range of diameters used here, with a = 10 μm and a = 15 μm having the highest diameter accuracy and a = 2 μm having the lowest diameter accuracy.

The accuracy of the pore diameter estimates in the plates are not perfect and depart from the ground truth values even for diameters of 7 or 10 μm, which should be more accurate given the powerful gradients of 800mT/m. This is due to the very low SNR in the sample, 7-15 for individual voxels. Based on numerical work in [24] and analytical work in [25], the resolution limit for 800mT/m and SNR=10 is 2.36 μm. Hence, the plates results obtained on the clinical scanner (Chapter 4), although achieved with lower gradient strength, are accurate as they have an order

of magnitude higher SNR.

Another compounding effect here are the susceptibility effects such as image distortion and signal dropouts. These artefacts arise from alterations to the homogenous magnetic field which are caused by the difference in susceptibility of our plates (susceptibility of -11.05 ppm) and water (-9.03 ppm [117]). At high magnetic field such as 9.4 T we use here, the susceptibility effects become larger. This is especially true when capillary diameter are very small (a<3 μm). As diameter decreases the number of capillaries within the plates increase, which in turn means that there are increased interactions between glass and water resulting in increased susceptibility effects [116]. In addition to ensuring the microcapillaries continue to be aligned to the main magnetic field, it is also possible to reduce the susceptibility effects by using microcapillaries that are longer than the sensitive area of the RF coil - however, this would require purchase of new phantoms which are costly [116].

SDE and OGSE protocols perform very similarly for most plate sizes across all number of directions. Based on [24, 25], the OGSE sequences have better sensitivity than SDE when imaging small diameters (below 5 μm), and here we have only a 2 μm plate in that range which is just below resolution limit for our SNR. Nevertheless, although both sequences provide non-perfect estimates of 2 μm, overall OGSE provides more accurate estimates on average especially as the number of directions reduces.

6.5 Conclusion

In conclusion, this chapter optimised and tested the performance of the SDE and OGSE protocols on simple phantoms. We found that both protocols provide good estimates of pore diameters that are within the resolution limit possible for the gradient strength and the SNR achieved. We found that for the smallest diameter of 2 μm OGSE provides slightly better sensitivity than SDE. In the next chapter we use these optimised protocols and design a simulation study to evaluate and compare the two protocols for a finer range of diameters using realistic digital substrates to represent rat nerve tissue.

Chapter 7

Preclinical scanner: Rat sciatic nerve - simulations and model selection

In the previous chapter we optimised SDE and OGSE protocols for rat nerve tissue, and evaluated their performance on the scanner using simple microcapillary array phantoms.

In this chapter, we assess the performance of the previously optimised protocol in the presence of extra-axonal space using digital substrates that represent rat sciatic nerve tissue.

Parts of this work are featured in the recently accepted paper to *NeuroImage*: *L S Kakkar, O F Bennett, B Siow, S Richardson, T Quick, D Atkinson, J B Phillips and I Drobnjak. Comparison of OGSE and SDE ActiveAx for axon diameter mapping: An experimental study in viable nerve tissue.*

7.1 Motivation

Although simple phantoms have been previously used for calibrating sequences such as DDE [17] and OGSE [116], the phantoms are not representative of biological tissues. Therefore they cannot be used to fully assess the extent of the performance of new or established diffusion sequences. For instance, Chapter 6 suggests that the range of diameters that are accessible to the optimised OGSE and SDE protocols are at least between 2 μm to 20 μm; however, in the presence of extra-axonal space and multi-diameter sizes, these results will deviate.

In the thesis so far, we have used a single 3D Gaussian displacement distribution, constrained by a tortuosity model and with fixed diffusion coefficients to represent tissue during the model fitting process. The tortuosity model has been used for a range of different studies in the past [62, 101, 110, 111, 124, 140]. However, as of recently, it has been questioned because it does not take into account the dependency of the hindered diffusivity on the diameter distribution of the substrates [131, 133, 141]. Furthermore, a recent study points out that fixing the parallel diffusivity can lead to erroneous conclusions [142].

In this chapter, our primary aim is to assess performance of the optimised protocols in the presence of extra-axonal space. We test the intrinsic sensitivity of our optimised protocols using synthetic substrates containing only single diameter cylinders and then test performance of our protocols using synthetic substrates containing multi-diameter cylinders to mimic axons in biological tissues.

The secondary aim of this chapter is to select the most realistic model to represent the rat sciatic nerve tissue when doing the fitting of model parameters. We test the standard model (with tortuosity assumption) against the new model (without the tortuosity assumption) and choose the one that provides more accurate model estimates when compared to ground truth axon diameters in the synthetic substrates. We do not fix the parallel diffusivity, in either cases, and estimate the diffusivity along with other parameters. We select the tissue model that provides the most accurate parameter estimates in realistic synthetic substrates across all of the optimised protocols. The best model will then be used for axon diameter mapping in sciatic nerve of a rat in Chapter 8.

7.2 Method

This section first introduces the two tissue models, the standard model (assumes tortuosity) and the new model (does not assume tortuosity). It then outlines the generation of two types of synthetic substrates, single and multi-diameter, after which the model fitting procedure is briefly described.

7.2.1 Tissue model

A simplified MMWMD with a two compartment model comprised of the extra-axonal and intra-axonal space only (i.e. CSF compartment, S_3, and dot compartment, S_4, are set to 0 and hence are excluded), is used to represent the rat sciatic nerve (see Chapter 2 Section 2.4.2.5 for more details).

In the standard model, d_h is defined by the tortuosity model (d_h=(1-f_{icvf})$d_{||}$), and so the parameters to be fitted are: axon diameter index (α), intra-axonal volume fraction (f_{icvf}) and intrinsic diffusivity ($d_{||}$)).

In the new model, we relax the tortuosity assumption and the parameters to be fitted are: axon diameter index (α), intra-axonal volume fraction (f_{icvf}), intrinsic diffusivity ($d_{||}$) and hindered diffusivity (d_h).

7.2.2 Simulations of synthetic substrates

We use Monte-Carlo diffusion simulations via the CAMINO framework [20, 129, 130] and generate synthesised data using 3-D digital phantoms representing the nerve tissue substrates. Two types of substrates are simulated: cylinders with single diameters and cylinders with various diameters (multi-diameter).

7.2.2.1 Single diameter substrates

Each of our single diameter substrates are characterised by a specific axon diameter α, intra-axonal volume fraction f_{icvf} and intrinsic diffusivity of spins $d_{||}$ to mimic the range of diameters and intra-axonal volume fraction present in the rat peripheral nerve [15]. Diameters of $\alpha \in \{0.5, 1, 1.5, 2, 2.5, 3, 3.5, 4, 4.5 , 5, 5.5\}$ μm, intra-axonal volume fractions of $f_{icvf} \in \{0.4, 0.5, 0.6, 0.7\}$ and diffusivity of $d_{||}$=1.7 μm^2/ms are used to construct 44 single diameter substrates in total. All substrates contain non-abutting parallel cylinders which are arranged in a uniform hexagonal geometry. We chose the synthetic substrates to match the substrates in the next section (Section 7.2.2.2)

All simulations are performed using 200000 spins, 6000 time steps and 500 cylinders. These values are optimal because they provide a precision of 10^{-10} of the unweighted diffusion signal, which is several orders of magnitude smaller than

realistic signal noise [130]. In order to make the synthetic dataset more realistic, 50 different instances of random Rician noise (SNR=10) are introduced to the final dataset. Finally the tissue models described in Section 7.2.1 are fitted to this noisy dataset to estimate the model parameters.

7.2.2.2 Multi-diameter substrates

Each of our multi-diameter substrate is characterised as a unique combination of four parameters: the shape k and the scale parameter θ of the axon radius distribution, the intrinsic diffusivity of spins $d_{||}$, and the intra-axonal volume fraction f_{icvf}. To mimic the structure of the rat peripheral nerve, we model the nerve as a collection of non-abutting parallel cylinders with radius drawn from a gamma distribution. The shape and the scale parameters of the gamma distribution are determined from a collective fibre radius histogram of normal rats shown in [15], which are further corrected to axon radius using g-ratio values reported there. We construct 28 unique nerve substrates, with substrate parameters: $(k,\theta) \in \{(4.08, 4.58 \times 10^{-7}), (7.49, 2.27 \times 10^{-7}), (4.08, 3.27 \times 10^{-7}), (7.49, 1.86 \times 10^{-7}), (7.49, 1.65 \times 10^{-7}), (7.49, 1.45 \times 10^{-7}), (7.49, 1.03 \times 10^{-7})\}$; $f_{icvf} \in \{0.4, 0.5, 0.6, 0.7\}$ and $d_{||}$=1.7 μm^2/ms. The cylinders are randomly packed in the substrates as described in [130], with example substrates shown in Figure 7.1.

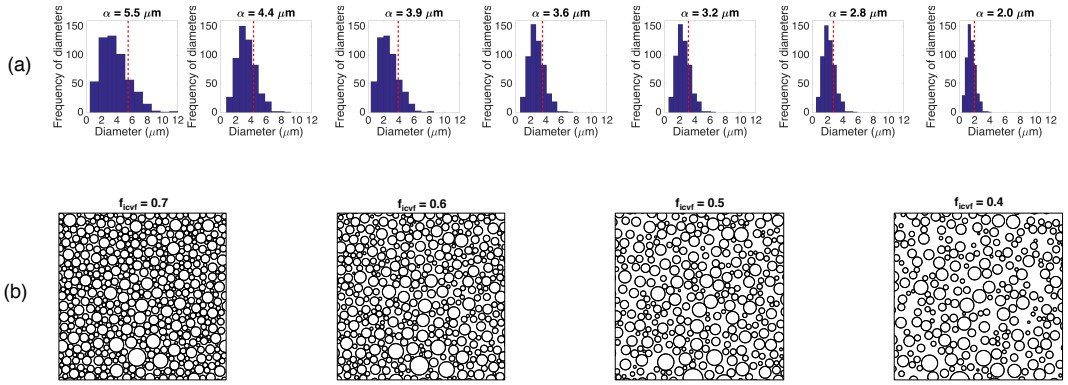

Figure 7.1: (a) shows histograms of axon diameter distributions we use to generate digital substrates for the Monte Carlo simulations. The axon diameter index is calculated for each and shown as a red dashed line. (b) shows digital tissue substrates for the histogram furthest to the right in a) and four different intra-axonal volume fractions we use in simulations. In simulations, each histogram is combined with each of the four volume fractions producing 28 different substrates.

The simulations here are performed using 200000 spins, 6000 time steps and 500 cylinders (same as for single diameter substrates). Similarly, the simulations here also introduce 50 different instances of random Rician noise (SNR=10) to the final dataset. Finally the tissue models described in Section 7.2.1 are fitted to this noisy dataset to estimate the model parameters.

7.2.3 Model fitting

A voxel-wise model fitting procedure involving diffusion tensor, grid search and active-set algorithm (detailed in Chapter 4 Section 4.1.3.2) is used to compute the model parameter estimates of the standard model (f_{icvf}, $d_{||}$ and α) and the new model (f_{icvf}, $d_{||}$, d_h and α).

An extra step is taken to carry out model fitting using the new tissue model. To avoid model fitting instability due to a larger number of free parameters in the new model than in the standard model, d_h is fixed to a range of values (0.03 μm^2/ms to 3 μm^2/ms with an interval of 0.01 μm^2/ms). Grid search and active-set algorithm are then carried out to find the estimate of d_h that maximises the maximum likelihood. Finally, the same two stage process (involving grid search and active-set algorithm) is performed to estimate f_{icvf}, $d_{||}$ and α using the calculated fibre orientation and the estimated d_h.

In order to test the precision of the estimates, we additionally run Markov Chain Monte Carlo (MCMC) procedure assuming Rician noise model. The gradient descent provides a starting point for the MCMC which then collects 125 samples at intervals of 30000 iterations after a burn in of 5000 iterations. We then calculate standard deviation of the posterior distribution of the parameter estimates and use it to test the precision of the protocols.

7.2.4 Model comparison

Lastly, we use the standard model (assumes tortuosity) and the new model (does not assume tortuosity) to carry out a small model comparison study.

The Akaike information criterion (AIC) [121] (Equation 7.1), as was used by [113], and Bayesian information criterion (BIC) [122] (Equation 7.2), as was used

by [102, 114] are used to find the best model across a sample of synthetic substrates (with SNR = ∞). The lower the AIC and BIC, the better the model.

$$AIC = -2log(L) + 2K \tag{7.1}$$

where L is the likelihood of the model and K is the number of free parameters.

$$BIC = -nlog(L) + Klog(n) \tag{7.2}$$

where L and K are as before and n is the sample size (i.e. number of measurements). The log(L) from Equation 4.1 from the active-set algorithm stage is used to calculate both AIC and BIC per voxel.

7.3 Results

In this section, we assess the performance of the optimised OGSE and SDE protocols from Chapter 6 in terms of both the standard tissue model and the new tissue model. In the first section, we demonstrate the intrinsic sensitivity of the protocols using the accuracy of parameter estimates for synthetic substrates with single diameter cylinders. In the second section, we use the synthetic substrates with multi-diameter cylinders to evaluate the performance of the protocols across three separate criteria: (i) Accuracy of parameter estimates compared to the ground truth; (ii) Precision of parameter estimates; (iii) Robustness of parameter estimates as the total number of diffusion measurements changes.

7.3.1 Single diameter substrates

Figure 7.2 displays the SDE and OGSE estimated parameters for the standard tissue model plotted against the ground truth diameter indices for a range of single diameter substrates with various intra-axonal volume fractions. The results are shown for the 32 gradient direction protocols. SDE shows a positive correlation of estimated axon diameter index with the ground truth in the first row, however, it underestimates the diameter index for almost all substrates. At low diameters ($\alpha \leq 3.5$ μm), majority of estimates hit the lower fitting limit of 0.2 μm. In contrast, the OGSE

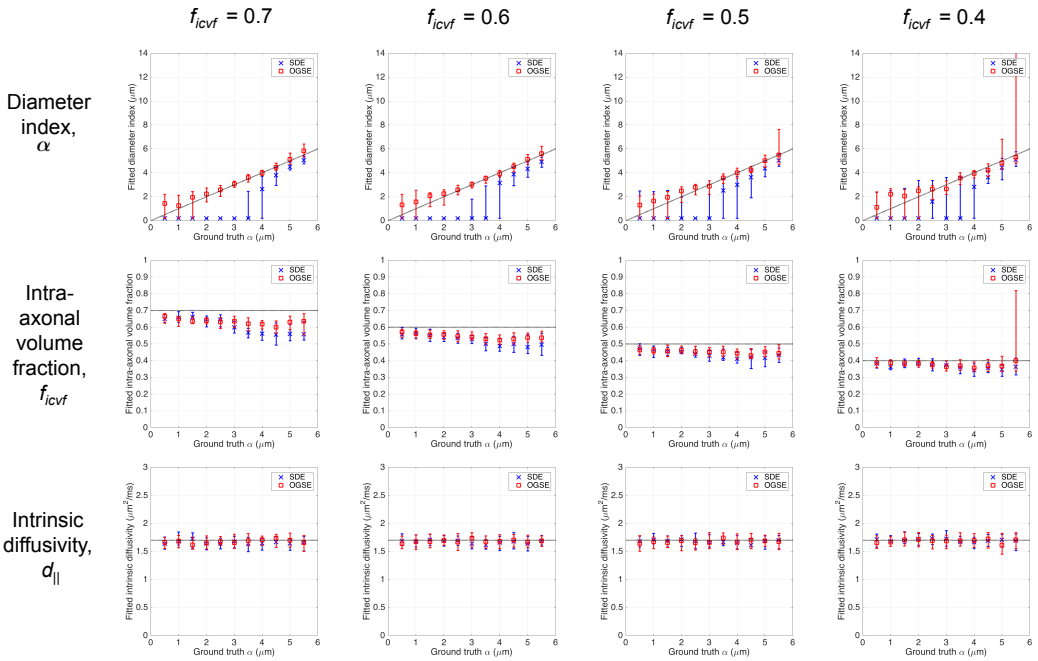

Figure 7.2: Accuracy of estimated parameters for single diameter substrates using the standard tissue model: axon diameter index (1st row), intra-axonal volume fraction (2nd row) and intrinsic diffusivity (3rd row) for a range of intra-axonal volume fractions. The median, 25th and 75th percentile of the estimates across 50 different instances of random Rician noise (SNR=10), are shown for each diameter index, with SDE median estimates in blue crosses and OGSE median estimates in red squares. The identity lines are shown in black.

protocol accurately estimates most axon diameters (estimates are much closer to the identity line), with the exceptions at smaller diameters (α <1.5 μm) and largest diameter (α> 5.5 μm), where overestimations occur. Similarly, OGSE intra-axonal volume fraction (in the second row) are much closer than the SDE ones, however both protocols show improved accuracy of intra-axonal volume fraction estimates as the ground truth intra-volume fraction decreases. In terms of the intrinsic diffusivity (third row), both OGSE and SDE sequences perform similarly. Overall, OGSE produces more accurate axon diameter index and intra-axonal volume fraction compared to SDE when using the standard tissue model.

Figure 7.3 displays the SDE and OGSE estimated parameters for the new tissue model plotted against the ground truth diameter indices across a range of volume fractions, similar to Figure 7.2. The first row shows that although SDE shows a positive correlation with the ground truth diameter indices, below α = 3 μm the axon

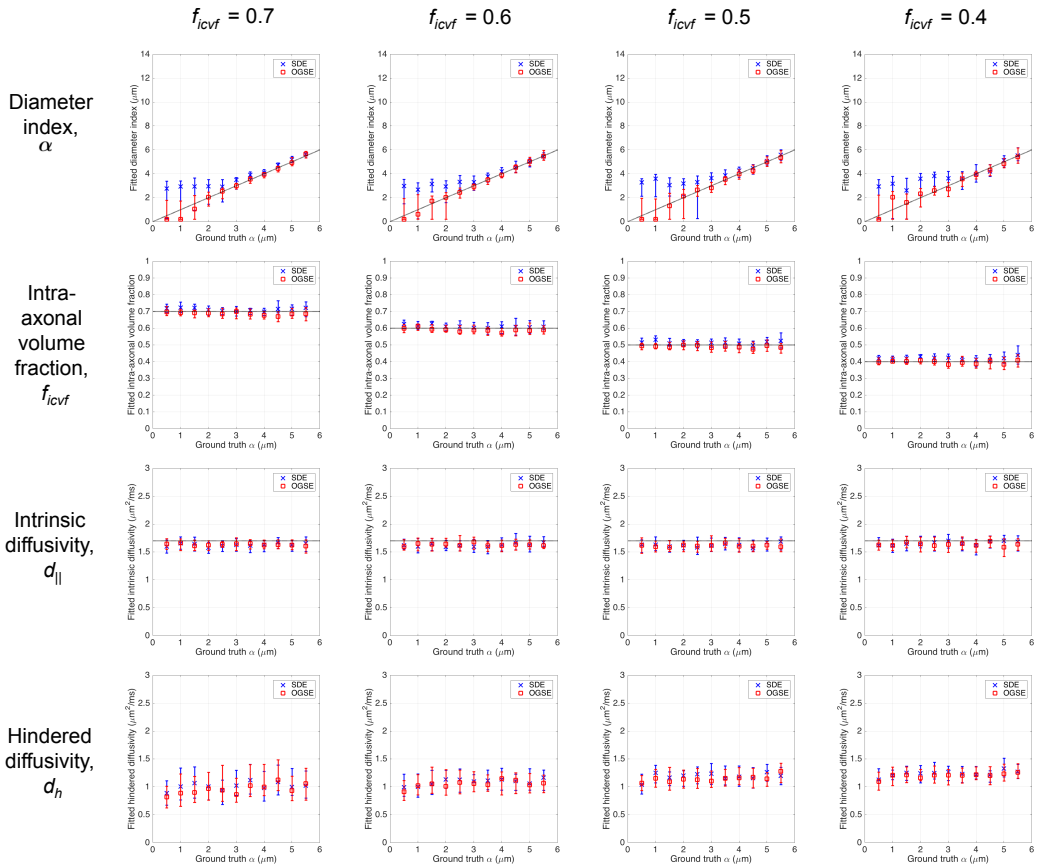

Figure 7.3: Accuracy of estimated parameters for single diameter substrates using the new tissue model: axon diameter index (1st row), intra-axonal volume fraction (2nd row) intrinsic diffusivity (3rd row) and hindered diffusivity (4th row) for a range of intra-axonal volume fractions. The median, 25th and 75th percentile of the estimates across 50 different instances of random Rician noise (SNR=10), are shown for each diameter index, with SDE median estimates in blue crosses and OGSE median estimates in red squares. The identity lines are shown in black. d_h plots do not have any identity lines as the ground truth for d_h is unknown and depends on the packing.

diameters cannot be distinguished from one another. In comparison, the OGSE protocol is much more accurate and only axon diameters below $\alpha = 2$ μm cannot be resolved. The intra-axonal volume fraction estimates in the second row are accurate for the OGSE sequences but are slightly overestimated for the SDE sequences. In terms of the diffusivities (third and fourth row), OGSE and SDE both perform similarly. In general, OGSE produces more accurate axon diameter index and intra-axonal volume fraction compared to SDE for a range of synthetic substrates when using the new tissue model.

The comparison between the accuracy of model parameter estimates for the standard model (Figure 7.2) and the new model (Figure 7.3) shows that the new model significantly improves on the accuracy of diameter indices and intra-axonal volume fractions for both OGSE and SDE sequences. This is observed as parameter estimates being much closer to the identity line for the new model than for the standard model. Similar observations are also made for the 8 and 16 gradient direction protocols and as expected the interquartile range of the estimates increase as the measurements are reduced (data not shown but similar to Figure 7.7 and Figure 7.8 in the later sections).

7.3.2 Multi-diameter substrates

Figure 7.4 shows the SDE and OGSE estimated model parameters plotted against the ground truth diameter indices for the simulated multi-diameter substrates using the standard tissue model. The results are shown for the 32 gradient direction protocol similar to the single diameter substrates. The first row shows that SDE has a positive correlation with the ground truth index but the diameter index for almost all substrates are underestimated while the OGSE protocol is much more accurate with estimates closer to the identity line. The intra-axonal volume fraction estimates in the second row are underestimated for both OGSE and SDE sequences, whereas the intrinsic diffusivity (third row) appear similar for both sequences. The observations align with the results for the single diameter substrates in Figure 7.2. Generally, OGSE appears to give more accurate diameter index and intra-axonal volume fraction estimates of multi-diameter substrates compared to SDE sequences when using the standard model.

Figure 7.5 displays the SDE and OGSE estimated parameters for the new tissue model plotted against the ground truth diameter indices across a range of volume fractions, similar to Figure 7.4. The first row shows that both OGSE and SDE have a positive correlation with the ground truth diameter indices, with OGSE showing diameter indices that are closer to the identity line. The intra-axonal volume fraction estimates in the second row are accurate for the SDE sequences but are slightly underestimated for the OGSE sequences, mainly at substrates with large diameters

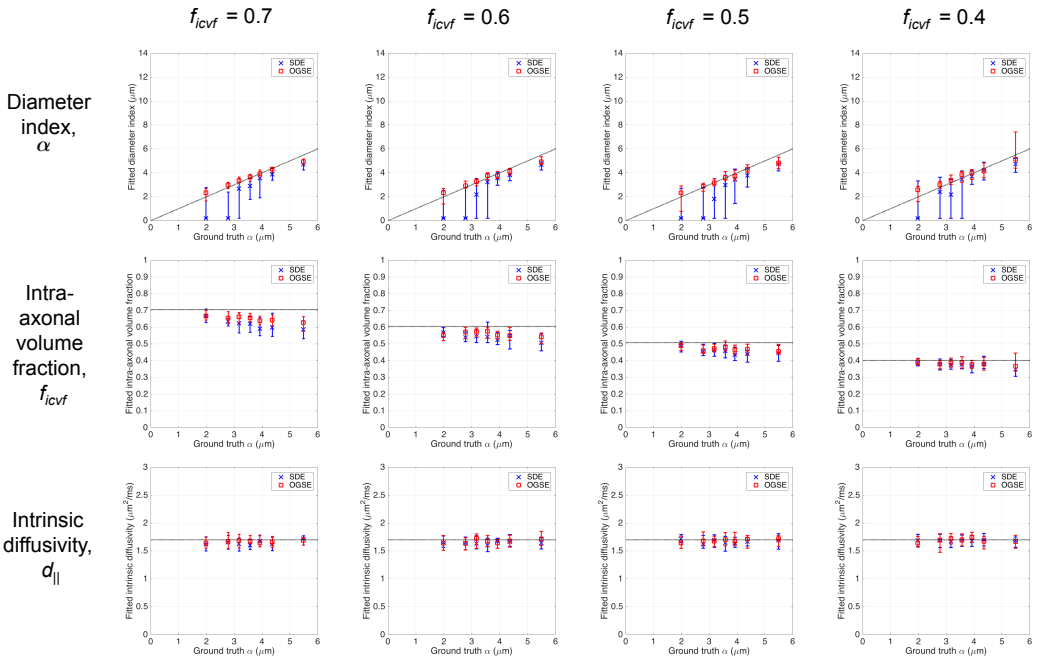

Figure 7.4: Accuracy of estimated parameters for multi-diameter substrates using the standard tissue model: axon diameter index (1st row), intra-axonal volume fraction (2nd row) and intrinsic diffusivity (3rd row) for a range of intra-axonal volume fractions. The median, 25th and 75th percentile of the estimates across 50 different instances of random Rician noise (SNR=10), are shown for each diameter index, with SDE median estimates in blue crosses and OGSE median estimates in red squares. The identity lines are shown in black.

(α = 5.5 μm). In terms of the diffusivities (third and fourth row), OGSE and SDE both perform similarly. These findings agree with the results for single diameter substrates in Figure 7.3. Overall, OGSE provides more accurate axon diameter index than SDE, but SDE shows better accuracy for intra-axonal volume fraction than OGSE when using the new model.

The comparison between the accuracy of model parameter estimates for the standard model (Figure 7.4) and the new model (Figure 7.5) shows that the new model improves accuracy of parameter estimates. The new model shows significant improvements for SDE when estimating intra-axonal volume fraction and axon diameter indices. For OGSE, the new model mostly improves intra-axonal volume fraction estimates but axon diameter indices are largely unaffected. Only substrates with large diameters, $\alpha > 5$ μm, and high intra-axonal volume fraction $f_{icvf} >$ 0.6 show significant improvement in their diameter accuracy. Overall, the new tis-

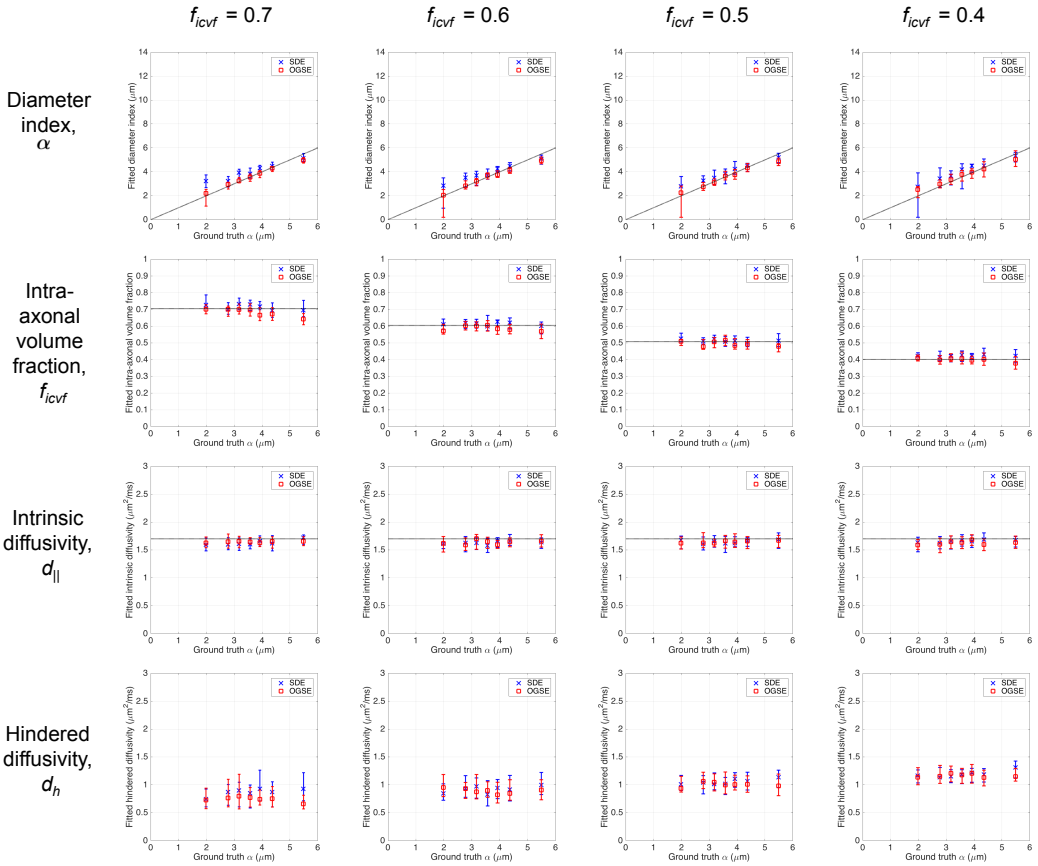

Figure 7.5: Accuracy of estimated parameters for multi-diameter substrates using the new tissue model: axon diameter index (1st row), intra-axonal volume fraction (2nd row) intrinsic diffusivity (3rd row) and hindered diffusivity (4th row) for a range of intra-axonal volume fractions. The median, 25th and 75th percentile of the estimates across 50 different instances of random Rician noise (SNR=10), are shown for each diameter index, with SDE median estimates in blue crosses and OGSE median estimates in red squares. The identity lines are shown in black. d_h plots do not have any identity lines as the ground truth for d_h is unknown and depends on the packing.

sue model appears to give more accurate diameter index and intra-axonal volume fraction estimates than the standard tissue model.

Figure 7.6 shows the precision results for the 32 gradient direction protocols using the standard (left panel) and the new (right panel) tissue model, respectively. Both display the uncertainty in SDE and OGSE model parameter estimates across all multi-diameter substrates, intra-axonal volume fractions and across the 50 different instances of random Rician noise (SNR=10). The uncertainty in the parameter estimates is represented by the standard deviation of the posterior distribution

on the model parameter estimate. The uncertainty in the diameter estimates and intra-axonal volume fraction estimates (first and second row, respectively) from the OGSE protocol is lower than the SDE protocol. By contrast, the uncertainty in the diffusivity (third row) is only slightly different between SDE and OGSE. For the new model, the uncertainty of hindered diffusivity is not calculated here because it is fixed to a pre-calculated value (mentioned above) throughout the fitting procedure. Overall, OGSE appears to estimate parameters with higher precision across the range of substrates compared to SDE.

The comparison between the two models show that the uncertainties on the estimates of the diameters and intra-axonal volume fractions from the SDE protocol are slightly higher for the new tissue model (assuming tortuosity, right panel) than for the standard model (not assuming tortuosity, left panel). The lower number of parameters in the standard model potentially contributes to the higher precision of diameter and intra-axonal volume fraction.

Figure 7.7 and Figure 7.8 demonstrate the effects of reducing the number of diffusion measurements for the standard (Figure 7.7) and the new (Figure 7.8) tissue model. Each figure compares the robustness of parameter estimates between SDE and OGSE protocols across the number of measurement directions (shown in columns) for the full range of synthetic substrates with multi-diameter cylinders. The box and whisker plots on each graph represent the range of estimates for each substrate across its 50 instances of added noise. The dashed lines indicate ground truth parameter values, and in the case of axon diameter index, the two dashed lines indicate the minimum and maximum ground truth diameter index for the synthetic substrates. Both figures show that OGSE protocols consistently deliver diameter indices that are within the ground truth range regardless of the number of gradient directions used. In addition to high accuracy, OGSE estimates also have lower interquartile range with respect to the noise and these ranges are consistent in size across most measurement directions. On the other hand, the figures show that SDE estimates of diameter indices reduce in accuracy and robustness to noise as the number of directions reduce. In terms of intra-axonal volume fractions and intrinsic

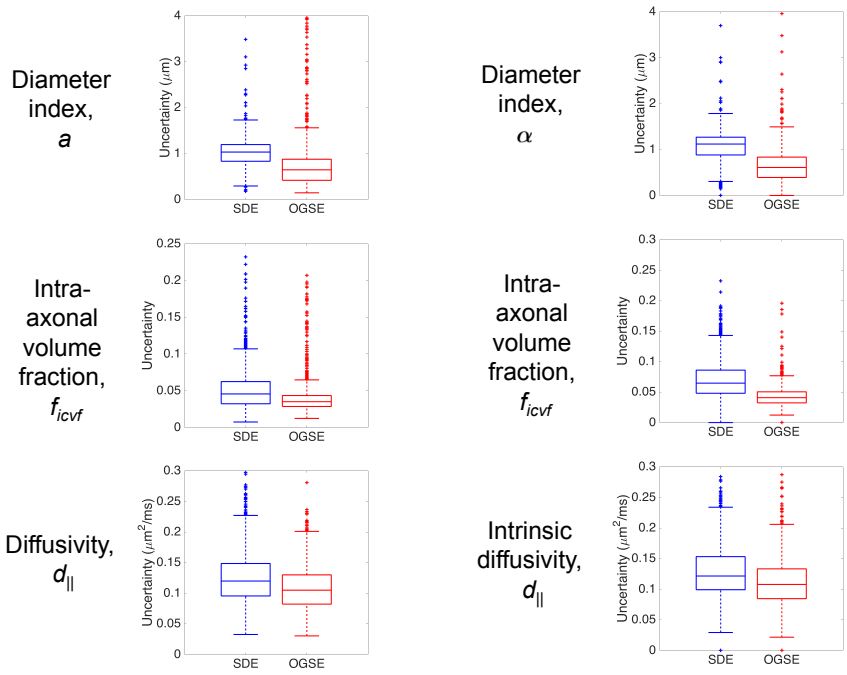

Figure 7.6: Precision of estimated parameters for multi-diameter substrates using the standard tissue model (assuming tortuosity, left panel) and new tissue model (not assuming tortuosity, right panel). Box-whisker plots of the standard deviation of the posterior distribution, i.e. uncertainty, on the estimated axon diameter index (1st row), intra-axonal volume fraction (2nd row) and intrinsic diffusivity (3rd row) for all substrates across all intra-axonal volume fractions and across 50 different instances of random Rician noise (SNR=10). SDE and OGSE values are shown in blue and red, respectively. The boxes show median, 25th and 75th percentiles of the uncertainty and the whiskers extend to the most extreme data points excluding outliers.

diffusivity (and hindered diffusivity), OGSE and SDE show similar range of estimates across the three sets of gradient directions for both of the tissue models. The protocols also show expected increase in the number of outliers as the number of directions are reduced. Overall, the observations on the robustness of the protocols are consistent across both tissue models.

Signal plots of sample voxels (shown in Appendix B) to assess the signal fits to the raw data do not show much difference when using the standard or the new model and this is true for both protocols, visually, and even quantitatively (using the objective function values). The low SNR of the data prevents making any conclusion on the improvement of signal fits when using different tissue models for both

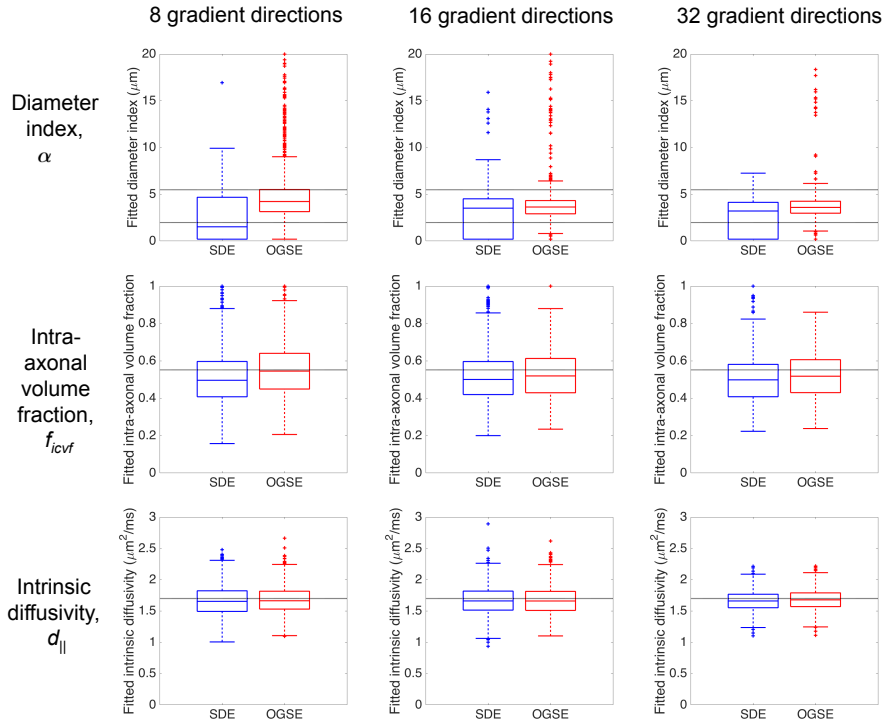

Figure 7.7: Robustness of estimated parameters for multi-diameter substrates with respect to the number of gradient directions using the standard tissue model. Box-whisker plots of the median estimates for each substrate across its 50 instances of added noise (SNR=10). All twenty eight substrates are included and the results plotted for SDE (in blue) and OGSE (in red) protocols. The boxes show median, 25th and 75th percentiles of the uncertainty and the whiskers extend to the most extreme data points excluding outliers. The dashed black lines show the ground truth values for f_{icvf} and $d_{||}$, the minimum and the maximum ground truth value for α.

of our sequences. Therefore, to assess the intrinsic model signal fits, it is easier to look at the signal fits for noise free data in Figure 7.9.

Figure 7.9 displays the signal fits for three sample voxels with noise free data for the standard and the new model, for both SDE and OGSE 32 gradient direction protocols. The new model mostly improves on the signal fits of the low b-value measurements (b_{SDE} = 695 s/mm^2 and b_{OGSE} = 528 s/mm^2) from the standard model across all substrates. This in turn seems to give sensitivity to smaller axon diameters and gives more accurate axon diameter index and intra-axonal volume fractions. On the other hand, the misfit between the ground truth and raw signal persists for the high-b value measurements of the largest substrate (α = 4.37 μm), suggesting the new tissue model is not ideal for large diameters. Overall, quali-

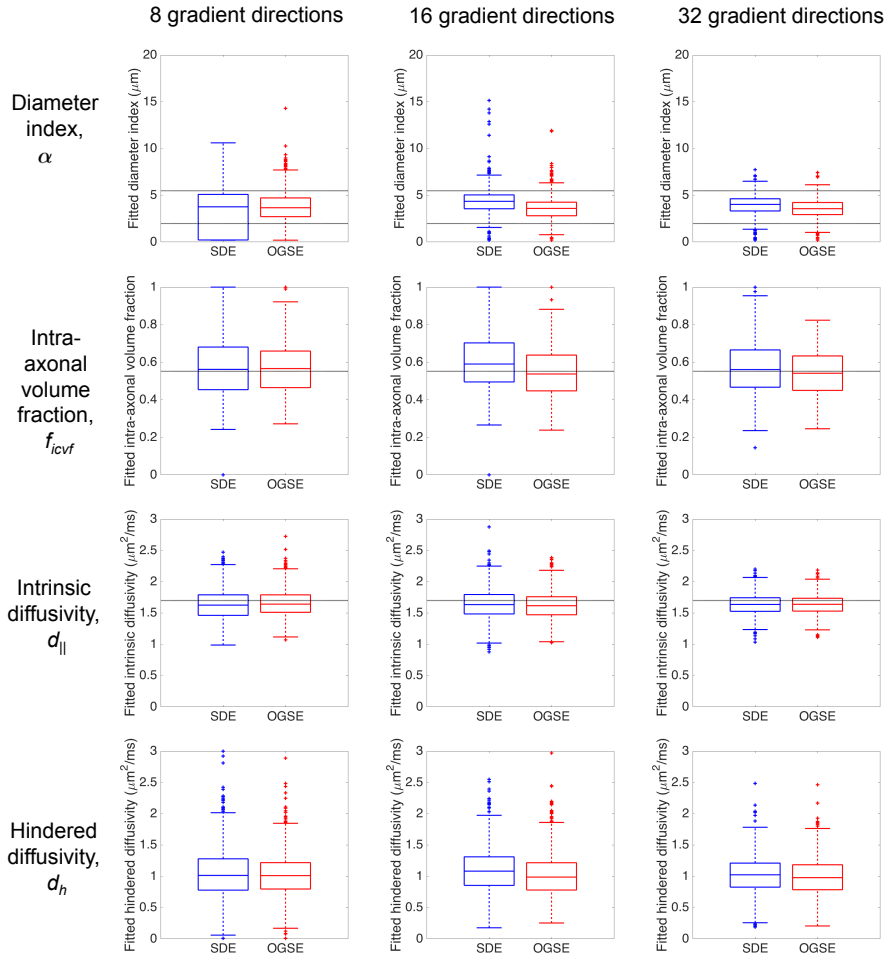

Figure 7.8: Robustness of estimated parameters for multi-diameter substrates with respect to the number of gradient directions using the new tissue model. Same caption as Figure 7.7 applies here. d_h ground truth values are not present as the value is unknown.

tatively, the new model significantly improves the signal fits and the accuracy of parameter estimates for our current protocols and majority of synthetic substrates.

Quantitatively, Table 7.1 displays the BIC values for the two tissue models across the three synthetic substrates from Figure 7.9 for both SDE and OGSE 32 gradient directions protocol datasets. As AIC performs very similar to BIC, here we only show the BIC values. The best model is confirmed to be the new model across all voxels and protocols.

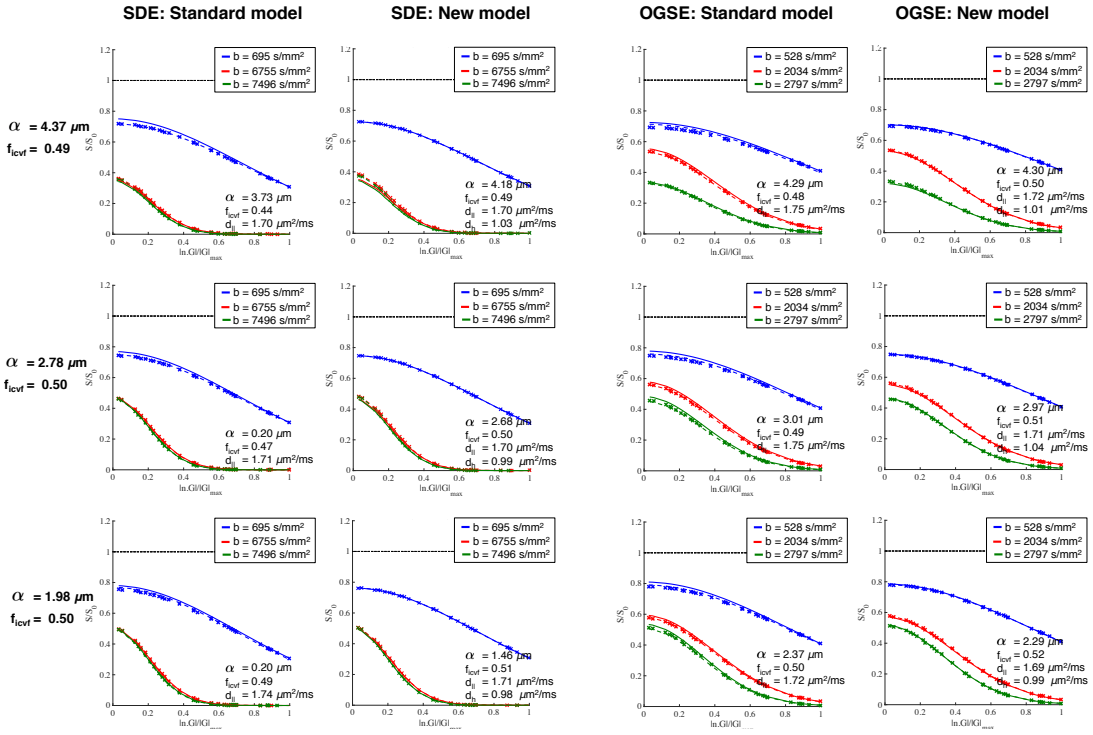

Figure 7.9: Graphs showing the raw (data points), fitted (dashed lines) and ground truth signals (solid lines) for three synthetic substrates ($\alpha = 4.37\ \mu$m, top row, $\alpha = 2.78\ \mu$m, middle row, and $\alpha = 1.98\ \mu$m, bottom row, with $f_{icvf} = 0.5$) using the 32 gradient directions SDE protocol (a and b) and OGSE protocol (c and d) for the standard model (a and c) and new model (b and d). The x-axis is the absolute dot product between the gradient directions and the estimated fibre orientation. The three different coloured curves represent the model fit to each of the three measurement shells. The estimated parameters are shown in the bottom right hand corner of each graph. The horizontal dashed lines at S/S_0=1 represent the b=0 measurements.

Table 7.1: The BIC values for the two tissue models across three different voxels (f_{icvf}=0.5, $\alpha \in \{4.37, 2.78, 1.98\}\ \mu$m) are displayed here for both SDE and OGSE cases.

	$SDE_{standard}$	SDE_{new}
$\alpha = 4.37\ \mu$m	2.09e+08	1.48e+08
$\alpha = 2.78\ \mu$m	8.45e+08	2.37e+08
$\alpha = 1.98\ \mu$m	37.4e+08	2.37e+08

	$OGSE_{standard}$	$OGSE_{new}$
$\alpha = 4.37\ \mu$m	65.5e+08	18.0e+08
$\alpha = 2.78\ \mu$m	33.5e+08	3.35e+08
$\alpha = 1.98\ \mu$m	28.7e+08	4.93e+08

7.4 Discussion

In this work, we have compared the performance of the optimised OGSE sequences with SDE sequences by comparing their ability to estimate axon diameters in synthetic substrates. We show that the optimal OGSE protocols (consisting of one single lobe and two low frequency oscillating diffusion waveforms) consistently out-

performs SDE in both simulated substrates of single and multi-diameter cylinders in terms of the accuracy of axon diameter indices. We also show that the standard model (assuming tortuosity) used so far in this work gives biased estimates of axon diameter indices, mainly for SDE sequences, and intra-axonal volume fractions for both OGSE and SDE sequences. The new model (not assuming tortuosity) overcomes this issue and significantly improves on these named parameter estimates for the given protocols, however at a cost of precision on the estimates. Furthermore, OGSE estimates are more robust compared to the SDE estimates when the number of measurements available for model fitting is reduced, and this is true regardless of the tissue model that was used in this chapter.

Our single diameter results help to explain the diameter estimates for the multi-diameter substrates. Focusing on just the new model, the single diameter substrates provide the resolution limit for our sequences, which are 3 μm and 1.5 μm for SDE and OGSE, respectively. This means that across the multi-diameter substrates, only 1-58% of the cylinders are measurable to the SDE protocol, whereas a much larger amount, 50-96%, are visible to the OGSE protocol. At the smallest multi-diameter substrates (α = 1.98μm and α = μm), SDE is only able to sense 1% and 16% of the cylinder diameters, respectively, which could explain the failure of SDE protocols in distinguishing between the diameter indices for these two substrates.

Our findings from this chapter agree with the results from Chapter 6 on the higher sensitivity of the optimised OGSE sequences to small axon diameters ($\alpha <$ 2 μm), especially as we reduce the number of diffusion measurements. This supports the theoretical results recently published in [24], which showed numerically that when gradient direction and short axis of the fibre is perfectly aligned, SDE sequences with high b-values are best. However, in the presence of misalignment, the intra-axonal SDE diffusion signal in the parallel direction of the fibre diminishes consequently reducing the total signal. In such cases, low frequency OGSE sequences are preferred because the total signal remains preserved. This can be seen in Figure 7.9, where the misalignment between the short axis of the cylinders and the closest gradient direction is $<2^o$ (calculated using diffusion tensor analysis

for the 32 gradient direction protocol). Results from both of our single and multi-diameter substrates confirm that OGSE sequences from our protocols indeed probe small diameters and this is true across a range of intra-axonal volume fractions.

Our results also confirm that the standard model is not ideal for axon diameter imaging using SDE sequences. This agrees with the findings from [131], who demonstrated that the tortuosity constraint biases axon diameter estimates. [143] also suggested that the tortuosity constraint makes the intra-axonal volume fraction estimates very sensitive to the intrinsic diffusivity estimates, which probably leads to the inaccuracy of intra-axonal volume fraction estimates observed for our protocols. The new model relaxes this tortuosity assumption and estimates the hindered diffusivity, which significantly improves axon diameter and intra-axonal volume fraction estimates.

In this chapter we have chosen a simple model of white matter tissue to represent our synthetic substrates. The model uses long straight circular cylinders that mimic axon bundles, and have the same intrinsic diffusivity in the intra- and extra-axonal compartment. These assumptions are true for our synthetic substrates but may not be fully valid in real biological tissue (for instance the rat sciatic nerve to be used in Chapter 8). Therefore, it is worth bearing in mind that the results for biological tissues may differ from our simulation work. However, the general trends, such as the better accuracy of OGSE than SDE, from our simulation work should still be valid.

7.5 Conclusion

Overall, this chapter confirms that low frequency OGSE sequences outperform SDE sequences in estimating axon diameters in simulations regardless of the type of tissue models that are used here. Between the tissue models, i.e the standard (assuming tortuosity) and the new (not assuming tortuosity) tissue model, the new tissue model is much more accurate and robust for axon diameter imaging, especially for SDE sequences. In the next chapter, we will be using this model to carry out axon diameter mapping on the rat sciatic nerve.

Chapter 8

Preclinical scanner: Rat sciatic nerve - Axon diameter mapping

Our work in Chapter 7 demonstrates that the standard tissue model, which assumes tortuosity does not fully describe the diffusion signal from the extra-axonal compartment. Instead a better model to use is by relaxing the tortuosity constraint on the hindered diffusivity of the extra-axonal compartment.

The purpose of this chapter is to compare the performances of OGSE and SDE protocols optimised in Chapter 6 for estimating axon microstructure in a viable nerve tissue, using a viable isolated tissue (VIT) system, with a direct comparison to histology. The MR imaging experiment is conducted on a 9.4 T preclinical scanner using gradient strength, G = 800 mT/m. Similar to Chapter 7, we evaluate the optimised OGSE and SDE protocols on three criteria: (i) Accuracy of the model estimates compared to the histology; (ii) Precision of the model estimates; (iii) Robustness of the model estimates as the total number of diffusion gradient directions reduces.

The experiments here are carried out with help from James B Phillips (for extracting the sciatic nerve), Simon Richardson (for setting up the VIT system), Bernard Siow (for fine tuning the imaging sequences to avoid artefacts) and Oscar F Bennett (for data analysis and for the histology results). Parts of this work are featured in the recently accepted paper to *NeuroImage*:

L S Kakkar, O F Bennett, B Siow, S Richardson, T Quick, D Atkinson, J B Phillips

and I Drobnjak. Comparison of OGSE and SDE ActiveAx for axon diameter mapping: An experimental study in viable nerve tissue.

8.1 Method

This section outlines the rat sciatic nerve tissue sample preparation procedure, briefly re-introduces the biophysical microstructure model representative of the tissue of interest and describes the imaging parameters used to acquire the raw data. The section continues by outlining the model fitting procedure used to acquire the tissue microstructure parameter estimates, and briefly describes the transmission electron microscopy method used to inspect the nerve microstructure, and the image analysis algorithm used to extract the microstructure ground truth measurements from the electron micrographs.

8.1.1 Tissue sample preparation

A sample of sciatic nerve tissue is freshly excised from an adult Sprague Dawley rat. The nerve is ligated carefully at both ends and is placed into a specially designed viable isolated tissue (VIT) chamber [137], which bathes the tissue in a temperature controlled (at 37^oC) oxygenated artificial cerebrospinal fluid (aCSF) solution in order to preserve viability during the course of the image acquisition. Figure 8.1 shows the nerve contained inside this chamber.

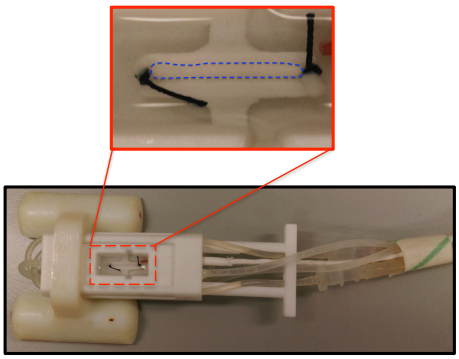

Figure 8.1: The bottom image shows the chamber used to hold the excised and ligated nerve tissue within the bore of the scanner during the image acquisition. The top image displays the magnified sciatic nerve (outlined in blue dashed lines) which is ligated at both ends. Details about the chamber can be found in [137].

The experiments comply with the ARRIVE guidelines and are carried out in

accordance with the U.K. Animals (Scientific Procedures) Act, 1986 and associated guidelines, EU Directive 2010/63/EU for animal experiments.

8.1.2 Tissue model

The new two compartment tissue model (the model that does not assume tortuosity) from Chapter 7 is used to represent the nerve microstructure. The final tissue model parameters to be estimated are: axon diameter index (α), intra-axonal volume fraction (f_{icvf}), intrinsic diffusivity ($d_{||}$) and hindered diffusivity (d_h).

8.1.3 Imaging protocol

The diffusion protocols from Chapter 6 Figure 6.1 are used to acquire the data for this experiments. All MR measurements are conducted with a small bore 9.4 T scanner (Agilent Inc., Santa Clara, CA, USA) equipped with 1000mT/m imaging gradients and a 33 mm RF bird cage volume coil (RAPID, Biomedical GmbH, Rimbar, Germany). A fast spin-echo readout is used with an echo train length of 8. The following imaging parameters were used: FOV = 6 mm $\times$ 6 mm $\times$ 2 mm, voxel dimensions = 93.8 μm $\times$ 93.8 μm $\times$ 2 mm, 8 signal averages, TR = 1100 ms, effective TE (SDE) = 20 ms and effective TE (OGSE) = 35 ms. The total time necessary to complete all imaging protocols is approximately 12 hours. Post data acquisition, the calibrated sequences from Chapter 6 are used to analyse the data.

8.1.4 Model fitting

A voxel-wise model fitting procedure involving diffusion tensor fit, grid search, active-set algorithm and MCMC is used to compute the tissue model parameter estimates (f_{icvf}, $d_{||}$, d_h and α). First, in order to reduce the number of combination of parameters a diffusion tensor is fitted to the data to find the fibre orientation. Next, to avoid model fitting instability due to larger number of free parameters than measurements, d_h is fixed to a range of values (0.03 μm^2/ms to 3 μm^2/ms with an interval of 0.01 μm^2/ms). A two stage fitting procedure (grid search and active-set algorithm) is then carried out to find the estimate of d_h that maximises the maximum likelihood. The same two stage process (involving grid search and active-

set algorithm) is performed to estimate f_{icvf}, $d_{||}$ and α using the calculated fibre orientation and the estimated d_h. In order to test the precision of the estimates, we additionally run Markov Chain Monte Carlo (MCMC) procedure assuming Rician noise model.

8.1.5 ROI selection

In order to perform quantitative analyses of the results from model fitting a region of interest (ROI) fully within the nerve is selected. The region corresponds to the approximate extent of the large upper axon-rich nerve fascicle seen in the histology. Voxels from this region are least likely to contain partial volume of the axon-free epineurium or of free water outside the nerve and so are most suitable to use for assessment of the chosen tissue model. A preprocessing step in the analysis excludes a small subset of the ROI voxels from each protocol which have a signal-to-noise ratio (SNR) < 10 and fractional anisotropy (FA) < 0.2.

8.1.6 Histology

Once the imaging is completed, the histology procedure is carried out as described in [137]. The nerve tissue sample is removed from the chamber and fixed in 2% paraformaldehyde, 2% glutaraldehyde and sodium cacodylate buffer (pH 7.3). The sample is post-fixed with 1% osmium tetraoxide, dehydrated, set in resin, sectioned and then stained with lead citrate in preparation for transmission electron microscopy. The tissue section is imaged with a Joel 1010 transmission electron microscope and the images recorded using a Gatan Orius CCD camera. The tissue section used comes from the middle of the tissue volume lying within the image slice selected during the MR scanning.

Twenty eight $64\times50\times5$ μm transmission electron micrographs (TEM), an example is shown in Figure 8.2, obtained at regularly spaced positions across the whole nerve section are acquired to sample the axon microstructure. An in-house MATLAB (The MathWorks, Natick MA.) based image processing algorithm is used to automatically extract the size and number of intra-axonal areas in each image. The algorithm involves a threshold segmentation of the axon myelin sheaths, fol-

lowed by morphological operations to clean up the resulting segmentations, and then finally a connected component analysis that extracts the intra-axonal regions from within the images.

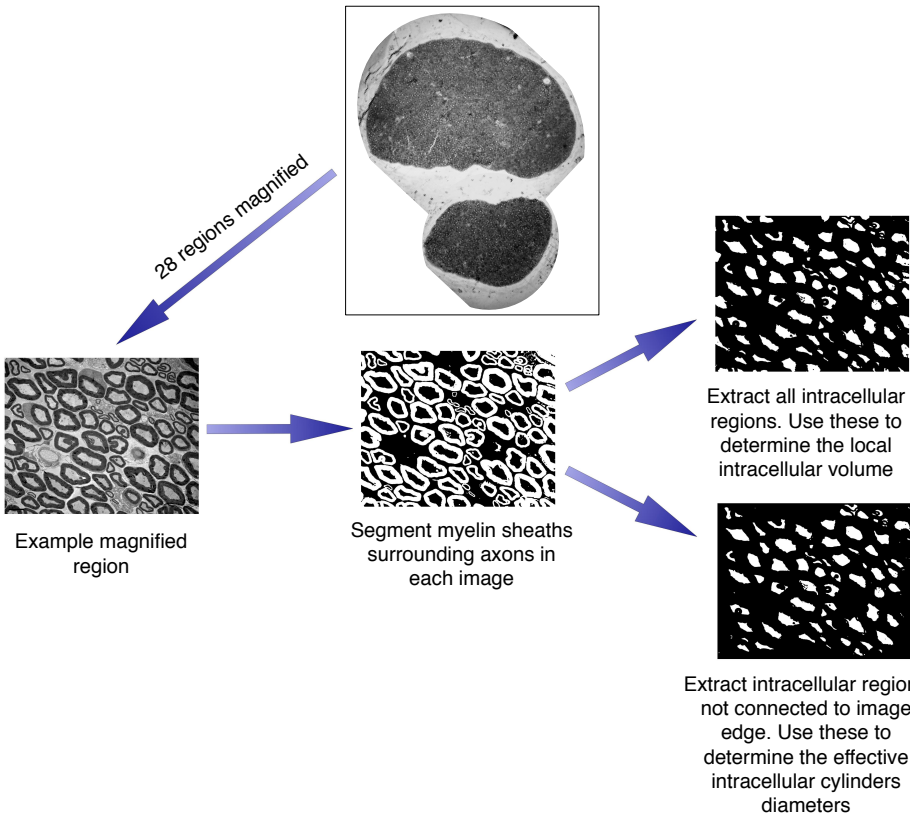

Figure 8.2: An outline of the main steps in the image processing algorithm implemented for histological microstructure measurements. Minor intermediate steps in the pipeline have been omitted.

These intra-axonal regions are then used to calculate the local intra-axonal volume fraction and the local axon diameter index. The local intra-axonal volume fraction is calculated by dividing the total area of all the intra-axonal regions with the total area in the image (excluding the myelin sheets). The local axon diameter index is calculated using Equation 2.53, where the effective diameters come from the intra-axonal regions not connected to the image edges, and additionally these effective diameters are corrected for tissue shrinkage of 30% as suggested by [30]. The local axon diameter index and local intra-axonal volume fraction for each TEM image are used for comparison with the parameter estimates obtained from model fitting. An outline of the TEM processing pipeline is shown in Figure 8.2.

8.2 Results

Here we characterise the performance of the two protocols using (i) Accuracy and (ii) Robustness of their microstructure estimates. The accuracy is measured as the proximity of the microstructure parameter estimates to histology. The robustness of parameter estimates with respect to the number of gradient directions is then evaluated.

8.2.1 Histology results

Figure 8.3 shows examples of micrographs obtained from the TEM procedure described in Section 8.1.6. The entire nerve section is shown with the upper and lower fascicles where the axons are located. The image of the nerve is created by composing two large scale TEM images, and has been rotated to visually coincide with the orientation of the nerve in the MR images and parameter maps presented later.

The ground truth microstructure measurements are obtained from 28 magnified regions using the image processing algorithm described earlier in Section 8.1.6. Interestingly, the majority of the sample regions do not seem to exhibit a gamma distribution of axon diameters. Often the smallest axons (below 3 μm) are the most numerous ($\approx$45% of the average sample) and the larger axons ($>5\mu$m) occur in fewer amounts ($\approx$13% of the average sample). Overall, the averaged local axon diameter index across the 28 samples is 4.80 ± 0.58 μm. The averaged local intra-axonal volume fraction is 0.44 ± 0.11.

8.2.2 Imaging results

The nerve imaging data is acquired using the protocols described in Figure 6.1. Voxel wise estimates of the model parameters (f_{icvf}, $d_{||}$, d_h and α) across the nerve are obtained using the tissue model and the fitting procedure described in the Methods section. Figure 8.4 shows a T_2 weighted cross-sectional image of the nerve with no diffusion weighting applied and a region of interest (ROI) used for model fitting. The red region covers the whole of the cross-sectional surface of the nerve. The green region covers the inner area of the upper fascicle of the nerve seen in Figure 8.3 to ensure no partial volume effects. We selected voxels at least one pixel

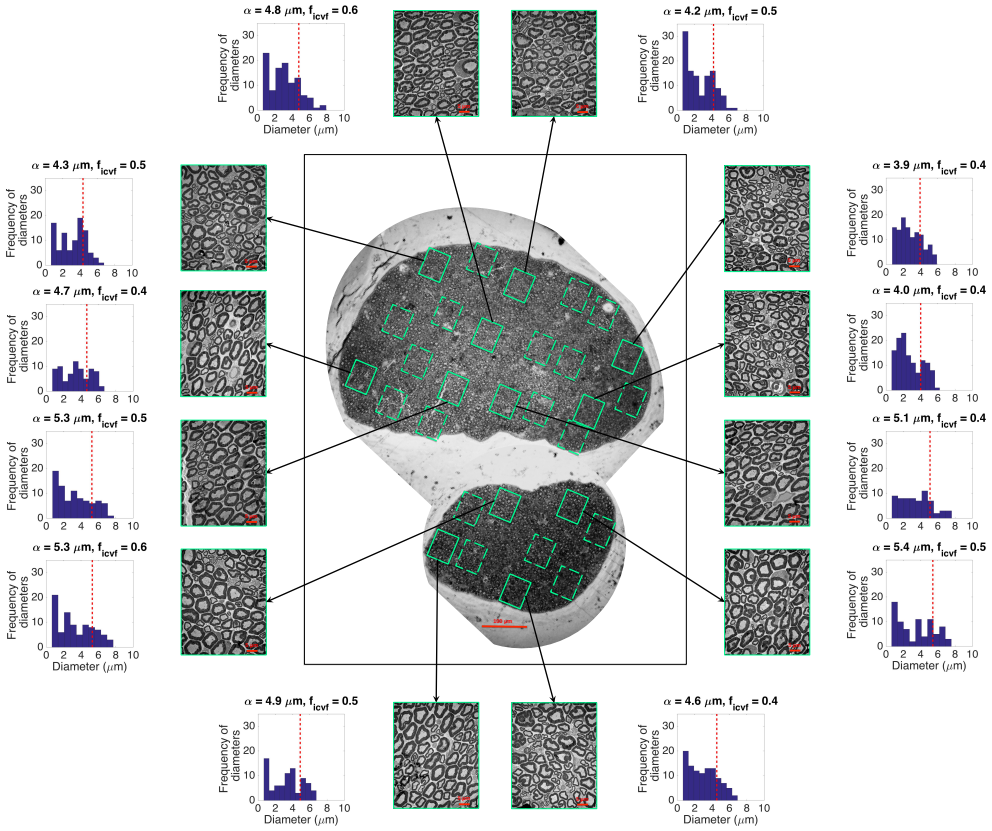

Figure 8.3: TEM image of the entire nerve tissue section taken from the nerve in the centre of the MR volume, with a scale bar = 100μm. 28 high magnification TEM images of the axons at the indicated positions within the nerve fascicles are also acquired. 12 examples of the magnified TEM images and their corresponding histograms of the axon diameter distributions (corrected for the 30% tissue shrinkage) are shown. The red bars on the high magnification TEM image indicate the scale bar = 5μm. The axon diameter index α for a given ROI is indicated as a red dashed line and the corresponding intra-axonal volume fraction is labelled on each histogram.

away from the edge of the nerve and also ensured that only voxels with FA > 0.2 and SNR > 10 are chosen. Model fitting is performed on all voxels, however, only voxels from the green region are used for the quantitative analysis.

Figure 8.5 shows a quality of fit for an example voxel in the green ROI of the nerve. Estimated model parameters are shown in the bottom right corner, the model predictions using those parameters are in dashed lines and the imaging data is marked with crosses. Similarly to the simulation results, the signal in the free diffusion direction (for $|\mathbf{n}.\mathbf{G}|/|\mathbf{G}_{max}| \rightarrow 1$) cannot be distinguished from the noise floor for b>2000s/mm^2. The model prediction shows a good fit with the measured

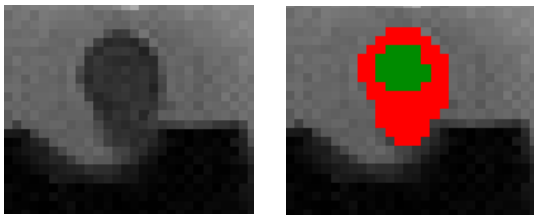

(a) (b)

Figure 8.4: (a) A T_2 weighted cross-sectional image of the nerve with no diffusion weighting applied. The black shape at the bottom of the image is the bench which the nerve is resting on. (b) Region of interest selected for the analysis. The red region covers the whole cross-sectional section of the nerve drawn on top of the b=0 image shown in (a). The green region is a selected subsection of the red region, fully within the upper fascicle, used for quantitative analysis.

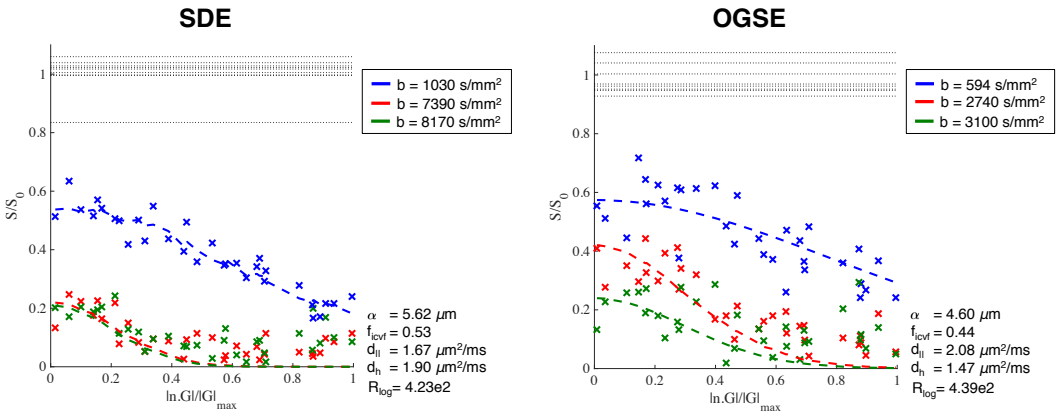

Figure 8.5: Graphs showing the model signals fitted (dashed lines) to the experimental data (data points) for an example voxel from the 32 gradient directions SDE (left) and OGSE (right) protocols. The x-axis is the absolute dot product between the gradient directions and the estimated fibre orientation. The three curves represent the model fit to each of the three measurement shells. b=594 and 3100 s/mm^2 from the OGSE protocols have oscillating waveforms. The estimated parameters (α, f_{icvf}, $d_{||}$ and d_h) and the quality of fit (R_{log}) are shown in the bottom right hand corner of each graph. The horizontal dashed lines around S/S_0=1 represent the spread in the b=0 measurements.

data both visually and quantitatively.

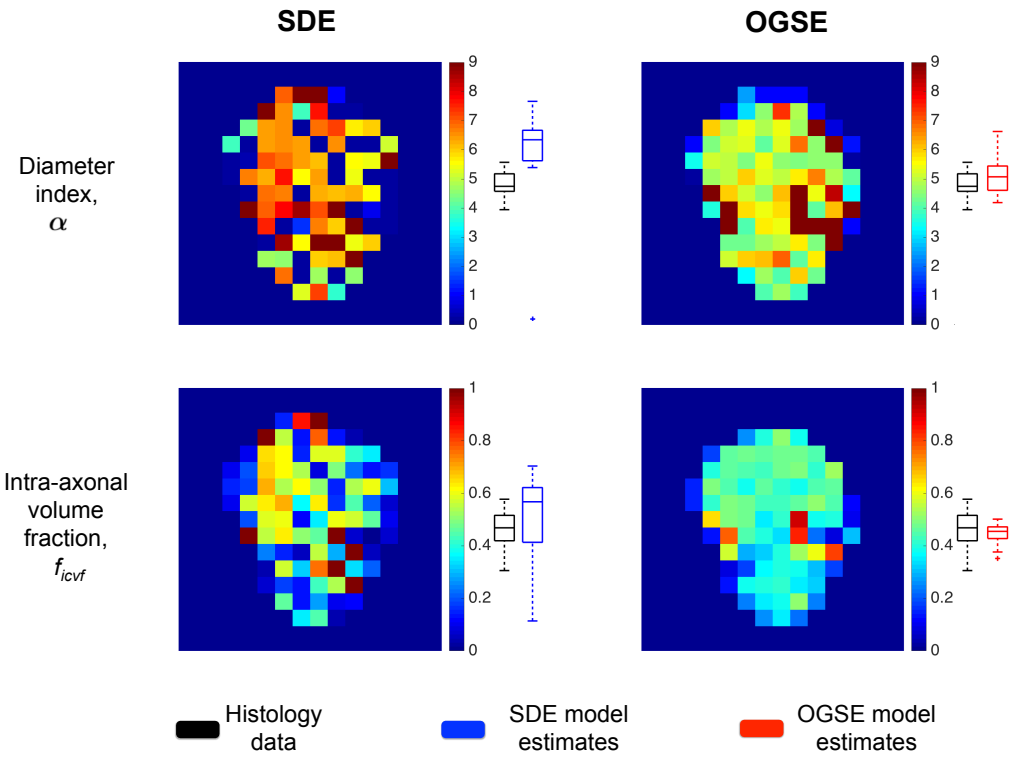

Figure 8.6: Accuracy of estimated parameters in the viable nerve experiment using the 32 direction SDE (left) and OGSE (right) protocols. Maps show the estimates for each individual voxel in the red ROI defined in Figure 8.4b). Blue crosses and red squares show the estimates from the green ROI for SDE and OGSE protocol respectively. Black circles are parameter estimates from the 28 histology regions. Axonal diameter indices in the colour bar are in μm.

Figure 8.6 shows the diameter index and intra-axonal volume fraction maps computed from the 32 gradient direction protocols. The estimated parameter values in the right (blue box plot for the SDE and red box plot for the OGSE) are from the green ROI shown in Figure 8.4. The figure shows that the SDE protocol mostly overestimates the axon diameter index compared to the histology based estimates (in black), while the OGSE protocol result is in excellent agreement with the histology. Both SDE and OGSE protocol estimates of intra-axonal volume fraction are aligned with histology, however OGSE is more tightly within the histology range while a majority of the SDE voxels are outside of that range. Estimates of diffusivity (data not shown here) show OGSE and SDE both give similar estimates of diffusivity. These results suggest that the OGSE protocol has better accuracy than

the SDE protocol, and this is also completely in line with the simulation results in Figure 7.5.

Figure 8.7 quantifies the uncertainty values of the axon diameter index (top), intra-axonal volume fraction (middle) and intrinsic diffusivity (bottom) from the green ROI in Figure 8.4b for both OGSE and SDE 32-direction protocols. The uncertainties across all parameter estimates for the SDE protocol are higher than those from OGSE protocols, which agree with the simulation results in Figure 7.6.

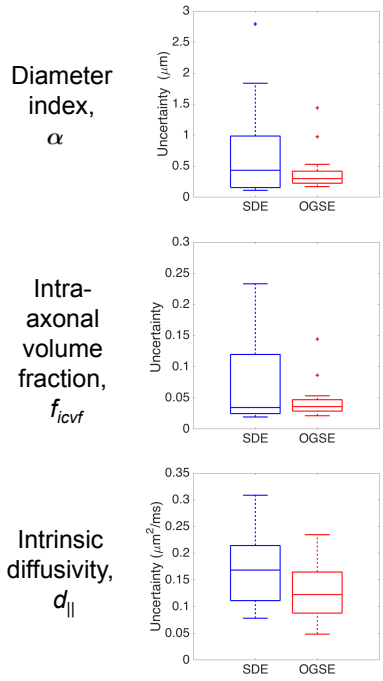

Figure 8.7: Precision of estimated parameters in viable nerve experiment using the 32 direction SDE (in blue) and OGSE (in red) protocols. Box-whisker plots of of the uncertainty calculated as the standard deviation of the posterior distribution are shown. The boxes show median, 25th and 75th percentiles of the uncertainty and the whiskers extend to the most extreme data points excluding the outliers.

Figure 8.8 quantitatively demonstrates how the parameter estimates from OGSE and SDE protocols are affected by the number of measurement directions included in the protocol. Similar to the simulation results in Figure 7.8 from Chapter 7, this figure suggests that changes in the number of measurements seem to affect the OGSE parameter estimates less than those of SDE as we move from 32 to 16 measurement directions. At 8 measurement directions both protocols begin to produce unstable parameter estimates. In the case of intrinsic diffusivity, both

OGSE and SDE provide robust estimates for all protocols (≈1.7-2.2 μm^2/ms). By comparison, the hindered diffusivity is extremely variable as we reduce the number of directions and especially for the SDE protocols.

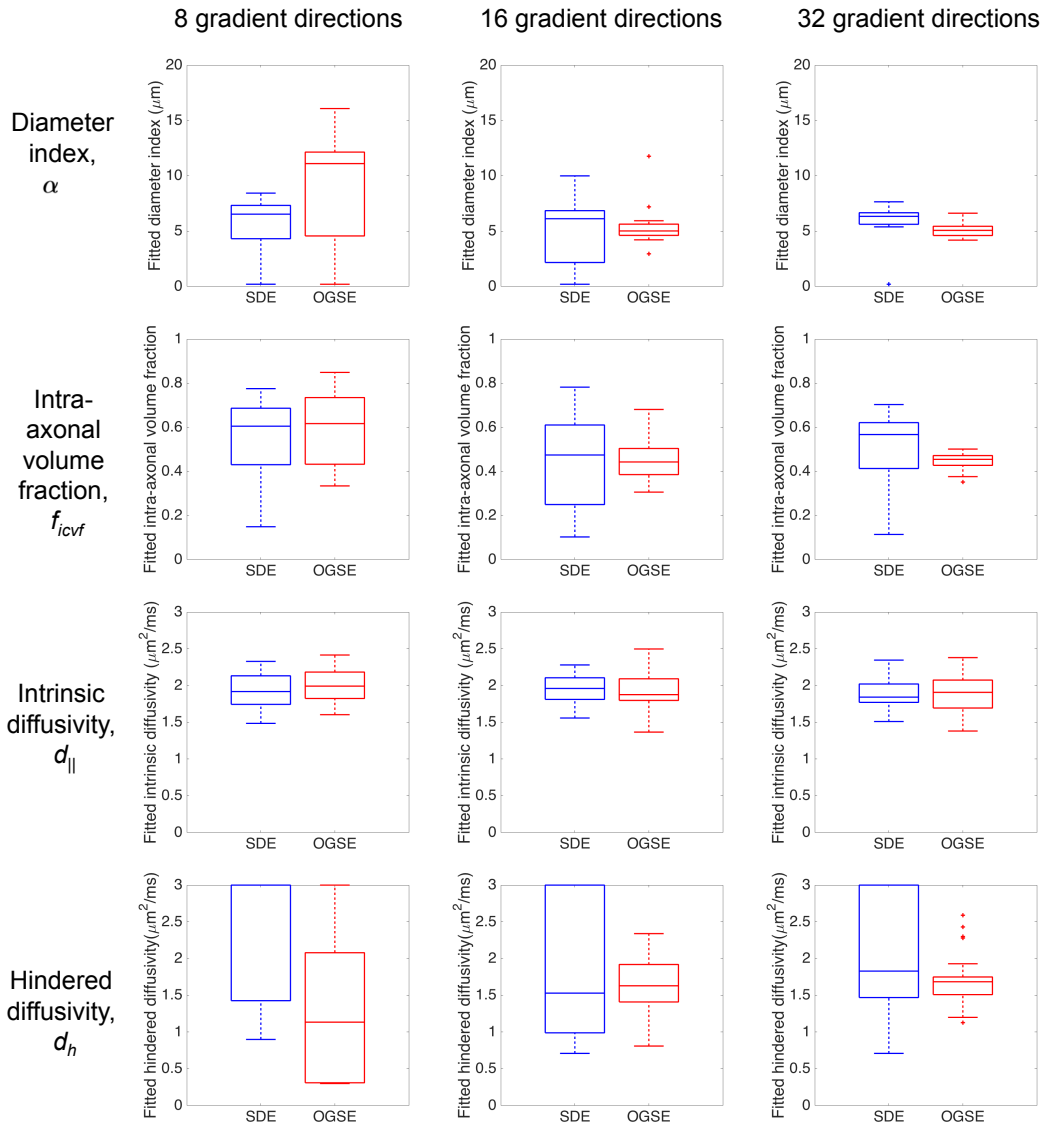

Figure 8.8: Robustness of estimated parameters in viable nerve experiments with respect to the number of gradient directions. The figure shows Box-whisker plots of the parameter estimates within the green ROI of the nerve obtained for SDE (blue) and OGSE (red) protocols. The boxes show median, 25th and 75th percentiles of the uncertainty with respect to the noise and the whiskers extend to the most extreme data points excluding the outliers.

8.3 Discussion

In this work, we have compared the performance of OGSE sequences with SDE sequences by comparing their ability to estimate axon diameters in tissue. Our work demonstrates that optimised OGSE protocols (consisting of one single lobe and two low frequency oscillating diffusion waveforms) outperform the optimised SDE protocols in a viable rat sciatic nerve. The OGSE estimates of axon diameter have a higher accuracy and a higher precision compared to those from SDE. Furthermore, OGSE estimates are more robust compared to the SDE estimates when the number of measurements available for model fitting is reduced. Finally, the OGSE estimates of axon diameter and volume fraction are in remarkable agreement with histology results. These results show for the first time, quantitatively and in an as close as possible to *in-vivo* conditions, that low-frequency OGSE improves accuracy of axon diameter mapping compared to using the standard SDE protocol.

The work from this chapter and the previous chapter (Chapter 7) show that the imaging results are in good agreement with the simulation results, which also demonstrates the nerve tissue is well represented by the synthetic substrates. Some differences were expected between the simulations and the tissue sample due to their different intrinsic diffusivity values ($d_{||}$ = 1.7 μm^2/ms in simulations and $d_{||}$ $\approx$ 2.1 μm^2/ms in tissue). The differences are observed as 10-20% drops in the signal intensities for tissue data (Figure 8.5) with respect to the synthetic data (Figure B.2 in Appendix B). Axon diameters for SDE are also more overestimated in tissue than in synthetic substrates, and this could be attributed to the differences in fitting hindered diffusivity in simulations and in tissue. However, the rest of the model estimates and the trends in the comparison between the OGSE and the SDE protocols are similar between the simulations and tissue. Furthermore, in the imaging data, the lack of signal above the noise floor at large b-values suggests an absence of the artefactual trapped water compartment that is often present in *ex vivo* experiments [101, 110], and emphasises the novelty and importance of this work in that it uses a viable nerve tissue.

Similar to simulations, the imaging results we obtain here further support the

theoretical results recently published in [24] and [123]. [24] showed numerically that in practical situations when the fibre direction is unknown and/or there is orientation dispersion, low frequency OGSE sequences are more sensitive to axon diameter than SDE. [123] confirmed this result analytically. In this study, for which we purposefully used high angular resolution diffusion imaging (HARDI) sequences to experimentally test the theory, we show that low-frequency OGSE provides more accurate estimates of axon diameter than the SDE protocol. The reasons behind this mechanism is that a low frequency OGSE provides the same sensitivity to axon diameter as a SDE sequence of the same squared gradient area, however for a much smaller b-value. Since the axon diameter in the nerve tissue is so small, in order to achieve sensitivity to it the squared gradient area needs to be extremely large. This results in an extremely large b-value for the SDE sequence, much larger than that of the OGSE. This can be seen in the optimal waveforms we obtained in Figure 6.1 in Chapter 6. Hence, the intra-axonal SDE diffusion signal in the parallel direction of the fibre diminishes and consequently reduces the total signal as well. In the case of the OGSE sequence the signal remains better preserved. This be seen both in simulations (Figure B.2 in Appendix B) and in imaging data (Figure 8.5).

In this chapter, we choose a simple model of white matter tissue. Specifically, the model uses long straight circular cylinders that mimic axon bundles and does not account for curvature of axons, dispersion or crossing fibres. However, the nerves in our tissue sample have been ligated and then stretched and tied in a taut manner onto the bench within the chamber (as in Figure 8.1), and hence we believe the effects of this simplification is minimised. Furthermore, although our model estimates hindered diffusivity d_h, which in itself is more realistic than using the simple tortuosity assumption, it assumes that d_h is not time dependent. Time dependence of d_h has been previously reported in [133] and [131], especially for our OGSE sequences which have a wider range of diffusion times (1.5-26 ms), compared to our SDE sequences (6.1-12.3 ms). However, our accurate OGSE and SDE parameter estimates in simulations and in tissue sample demonstrate that the current tissue model correctly describes the synthetic substrates, and thereby we expect the effects

of time dependency on the d_h to be minimal. Finally, we assume that the intra- and extra- axonal intrinsic diffusivity is the same and it was suggested that they are different in tissue [142]. However, as pointed out in [114], this particular assumption of separate diffusivities mainly affects our model results if the dispersion occurs in tissue, which we do not expect to see in our tissue as the nerve is stretched.

The model parameters used to optimise the protocols were not the same as the values determined here from the histology of the nerve tissue. In Appendix C, we tested the consequence of using histology based values to optimise the sequences and also tested their effects on analysing synthetic data with an intrinsic diffusivity of $d_{||} = 2.1\mu m^2/ms$ (similar to histology). We found that using histology values for the optimisation gives sequences with slightly lower b-value and more variations within protocols, however, no statistical differences in the parameter estimates are observed, especially for SDE protocols and for low intra-axonal volume fractions. The experiments were done for only one gradient strength of G=800mT/m but the conclusions of the paper are valid for any gradient strength as shown theoretically in [24] and [25].

8.4 Conclusion

In general, the results for the viable nerve tissue presented here are encouraging and are mostly supported by simulations in the previous chapter (Chapter 7). However, in reality, tissue samples are not straightened and do not appear in isolation. They are much more complex and at the simplest will contain fibre dispersion. We expect that the advantage of OGSE against SDE will hold even in such conditions as OGSE has been theoretically shown to handle fibre dispersion much better than SDE sequences [24, 25]. More importantly, our work demonstrates that OGSE gives accurate diameter estimates even when the number of directions are significantly reduced. All of this suggests that OGSE waveforms are a more suitable choice in potential future applications of axon diameter mapping.

Chapter 9

Conclusions and future work

9.1 Summary

The aim of this thesis was to test the feasibility of axon diameter imaging using diffusion MRI. The motivation of this research was to contribute towards the development of biomedical imaging techniques that are applicable to the human nervous system.

Current techniques for axon diameter imaging, such as AxCaliber [19] or ActiveAx [101] use the standard single diffusion encoding sequences which have been known to give overestimated axon diameters. Replacement of the standard SDE sequences with OGSE sequences that can probe shorter diffusion time scales, have been theoretically shown to improve sensitivity towards axon diameter [24, 123], where the improvement increases with gradient strengths. This is only true in realistic scenarios where fibre direction are unknown or when fibre dispersion exists. To date, the performance of OGSE and SDE in axon diameter imaging in practice has not yet been compared experimentally. The experiments in this thesis were therefore designed with the following objectives:

1. To design a physical phantom that represents the cylindrical geometry of axons in nerve tissue, which can be used for evaluation of the intrinsic sensitivity of sequences to pore diameters.

2. To compare the performance of OGSE and SDE sequences for measuring diameters of a range of substrates over various gradient strengths.

3. To evaluate the performance of the optimal protocols when compared to ground truth or histology.

The conclusions of the investigations are discussed below.

9.1.1 A physical phantom to geometrically represent axons

A physical phantom with microstructural features is always necessary to assess the performance of diffusion MR techniques. Chapter 4 introduced the phantoms used in this thesis, which are glass plates containing many parallel microcapillaries. The microcapillaries of each plate are of a single diameter. For instance in Chapter 4, diameters of 5, 10 and 20 μm were available and by Chapter 6, additional diameters of 2, 7 and 15 μm were purchased.

However, initial imaging experiments without a phantom holder were difficult. Phantoms were prone to motion during scans and scan times were long because every scan had to be repeated for each plate. Hence a lot of time was invested in designing a phantom holder to secure the phantoms in place and enable simultaneous scanning. Chapter 4 and Chapter 6 show two different phantom holders, which were 3D printed with the same MR invisible material. Both holders were effective for their respective scanners and this is demonstrated by the accurate estimates of micro-capillary diameter and intrinsic diffusivity in both cases.

One limitation of the work stems from the use of only single diameter microcapillaries with a single orientation. It is possible to combine multiple plates to experimentally simulate multi-diameter phantoms [144]. However, due to the inflexibility of the phantom holders to house these combinations, this was not attempted and so currently numerical simulations using the CAMINO framework is the only method of testing the performance of the diffusion sequences for substrates with multi-diameter cylinders. A potential future work here could be to design a new phantom to enable stacking of multiple plates. In terms of fibre orientation, various orientations may not be possible due to the susceptibility effects from the glass and water interface [116, 117]. The effects are only at minimum when the microcapillaries are aligned parallel to the main magnetic field, hence the positioning of plates is limited [116].

Another limitation of the work is that although microcapillaries have the benefits of clearly defined diameters, they do not have extra-axonal space. This is fine for calibrating axon diameter sequences across different MR scanners, however the method does not fully assess how the sequences may perform in tissue, where extra-axonal space is present. One main reason is that the phantoms are made up of glass and so at high magnetic field strength they may suffer from susceptibility effects. Secondly and more importantly, the extra-axonal space is absent in the phantoms used here and recently the importance of extra-axonal space in axon diameter imaging have been highlighted by [131, 133]. Therefore, to achieve a more realistic tissue microstructure phantom for testing axon diameter imaging, in the future, biomimetic phantoms [125] may be the way forward.

9.1.2 Comparison of OGSE and SDE sequences for measuring diameters of a range of substrates over various gradient strengths

Throughout the thesis, the running theme has been to compare the performance of OGSE and SDE sequences for estimating axon diameters. In Chapter 5 and Chapter 8, *ex vivo* monkey brain and a *viable* sciatic nerve tissue are used, respectively, to test the performance of the sequences under different axon diameter distributions (0-3 μm [29–31] and 1-14 μm [14, 36] respectively), diffusivities ($d_{||} \approx 0.6$ μm^2/ms and $d_{||} \approx 2.1$ μm^2/ms, respectively), intra-axonal volume fractions (f_{icvf} ≈ 0.8 and $f_{icvf} \approx 0.5$, respectively) and using different gradient strengths (G = 300 mT/m and G = 800 mT/m respectively) and number of gradient directions (60 directions and ≤ 32 directions, respectively). Additionally, in Chapter 7, different tissue models (the ActiveAx model assuming tortuosity and without tortuosity) are also tested using both OGSE and SDE sequences. Across all of these instances, OGSE sequences were more sensitive to small axon diameters than SDE sequences in both simulations and in tissue. Small angular differences between fibre orientation and gradient directions and additional dispersed fibres in tissue probably contributes towards the success of OGSE sequences in imaging small axon diameters [24, 123].

This, therefore, allows OGSE sequences to give more accurate diameter estimates.

OGSE sequences only require an extra parameter, the number of half oscillations (lobes), to achieve this additional sensitivity to small diameters that standard SDE sequences cannot provide in realistic scenarios of fibre dispersion and unknown fibre directions. On a standard clinical scanner, OGSE is very easy to use. Chapter 3 demonstrates this by implementing and validating OGSE sequences on a 3 T scanner with a maximum gradient strength of G = 62 mT/m. The OGSE sequence implementation was straightforward with no major changes to the software and the sequences were safe to use both in terms of patient and scanner hardware safety. The OGSE implementation was successful because the acquired images for gelatine phantoms (Chapter 3) and micro-capillary phantoms (Chapter 4) were free of artefacts and the OGSE sequences were able to recover the true micro-capillary diameter and intrinsic diffusivity for phantoms with microcapillaries of diameters between 10 μm and 20 μm. OGSE sequences, in general, are easy and safe to use.

9.1.3 Evaluating the performance of the optimal protocols when compared to ground truth or histology

The gradient strength and SNR limit the smallest diameter that can be detected by the OGSE sequences as with the standard SDE sequences. In a current clinical setting, where gradient strength of 60-80 mT/m and SNR=20 are typical, there is no sensitivity to axon diameters below 5 μm regardless of the type of diffusion gradient waveform used. This was experimentally demonstrated in Chapter 4 and theoretically stated by [24, 123].

Since the majority of the axons in the brain are between $0.1-3$ μm [29, 30], axon diameter mapping in the brain is mainly sensitive to the few larger axons and hence has limited use for brain tissue at current gradient strengths (Chapter 5). At G=300 mT/m, the optimal protocol, which is the OGSE protocol, still overestimates the diameters compared to histology reported in literature, however we see the low-high-low axon diameter trend across the corpus callosum which is good. The simulations for the monkey data suggest a resolution limit of approximately 2.5 μm, which agrees very well with theoretical predictions published in [24, 25].

Axons of the peripheral nervous system tend to be much larger (1-14 μm [36, 37]) than those from the CNS. At G=800 mT/m and SNR=10, when compared to histology the most optimal protocol, which is the OGSE protocol, gives an excellent match which suggests that for 800 mT/m and the sizes reported in the sciatic nerve the diameter estimates can be extremely accurate. In line with this, the simulation data reports a resolution limit between 2.5-3 μm, which agrees with the resolution limit reported in [24, 25] ($\approx$3 μm).

In both monkey and rat nerve tissue data, overestimated axon diameters occur. In simulations, over- or underestimated axon diameters exist for substrates with either small axons or large axons, respectively. A reason could be the use of the axon diameter index to describe the axon diameter distribution as a single summary statistic of the diameter distribution [101]. Overestimated axon diameter indices observed in tissue data can result from existence of small axons that are below the resolution limit and thus have negligible signal attenuation making them indistinguishable from each other, whereas larger diameters within the sample could contribute more towards the total signal attenuation causing the diameter index to be weighted towards the larger diameters [24, 25, 101]. On the other hand, when axon diameters are very large (such as those simulated in Chapter 5, Chapter 7 and in simulation studies [101, 110]), the axons cannot be detected because the diffusion time of the protocols are not long enough to probe the restriction. This upper resolution limit leads to underestimated axon diameters in substrates with large axons. Within the diameter range of the lower and upper resolution limit, the diffusion model for the extra-axonal space plays an important role in increasing the accuracy of the estimated diameter index. [131] demonstrated that the tortuosity constraint on the hindered diffusivity of the extra-axonal space biases axon diameter estimates. [143] further suggested that the tortuosity constraint makes the intra-axonal volume fraction estimates very sensitive to the intrinsic diffusivity estimates, which probably leads to the inaccuracy of intra-axonal volume fraction and diameter indices estimates. Thus by relaxing this tortuosity assumption and estimating the hindered diffusivity significantly improves axon diameter and intra-axonal volume fraction

estimates, as has been demonstrated in Chapter 7. Another more accurate method of describing the diameter distribution is the Gamma distribution, which appears frequently in biological tissues [19, 29], however a much larger number of measurements are required to approximate this distribution accurately [101]. In the future, the diameter distribution could potentially be modelled using a simpler distribution, Poisson distribution (has only one parameter), as in the recent work by [131]. However, as the simulation work presented in this thesis, as well as previous simulation work by [101], show that the volume weighted diameters are described by the estimates of axon diameter indices, it is also equally fine to use the axon diameter index to represent the underlying diameter distribution. Additional improvements to tissue models, such as considering the effects of fibre undulation [112] and dispersion [111], as well as incorporating further effects of modelling the extra-axonal space such as the time dependency of the diffusivities [131, 133, 134], could also increase the axon diameter accuracy; hence is definitely for future work.

9.2 Future work

There are some general future directions that could further improve on the contributions made in this thesis to improve the accuracy of axon diameter estimates using diffusion MRI.

9.2.1 Tissue models

In this thesis, the multi-compartment tissue models assume hindered diffusion in the extra-axonal space. More recently, the diffusivity in the extra-axonal space has been shown to be dependent on diffusion time [133, 134, 145] and so only affects models when diffusion measurements are acquired at different diffusion times. The time dependency model effectively creates multiple 3D Gaussian displacement distributions which is dependent on the geometry of the substrates. This has been shown to significantly improve axon diameter estimates in synthetic substrates and in tissue [131, 133]. Low frequency OGSE sequences provides diffusivity in *ex vivo* brain that is linearly dependent on their frequency, whereas standard SDE sequences are not as much affected because pronounced time dependency is only observed at dif-

fusion times larger than 100 ms [131, 133]. This also suggests that when using SDE sequences at very low intra-axonal volume fractions such as those in the rat sciatic nerve, time dependence of the diffusion in the extra-axonal space is not a limitation. However, in the brain, where intra-axonal volume fractions are high, or when OGSE sequences are being used, modelling the time dependence may be essential for improving the accuracy of diameter estimates.

The above time dependence of diffusivity occurs perpendicular to the main orientation of the axon. Time dependence of diffusivity (both intra- and extra-axonal) parallel to the main axon orientation have been demonstrated by [134] in *in vivo* white matter. It has been suggested that undulations of axon can cause this time dependence and can potentially cause overestimated axon diameters [112]. Therefore another factor in improving axon diameter estimates could be to incorporate the time dependence along the axon length.

Lastly, dispersed axons are prevalent in the nervous system. [111] demonstrated that if dispersion is not accounted for in modelling, axons that otherwise are oblique to the assumed single axon orientation will have a larger cross section than in reality, which can lead to overestimate diameters. Hence accounting for dispersion can potentially further improve axon diameter estimates. However, the number of model parameters and in turn the number of measurements would increase if dispersion is also accounted for.

One potential for future work could be to invest in implementing a tissue model for OGSE sequences that accounts for majority of these factors affecting diameter accuracy. A large dataset (similar to [114]) could then be used to compute model parameter estimates. However, tolerable scan times for humans, stability of the tissue model and acquisition of histology for validation are few of the challenges that would need to be tackled.

9.2.2 Optimisation

Our current work uses optimised sequences to maximise sensitivity towards the tissue model parameters of the samples of interest. It is otherwise difficult to decide the range of sequence parameters that are sensitive to the model parameters and at

the same time ensure that the number of sequences do not cause scan times to be exceedingly long. However, to date, the optimisation itself has not been validated thoroughly, especially the noise model used and the effect it has on the sequence parameters. A potential and interesting idea for future work would be to explore the whole range of sequence parameters space and to test whether the optimised sequences for this particular case agree with the empirically optimised sequences. Preliminary optimisation of sequences for water-filled microcapillaries with single diameters of 10 and 20 μm with the assumption of unknown fibre orientation, long T2 (70ms) and 30 gradient directions at G = 60mT/m outputs N = 4 as the number of lobes for the optimal OGSE sequences with TE = 120ms. This is in agreement with the empirically optimised OGSE sequences from Chapter 4, where the optimal number of lobes are N $\in \{3,4\}$.

9.2.3 Diffusion sequences

Trapezoidal OGSE sequences with a sine profile have been used throughout this thesis. Our method of estimating axon diameters involve directly fitting the analytical signal from the biophysical model to the measured signal. We use a number of gradient directions to determine fibre orientation and using this further determine the diffusivity parallel to the fibre orientation (i.e the intrinsic diffusivity). In the presence of straight cylinders, our OGSE sequences with sine profile should estimate the true diffusivity of the substrate. However, in the presence of dispersed or undulated fibres, the apparent diffusivity would be probed. In this case, it may be necessary to use trapezoidal OGSE sequences with a cosine profile which would give a more accurate diffusivity estimate for a given frequency than OGSE sequences with sine profiles. Furthermore, cosine waveforms also have higher b value than their sine counterparts, which is an additional benefit in imaging biological tissue, as this would lead to reduced TE, and hence higher SNR.

Recently, ActiveAx optimisation of apodized cosine waveforms have been made available. Therefore it would be very interesting to carry out experiments, for instance on a monkey brain, to show the effect of using these waveforms on the accuracy of axon diameter estimates.

9.2.4 Validation

Validation is important for the development of imaging techniques, which in our case would involve new sequences and new tissue models. The current simulations and phantoms are too simple to assess the complex tissue models suggested in Section 9.2.1. Experimental validation of the tissue models therefore would require more realistic substrates such as numerical simulations considering fibre complexities [146], biomimetic phantoms [125] and viable tissues (similar to Chapter 8) with histology.

9.2.5 Applications

9.2.5.1 Central nervous system

Majority of the axons in the brain (0.1-3μm [6, 29]) tend to be much smaller than those found within peripheral nerves (1-14 μm [14, 36]). At current clinical gradient strengths of 60-80 mT/m, the diameter resolution is not enough to measure these white matter axons in the central nervous system. Even at the highest gradient strength used for human imaging (G = 300 mT/m on the MGH *Connectom* scanner [90, 91]), where the diameter resolution is around 3 μm, only $<$1% of the fibre population in the brain may be captured at this gradient strength. Imaging the large axons on its own can have benefits for monitoring some diseases, such as ageing [7], where the large axons shrink and where the careful interpretation of the axon diameter index could still provide a useful biomarker.

Axon diameters in the spinal cord are much larger (1-10 μm [32, 33]) and here axon diameter imaging can open doors to clinical applications in diseases such as amyotrophic lateral sclerosis (ALS) [147]. Additionally, preclinical settings with gradient strengths greater than 300 mT/m can still be used to understand the structure and function of the brain from animal models. At such high gradient strengths, OGSE sequences are theoretically superior to SDE sequences for estimating axon diameters. Hence accurate axon diameter mapping in *viable* or *ex vivo* brain is another one of the many applications for axon diameter imaging in the central nervous system.

9.2.5.2 Peripheral nervous system

The translation of axon diameter imaging using diffusion MRI to a clinical environment setting for imaging peripheral nerves is an intriguing possibility. Axon diameter sizes of 1-14 μm in PNS make axon diameter imaging possible even using clinical strength scanners. Recent studies have demonstrated that DTI using SDE sequences of the human peripheral nerves *in vivo* [148, 149] is possible and this can be easily and safely extended to OGSE sequences as shown in Chapter 3.

One of the most promising areas for applications in peripheral nervous system is imaging nerve regeneration after injury. Nerve regeneration in the PNS plays a key role in returning limb function after injury. Microstructural changes involved, such as changes in density, orientation and size of the axons determine surgery outcomes and recovery. However, in current clinical practice the assessment techniques remain crude: they are subjective and inaccurate (Tinels sign), or are invasive. Axon diameter techniques developed here could provide quantitative, objective and non-invasive measures of extent and quality of neuronal growth.

Appendix A

Comparison of CAMINO codes

This section aims to validate the differences in our SDE simulation results from Chapter 5 with the previous SDE simulation studies [110]. Figure A.1 compares the estimated axon diameter index across two instances. (1) Diameter index estimates for simulated substrates generated using SDE protocols from [110] and the *previous* version of CAMINO and (2) diameter index estimates for simulated substrates generated using SDE protocols from [110] and the *current* version of CAMINO.

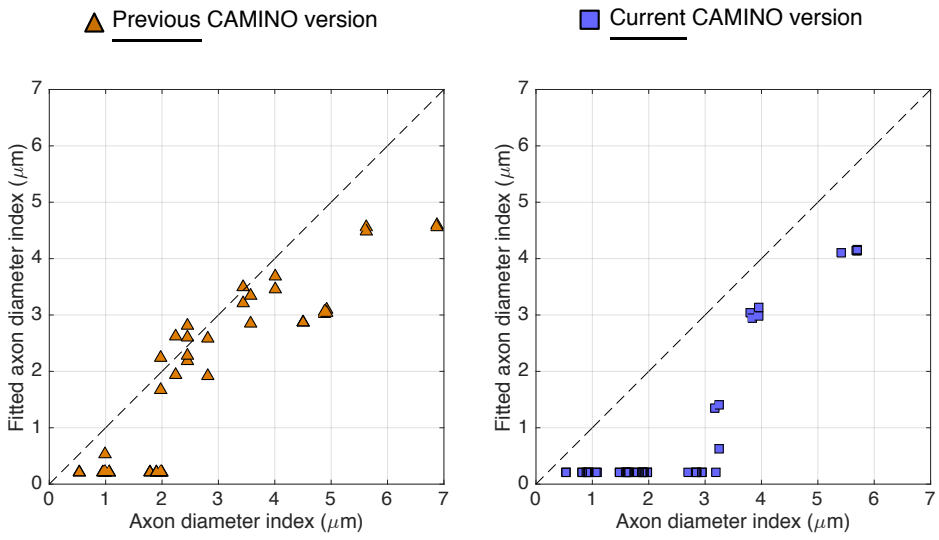

Figure A.1: Graphs show the axon diameter index estimates plotted against the true axon diameter indices across two instances: (1) estimates for simulated substrates generated using SDE protocols from [110] and the previous version of CAMINO and (2) estimates for simulated substrates generated using SDE protocols from [110] and the current version of CAMINO. The same two-parameter gamma-distributions are used to simulate all voxels for all cases.

Figure A.1 demonstrates that there are large differences between the estimates

obtained from the previous (on the left) and current (on the right) CAMINO versions, especially at or below 3μm. As expected, the previous CAMINO version diameter estimates (on the left of Figure A.1) and the diameter estimates from [110] are in good agreement with each other. The current CAMINO version diameter estimates (on the right of Figure A.1) and the SDE diameter estimates from Figure 5.3 in Chapter 5 also agree with each other.

The changes in the results between the previous and current CAMINO versions are expected because the CAMINO simulation code has improved over the years to allow for better sampling of the parametrized gamma distributions. In the current version, there is a higher number of small-diameter cylinders that are allowed and therefore the changes are seen as lower axon diameter index and lower intra-axonal volume fractions in the current CAMINO version. This is observed in Figure A.2, Figure A.3 and Figure A.4 for the same number of cylinders packed into the same voxel size.

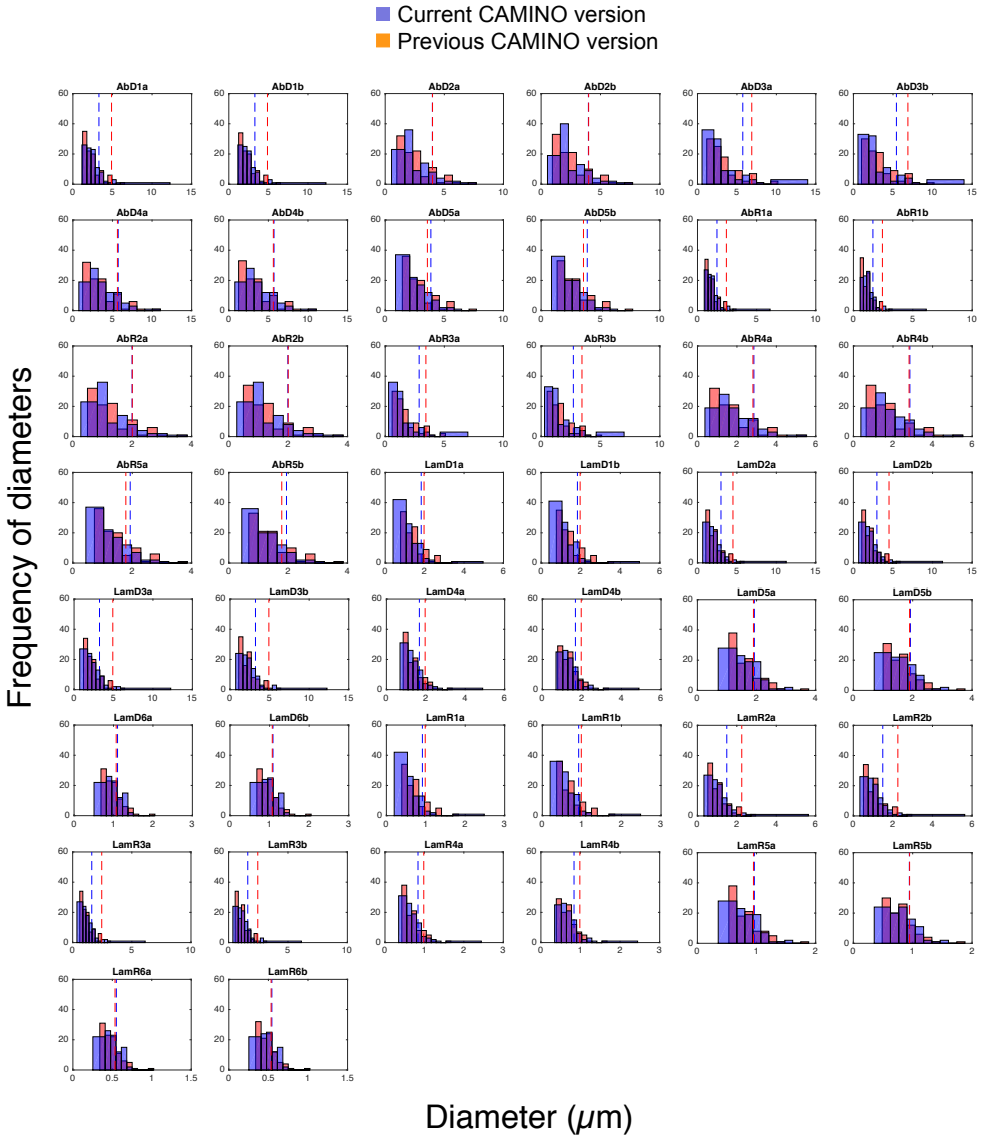

Figure A.2: Histograms of the axonal diameter distributions across the corpus callosum for an *ex vivo* human brain and for an *ex vivo* monkey brain generated using the previous (orange) and current (blue) version of CAMINO simulation framework. There are 44 substrates in total. The axon diameter index are indicated as dashed lines. Note that the diameter scale varies across all histograms.

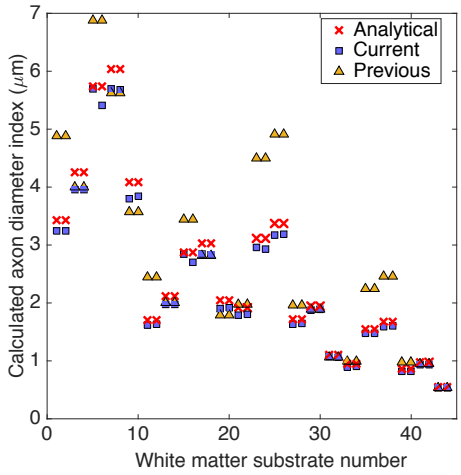

Figure A.3: Computed diameter indices of the 44 white matter substrates generated using the analytical expression for gamma probability distribution function (red crosses), the previous version of CAMINO (orange triangles) and current version of CAMINO (blue squares). The red crosses (analytical diameter index) and the blue squares (diameter index from current version of CAMINO) are near each other across majority of the substrates.

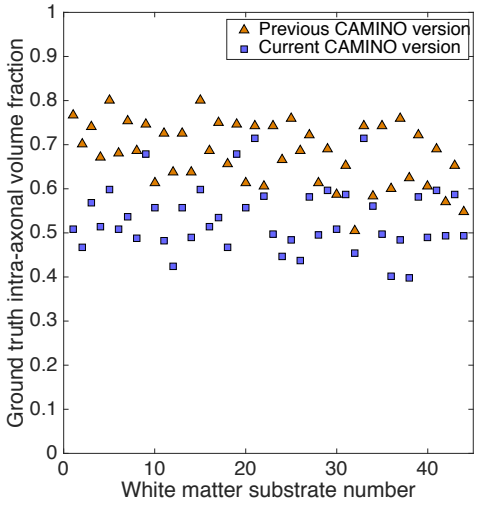

Figure A.4: The ground truth intra-axonal volume fraction of the 44 white matter substrates generated using the previous version of CAMINO (orange triangles) and current version of CAMINO (blue squares).

Appendix B

Signal fits for synthetic substrates using the standard and new model

The fitted signal for two example substrates for the 32 gradient direction SDE and OGSE protocols are displayed in Figure B.1 and Figure B.2 for the standard model (assumes tortuosity) and the new model (does not assume tortuosity), respectively. The signal fits here are for the noisy data with SNR=10, in contrast to Figure 7.9 which is for SNR = ∞. As expected, both figures show that the substrate with the small diameter index (α = 2.70 μm) shows lower attenuation than the substrate with the larger diameter index (α = 4.37 μm). The figures also show a good match between the raw signal and the fitted signal.

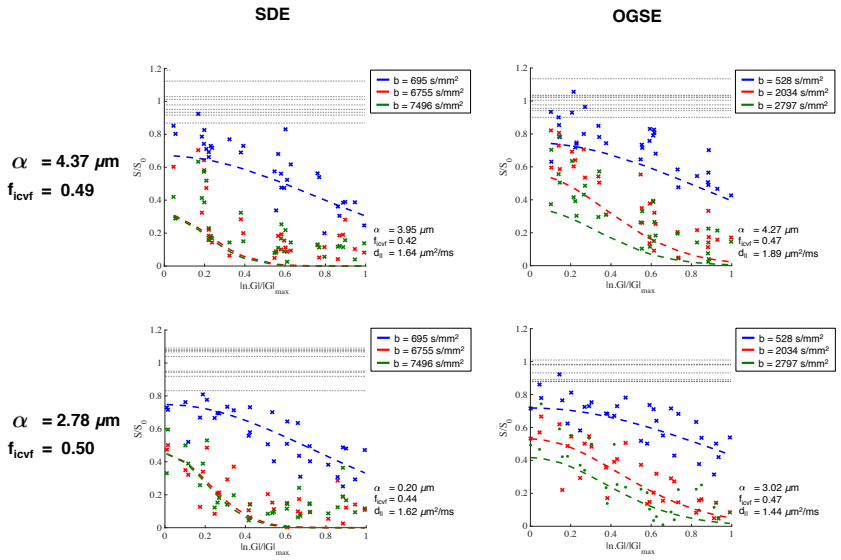

Figure B.1: Graphs showing the signals of the standard tissue model fitted (dashed lines) to the simulated data (data points) for two example substrates (α = 4.37 μm, top row, and α = 2.78 μm, bottom row, with f_{icvf} = 0.5) from the 32 gradient directions SDE (left column) and OGSE (right column) protocols. The x-axis is the absolute dot product between the gradient directions and the estimated fibre orientation. The three curves represent the model fit to each of the three measurement shells. b=528 and 2797 s/mm^2 from the OGSE protocols have oscillating waveforms. The estimated parameters are shown in the bottom right hand corner of each graph. The horizontal dashed lines around S/S_0=1 represent the spread in the b=0 measurements.

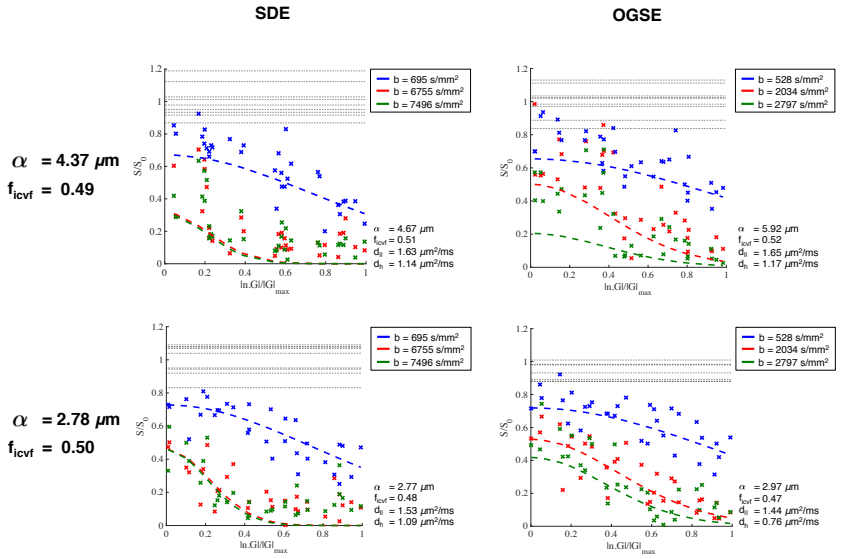

Figure B.2: Graphs showing the signals of the new tissue model fitted (dashed lines) to the simulated data (data points) for two example substrates (α = 4.37 μm, top row, and α = 2.78 μm, bottom row, with f_{icvf} = 0.5) from the 32 gradient directions SDE (left column) and OGSE (right column) protocols. Same caption as Figure B.1 applies here.

Appendix C

Optimisation for rat sciatic nerve using histology results

This section tests the effects of using the rat sciatic nerve histology results from Chapter 8 to re-optimise the 32 gradient directions OGSE and SDE sequences. Here we carry out simulation experiments to test the accuracy of parameter estimates using the newly optimised protocols and compare them to the simulation results in Chapter 7.

C.1 Methods

C.1.1 Tissue model

The standard tissue model from Chapter 7, Section 7.2.1 is used for optimisation and the new tissue model is used for model fitting.

C.1.2 Optimisation

The same optimisation procedure as in Chapter 6, Section 6.2.2 is used. The exceptions are the new *a priori* tissue model parameter settings, which are now based on the histology results from Chapter 8: f_{icvf}=0.46 (median intra-axonal volume fraction), $d_{||}$ = 2.1 μm^2/ms (median diffusivity from the 32 gradient direction OGSE protocols), d_h = 0.68 [109] and axon diameter indices of 3.9, 4.7 and 5.5 μm (the minimum, median and maximum axon diameter index from histology).

C.1.3 Synthetic substrates

Synthetic substrates with multi-diameter cylinders from Chapter 7 with $f_{icvf} \in \{0.4, 0.6\}$ are generated using the Monte-Carlo diffusion simulations via the CAMINO framework. All simulation settings are the same as in Chapter 7, Section 7.2.2.2 except for the intrinsic diffusivity, which is fixed at $d_{||}$ of 2.1 μm^2/ms to match the *a priori* value.

C.1.4 Model fitting

The voxel-wise model fitting procedure from Chapter 7 Section 7.2.3, involving diffusion tensor, grid search and active-set algorithm is used to compute the tissue model parameter estimates (f_{icvf}, $d_{||}$, d_h and α) of the synthetic substrates.

C.2 Results and discussion

Figure C.1 shows the optimised 32 gradient directions OGSE and SDE protocols. The OGSE protocol has a lower frequency than the previous version in Figure 6.1 from Chapter 6 because the sequence optimisation is now for slightly larger diameters (diameters between 3.9-5.5 μm instead of the previous 2.3-6.7 μm). In the SDE protocol, lower b-value sequences occurs than in Figure 6.1 from Chapter 6.

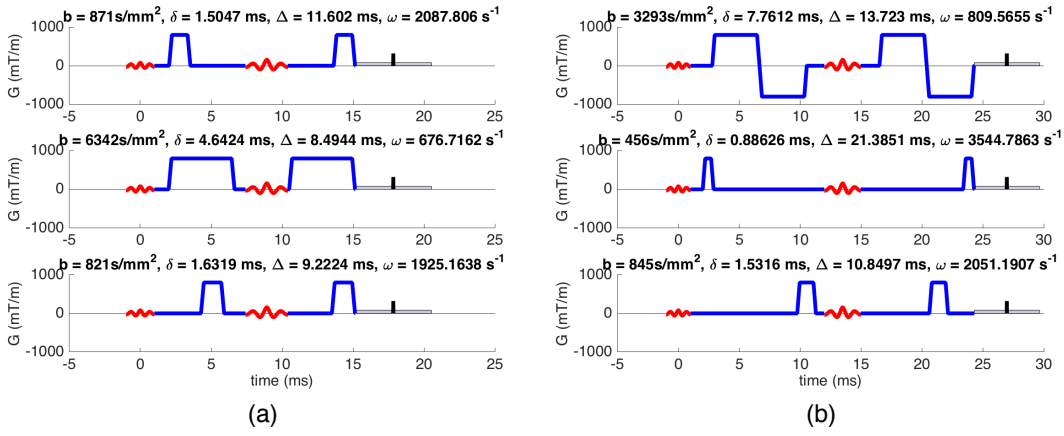

Figure C.1: Optimised 32 gradient directions protocols for (a) SDE and (b) OGSE using the histology axon diameter index, intra-axonal volume fraction and intrinsic diffusivity as *a priori* parameters.

Figure C.2 shows the fitted parameter estimates for the synthetic substrates. OGSE diameter estimates appear more accurate and precise than for the SDE pro-

tocol at $f_{icvf} = 0.4$. At $f_{icvf} = 0.6$, both OGSE and SDE diameter estimates fluctuate similarly in accuracy but OGSE still shows higher precision for diameter estimates across all diameters. In terms of intra-axonal volume fraction and intrinsic diffusivity, both OGSE and SDE show equal accuracy and precision.

The comparison between the newly analysed results from this section and the original simulations results in Figure 7.5 shows that at low f_{icvf} ($f_{icvf} = 0.4$), both OGSE and SDE do not show significant differences in diameter and intra-axonal volume fraction estimates. At $f_{icvf} = 0.6$, differences in accuracy of parameter estimates start to emerge for OGSE - the newly optimised OGSE waveforms tend to give slightly overestimated diameters than for original protocol. For SDE, at $f_{icvf} = 0.6$, the uncertainty of the parameter estimates increase, which is indicated by the large interquartile range in Figure C.2. Higher diffusivity of the new synthetic substrates and optimisation of protocols for larger diameters and higher diffusivity potentially causes the newly optimised protocols to be less sensitive towards small diameters. This can result in the loss of accuracy and precision for OGSE and SDE, respectively, for substrates with small axon diameter indices.

Overall, this section demonstrates that even when the sequences are optimised using the histology results, OGSE performs more accurately and precisely than SDE sequences for diameter estimation.

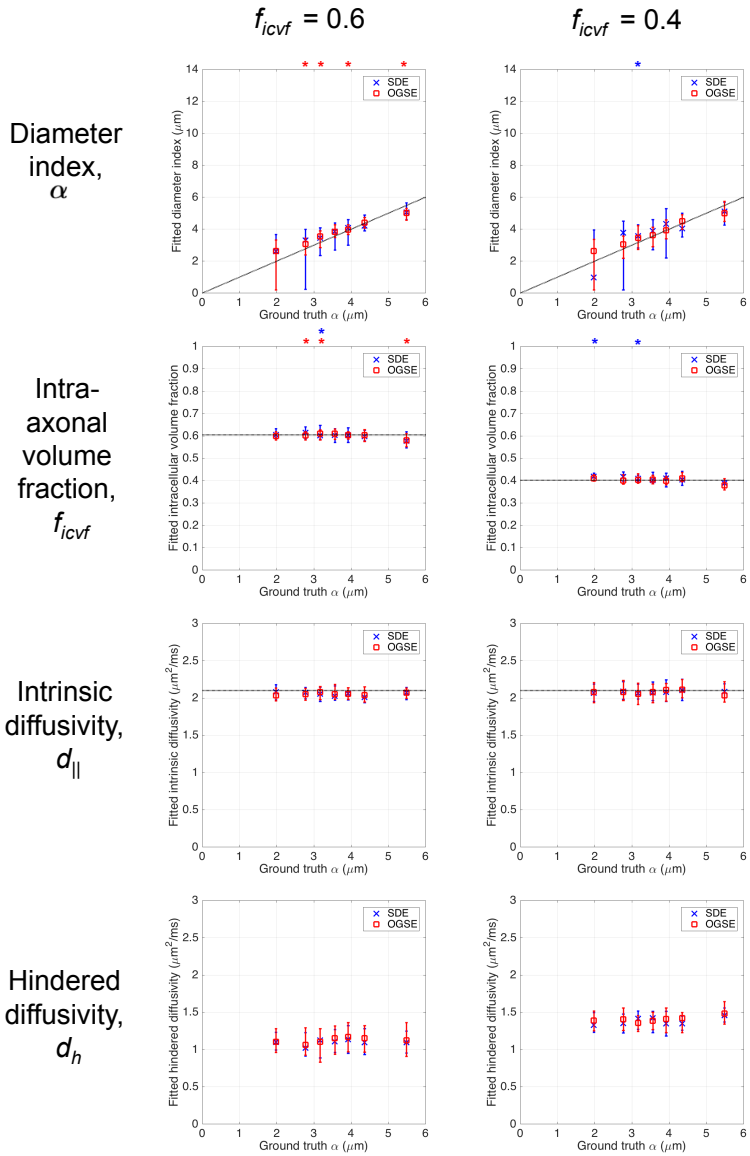

Figure C.2: Accuracy of estimated model parameters in simulation experiments: axon diameter index (1st row), intra-axonal volume fraction (2nd row) and intrinsic diffusivity (3rd row) for intra-axonal volume fractions of 0.6 and 0.4. The median, 25th and 75th percentile of the estimates across 50 different instances of random Rician noise (SNR=10), are shown for each diameter index, with SDE median estimates in blue crosses and OGSE median estimates in red squares. The identity lines are shown in black. The * above the ground truth α indicate significant difference between estimates of the newly optimised protocol and the original protocol. Red * is for SDE and blue * is for OGSE.

Bibliography

[1] J B Hursh. Conduction velocity and diameter of nerve fibers. *Amercan Journal of Physiology*, 127:131–139, 1939.

[2] J M Ritchie. On the relation between fibre diameter and conduction velocity in myelinated nerve fibres. *Proceedings of the Royal Society of London. Series B, Biological Sciences*, 217(1206):29–35, 1982.

[3] F Aboitiz, J Lopez, and J Montiel. Long distance communication in the human brain: timing constraints for inter-hemispheric synchrony and the origin of brain lateralization. *Biological Research*, 36(101):89–99, 2003.

[4] H Johansen-Berg and T E J Behrens. *Diffusion MRI: From quantitative measurement to in-vivo neuroanatomy*. Academic Press, 1 edition, 2009.

[5] C Hildebrand, S Remahl, H Persson, and C Bjartmar. Myelinated nerve fibres in the CNS. *Progress in Neurobiology*, 40:319–384, 1993.

[6] G Lovas, N Szilagyi, K Majtenyi, M Palkovits, and S Komoly. Axonal changes in chronic demyelinated cervical spinal cord plaques. *Brain*, 123:308–317, 2000.

[7] L Marner, J R Nyengaard, Y Tang Y, and B Pakkenberg. Marked loss of myelinated nerve fibers in the human brain with age. *Journal of Computational Neuroscience*, 462(2):144–152, 2003.

[8] S Sasaki and S Maruyama. Increase in diameter of the axonal initial segment is an early change in amyotrophic lateral sclerosis. *Journal of Neurological Science*, 110:114–120, 1992.

[9] S Cluskey and D B Ramsden. Mechanisms of neurodegeneration in amyotrophic lateral sclerosis. *Molecular Pathology*, 54(6):386, 2001.

[10] P L Randall. Schizophrenia, abnormal connection, and brain evolution. *Medical Hypotheses*, 10(3):247–280, 1983.

[11] D Rice and S Barone Jr. Critical periods of vulnerability for the developing nervous system: evidence from humans and animal models. *Environmental Health Perspectives*, 108(Suppl 3):511, 2000.

[12] J Piven, J Bailey, B J Ranson, and S Arndt. An MRI study of the corpus callosum in autism. *American Journal of Psychiatry*, 154(8):1051, 1997.

[13] B Zikopoulos and H Barbas. Changes in prefrontal axons may disrupt the network in autism. *Journal Of Neuroscience*, 30(44):14595–14609, 2010.

[14] F K Sanders. The thickness of the myelin sheaths of normal and regenerating peripheral nerve fibres. *Proceedings of the Royal Society of London. Series B, Biological Sciences*, 135(880):323–357, 1948.

[15] M Ikeda and Y Oka. The relationship between nerve conduction velocity and fiber morphology during peripheral nerve regeneration. *Brain and Behavior*, 2:382–390, 2012.

[16] H H Ong and F W Wehrli. Quantifying axon diameter and intra-cellular volume fraction in excised mouse spinal cord with q-space imaging. *NeuroImage*, 51:1360–1366, 2010.

[17] M E Komlosh, E Özarslan, M J Lizak, F Horkay, V Schram, N Shemesh, Y Cohen, and P J Basser. Pore diameter mapping using double pulsed-field gradient MRI and its validation using a novel glass capillary array phantom. *Journal of Magnetic Resonance*, 208:128–135, 2011.

[18] M E Komlosh, E Özarslan, M J Lizak, I Horkayne-Szakaly, R Z Freidlin, F Horkay, and P J Basser. Mapping average axon diameters in porcine spinal

cord white matter and rat corpus callosum using d-PFG MRI. *NeuroImage*, 78:210–216, 2013.

[19] Y Assaf, T Blumenfeld-Katzir, Y Yovel, and P J Basser. AxCaliber: a method for measuring axon diameter distribution from diffusion MRI. *Magnetic Resonance in Medicine*, 59(6):1347–1354, 2008.

[20] D C Alexander. A general framework for experiment design in diffusion MRI and its application in measuring direct tissue-microstructure features. *Magnetic Resonance in Medicine*, 60(2):439–448, 2008.

[21] S N Jespersen. Equivalence of double and single wave vector diffusion contrast at low diffusion weighting. *NMR in Biomedicine*, 25:813–818, 2012.

[22] S N Jespersen, H Lundell, C K Sonderby, and T B Dyrby. Commentary on microanisotropy imaging: quantification of microscopic diffusion anisotropy and orientation of order parameter by diffusion MRI with magic-angle spinning of the q-vector. *Magnetic Resonance Imaging*, 31(9):1643–1644, 2013.

[23] E C Parsons, M D Does, and J C Gore. Temporal diffusion spectroscopy: Theory and implementation in restricted systems using oscillating gradients. *Magnetic Resonance in Medicine*, 55:75–84, 2006.

[24] I Drobnjak, H Zhang, A Ianus, E Kaden, and D C Alexander. PGSE, OGSE, and sensitivity to axon diameter in diffusion MRI: Insight from a simulation study. *Magnetic Resonance in Medicine*, 75:688–700, 2016.

[25] M Nilsson, S Lasic, I Drobnjak, D Topgaard, and C F Westin. Resolution limit of cylinder diameter estimation by diffusion MRI: The impact of gradient waveform and orientation dispersion. *NMR in Biomedicine*, pages e3711–n/a, 2017.

[26] Antranik. Conduction of the action potential along the nerve fiber, 2012.

[27] T W Vanderah and D Gould. *Noltes The Human Brain: An Introduction to its Functional Anatomy*. Elsevier Inc, 7 edition, 2016.

[28] J Hubbard. The peripheral nervous system.

[29] F Aboitiz, A B Scheibel, R S Fisher, and E Zaidel. Fiber composition of the human corpus callosum. *Brain Research*, 598(100):143–153, 1992.

[30] G M Innocenti, A Vercelli, and R Caminiti. The diameter of cortical axons depends both on the area of origin and target. *Cerebral Cortex*, 24(8):2178–2188, 2014.

[31] G M Innocenti, R Caminiti, and F Aboitiz. Comments on the paper by Horowitz et al. *Brain Structure and Function*, 220(3):1789–1780, 2014.

[32] S G Waxman, J D Kocsis, and P K Stys. *The Axon: Structure, Function, and Pathophysiology*. Oxford University Press, 7 edition, 1995.

[33] H Y Ko, J H Park, Y B Shin, and S Y Baek. Gross quantitative measurements of spinal cord segments in human. *Nature*, 42:35–40, 2004.

[34] G L Morgan. *Regional variation models of white matter microstructure*. University College of London, 1 edition, 2012. PhD Thesis.

[35] D S Butler and J Matheson. *The Sensitive Nervous System*. Noigroup Publications, 2000.

[36] J M Jacobs and S Love. *Qualitative and quantitative morphology of human rural nerve at different ages*, volume 108. 1985.

[37] J M Schroder, J Bohl, and K Brodda. Changes of the ratio between myelin thickness and axon diameter in the human developing sural nerve. *Journal of Neurological Science*, 76(5):114–120, 1988.

[38] S Hofer and J Frahm. Topography of the human corpus callosum revisited comprehensive fiber tractography using diffusion tensor magnetic resonance imaging. *NeuroImage*, 32:989–994, 2006.

[39] A S LaMantia and P Rakic. Cytological and quantitative characteristics of four cerebral commissures in the rhesus monkey. *The Journal Of Comparative Neurology*, 291:520–537, 1990.

[40] D Burke. The properties of axons differ according to their function. *Journal of Physiology*, 578(1):1–2, 2007.

[41] H J Seddon. Three types of nerve injury. *Brain*, 66(4):237–288, 1943.

[42] P.M. Richardson. Peripheral nerve regeneration: An overview. In L R Squire, editor, *Encyclopedia of Neuroscience*, pages 557 – 560. Academic Press, Oxford, 2009.

[43] V E Johnson, W Stewart, and D H Smith. Axonal pathology in traumatic brain injury. *Experimental Neurology*, 246:35–43, 2013.

[44] A Chhabra, S Ahlawat, A Belzberg, and G Andreseik. Peripheral nerve injury grading simplified on MR neurography: As referenced to seddon and sunderland classifications. *The Indian Journal of Radiology & Imaging*, 24(3):217–224, 2014.

[45] R Caminiti, H Ghaziri, R Galuske, P R Hof, and G M Innocenti. Evolution amplified processing with temporally dispersed slow neuronal connectivity in primates. *Proceedings of the National Academy of Sciences of the United States of America*, 106(46):19511–19556, 2009.

[46] G J Stanisz, A Szafer, G A Wright, and R M Henkelman. An analytical model of restricted diffusion in bovine optic nerve. *Magnetic Resonance in Medicine*, 37(1):103–111, 1997.

[47] K Shmueli. Theory of MRI. In *Imaging with non-ionising radiation: Magnetic Resonance Imaging and Ultrasound MSc Lecture series*. University College London, London, 2013.

[48] D W McRobbie, E A Moore, M J Graves, and M R Prince. *MRI from Picture to Proton*. Cambridge University Press, 2 edition, 2006.

[49] E M Haacke, R W Brown, M R Thompson, and R Venkatesan. *Magnetic Resonance Imaging: Physical Principles and Sequence Design*. John Wiley and Sons, 1 edition, 1999.

[50] G J Stanisz, R Midha, C A Munro, and R M Henkelman. Mr properties of rat sciatic nerve following trauma. *Magnetic Resonance in Medicine*, 45:415–420, 2001.

[51] R J Gillies. *NMR In Physiology and Biomedicine*. Academic Press, 1994.

[52] U Ferizi. *Compartment models and model selection for in vivo diffusion MRI of human brain white matter*. University College London, 1 edition, 2014. PhD Thesis.

[53] A Savickas. Advanced diffusion mri for microstructure imaging: Theoretical developments. 2016. PhD Thesis.

[54] D K Jones. *Diffusion MRI: Theory, Methods, and Applications*. Oxford University Press, 2010.

[55] J Stepisnik. Time-dependent self-diffusion by NMR spin-echo. *Physica*, 183B:343–350, 1993.

[56] D J McHugh. *The effect of tumour microstructure on diffusion-weighted MRI measurements*. University of Manchester, 1 edition, 2014. PhD Thesis.

[57] N Shemesh, E Özarslan, P J Basser, and Y Cohen. Measuring small compartmental dimensions with low-q angular double-PGSE NMR: The effect of experimental parameters on signal decay. *Journal of Magnetic Resonance*, 198(1):15–23, 2009.

[58] J D Clayden, Z Nagy, N Weiskopf, D C Alexander, and C A Clark. Microstructural parameter estimation in vivo using diffusion MRI and structured prior information. *Magnetic Resonance in Medicine*, 75(4):1787–1796, 2016.

[59] I Drobnjak, B Siow, and D C Alexander. Optimizing gradient waveforms for microstructure sensitivity in diffusion-weighted MR. *Journal of Magnetic Resonance*, 206:41–51, 2010.

[60] I Drobnjak and D C Alexander. Optimising time-varying gradient orientation for microstructure sensitivity in diffusion-weighted MR. *Journal of Magnetic Resonance*, 212:344–354, 2011.

[61] M D Does, E C Parsons, and J C Gore. Oscillating gradient measurements of water diffusion in normal and globally ischemic rat brain. *Magnetic Resonance in Medicine*, 49:206–215, 2003.

[62] B Siow, I Drobnjak, A Ianus, I N Christie, M F Lythgoe, and D C Alexander. Axon radius estimation with oscillating gradient spin echo (OGSE) diffusion MRI. *diffusion-fundamentals.org*, 18:1–6, 2013.

[63] I Drobnjak, G Cruz, and D C Alexander. Optimising oscillating waveform-shape for pore size sensitivity in diffusion-weighted MR. *Microporous and Mesoporous Materials*, 178:11–14, 2013.

[64] A Ianus, B Siow, I Drobnjak, H Zhang, and D C Alexander. Gaussian phase distribution approximations for oscillating gradient spin echo diffusion MRI. *Journal of Magnetic Resonance*, 227:25–34, 2013.

[65] Chris73. Action potential, 2012.

[66] European Committee for Electrotechnical Standardization. *Medical electrical equipment Part 2-33: Particular requirements for the safety of magnetic resonance equipment for medical diagnosis*. IEC, 2 edition, 2008.

[67] A Oppelt. *Imaging Systems for Medical Diagnostic*. John Wiley and Sons, 2 edition, 2011.

[68] F X Hebrank and M Gebhardt. Safe model - a new method for predicting peripheral nerve stimulation in MRI. In *International Society for Magnetic Resonance in Medicine, Berlin, Germany*, 2007.

[69] M A Bernstein, K F King, and X J Zhou. *Handbook of MRI Pulse Sequences*. Elsevier Inc, 1 edition, 2004.

[70] E N Ivanov. *Optimization of duty cycles in Magnetic Resonance Imaging systems*. Eindhoven University of Technology, 1 edition, 2012. PhD Thesis.

[71] C A Baron and C Beaulieu. Oscillating gradient spin-echo (OGSE) diffusion tensor imaging of the human brain. *Magnetic Resonance in Medicine*, Early View, 2013.

[72] A T Van, S J Holdsworth, and R Bammer. In vivo investigation of restricted diffusion in the human brain with optimized oscillating diffusion gradient encoding. *Magnetic Resonance in Medicine*, 71(1):83–94, 2014.

[73] D G Coy and A N Garroway. Measurement of translational displacement probabilities by NMR: An indicator of compartmentation. *Magnetic Resonance in Medicine*, 14:435–444, 1990.

[74] Y Assaf, A Mayk, and Y Cohen. Displacement imaging of spinal cord using q-space diffusion-weighted MRI. *Magnetic Resonance in Medicine*, 52(5):965–978, 2004.

[75] P T Callaghan. A simple matrix formalism for spin echo analysis of restricted diffusion under generalized gradient waveforms. *Journal of Magnetic Resonance*, 129(1):74–84, 1997.

[76] D C Douglass, D W McCall, P Linse, and O Soderman. Diffusion in paraffin hydrocarbons. *The Journal of Physical Chemistry*, 62:1102–1107, 1958.

[77] W S Price. Pulsed-field gradient nuclear magnetic resonance as a tool for studying translational diffusion: Part I.basic theory. *Concepts in Magnetic Resonance*, 9:299–336, 1997.

[78] J Mattiello, P Basser, and D LeBihan. Analytical expressions for the b matrix in NMR diffusion imaging and spectroscopy. *Journal of Magnetic Resonance*, 108:131–141, 1994.

[79] C H Neuman. Spin echo of spins diffusing in a bounded medium. *The Journal of Chemical Physics*, 60(11):4508–4511, 1974.

[80] B Balinov, B Jonsson, P Linse, and O Soderman. The nmr self-diffusion method applied to restricted diffusion. simulation of echo attenuation from molecules in spheres and between planes. *Journal of Magnetic Resonance*, 104:17–25, 1993.

[81] J S Murday and R M Cotts. Self-diffusion coefficient of liquid lithium. *The Journal of Chemical Physics*, 48(11):4938–4945, 1968.

[82] P J Basser, J Mattiello, and D LeBihan. MR diffusion tensor spectroscopy and imaging. *Biophysical Journal*, 66(1):259–267, 1994.

[83] D K Jones and A Leemans. Diffusion tensor imaging. *Methods in Molecular Biology*, 711:127–144, 2011.

[84] S Mori and P Barker. Diffusion magnetic resonance imaging. *The Anamotical Record*, 257:102–109.

[85] C F Westin, S E Maier, H Mamata, A Nabavi, F A Jolesz, and R Kikinis. Processing and visualization for diffusion tensor MRI. *Medical Image Analysis*, 6:93–108, 2002.

[86] T E J Behrens, M W Woolrich, M Jenkinson, H Johansen-Berg, R G Nunes, S Clare, P M Matthews, J M Brady, and S M Smith. Characterization and propagation of uncertainty in diffusion-weighted mr imaging. *Magnetic Resonance in Medicine*, 50:1077–1088, 2003.

[87] P T Callaghan and J Stepisnik. Frequency-domain analysis of spin motion using modulated-gradient NMR. *Journal of Magnetic Resonance, Series A*, 117(1):118–122, 1995.

[88] S Peled, D G Cory, S A Raymond, D A Kirschner, and F A Jolesz. Water diffusion and compartmentation in frog sciatic nerve. *Magnetic Resonance in Medicine*, 42:911–918, 1999.

[89] H H Ong, A C Wright, S L Wehrli, E D Schwartz, N Hwang, and F W Wherli.

[90] K Setsompop, R Kimmlingen, E Eberlein, T Witzel, J Cohen-Adad, J A McNab, B Keil, M D Tisdall, P Hoecht, P Dietz, S F Cauley, V Tountchev, V Matschl, V H Lenz, K Heberlein, A Potthast, H Thein, J Van Horn, A Toga, F Schmitt, D Lehne, B R Rosen, V Wedeen, and L L Wald. Pushing the limits of in vivo diffusion MRI for the human connectome project. *NeuroImage*, 80:220–233, 2013.

[91] J A McNab, B L Edlow, T Witzel, S Y Huang, H Bhat, K Heberlein, T Feiweier, K Liu, B Keil, J Cohen-Adad, M D Tisdall, R D Folkerth, H C Kinney, and L L Wald. The human connectome project and beyond: Initial applications of 300 mt/m gradients. *NeuroImage*, 80:234–245, 2013.

[92] Y Suzuki, M Hori, K Kamiya, I Fukunaga, S Aoki, and M Van Cauteren. Estimation of the mean axon diameter and intra-axonal space volume fraction of the human corpus callosum: diffusion qspace imaging with low q-values. *Magnetic Resonance in Medical Sciences*, 2015.

[93] P P Mitra. Multiple wave-vector extensions of the NMR pulsed-field-gradient spin-echo diffusion measurement. *Physical Review B*, 51(21):15074–15078, 1995.

[94] N Shemesh and Y Cohen. The effect of experimental parameters on the signal decay in double-pgse experiments: negative diffractions and enhancement of structural information. *Journal of Magnetic Resonance*, 195:153–161, Jan 2008.

[95] E Özarslan and P J Basser. Microscopic anisotropy revealed by NMR double pulsed field gradient experiments with arbitrary timing parameters. *The Journal of Chemical Physics*, 128:154511, 2008.

[96] A V Avram, E Özarslan, J E Sarlls, and P J Basser. In vivo detection of microscopic anisotropy using quadruple pulsed-field gradient (qPFG) diffusion MRI on a clinical scanner. *NeuroImage*, 63:229–239, 2013.

[97] N Shemesh, G A Alvarez, and L Frydman. Size distribution imaging by non-uniform oscillating-gradient spin echo (NOGSE) MRI. *PLoS ONE.*, 10(7), 2015.

[98] S Portnoy, J J Flint, S J Blackband, and G J Stanisz. Oscillating and pulsed gradient diffusion magnetic resonance microscopy over an extended b-value range: Implications for the characterization of tissue microstructure. *Magnetic Resonance in Medicine*, 69:1131–1145, 2013.

[99] J Xu, H Li, K D Harkins, X Jiang, J Xie, H Kang, M D Does, and J C Gore. Mapping mean axon diameter and axonal volume fraction by MRI using temporal diffusion spectroscopy. *NeuroImage*, 103:10–19, 2014.

[100] Y Assaf and P J Basser. Composite hindered and restricted model of diffusion (CHARMED) mr imaging of the human brain. *NeuroImage*, 27:48–58, 2005.

[101] D C Alexander, P L Hubbard, M G Hall, E A Moore, M Ptito, G J Parker, and T B Dyrby. Orientationally invariant indices of axon diameter and density from diffusion MRI. *NeuroImage*, 52:1374–1389, 2010.

[102] E Panagiotaki, T Schneider, B Siow, M G Hall, M F Lythgoe, and D C Alexander. Compartment models of the diffusion MR signal in brain white matter: A taxonomy and comparison. *NeuroImage*, 59:2241–2254, 2012.

[103] J Xu, M D Does, and J C Gore. Quantitative characterization of tissue microstructure with temporal diffusion spectroscopy. *Journal of Magnetic Resonance*, 200:189–197, 2009.

[104] H Li, J C Gore, and J Xu. Fast and robust measurement of microstructural dimensions using temporal diffusion spectroscopy. *Journal of Magnetic Resonance*, 242:4–9, 2014.

[105] Y Assaf, R Z Freidlin, G K Rohde, and P J Basser. New modeling and experimental framework to characterize hindered and restricted water diffusion in brain white matter. *Magnetic Resonance in Medicine*, 52(5):965–978, 2004.

[106] D Barazany, P J Basser, and Y Assaf. In vivo measurement of axon diameter distribution in the corpus callosum of rat brain. *Brain*, 132(5):1210, 2009.

[107] S Y Huang, A Nummenmaa, T Witzel, T Duval, J Cohen-Adad, L L Wald, and J A McNab. The impact of gradient strength on in vivo diffusion mri estimates of axon diameter. *NeuroImage*, 106:464–472, 2015.

[108] D Barazany, D Jones, and Y Assaf. Axcaliber 3d. In *ISMRM Annual Meeting*, page 76, 2011. ISMRM Abstract.

[109] A Szafer, J Zhong, and J C Gore. Theoretical model for water diffusion in tissues. *Magnetic Resonance in Medicine*, 33(5):697–712, 1995.

[110] T B Dyrby, L V Soggard, M G Hall, M Ptito, and D C Alexander. Contrast and stability of the axon diameter index from microstructure imaging with diffusion MRI. *Magnetic Resonance in Medicine*, 70(3):711–721, 2013.

[111] H Zhang andd P L Hubbard, G J M Parker, and D C Alexander. Axon diameter mapping in the presence of orientation dispersion with diffusion MRI. *NeuroImage*, 56:1301–1315, 2011.

[112] M Nilsson, J Ltt, F Sthlberg, D V Westen, and H Hagsltt. The importance of axonal undulation in diffusion MR measurements: a monte carlo simulation study. *NMR in Biomedicine*, 25:795–805, 2012.

[113] U Ferizi, T Schneider, T Witzel, L L Wald, H Zhang, C A M Wheeler-Kingshott, and D C Alexander. White matter compartment models for in vivo diffusion MRI at 300 mT/m. *NeuroImage*, 118:468–483, 2015.

[114] U Ferizi, T Schneider, E Panagiotaki, G Nedjati-Gilani, H Zhang, C A M Wheeler-Kingshott, and D C Alexander. A ranking of diffusion MRI compartment models with in vivo human brain data. *Magnetic Resonance in Medicine*, 2013.

[115] A Hellerbach, V Schuster, A Jansen, and J Sommer. Mri phantoms are there alternatives to agar. *PLoS ONE*, 8:1–8, 2013.

[116] B Siow, I Drobnjak, A Chatterjee, M F Lythgoe, and D C Alexander. Estimation of pore size in a microstructure phantom using the optimised gradient waveform diffusion weighted nmr sequence. *Journal of Magnetic Resonance*, 214:51–60, 2012.

[117] M C Wapler, J Leupold, I Dragonu, D Elverfeld, M Zaitsev, and U Wallrabe. Magnetic properties of materials for MR engineering, micro-MR and beyond. *Journal of Magnetic Resonance*, 242:233–242, 2014.

[118] M Jenkinson, P Bannister, J M Brady, and S M Smith. Improved optimisation for the robust and accurate linear registration and motion correction of brain images. *NeuroImage*, 17(2):825–841, 2002.

[119] MathWorks. Constrained nonlinear optimization algorithms, 2017a.

[120] M Holz, S R Heila, and A Saccob. Temperature-dependent self-diusion coefficients of water and six selected molecular liquids for calibration in accurate 1H NMR PFG measurements. *Physical Chemistry Chemical Physics*, 2:4740–4742, 2000.

[121] H Akaike. A new look at the statistical model identification. *IEEE Transactions on Automatic Control*, 19(6):716–723, 1974.

[122] G Schwarz. Estimating the dimension of a model. *The Annals of Statistics*, 6:461–464, 1978.

[123] M Nilsson, S Lasic, D Topgaard, and C F Westin. Estimating the axon diameter from intra-axonal water diffusion with arbitrary gradient waveforms: Resolution limit in parallel and dispersed fibers. In *ISMRM Annual Meeting*, volume 24, page 663, 2016. ISMRM Abstract.

[124] H Zhang andd T Schneider, C A Wheeler-Kingshott, and D C Alexander. Noddi: Practical in vivo neurite orientation dispersion and density imaging of the human brain. *NeuroImage*, 61(4):1000–1016, 2012.

[125] P L Hubbard, F L Zhou, S J Eichhorn, and Geoffrey J M Parker. Biomimetic phantom for the validation of diffusion magnetic resonance imaging. *Magnetic Resonance in Medicine*, 73:299–305, 2015.

[126] R Caminiti, F Carducci, C Piervincenzi, A Battaglia-Mayer, G Confalone, F Visco-Comandini, P Pantano, and G M Innocenti. Diameter, length, speed, and conduction delay of callosal axons in macaque monkeys and humans: Comparing data from histology and magnetic resonance imaging diffusion tractography. *Journal of Neuroscience*, 33(36):14501–14511, 2013.

[127] T B Dyrby, William F C Baare, D C Alexander, J Jelsing, E Garde, and L V Sgaard. An ex vivo imaging pipeline for producing high- quality and high-resolution diffusion-weighted imaging datasets. *Human Brain Mapping*, 32:544–563, 2011.

[128] A S LaMantia and P Rakic. Axon overproduction and elimination in the corpus callosum of the developing rhesus monkey. *Journal of Neuroscience*, 10(7):2156–2175, 1990.

[129] P A Cook, Y Bai, S Nedjati-Gilani, K K Seunarine, M G Hall, G J Parker, and D C Alexander. Camino: Open-source diffusion-MRI reconstruction and processing. In *ISMRM Annual Meeting*, page 2759, 2006. ISMRM Abstract.

[130] M G Hall and D C Alexander. Convergence and parameter choice for monte-carlo simulations of diffusion MRI. *IEEE Trans. Medical Imaging*, 28:1354–1364, 2009.

[131] S D Santis, D K Jones, and A Roebroeck. Including diffusion time dependence in the extra-axonal space improves in vivo estimates of axonal diameter and density in human white matter. *NeuroImage*, Early View, 2016.

[132] T B Dyrby, D C Alexander, and M Ptito. Undulating and crossing axons in the corpus callosum may explain the overestimation of axon diameters with activeax. In *ISMRM-ESMRMB Joint Annual Meeting*, page 2619, 2014. ISMRM Abstract.

[133] L M Burcaw, E Fieremans, and D S Novikov. Mesoscopic structure of neuronal tracts from time-dependent diffusion. *NeuroImage*, 114:18–37, 2015.

[134] E Fieremans, L M Burcaw, H H Lee, G Lemberskiy, J Veraart, , and D S Novikov. In vivo observation and biophysical interpretation of time-dependent diffusion in human white matter. *NeuroImage*, 129:414–427, 2016.

[135] P E Thelwall, T M Shepherd, G J Stanisz, and S J Blackband. Effects of temperature and aldehyde fixation on tissue water diffusion properties, studied in an erythrocyte ghost tissue model. *Magnetic Resonance in Medicine*, 56:282–289, 2006.

[136] T M Shepherd, P E Thelwall, G J Stanisz, and S J Blackband. Aldehyde fixative solutions alter the water relaxation and diffusion properties of nervous tissue. *Magnetic Resonance in Medicine*, 62:26–34, 2009.

[137] S Richardson, B Siow, A M Batchelor, M F Lythgoe, and D C Alexander. A viable isolated tissue system: A tool for detailed mr measurements and controlled perturbation in physiologically stable tissue. *Magnetic Resonance in Medicine*, 69:1603–1610, 2013.

[138] L B Kempton, M H Gonzalez, R M Leven, W F Hughes, S Beddow, Y Santhiraj, S J Archibald, B El Hassan, S Shott, and J M Kerns. Assessment of axonal growth into collagen nerve guides containing vegf-transfected stem cells in matrigel. *The Anatomical Record*, 29(2):214–224, 2009.

[139] J O Callaghan, J Wells, S Richardson, H Holmes, Y Yu, S Walker-Samuel, B Siow, and M F Lythgoe. Is your system calibrated? MRI gradient system calibration for pre-clinical, high-resolution imaging. *PLoS ONE*, 9(5):1–9, 2014.

[140] F Sepehrband, D C Alexander, N D Kurniawan, D C Reutens, and Z Yang. Towards higher sensitivity and stability of axon diameter estimation with diffusion-weighted MRI. *NMR in Biomedicine*, 29(3):293–308, 2016.

[141] H M Fonteijn and M G Hall nd D C Alexander. A study on the validity of the tortuosity approximation for extracellular diffusion using monte carlo simulations. In *ISMRM Annual Meeting*, volume 17, page 1361, 2009. ISMRM Abstract.

[142] I O Jelescu, J Veraart, V Adisetiyo, S S Milla, D S Novikov, and E Fieremans. One diffusion acquisition and different white matter models: How does microstructure change in human early development based on WMTI and NODDI? *NeuroImage*, 107:242–256, 2015.

[143] B Lampinen, F Szczepankiewicz, J Mrtensson, D van Westen, P C Sundgren, and M Nilsson. Neurite density imaging versus imaging of microscopic anisotropy in diffusion MRI: A model comparison using spherical tensor encoding. *NeuroImage*, 147:517–531, 2017.

[144] D Benjamini, M E Komlosh, L A Holtzclaw, U Nevo, and P J Basser. White matter microstructure from nonparametric axon diameter distribution mapping. *NeuroImage*, 135:333–344, 2016.

[145] D Novikov, J H Jensen, J A Helpern, and E Fieremans. Revealing mesoscopic structural universality with diffusion. *PNAS*, 111(14):5088–5093, 2014.

[146] E Panagiotaki, M G Hall, H Zhang, B Siow, M F Lythgoe, and D C Alexander. High-fidelity meshes from tissue samples for diffusion MRI simulations. *Medical Image Computing and Computer-Assisted Intervention, MICCAI 2010, Lecture Notes in Computer Science*, 6362/2010:404–411, 2010.

[147] T Duval, J A McNab, K Setsompop, T Witzel, T Schneider, S Y Huang, B Keil, E C Klawiter, L L Wald, and J Cohen-Adad. In vivo mapping of human spinal cord microstructure at 300 mT/m. *NeuroImage*, 118:494–507, 2015.

[148] C Mathys, J Aissa J, Z Meyer, G Horste, D C Reichelt, G Antoch, B Turowski, H P Hartung, K A Sheikh, and H C Lehmann. Peripheral neuropathy:

assessment of proximal nerve integrity by diffusion tensor imaging. *Muscle Nerve*, 48:889–896, 2013.

[149] B Kim, A Srinivasan, B Sabb, E L Feldman, and R Pop-Busui. Diffusion tensor imaging of the sural nerve in normal controls. *Clinical Imaging*, 38:648–754, 2014.